AD-A239 019

(2)

NORTHWESTERN UNIVERSITY
Department of Civil Engineering
McCormick School of Engineering and Applied Science
The Technological Institute
Evanston, Illinois 60208-3109

1851

DTIC

AFOSR-TR- 91 0674

DYNAMIC RESPONSE OF EMBEDDED STRUCTURES
AFOSR-89-0255

FINAL REPORT

AIR [illegible]
NOTI[illegible]

12

July 1991

Best Available Copy

91-06400

91 [illegible] 02

DYNAMIC RESPONSE OF EMBEDDED STRUCTURES
AFOSR-89-0255

COPY INSPECTED 4

FINAL REPORT

Submitted to

Lt Col Steven C. Boyce
Air Force of Scientific Research
Bolling Air Force Base
Washington, D. C. 20332

Dist
A-1

Submitted by

Professor Leon M. Keer
Professor Surendra P. Shah
Avraham N. Dancygier

Department of Civil Engineering
The Robert R. McCormick School of Engineering and
Applied Science in The Technological Institute
Northwestern University
Evanston, Illinois 60208

July 1991

UNCLASSIFIED
SECURITY CLASSIFICATION OF THIS PAGE

REPORT DOCUMENTATION PAGE

1a. REPORT SECURITY CLASSIFICATION UNCLASSIFIED

1b. RESTRICTIVE MARKINGS

2a. SECURITY CLASSIFICATION AUTHORITY

2b. DECLASSIFICATION/DOWNGRADING SCHEDULE

3. DISTRIBUTION/AVAILABILITY OF REPORT Approved for public release; distribution unlimited.

4. PERFORMING ORGANIZATION REPORT NUMBER(S)

5. MONITORING ORGANIZATION REPORT NUMBER(S)

6a. NAME OF PERFORMING ORGANIZATION
Northwestern University
Dept. of Civil Engineering

6b. OFFICE SYMBOL *(If applicable)*

7a. NAME OF MONITORING ORGANIZATION AFOSR/NA

6c. ADDRESS *(City, State and ZIP Code)*
Evanston, Illinois 60208

7b. ADDRESS *(City, State and ZIP Code)*
Building 410
Bolling AFB, Washington, D. C. 2033206488

8a. NAME OF FUNDING/SPONSORING ORGANIZATION AIR FORCE OFFICE OF SCIENTIFIC RESEARCH

8b. OFFICE SYMBOL *(If applicable)* NA

9. PROCUREMENT INSTRUMENT IDENTIFICATION NUMBER AFOSR-89-0255

8c. ADDRESS *(City, State and ZIP Code)*
Building 410
Bolling AFB, Washington, D. C. 20332-6488

10. SOURCE OF FUNDING NOS.

PROGRAM ELEMENT NO.	PROJECT NO.	TASK NO.	WORK UNIT NO.
6/1102F	~~2320~~ 2302	C1	

11. TITLE *(Include Security Classification)* Dynamic Response of Embedded Structures

12. PERSONAL AUTHOR(S) Leon M. Keer, Surendra P. Shah, and Avraham N. Dancygier

13a. TYPE OF REPORT Final

13b. TIME COVERED FROM 89-1-15 TO 91-1-15

14. DATE OF REPORT *(Yr., Mo., Day)* 91-7-15

15. PAGE COUNT 278

16. SUPPLEMENTARY NOTATION

17. COSATI CODES

FIELD	GROUP	SUB. GR.

18. SUBJECT TERMS *(Continue on reverse if necessary and identify by block number)*
Dynamic Loading
Embedded Structures
Soil-Structure Interaction

19. ABSTRACT *(Continue on reverse if necessary and identify by block number)*

Structures that have to resist impact loading are often designed to be embedded under soil backfill. The backfill attenuates the external surface load and decreases the free field stresses at the level of the structure. Physical mechanisms which are associated with the soil-structure interaction further affect the loading and response of the structure, and are important to understand for better, more efficient design of these structures.

The response to an external surface impact of a structure with a reinforced concrete roof, embedded in a shallow depth of burial, was studied here. The research employed an experimental investigation of a small scale radial model and numerical analysis based on the finite element method to evaluate the mechanisms associated with the experimental results.

(continued on reverse side)

20. DISTRIBUTION/AVAILABILITY OF ABSTRACT
UNCLASSIFIED/UNLIMITED ☒ SAME AS RPT. ☐ DTIC USERS ☐

21. ABSTRACT SECURITY CLASSIFICATION UNCLASSIFIED

22a. NAME OF RESPONSIBLE INDIVIDUAL Lt Col Steven C. Boyce

22b. TELEPHONE NUMBER *(Include Area Code)* (202) 767-6963

22c. OFFICE SYMBOL AFOSR/NA

DD FORM 1473, 83 APR EDITION OF 1 JAN 73 IS OBSOLETE.

UNCLASSIFIED
SECURITY CLASSIFICATION OF THIS PAGE

19. Abstract (continued)

The small scale experimental system consisted of a circular model Plexiglas cylinder supporting a reinforced micro-concrete roof, and embedded under a shallow depth of burial (DOB) of dry Ottawa sand. The surface of the sand backfill was subjected to an impact, generated by a drop of a steel ball on an aluminum circular target plate. Precise measurements of the roof motion and load over the roof and in the free field were acquired. The small scale system enabled an extensively instrumented laboratory investigation of the problem. This small scale result was valuable because such precise experimental measurements are not always possible in field experiments of similar larger scale systems.

The numerical analysis simulated both the laboratory small scale system as well as a field soil-structure test of larger dimensions, different geometry, and higher external load.

The experimental results identified stages of the response of the structure. They indicated the importance of the first peak of the incident impact load to the early-time structural response. A general trend of releasing the load from the central region of the deflecting structure is contributed by soil-structure mechanisms, related to the motion of the structure, and to a possible tension wave reflected from the bottom surface of the roof slab. The interface pressure loading the structure is first affected by the velocity of the roof center through a mechanism associated with the acoustic impedance of the soil medium. Subsequent developing displacement causes arching in the soil over the structure, which further decreases the load acting on the central portion of the roof. The release of the load limits the impulse acting on the structure and might prevent further or larger structural damage.

A finite element simulation of a similar larger scale system with different geometry, and higher external impact indicated soil-embedded structure response, which consiste of similar stages.

Dimensional analysis of the model system proposes extrapolation ratios and a methodology to evaluate the distortion due to gravitational effects, for extrapolatio of the small scale model results into a larger scale system. In cases of dynamic phenomena which are dominant, compared to the static effect caused by gravitational acceleration, and in the lack of gravity scaling, dimensional analysis suggests the distortion in the results of the small scale model are in the range of the experimental error, and therefore are relatively insignificant.

ABSTRACT

Dynamic Response of Embedded Structures

AFOSR-89-0255

Structures that have to resist impact loading are often designed to be embedded under soil backfill. The backfill attenuates the external surface load and decreases the free field stresses at the level of the structure. Physical mechanisms which are associated with the soil-structure interaction further affect the loading and response of the structure, and are important to understand for better, more efficient design of these structures.

The response to an external surface impact of a structure with a reinforced concrete roof, embedded in a shallow depth of burial, was studied here. The research employed an experimental investigation of a small scale radial model and numerical analysis based on the finite element method to evaluate the mechanisms associated with the experimental results.

The small scale experimental system consisted of a circular model Plexiglas cylinder supporting a reinforced micro-concrete roof, and embedded under a shallow depth of burial (DOB) of dry Ottawa sand. The surface of the sand backfill was subjected to an impact, generated by a drop of a steel ball on an aluminum circular target plate. Precise measurements of the roof motion and load over the roof and

in the free field were acquired. The small scale system enabled an extensively instrumented laboratory investigation of the problem. This small scale result was valuable because such precise experimental measurements are not always possible in field experiments of similar larger scale systems.

The numerical analysis simulated both the laboratory small scale system as well as a field soil-structure test of larger dimensions, different geometry, and higher external load.

The experimental results identified stages of the response of the structure. They indicated the importance of the first peak of the incident impact load to the early-time structural response. A general trend of releasing the load from the central region of the deflecting structure is contributed by soil-structure mechanisms, related to the motion of the structure, and to a possible tension wave reflected from the bottom surface of the roof slab. The interface pressure loading the structure is first affected by the velocity of the roof center through a mechanism associated with the acoustic impedance of the soil medium. Subsequent developing displacement causes arching in the soil over the structure, which further decreases the load acting on the central portion of the roof. The release of the load limits the impulse acting on the structure and might prevent further or larger structural damage.

A finite element simulation of a similar larger scale system with different

geometry, and higher external impact indicated soil-embedded structure response, which consisted of similar stages.

Dimensional analysis of the model system proposes extrapolation ratios and a methodology to evaluate the distortion due to gravitational effects, for extrapolation of the small scale model results into a larger scale system. In cases of dynamic phenomena which are dominant, compared to the static effect caused by gravitational acceleration, and in the lack of gravity scaling, dimensional analysis suggests the distortion in the results of the small scale model are in the range of the experimental error, and therefore are relatively insignificant.

CONVERSION FACTORS FOR UNITS OF MEASUREMENT

Units of measurement used in this work can be converted as follows:

Multiply	By	To Obtain
	Metric (SI) to Inch-Pound	
centimeters	0.3937	inches
meters	3.28084	feet
meters	39.37008	inches
centimeters per second	0.3937	inches per second
meters per second	3.28084	feet per second
g's (acceleration of gravity)	32.174	feet per second squared
kilograms per cubic meter	0.06243	pounds (mass) per cubic foot
kilopascals	0.1450377	pounds (force) per square inch
megapascals	145.0377	pounds (force) per square inch
newtons	0.2248	pounds
	Inch-Pound to Metric (SI)	
inches	2.54	centimeters
inches	0.0254	meters
feet	0.3048	meters
square inches	6.4516	square centimeters
inches per second	0.0254	meters per second
feet per second	0.3048	meters per second
g's (acceleration of gravity)	9.80665	meters per second squared
pounds (mass) per cubic foot	16.01846	kilograms per cubic meter
pounds (force)-second squared per inch per cubic inch	10687324	kilograms per cubic meter
pounds (force) per square inch	6.894757	kilopascals
pounds (force) per square inch	0.006895	megapascals
pounds	4.4484	newtons

TABLE OF CONTENTS

List of Tables xi

List of Figures xii

CHAPTER 1

INTRODUCTION 1

1.1 Presentation of the Problem and Report Layout. 1

1.2 Literature Survey 6

CHAPTER 2

EXPERIMENTS 16

2.1 Description of the Experimental System. 16

2.1.1 Experimental Setup. 17

2.1.2 Equipment. 19

2.2 Test Plan. 20

2.2.1 External Impact Measurements. 20

2.2.1.1 Approximation for the Total Load Induced under the Target Plate. 23

2.2.2 Free Field Measurements. 26

2.2.3 Experiment with an Elastic Plexiglas Roof Slab. 27

2.2.4 Experiments with Reinforced Micro-concrete Roof Slabs. 28

2.2.4.1 Reinforced micro-concrete slabs. 28

2.2.4.2 Boundary conditions. 30

2.2.4.3 Test procedure. 34

2.3 Results. 36

2.3.1 Experiment with an Elastic Plexiglas Roof Slab. 36

2.3.2 Experiments with Reinforced Micro-concrete Roof Slabs. 37

2.4 Discussion. 40

2.4.1 Physical Mechanisms and Phenomena that are Expected to be involved. 40

2.4.2 Sequence of the Phenomena in the Response of the Soil-Structure System. 43

2.4.3 Influence of the Involved Phenomena on the Soil-Structure Response. 49

2.4.4 Influence of the Boundary Conditions. 51

2.4.5 Effect of DOB. 53

2.5 The Value of the Results from the Small Scale Experimental System . . 54

CHAPTER 3

NUMERICAL ANALYSIS 99

3.1 Description of the Numerical Method. 99

3.2 Numerical Models and Simulations. 103

3.2.1 External Input Load for the Soil-Structure System. 103

3.2.2 Numerical Model of Plexiglas. 103
3.2.3 Numerical Model of Sand. 105
3.2.3.1 Literature survey of experiments with 20-30 Ottawa Sand. 109
3.2.3.2 Calibration of the numerical model for sand. 111
3.2.4 Numerical Simulation of the Soil-Elastic Structure System. 112
3.2.5 Numerical Model of Reinforced Concrete. 113
3.2.6 Numerical Simulation of the Soil-Micro-concrete Structure System118
3.3 Discussion of the Numerical Simulations for the Experimental Results. 120
3.3.1 Displacement of the Roof Slab. 120
3.3.2 Transverse Stresses through the Slab. 121
3.3.3 Soil-Structure Displacements. 121
3.3.4 Shear Stresses in the Soil above the Structure. 122
3.3.5 Effect of the Boundary Conditions. 123
3.3.6 Effect of the Soil-Structure Interface Properties. 124

CHAPTER 4

SIMULATION AND ANALYSIS OF A LARGER SCALE SYSTEM 166
4.1 The Reference System and its Numerical Model. 166
4.1.1 Description of the Soil-Structure System. 166
4.1.2 Numerical Modeling of the Soil-Structure System. 167
4.1.2.1 Geometrical modeling. 167
4.1.2.2 Material modeling. 168

4.1.2.3 Load modeling. 169
4.2 Results. 171
4.2.1 Comparison of the Numerical and Experimental Results. 171
4.2.2 Discussion. 173

CHAPTER 5

CONCLUSIONS 191
5.1 Response of A Soil-Structure System. 191
5.2 Application of the Small Scale System Observations and of the Computer Code. 194

APPENDIX A

MEASUREMENTS OF LOADS 196

APPENDIX B

MEASUREMENTS OF DYNAMIC DISPLACEMENTS 200

APPENDIX C

DIMENSIONAL ANALYSIS OF A SMALL SCALE SOIL-STRUCTURE SYSTEM

APPENDIX D

EXPERIMENTAL RESULTS 235

REFERENCES 246

PUBLICATIONS 255

List of Tables

Table		Page
2-1	Properties of the Micro-Concrete Slabs	59
2-2	Sequence of the Impactor Hits	60
2-3	Method of Data Acquisition	61
2-4	Wave Velocities and Propagation Time in Micro-Concrete Slabs	62
2-5	Extrapolation Ratios from a Small Scale System to a Larger Scale System	63
B-1	First Five Eigenvalues of kl for a Cantilever Beam	203
C-1	Three Possible Prototype/Model Ratios	227

List of Figures

Figure Page

CHAPTER 1

1-1 Terzaghi's model for arching over a trap-door 14

1-2 Arching over a buried structure - pattern of the principal stresses in the numerical analysis of Yankelevsky 15

CHAPTER 2

2-1 Experimental set-up for a small scale model of a soil-embedded structure system 64

2-2 External load measurement set-up 65

2-3-a Pressure distribution under the target plate (H = 25 inches) 66

2-3-b Pressure distribution under the target plate (H = 25 inches) 67

2-4 Equivalent SDOF system for estimation of the total load induced under the target plate 68

2-5 The total force, F_{sand}, applied under the target plate (H = 25 inches) 69

2-6 Set-up for measurements of the free field vertical stress distribution 70

2-7-a Free field pressure; DOB = 3 inches, H = 25 inches 71

2-7-b Free field pressure; DOB = 2.5 inches, H = 25 inches 72

List of Figures

Figure		Page
2-8	Soil-structure experimental set-up	73
2-9	Sieved portions of the sand used for the micro-concrete specimens	74
2-10-a	Form and reinforcement ready for casting of micro-concrete slabs	75
2-10-b	Casting of micro-concrete slabs - detailed view of the double reinforcement placed in the form (The spot welded meshes are held apart with vertical spacers)	75
2-10-c	Removal of the specimen from the form after casting	76
2-10-d	Casting of micro-concrete slabs - the final product, a doubly reinforced micro-concrete slab (Actual dimensions: 0.45 inch thick, 6 inches diameter)	76
2-11	Set-up for testing the micro-concrete slabs under direct uniform pressure	77
2-12-a	Details of a structure with a SIMPLY SUPPORTED roof	78
2-12-b	Detail of the model structure with a SIMPLY SUPPORTED roof	79
2-13-a	Details of a structure with a CLAMPED roof	80
2-13-b	Detail of the model structure with a CLAMPED roof	81
2-14-a	Free field Vibration of a simply supported slab	82

List of Figures

Figure **Page**

2-14-b Free field Vibration of a clamped slab 83

2-15 Displacement records of the roof center and of the rigid structure (Plexiglas roof) 84

2-16 Pressure and velocity signals of the Plexiglas roof (DOB = 3 inches, H = 25 inches) 85

2-17 Response of the Plexiglas roof (DOB = 3 inches, H = 25 inches) 86

2-18 Pressure at buried roof level v.s. free field (Plexiglas roof; DOB = 3 inches, H = 25 inches) 87

2-19 Impulse records over the Plexiglas roof (DOB = 3 inches, H = 25 inches) 88

2-20 Pressure over the clamped roof of test 8 (5th hit) v.s. free field. 89

2-21 Response of the clamped roof in test 8 (5th hit) 90

2-22 Impulse records over the clamped roof in test 8 (5th hit) 91

2-23 Load-displacement curves of micro-concrete plates under pressure applied at different rates 92

2-24 Pressure induced under the target plate center in the tests with DOB = 3 inches (H = 25 inches) 93

List of Figures

Figure **Page**

2-25 Simply supported v.s. clamped roof - displacement of the center (DOB = 3 inches; H = 25 inches) 94

2-26 Simply supported v.s. clamped roof - impulse records. (DOB = 3 inches; H = 25 inches) 95

2-27 Pressure under the target plate center - H = 25 inches, DOB = 2.5 inches 96

2-28 Simply supported v.s. clamped roof - displacement of the roof center (DOB = 2.5 inches; H = 25 inches) 96

2-29 Simply supported v.s. clamped roof - impulse records. (DOB = 2.5 inches; H = 25 inches) 97

2-30 Impulse records over roof slabs at different DOB 98

CHAPTER 3

3-1 Input of the external pressure in the finite element analysis 124

3-2 Axisymmetric shell element 125

3-3 Free vibration of a simply supported PLEXIGLAS slab. (Displacement of the slab center; $E = 3.25 \cdot 10^5$ psi, h = 0.235 inch) 126

3-4 Numerical modeling of soil 127

List of Figures

Figure **Page**

3-5 Bulk modulus, K, as a function of the volumetric strain, ϵ_v during loading of Ottawa sand - experimental measurements[28,29,38,39,50,53] and actual values used for the FEM analysis 128

3-6 Bulk modulus, K, as a function of the volumetric stress, σ_v during unloading of Ottawa sand - experimental measurements[28,29,38,39,50,53] and actual values used for the FEM analysis 129

3-7 Loading and unloading curves for numerical modeling of Ottawa sand 130

3-8 Yield surface for Ottawa sand - experimental measurements and actual values used for the FEM analysis 131

3-9 Finite elements mesh for numerical modeling of the free field. 132

3-10 Free field pressure at the center - numerical v.s. experimental results (DOB = 3 inches; H = 25 inches) 133

3-11 Free field pressure 2 inches off center - numerical v.s. experimental results (DOB = 3 inches; H = 25 inches) 134

3-12 Free field pressure 2.5 inches off center - numerical v.s. experimental results (DOB = 3 inches; H = 25 inches) 135

3-13 Finite elements mesh for numerical modeling of the soil-elastic structure system 136

List of Figures

Figure		Page
3-14	Displacement of the roof center - FEM analysis v.s. experimental results (Plexiglas roof; DOB = 3 inches; H = 25 inches)	137
3-15	Velocity of the roof center - FEM analysis v.s. experimental results (Plexiglas roof; DOB = 3 inches; H = 25 inches)	138
3-16	Pressure at the roof center - FEM analysis v.s experimental results (Plexiglas roof; DOB = 3 inches; H = 25 inches)	139
3-17	Pressure over the roof edge - FEM analysis v.s experimental results (Plexiglas roof; DOB = 3 inches; H = 25 inches)	140
3-18	Finite element mesh model of a simply supported circular reinforced concrete slab	141
3-19	Forces of the reinforcing bars at an arbitrary cross-section	142
3-20	Normalized loading and unloading curves for numerical modeling of micro-concrete (Normalized stress = σ_v/f'_c)	143
3-21	Yield surface for the numerical modeling of micro-concrete	144
3-22	Vibration of a simply supported micro-concrete slab	145
3-23	Time record of the uniformly distributed high rate pressure over a micro-concrete slab	146
3-24	Mid-point displacement of the slab under a high rate, uniformly distributed pressure (f'_c = 6500 psi, ν = 0.2, h = 0.47 inch)	147

List of Figures

Figure **Page**

3-25 FEM analysis of test 6, 2^{nd} drop: Pressure input under the center of the target plate 148

3-26 Finite elements mesh for modeling of test No. 6 149

3-27 FEM analysis v.s. experimental results (test 6, 2^{nd} drop): Displacement of the roof center 150

3-28 FEM analysis v.s. experimental results (test 6, 2^{nd} drop): Velocity of the roof center 151

3-29 FEM analysis v.s. experimental results (test 6, 2^{nd} drop): Pressure at the center of the roof 152

3-30 FEM analysis v.s. experimental results (test 6, 2^{nd} drop): Pressure at the edge of the roof 153

3-31 Vertical (transverse) stresses in the slab center (Numerical analysis of test 6, 2^{nd} drop; free sliding at soil-structure interface) 154

3-32 Vertical displacements at the sand-roof interface, 0.5 inch from center (Simulation of test 6, 2^{nd} drop) 155

3-33 FEM analysis - shear stresses, τ_{ry}, in the soil over the roof (Plexiglas roof; DOB = 3 inches; H = 25 inches) 156

3-34 Pressure distribution above the roof level. (Numerical analysis; Plexiglas roof; DOB = 3 inches; H = 25 inches) 157

List of Figures

Figure **Page**

3-35 Shear stresses, τ_{ry}, in the soil elements over the roof. (Free sliding at the roof-sand interface; Simulation of test 6, 2^{nd} drop) 158

3-36 Pressure distribution above the roof level. (Numerical analysis of m.c. roof, test 6, 2^{nd} hit) 159

3-37 Numerical analysis of a simply supported v.s. clamped micro-concrete roof - center displacement 160

3-38 Numerical analysis of a simply supported v.s. clamped micro-concrete roof - vertical pressure at the center of the roof 161

3-39 Numerical analysis of a simply supported v.s. clamped micro-concrete roof - vertical pressure over the edge of the roof 162

3-40 FEM analysis of test 6, (2^{nd} drop) - effect of the soil-structure interface properties on the displacement of the roof center 163

3-41 FEM analysis of test 6, (2^{nd} drop) - effect of the soil-structure interface properties on the vertical pressure at the roof center 164

3-42 FEM analysis of test 6, (2^{nd} drop) - effect of the soil-structure interface properties on the vertical pressure over the edge of the roof 165

CHAPTER 4

4-1 Finite element mesh for the numerical modeling of the test which was performed by Kiger, Eagles, and Baylot[27] 175

List of Figures

Figure **Page**

4-2 Numerical modeling of a larger scale test[27] - Loading and unloading curves of concrete 176

4-3 Numerical modeling of a larger scale test[27] - Yield surface of concrete 177

4-4 Numerical modeling of a larger scale test[27] - Loading and unloading curves of the sand 178

4-5 Numerical modeling of a larger scale test[27] - Yield surface of the sand 179

4-6 Numerical modeling of a larger scale test[27] - Input pressure at the surface (assumed uniformly distributed) 180

4-7 Numerical modeling of a larger scale test[27] - Displacement of the roof center 181

4-8 Numerical modeling of a larger scale test[27] - Pressure at the center 182

4-9 Numerical modeling of a larger scale test[27] - Pressure over the roof 7 inches from the center 183

4-10 Numerical modeling of a larger scale test[27] - Pressure over 11 inches from the center 184

4-11 Numerical modeling of a larger scale test[27] - Pressure over the support of the roof 185

4-12 Numerical modeling of a larger scale test[27] - Vertical (transverse) stresses across the roof center cross-section 186

List of Figures

Figure **Page**

4-13 Numerical modeling of a larger scale test[27] - Pressure and velocity at the center 187

4-14 Numerical modeling of a larger scale test[27] - Pressure distribution over the roof 188

4-15 Numerical modeling of a larger scale test[27] - Pressure over the roof and motion records of the roof center ... 189

4-16 Numerical modeling of a larger scale test[27] - Shear stresses in the soil above the roof 190

APPENDIX A

A-1 Load cells measurements configuration 198

A-2 Output of the load cells, located under the target plate as described in Fig. A-1 199

APPENDIX B

B-1 Set-up for the dynamic calibration test 208

B-2(a) Displacement of a cantilever at L = 6 5/8 inches 209

B-2(b) Velocity of a cantilever at L = 6 5/8 inches 209

B-2(c) Acceleration of a cantilever at L = 6 5/8 inches 209

B-3(a) Displacement of a cantilever at L = 8 inches 210

List of Figures

Figure **Page**

B-3(b) Velocity of a cantilever at L = 8 inches 210

B-3(c) Acceleration of a cantilever at L = 8 inches 210

B-4(a) Displacement of a cantilever at L = 9 7/16 inches 211

B-4(b) Velocity of a cantilever at L = 9 7/16 inches 211

B-4(c) Acceleration of a cantilever at L = 9 7/16 inches 211

APPENDIX C

C-1 Soil-structure system for dimensional analysis 228

C-2 Distortion in displacement modeling; h = 0.38 inch, x_m(total) = 0.01 inch (clamped slab) 229

C-3 Distortion in displacement modeling; h = 0.38 inch, x_m(total) = 0.04 inch (simply supported slab) 230

C-4 Distortion in stress modeling; h = 0.5 inch, σ_m(total) = 100 psi 231

C-5 Distortion in stress modeling; h = 0.5 inch, σ_m(total) = 25 psi 232

C-6(a) Distortion in modeling of time dependent variables 233

C-6(b) Distortion in modeling of time dependent variables 234

APPENDIX D

List of Figures

Figure		Page
D-1	Pressure records over a simply supported roof in test 2 v.s. free field (4th hit)	236
D-2	Response of the simply supported roof in test 2	237
D-3	Impulse records over a simply supported roof in test 2 (4th hit)	238
D-4	Pressure over the simply supported roof in test 6 (4th hit) v.s. free field	239
D-5	Response of the simply supported roof in test 6 (4th hit)	240
D-6	Impulse records over the simply supported roof in test 6 (4th hit)	241
D-7	Pressure records over the clamped roof in test 8 v.s. free field (3rd hit)	242
D-8	Response of a clamped roof in test 8 (3rd hit)	243
D-9	Impulse records over a clamped roof in test 8 (3rd hit)	244
D-10	Pressure induced under the target plate center in the tests with DOB = 2.5 inches	245

CHAPTER 1

INTRODUCTION

1.1 Presentation of the Problem and Report Layout.

This report summarizes a study of the response of a soil-embedded structure system, which is subjected to a short impact applied at the soil surface. In the absence of a buried structure, those stresses induced in a granular medium (soil) subjected to an external dynamic load (e.g., explosive load) are denoted as the "free field stresses". When a structure is embedded in the soil the field stresses, induced under the same external load, differ from the free field stresses, and they now are also affected by the response of the structure. The response of the structure, which is affected by the stresses acting on it, is called *soil-structure interaction*.

Four basic phenomena were observed to influence the total response of the system:

1. The external loading, which can be either static or dynamic. In the present study the external loading is an impact load applied at the soil surface. That generates a compression wave, which propagates into the soil medium. By itself it constitutes the incident free field stress distribution.
2. A tension wave reflected from the bottom free surface of the structural element. In the case of an impact generated at the soil surface, that element is the roof of the embedded structure. Until the arrival of the reflected wave

to the upper surface of the roof, the incident wave is amplified at the initially rigid soil-structure interface. However, since the velocity of the elastic wave in the structure is relatively high, the reflected tension wave reaches the soil-structure interface at a relatively early time of the response and tends to decrease the pressure level.

3. The structural element, which also forms a physical boundary of the soil, gains velocity upon being hit. Thus, as long as there is no gap between the structure and the soil particles, their velocity is dictated by their boundary, that is, the structure. The interface pressure on the structure is, therefore, influenced also by the velocity of the interface: When the velocity of the soil particles (at the interface) increases, the interface pressure decreases, and vice versa. The variation in the interface pressure is considered relative to the free field pressure at the same location.

4. When the external load is static a phenomenon called *arching* has been observed. Due mainly to its shear capacity, the soil transfers the load from the more flexible parts of the structure to its more rigid parts, creating an arch-like stress field over the structure that is caused by the displacement of the structure. Large scale experiments indicate that dynamic soil-structure interaction occurs. They also indicate the transfer of load from the more flexible parts of the structure (mid-span of the roof) to its rigid supports. This behavior indeed resembles arching as observed in the static cases.

These mechanisms and the embedded structure behavior are coupled because they influence the response of the structure, and are also initiated by it. Their influence may differ according to their timing. For example, prior to the development of a structural displacement sufficient to cause arching, the structure will for dynamic loads, accelerate and gain velocity, thereby defining a moving boundary for the pressure wave propagating in the soil. The possibility of initiating the development of arching may occur as a result of this wave. At some subsequent time the structure might rebound, gaining an upward velocity, and altering the stress field which was initially created by the prior occurrence of the mechanisms described above.

In the present study, better understanding of these fundamental phenomena is sought through a small scale experimental system. By closely monitoring the loads over the buried structure and recording its associated velocity and displacement, appropriate conclusions may be drawn regarding the existence and influence of these mechanisms on the soil-structure system.

The second part of this chapter is a literature survey detailing the various approaches to the problem and the pertinent observations and conclusions drawn by other researchers. The experimental part of this research is described in Chapter 2, which includes a description of the experimental setup, the test plan, results and the conclusions. The last section of Chapter 2 discusses the value of the results obtained in the small scale system, as reflected by the pertinent scaling considerations.

Based on the experimental results, a non-linear, dynamic, finite element computer code, "SAMSON2", was calibrated and used for further numerical analysis. The code, the numerical parameters used, and the calibration process are described in Chapter 3. The parameters of the materials models were calibrated according to the experimental results of the small scale system. Further output of the numerical analysis of the system, such as the shear stresses in the soil, or the vertical stresses in the soil adjacent to the structure, was obtained. These records were not measured in the experiments, and contributed additional, and better insight into the study of the soil-structure system.

Chapter 4 presents the application of the computer program to further analytical study of the similar, but larger scale problem of a soil-embedded structure system subjected to an impact load. A reference field test which had planar geometry of larger dimensions, and a higher external load, generated by an explosive charge, was simulated numerically. The significant difference between this soil-structure system and the smaller one was the level of the external load. This difference was reflected in the results of the analysis by the higher initial loading of the structure. However, the mechanisms which occurred in the smaller scale system, were also observed in the larger reference system.

The small scale laboratory experiments together with the subsequent numerical analysis indicate patterns of behavior, which are typical to the response of a shallow embedded structure, subjected to an external impact. They emphasize the dominant effect of the early-time response, and the succeeding influence of the later mechanisms. These are summarized in the closure, Chapter 5.

1.2 Literature Survey

The response of a structure to external load is measured by its deflections, strains, and ultimately, by its capacity to sustain the load. Embedded structures are usually constructed inside an excavation in the soil, which is then backfilled around and over the structure. In this case the load is usually not acting directly on the structure, but on and through the soil in which it is embedded. Load may be applied to the soil surface, as in the case of a railroad over a conduit, or it may be an external explosive load. It can also be a lateral load which is typical for earthquakes. The response of the embedded structure is caused and affected by the load induced on it. However, because that load is applied through the soil it is also affected by the response of the soil and by its strain field, and the state of the soil is influenced by the response of the structure embedded in it. This coupled behavior is called soil-structure interaction.

Early works on soil-structure interaction related to embedded structures dealt only with external static loads. In his book, Terzaghi[47] analyzed experimental observations which indicated the formation of failure shear planes above a horizontal trap-door that was displaced uniformly downward (Fig. 1-1). This example demonstrated the influence of the structural displacement on the load acting on it: Assuming development of shear stresses along the failure shear planes, and their relation with the vertical and horizontal stresses, Terzaghi suggested the following expression for the average vertical pressure, p, over the deflecting trap-door:

$$p=\frac{B(\gamma-\frac{C}{B})}{K\tan\phi}\left(1-e^{-K\tan\phi\cdot\frac{D}{B}}\right)+q\cdot e^{-K\tan\phi\cdot\frac{D}{B}} \tag{1.1}$$

where: p is the average pressure over the trap-door (p = σ_v(Z=D)).

B is half of the trap-door span.

γ is the soil weight density.

C is the soil cohesion.

K is the lateral pressure coefficient.

ϕ is the internal friction angle.

D is the depth from the surface to the structure.

q is a uniform external pressure on the surface.

Although equation 1.1 was developed for a particular case and under certain assumptions, it is representative of the influence of a buried structure's deflection on the average load acting on it:

a. The larger the depth to span ratio (D/B) the smaller the load.

b. Beyond a certain depth to span ratio (~5) the influence of the external load, q, disappears, and the average load becomes constant and equal to $\frac{B\gamma-C}{K\tan\phi}$.

c. The average load over the structure decreases as the cohesion and angle of internal friction of the soil increase.

These conclusions remain essentially the same when the expression for the average pressure, p, is compared with the free field pressure at the same level, $q + \gamma D$. Such a comparison shows that the pressure level over the relatively flexible structure to be less than that of the free field. To maintain vertical equilibrium, the pressure at both sides of the structure must increase.

Using a similar approach[1,2,34,41] exponential decrease of the pressure over a buried structure has also been suggested by other researchers. This approach, which assumes that shear planes have already developed in the soil provides a basic understanding for the mechanism causing the load reduction above a buried structure which settles relatively to the surrounding soil, and give an estimate of the overall load acting on the structure. The failure mechanism is one in which shear stresses act along the shear planes thereby reducing the load acting on the structure below.

Formation of failure shear planes, however, is not essential for the existence of this phenomenon of pressure decrease over the structure. As it was observed in experimental studies with static load[21,23,33,26,27,45], the pressure acting on a relatively flexible structure decreases while the pressure at both sides increases even before the soil reaches a state of failure. Numerical analyses[14,20,44,55] show that the distribution of the principal compression stresses in the soil above the structure constructs an arch action (Figure 1-2). Thus, this phenomenon of decreasing pressure over a relatively flexible buried structure is commonly referred to as *positive* or *active arching*. In the opposite case when the structure is relatively rigid, the pressure over the structure (or rigid structural elements) increases (relative to the adjacent medium). This case is referred to as *negative* or *passive arching*. It was further found, in the studies mentioned above, that arching in soils is enabled mainly through shear stresses, which at a high level of load and structural deflection, generate failure shear planes in the soil. Increasing depth of burial (DOB) causes increasing arching, i.e., decrease of the load over the flexible structure, yet arching was also observed at a DOB as shallow as 20% of the structure span, L[19].

The extensive research of the static phenomenon lead to its fundamental understanding and has been used as a basis for the research of the behavior of a soil-embedded structure subjected to a dynamic external load. Kiger and Getchell performed a series of tests in which reinforced concrete box-type structures where buried under a relatively shallow DOB (≤L/2) of two different backfills, and subjected to external explosive loads generated by High Explosive Simulation Technique (HEST)[18,19,25]. These notable experiments contributed important information to the research of the behavior of shallow buried structures. In three tests (HEST 1, 3, and 4) the roof of the structure was damaged but did not totally collapse. In these tests the pressure records that were measured at the roof center were different from those that were measured over the supporting walls. The pressure over the center decreased and was lower than that over the walls. This difference occurred late in the response, within 1 to 5 msec after the roof was hit by the compression wave and was reflected in a similar way on the corresponding calculated impulse records. These results were obtained at a DOB of L/2, but even when the DOB was as shallow as 0.2L (HEST 4) the impulse over the roof center was reported to be less than one third of the impulse over the walls. In the former case the response of the roof was flexural, while a mixed mode (flexural and shear) response was reported in the latter.

In the only two tests where the roof totally collapsed the external peak pressure was well above that of the other tests and failure occurred at a time much shorter than the longest calculated period of the roof. The failure mode was dominated by strong shear near the walls. It was believed that in these tests early failure occurred under the high level of loading, before any interaction between the structure and the soil could become significant enough to prevent it or to reduce its severity. In the other cases the authors considered relief waves reflecting back from the concrete-air interface on the bottom face of the roof, as a possible cause for the fast reduction of the interface pressure at the roof center. They dismissed it, however, and attributed the explanation to *dynamic soil arching* as, indeed, transfer of pressure from the flexible part of the structure to its more rigid elements is indicative of arching.

A late time (relative to the initial structural response) effect, which was attributed to dynamic soil arching, was reported by Kiger, Eagles, and Baylot[27]. The dynamic part of their experimental program consisted of a reinforced concrete slab embedded in the soil with a depth to span ratio of 0.5, and subjected to a surface Foam HEST overpressure. They measured a relatively higher impulse over the embedded slab supports that was interpreted as possible soil arching. Similar experimental observation is pointed out in tests that were made with buried reinforced concrete arches subjected to explosive overpressure[30]. Late time behavior of buried arch-type structures was found to be affected by soil-structure interaction, especially in inducing relative motions between the arch walls and the floor after damage initiates at the arch-to-floor connection. It was also found that the properties of the soil-structure interface can have an influence on the structural performance by inducing friction loads.

Windham[54] used the finite element method to investigate the dynamic response of a box-type, 40 ft by 25 ft (12.2 m by 7.6 m) structure. He examined the influence of the backfill parameters on the behavior of the system. The late-time pressure distribution over the roof showed a relatively uniform distribution over the center portion of the roof, and a sharp normal stress concentration over the walls. No significant difference between dense and loose backfill, of the level or distribution of the pressure, is reported in this work. The only noticeable influence of the backfill density is on the normal stresses on the regions of the roof located over the walls and on the side walls at the roof level, which were higher under the loose backfill.

Soil backfill above the structure affects its frequency response through stiffening, and by an added mass effect. At a shallow DOB of about 20% of the roof span the added mass of the soil appears to be dominant in its effect on the response of the structure, as shown and discussed by Dallriva and Kiger[13], who also observed in their experiments an increase in the system's damping when soil is added as backfill.

It should be noted that the decrease of pressure which was observed in the dynamic experiments at a very shallow DOB, and with a clay backfill, can also occur due to the velocity difference between the structure and the medium, at least at the beginning of the roof motion. This interface pressure is governed by the relative velocity between the structure and the medium in which it is embedded, and by the *acoustic impedance*, ρc of the medium. The acoustic impedance gives a relation between the pressure induced in a medium and its particle velocity, v. For example, the relation $p=(\rho c)v$ can be applied, for a plane wave, at the boundary of the medium, such as the soil-structure interface.

This approach was used by Weidlinger and Hinman[51], who employed this pressure-velocity relation with a nonlinear response of the structure into a single degree of freedom system (SDOF). They also allowed for the formation of a gap between the sand particles and the structure by setting the interface pressure to zero when such a gap occurs, and suggested that the pressure relief over the roof center might be denoted as dynamic arching. This notation, however, should be distinguished from static arching which is driven by a different mechanism.

With the exception of finite element computations, numerical methods which deal with the dynamic response of buried structures, usually consider the inertial effect and the conditions at the soil-structure interface, or the influence of the acoustic impedance, but do not include in their consideration the soil arching effect[16,22]. Nevertheless, these papers usually give good agreement of their results with experimental or other numerical results, thus questioning the feasibility of soil arching, or the level of its effect, on the dynamic behavior of a soil-embedded structure systems.

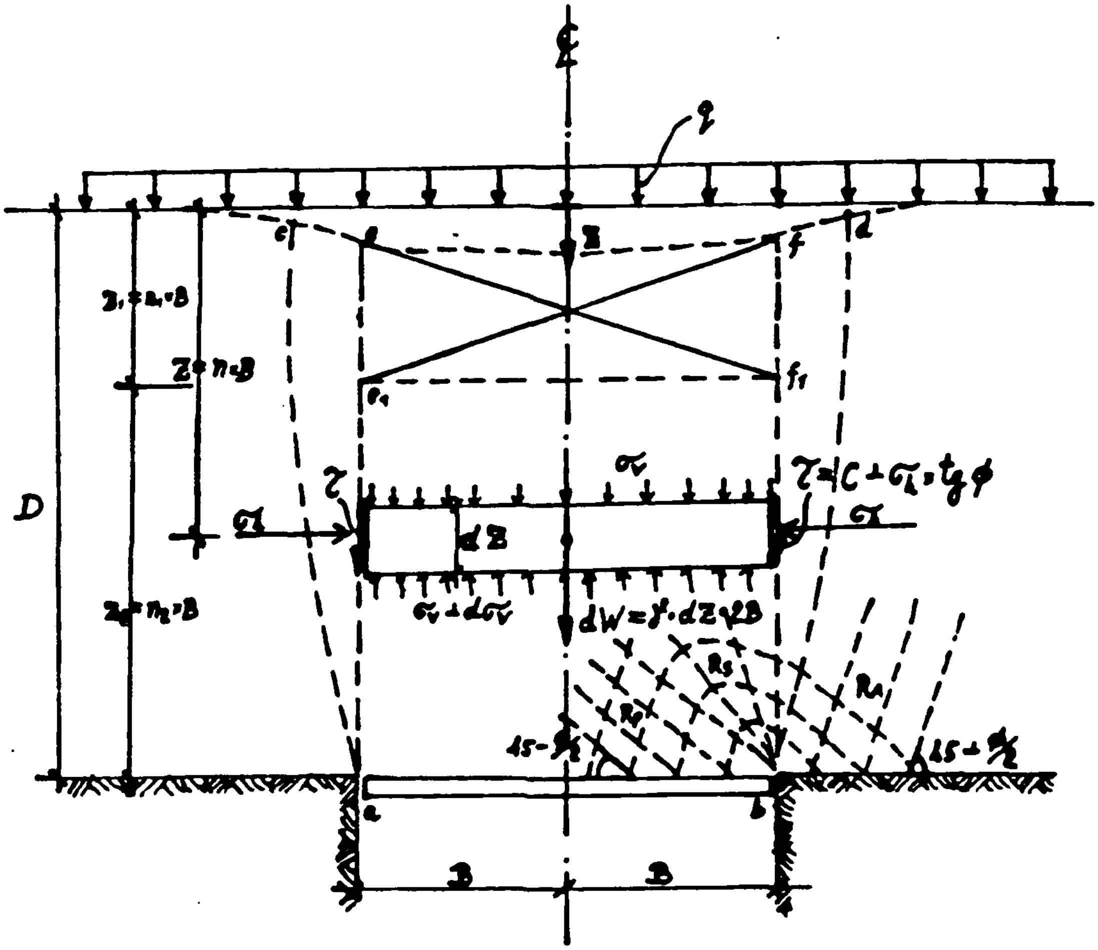
℄
q
e
f
d
Z
Z₁=n₁·B
Z=n·B
D
e₁
f₁
σv
τ
τ=C+σh·tgφ
σh
dZ
σv+dσv
dW=γ·dZ·2B
Z₂=n₂·B
R₁
R₂
45-φ/2
45+φ/2
a
b
B
B

Fig. 1-1: Terzaghi's analysis of arching over a trap-door[47].

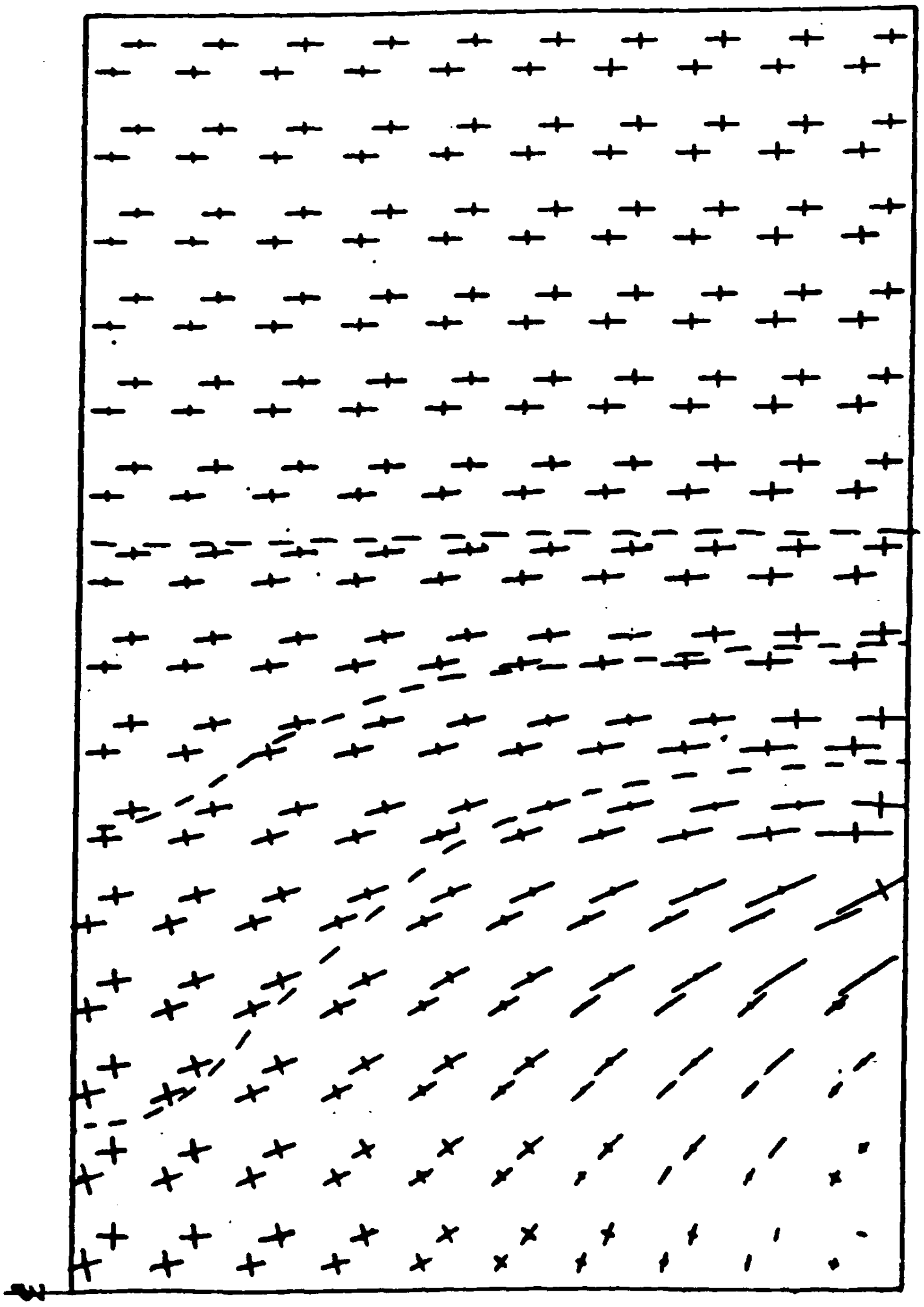

Fig. 1-2: Pattern of the principal stresses for DOB/span = 1 in Yankelevsky's numerical analysis[55].

CHAPTER 2

EXPERIMENTS

2.1 Description of the Experimental System.

Full or large scale experimental research of the response of buried structures to external impact, has the advantage of employing realistic parameters: The external impact can be generated by actual blast load, local soil may be used for the backfill, and the size of the structure is either full scale or close to it. The difficulties that are involved in such programs are their relative high cost, and inability to precisely determine those parameters. For example, it is difficult to accurately measure the pressure which is generated by a blast or to delineate its distribution.

The purpose of the current research was to focus on the response of the structure, and to study the basic mechanisms that are involved in a soil-embedded structure system subjected to external impact by eliminating the number of its unknown parameters. The approach that was selected was to employ an experimental program which consisted of small scale soil-structure system (Figure 2-1). Such a system enabled, within a relatively low budget, detailed measurements and information which provide an insight to the problem, and are complementary to similar larger scale experiments.

2.1.1 Experimental Setup.

The experimental setup was developed and constructed in the research laboratory of Northwestern University[8]. A circular steel tank, 42 in (107 cm) in diameter and about the same height, contained 20-30 dry Ottawa sand. A steel pipe frame was mounted around and above the tank and supported an electromagnet which was placed along the height of the frame at variable altitudes. A 4 pound (17.8 N), 3 in (7.62 cm) diameter, steel ball was used as an impactor. By dropping the ball on a relatively rigid target plate, resting on the soil surface, a short impact was generated, which then propagated into the soil. The minimal height of drop was 25 in (63.5 cm) and the maximum was 90 in (228.6 cm). The height of drop was measured from the target plate to the bottom of the impactor ball. The target plate was made of aluminum, 0.5 in (1.24 cm) thick and 12 in (30.48 cm) in diameter, sufficiently rigid to distribute the concentrated impact generated by the steel ball into the soil, and light enough to avoid excessive artificial static load. Extensive investigation of the target plate response was done by Chen[8].

The experimental system had an axially symmetric configuration that enabled a convenient experimental as well as a later numerical analysis. Accordingly, the embedded small scale structure was a vertical cylinder, which had an external diameter and a height of 6 in (15.24 cm). This experimental research was focused on the response of the roof of the structure. The circular roof slab was supported by a plexiglas cylindrical wall with a circular, 1 in (2.54 cm) thick, floor. In the first stage of the experimentation a linear elastic plexiglas slab was used for the roof. It was 0.23 in (0.58 cm) thick, and was simply supported by a 0.25 in (0.64 cm) thick wall. In the second and main phase of the experimentation the roof slab was made of micro-concrete and reinforced with micro-reinforcement. The preparation and properties of these slabs are described later in the text, together with the results. The micro-concrete roof slabs were supported by a 0.5 in (1.27 cm) thick wall, which together with the 1 in (2.54 cm) thick floor formed a relatively rigid structure, and enabled the structural behavior to be focused on, and dominated by the response of the roof.

2.1.2 Equipment.

Measurements of load and motion were performed. It is believed that by obtaining and analyzing the pressure distribution and the related structural motion (velocity and displacement), the mechanisms involved in this soil-structure system can be studied and understood. Modified ELF-500-100 "Entran" load cells were used to measure the pressure at the points where they were located. Interpolation of the pressure records acquired by load cells at different locations provided the pressure distribution. Description of the load cells and the modification needed in order to use them in this particular system, is given in Appendix A.

The motion of the roof center was recorded by a Linear Variable Differential Transformer (LVDT). This transducer demonstrated reliable displacement output as shown and discussed in Appendix B. The time derivative of the LVDT output signal provided the velocity record. It should be noted however, that the LVDT measured the motion of the roof relative to the structure floor. In addition to the LVDT two 4374 "Bruel & Kjaer" accelerometers were mounted at the roof center and on the floor. The lower accelerometer provided the floor motion record, which was also assumed to be the motion of the whole structure, while the upper accelerometer, after double integration, provided the absolute displacement record at that point. The signal from the accelerometer was used to indicate the exact starting time of the roof motion, as its initial response was faster than that of the LVDT. Because the double integrated acceleration signals were less accurate than the LVDT signal, they were considered to be more indicative rather than precise records. This feature is also discussed in the plexiglas slab test results (see 2.3.2) and demonstrated in Appendix B.

Acquisition of the output signals from the transducers was performed with a 4094 Nicolet Digital Oscilloscope, and two 2232 Tektronix Digital Storage Oscilloscopes.

2.2 Test Plan.

The soil-structure experimental program included four main stages:

a. Experiments intended to measure the external impact input generated under the target plate by the drop of the steel impactor ball.

b. Free field measurements.

c. Experiment with a plexiglas roof slab.

d. Experiments with reinforced micro-concrete roof slabs.

2.2.1 External Impact Measurements.

The external load that developed under the target plate, as well as the free field stress distribution, are two important reference records for this research. The external load, i.e. the pressure generated beneath the target plate, is the input to the soil-structure system, and once determined experimentally, was used as an input for the subsequent numerical analysis. It was also used as a reference for the experiments that were performed during succeeding stages, which involved the embedded structure. In these experiments a measurement of the pressure generated under the target plate center was taken to confirm that the external input was similar to that of the free field under similar drop of height of the impactor. This record, together with the free field records, well define the experimental system.

With no buried structure, the target plate and four load cells distributed beneath it were placed on the sand surface, Figure 2-2. The normal pressure was recorded at the center (load cell 'T'), 1.75 in (4.45 cm) away from the center (load cell 'A'), 3.25 in (8.26 cm) away from the center (load cell 'B'), and 5 in (12.7 cm) away from the center (load cell 'C'). With the assumption of axisymmetry a fourth order polynomial was used for the radial load distribution under the target plate, as follows:

$$p(r,t) = a_4 r^4 + a_3 r^3 + a_2 r^2 + a_1 r + a_0 \tag{2.1}$$

where the requirement for axisymmetry, yields :

$$\left.\frac{\partial p}{\partial r}\right|_{r=0} = a_1 = 0 \tag{2.2}$$

Hence: $$p(r,t) = a_4 r^4 + a_3 r^3 + a_2 r^2 + a_0 \tag{2.3}$$

By substituting the recorded data p(0cm,t), p(4.45cm,t), p(8.26cm,t), and p(12.7cm,t), the following matrix is obtained:

$$\begin{pmatrix} p(0",t) \\ p(1.75",t) \\ p(3.25",t) \\ p(5",t) \end{pmatrix} = \begin{pmatrix} 0 & 0 & 0 & 1 \\ 9.38 & 5.36 & 3.06 & 1 \\ 111.57 & 34.33 & 10.56 & 1 \\ 625.00 & 125.00 & 25.00 & 1 \end{pmatrix} \begin{pmatrix} a_4 \\ a_3 \\ a_2 \\ a_0 \end{pmatrix} \tag{2.4}$$

from which a_4, a_3, a_2 and a_0 are determined as follows :

$$\begin{Bmatrix} a_4 \\ a_3 \\ a_2 \\ a_0 \end{Bmatrix} = \begin{bmatrix} -0.038 & 0.067 & -0.036 & 0.007 \\ 0.344 & -0.553 & 0.243 & -0.035 \\ -0.813 & 1.088 & -0.316 & 0.040 \\ 1.000 & 0.000 & 0.000 & 0.000 \end{bmatrix} \begin{Bmatrix} p(0",t) \\ p(1.75",t) \\ p(3.25",t) \\ p(5",t) \end{Bmatrix} \tag{2.5}$$

It should be noted that a_4, a_3, a_2 and a_0 are also functions of time. Thus, based on the recorded vertical pressure (and assuming a fourth order distribution, according to equation 2.3), the full spatial and time distributions of the external load are obtained as:

$$\left.\begin{matrix} a_4 = a_4(t) \\ a_3 = a_3(t) \\ a_2 = a_2(t) \\ a_0 = a_0(t) \end{matrix}\right\} \Rightarrow p(r,t)$$

Figures 2-3-a and 2-3-b show this distribution under a height of drop, H = 25 in (63.5 cm). This pressure distribution was used later as an input for the finite element numerical analysis, thereby eliminating the need for numerical modeling of the load input transmitted from the impactor ball at the center of the target plate and decreasing the error that might have been introduced by doing so. The duration of the total loading pressure wave as seen in figure 2-3-a, generated under the target plate, was about 1 msec. The pressure under the plate center, however, had a duration of less than 0.5 msec, and a peak of about 325 psi (2.2 MPa). It was the vibration of the plate that transmitted the pressure wave from the center to its edge, where it had a peak of about 100 psi (0.7 MPa) at about 0.6 msec (Fig. 2-3-b).

2.2.1.1 Approximation for the Total Load Induced under the Target Plate.

The purpose of the following discussion is to verify the external input load measurements by approximating the total load induced under the target plate. When dropped from a height H, the impactor ball hits the target plate with a velocity equal to $(2gH)^{1/2}$, where g is the acceleration of gravity. The softer aluminum plate undergoes some plastic deformation. The contact area, as measured on the target plate, had an average diameter of 3/16 in (0.48 cm). The yield stress of aluminum is 8000 psi (55.2 MPa), therefore a force of about 200 pounds (890 N) was applied to cause local yielding and plastic deformation at the contact area. The ball and the plate move together for a period of time t_c, which was measured by Chen[8]. For H=25 in (63.5 cm) the contact time, t_c, was equal to 0.77 msec. Then, the ball was observed to rebound off the plate. Assuming that the ball and the plate move together after the local yielding occurs, by momentum conservation their initial velocity, V_0 is:

$$V_0 = \frac{M_b}{M_b+M_p}\sqrt{2gH} \tag{2.6}$$

where M_b and M_p are the masses of the ball and of the plate, respectively. The force induced under the plate is assumed to be generated by the weight of the ball and of the target plate, and by the resistance of the sand to their deceleration. Consider an equivalent SDOF system with the following parameters (figure 2-4):

Lumped mass, $M = M_b + M_p$

Equivalent resistance of the sand, K.

Although it is evident that the response of such system is not linear and that it is damped, because of the short duration of the ball-plate contact (less than 1 msec) a linear undamped analysis may be sufficient for such an estimation. The equation of motion is:

$$M\ddot{x} + Kx = Mg \tag{2.7}$$

where x = x(t) is the vertical displacement. The initial conditions are:

$$\begin{aligned} x(0) &= \frac{M_p g}{K} \\ \dot{x}(0) &= V_0 = \frac{M_b}{M_b+M_p}\sqrt{2gH} \end{aligned} \tag{2.8}$$

The solution for the displacement x(t) is:

$$x(t) = \frac{V_0}{\omega}\sin\omega t + \frac{M_b g}{K}(1-\cos\omega t) + \frac{M_p g}{K} \tag{2.9}$$

where $\omega^2 = \frac{K}{M} = \frac{K}{M_b+M_p}$

According to this model, the total load applied under the target plate, F_{sand} is:

$$F_{sand} = Kx = W_p + W_b(1-\cos\omega t) + \frac{KV_0}{\omega}\sin\omega t \tag{2.10}$$

where W denotes weight (of the ball or of the plate).

The equivalent parameter K can be determined semi-empirically, since the duration of the load under the target plate, t_d, was measured and recorded, and $F_{sand}(t=t_d)$ can therefore be set to equal W_p, the static load of the plate. Note that according to equation 2.10, W_p is also the initial load, $F_{sand}(t=0)=W_p$. This additional condition allows the semi-empirical determination of K. Once K is obtained it may be substituted into equation 2.10 to obtain $F_{sand}(t)$ for $t \le t_d$.

The loading duration, t_d for a height of drop H=25 in was 0.4 to 0.5 msec (figure 2-3-a and 2-3-b). Note that it was of the same order of magnitude as the contact time, measured by Chen[8]. The weight of the target plate, W_p, and of the ball, W_b, was 5.4 pounds and 4 pounds, respectively. For $t_d=0.4$ msec equation 2.10 yields K=1501000 lb/in and for $t_d=0.5$ msec K=961000 lb/in. The measured and interpolated pressure distributed under the target plate was integrated numerically over its area to produce the total load. The experimental value is plotted together with the analytical prediction (for $t_d=0.4$ and 0.5 msec) in figure 2-5. As it can be seen the SDOF model gives a reasonable theoretical prediction for the total load exerted under the target plate. It should also be noted that the experimental value was obtained from load cells which were located at a maximum distance of 5 in from the plate center. Since no extrapolation was done (see previous section), the experimental total load does not reflect the load contributed from the external perimeter of the plate (which had a radius of 6 in).

This result is another verification for the pressure measurements as recorded by the setup of load-cells described in Appendix A.

2.2.2 Free Field Measurements.

The vertical free field stress distribution under the target plate is important to provide a reference for comparison to the distribution of the stresses when a buried structure is present. Furthermore, the free field distribution provides a reference to check the numerical model used for the soil constitutive relationship in the finite element analysis.

With no structure present, load cells buried in the soil measured the vertical pressure that developed under external impact similar to the impact generated later in the following stages of the experimental program. Figure 2-6 describes the test configurations which were used to measure the free field vertical stresses 2.5 in (6.35 cm) and 3 in (7.62 cm) beneath the target plate at three locations: directly under the center, 2 in (5.08 cm) and 2.5 in (6.35 cm) away from the center. Figures 2-7-a and 2-7-b show some results obtained from these tests, which together with the external load measured under the target plate, complete the reference data. Additional pressure records that were obtained in these tests are shown together with the soil-structure results from the next two stages of the experimental program.

2.2.3 Experiment with an Elastic Plexiglas Roof Slab.

Once the input loads and the free field stress distribution have been established, the soil-structure system consisting of an elastic buried structure was tested (Figure 2-8). This experiment was performed with a plexiglas roof in order to obtain a full response of the structure in its linear elastic range. It was also used for the inspection of the setup and its measuring and recording equipment.

The plexiglas cylinder caped with a plexiglas roof slab, and fully instrumented with the transducers described above, was placed in the soil under the target plate. The plexiglas slab was simply supported, and since there was no attempt to reach its failure, the external impact was generated by the lowest height of drop of the impactor, 25 in (63.5 cm). The slab thickness was 0.23 in (0.58 cm), and the depth of sand cover above it, and below the target plate was 3 in (7.62 cm), one half of the roof outer diameter. The structure was set in an excavation ensuring that its center is under the center of the electromagnet holding the impactor ball. Special attention was given to insure leveling of the roof surface and sufficient density of the founding sand under the structure floor. Then the sand backfill was poured and tapped in layers of about 2 in around and above the structure. The target plate was placed on the soil surface and centered under the impactor ball. It was then leveled and tapped to provide proper contact with the sand. The system was impacted several times to assure consistent response of motion and pressure records.

2.2.4 Experiments with Reinforced Micro-concrete Roof Slabs.

2.2.4.1 Reinforced micro-concrete slabs.

An appropriate way to model reinforced concrete structural elements was recommended in research by Cunnigham, Townsend, and Fagundo[12]. The preparation and treatment of the mixture, as well as of the micro-reinforcement, were performed following their modeling technique. The slabs were reinforced with spot welded meshes. The mixture for the micro-concrete slabs was made of gypsum, fine sand, and water. The use of gypsum cement provided rapid curing time, small particle size, and low distortion[37]. The sand was sieved into three portions, as described in Figure 2-9. The average weight density of the reinforced slabs was 130 pcf (20.4 kN/m^3). All the reinforcing wires were deformed to obtain similarity to the cold deformed conventional reinforcement. The desired deformation was obtained by passing the wire through two pairs of perpendicular knurls[12]. The wires were preloaded to a stress near the yield point to remove any initial deformation. After preloading the wires, the miniaturized reinforcing mesh was spot welded. Specimens of the wires were tested in tension in a Material Testing System (MTS) machine and had an average yield strength of 51000 psi (352 MPa).

The compressive strength of the micro-concrete mixture was tested on 1 in by 3 in (2.54 cm by 7.62 cm) cylinders, and the micro-reinforcement wires were tested in simple tension tests. These tests were performed on an MTS on samples of wires that were not welded, and on specimens from the spot welded meshes, to verify that the spot welding technique does not influence the properties of the reinforcement. No significant difference was found between the two, in their yield strength or general stress-strain behavior. The properties of the slabs are given in Table 2-1. The forms for the slabs were made of plexiglas. Figures 2-10-a through 2-10-d show a typical process of casting the roof slab specimens.

In addition to the strength tests, two sets of structural tests were performed with the circular slab specimens. The slabs were subjected to a uniformly distributed pressure and their midspan displacement was measured. The uniform load was applied through oil pressure in a steel chamber above the plate, and the pressure and displacement were measured by a pressure transducer and an LVDT, respectively (Figure 2-11). In the first set of tests the pressure was static, and the tests were controlled by a constant rate deflection of the slab center. The purpose of the static tests was to ascertain the structural behavior of the small scale slabs as compared to larger similarly reinforced concrete elements. The results also assisted in analyzing the soil-structure system. The slab specimens, similar in geometry to the roof slabs, were tested under controlled conditions and were observed for cracking, reinforcement yielding, and ultimate capacity. This study enabled a better analysis of the response of the roof slabs (see also 2.3.2 and 2.4.2). The experimental system, and the results of the static tests are described in detail by Chen et. al.[10]. The second set of experiments were performed with dynamic loading on the same setup but with load control instead of displacement control.

It was found in the static tests that the small scale specimens behave in a comparable manner to larger scale, similar slabs. The impact pressure induced by the test apparatus, had a much larger duration than that which loaded the roof in the soil-structure system. It was, therefore, not possible to study directly the uncoupled response of the roof slab specimens under such impact loading. Nevertheless, the pressure in those tests had a rise time of about 20 msec, which was about 300 times faster than the highest rate of loading in the static tests. Therefore, the mid-span displacement record was used in the evaluation of the buried roof response, and as a reference in the numerical analysis (see 2.4.3 and 3.2.5).

2.2.4.2 Boundary conditions.

With the assumption that the plexiglas walls are rigid enough, the boundary conditions of the roof were determined according to its means of support. Two types of supports were used: simply supported and clamped. The simply supported fixture consisted of three "L" shaped aluminum clamps, 3/8 in (0.95 cm) wide, which were attached to the plexiglas walls, equally spaced, 120 degrees apart from each other. The top portion of these clamps provided, together with the walls of the structure, a vertical support that did not carry any moment (figures 2-12-a and 2-12-b). The clamped support (figures 2-13-a and 2-13-b) consisted of an aluminum annular cap which was mounted over the slab and had an "L" shaped cross section. The cap had an interior diameter identical to the plexiglas cylinder (5 in) and was attached to it by 6 steel studs that prevented any vertical movement of the clamping cap. A flat, 1/32 in (0.08 cm) thick, and 1/2 in (1.27 cm) wide, steel ring was placed over the roof slab and under the clamping aluminum cap, and was tightened against the slab by 8 screws. The wall and top part of the clamping cap were 3/16 and 1/8 in thick (0.48 and 0.32 cm), respectively. The cap was rigid enough to clamp the roof (by preventing a rotation of its edge) but not too large or thick to affect the general shape of the structure.

In order to examine the effectiveness of the supports the following test was conducted: a doubly reinforced slab (#20 wire, $A_s = 9.5115 \cdot 10^{-4}$ in^2 (0.0061 cm^2), @ 1" (2.54 cm) in each direction), 0.43 in (1.1 cm) thick, was loaded by a short, concentrated, low impact at its center (see also test No. 6 in Table 2-1). The free vibration response of the slab was recorded to obtain its fundamental natural frequency. If the clamped boundary fixture is effective, it is expected to cause a natural frequency higher than the frequency of the simply supported slab. An upper bound for the natural frequency of a circular slab is given by the expression[32,43,49]:

$$\omega = \frac{\alpha}{R^2}\sqrt{\frac{D}{\rho h}} \tag{2.11}$$

where: ω is the frequency (rad/sec)

D is the stiffness of the slab, defined as:

$D = E \cdot h^3 / 12(1-\nu^2)$

E is Young's modulus

h is the thickness of the slab (0.43 in; 1.09 cm)

ν is Poisson ratio

ρ is the mass density of the slab ($1.95 \cdot 10^{-4}$ lbs.-sec^2/in^4; 2084 KgM/m^4 , calculated by dividing the actual weight of the slab by its volume and by g)

R is the radius of the slab (2.5 in; 6.35 cm)

α is a constant which depends on the boundary conditions and on the vibration mode.

For the case of a fixed circular plate $\alpha = 10.22$ for the lowest mode of vibration. In the case of a simply supported plate, there is also a dependency on ν (e.g., Ref. 32): For $\nu = 0.3$, and 0.25, $\alpha = 4.977$, and 4.858, respectively. Poisson's ratio of 0.2 was assumed for the micro-concrete.

Figures 2-14-a and 2-14-b show the response of the slab. The results indicate that the clamping fixture is relatively effective, as it raised the natural frequency of the slab from about 2800 rad./sec. (446 Hz) under simple support conditions to about 14000 rad./sec. (2230 Hz) when it was clamped. From equation 2.11 and the corresponding values of α, the theoretical values of a simply supported slab is expected to be about half of that of a fixed slab. The experimental frequency of the slab under simply supported boundary conditions was even lower, compared to that of the clamped case. However, the main objective of this part of the experiment was achieved by obtaining two different types of boundary conditions which generated two different natural frequencies for the embedded roof. It should be noted that while the theoretical analysis does not take into account lateral displacement of the slab edge, such displacement is possible, especially when a concrete slab is resting on a plexiglas support. Boundary lateral motion decreases the stiffness of the slab, thereby decreasing its natural frequency, as indeed was observed in the above test. Additional indication for possible lateral motion in the simply supported case is given in the numerical analysis (see 3.2.5).

This test also served as an indirect method to evaluate the initial Young's modulus, E, of the micro-concrete with the above parameters. The analytical upper bound for the lowest natural frequency of a fixed slab is $15.18\sqrt{E}\ rad/sec$. The measured frequency value of 14000 rad/sec yields a relatively low Young's modulus of $0.89 \cdot 10^6$

psi (6137 MPa). Similar measurements were taken for the slabs of tests 7 and 8 and yielded corresponding values of $1.05 \cdot 10^6$ and $0.98 \cdot 10^6$ psi (7240 and 6757 MPa), respectively. Values of Young's modulus which were measured in compression tests of micro-concrete indicated higher values but also showed considerable scattering. It is interesting to note that a similar small value of elastic modulus for micro-concrete was also reported by Shin[40].

2.2.4.3 Test procedure.

The configuration of the test setup was similar to that of the experiment with the plexiglas roof (see section 2.2.3). In tests 1 to 5_a the roof was embedded 3 in (7.62 cm) under the soil surface and in the other tests the DOB was decreased to one half of the roof clear span, i.e. 2.5 in (6.35 cm). The boundary conditions of the roof were described in the previous section and are given for each test in Table 2-1. In the tests where the roof slab was simply supported, the load was measured at the center, 2 in (5.08 cm) from the center, and 2.5 in (6.35 cm) from the center. This configuration of load measurement was not possible in the case of the clamped slabs, because the inner diameter of the clamping cap was 5 in (12.7 cm) and each load cell had a diameter of 0.5 in (1.27 cm). Therefore, in tests 3 through 5_b and in test 8 the load cells were located at the center and 2 in (5.08 cm) from the center.

The steel ball impactor was dropped from an initial height of 25 in (63.5 cm) or 50 inches (127 cm), and the center displacement signal was examined after each drop for residual plastic deflection, indicating possible failure. When such indication was observed, the structure was excavated and examined. Table 2-2 lists the sequence of hits in the tests. As a consequence of the preliminary test with the plexiglas roof, the target plate was pressed and tapped into the soil surface to avoid a relatively large settlement under the first impact.

2.3 Results.

2.3.1 Experiment with an Elastic Plexiglas Roof Slab.

It was observed, in both free field experiments, and the experiments with the structure, that under the first impact there was a relatively significant settlement, up to 0.5 inch (1.27 cm), of the target plate. Therefore, the initial cover was 0.5 inch deeper than the test design cover, and the results of the first hit were usually disregarded. This approach was confirmed to be appropriate, by measuring a constant depth of cover, and similar pressure and motion records in the results succeeding the second hit, for each drop of the impactor. It was also reasonable to anticipate this behavior, since the plexiglas slab neither failed nor yielded in any of the tests performed at this stage.

Figure 2-15 shows the displacement records, w_1, w_2, and w_3. Theoretically, a double integration of the acceleration records should provide the **absolute** vertical displacement of the center of the roof (denoted as w_2) and of the whole (rigid) structure (denoted as w_3), such that $w_1=w_2-w_3$, where w_1 is the LVDT output (see figure 2-8). As shown in Appendix B the LVDT signal is more accurate than that of the doubly integrated accelerometer signal but slower to respond. Since the records taken during the first 100 μsec of loading are important, the signal of the accelerometer serves to indicate the beginning of the motion of the structure. Accordingly, Table 2-3 describes the data acquisition method for these experiments.

Figure 2-16 shows the pressure and corresponding velocity signals as were recorded in the test, over a period of 4 msec. As can be seen, the significant portion of these signals occurred only within the first 2 msec of the test, where the time of impact initiation under the target plate center was set to 0.0 sec. Therefore, the response over that period was magnified and shown in figures 2-17 and 2-18. The vertical stresses, together with the velocity and displacement of the roof, are shown in figure 2-17. Figure 2-18 demonstrates the difference between the stress distribution in the free field and over the buried structure. The impulse records, integrated from the pressure signals, are given in figure 2-19.

2.3.2 Experiments with Reinforced Micro-concrete Roof Slabs.

The roof slabs which were buried under 3 inches (7.62 cm) of sand (tests 1 through 5_a in Tables 2-1 and 2-2) showed slight or no visible damage. The most visible damage was observed in tests 1 and 2. Under an external impact, which was generated by a height of drop of 50 inches (127 cm), the slab was cracked and the LVDT was detached. The cracks were at the bottom of the plate, and had a radial shape. These cracks were the only damage caused and indicate that the response was flexural. In tests 3, 4 and 5a there was only slight radial cracking, even under external impact from a height of drop of 90 inches (228.6 cm).

In several cases the signal of the LVDT indicated relatively large displacements. When the structure was excavated no visible damage was observed, but the core of the LVDT was detached from the roof slab. Due to the high acceleration of the roof center (up to 5000 g's) the fixture which held the core and was glued to the slab, became detached, although it had a relatively low mass (0.0178/g lb/g; 8.1 gr). The detachment of the LVDT fixture also indicates transmission of a tension wave from the bottom surface of the roof. (see also the discussion of the results in the next section).

Similar types of response and damage to the roof slabs were observed in tests 5b through 8, where the DOB was decreased to 2.5 in (6.35 cm). A permanent residual deflection of the roof center was observed after the impactor ball was dropped from a height of 90 in (228.6 cm), except for test 7, where initial cracks appeared under an impact generated by a height of drop of 25 in (63.5 cm), more cracking was seen under an impact from a drop of 75 in (190.5 cm).

Structural damage to the slabs was indicated by the appearance of visible cracking and plastic residual displacement. Slight to mild degree of damage of the roof slab was observed in all tests, but there was no catastrophic failure. In general, the clamped slabs showed higher stiffness, which was demonstrated by higher frequency response, and relatively lower amplitude of the displacement and velocity. Nevertheless, no cracks were detected on top of the clamped slabs, which indicates that these slabs were not fully fixed at their supports, section 2.2.4.2. The maximum measured central deflection in the tests was only about 0.07 in (0.18 cm) in test 6, under the highest drop of the impactor ball (see also results of test 6, 4th hit, in Appendix D). These relatively low displacements also explain the mild level of damage which was observed (see also Table 2-2 and the discussion in section 2.4.3).

Table 2-2 lists the sequence of the hits in the tests that were performed and their intermediate and final observations. A typical result, which includes measurements of the pressure at the roof-soil interface, and of the roof motion, are given in figures 2-20 through 2-23 and discussed in the following sections. Other results are shown in Appendix D.

2.4 Discussion.

2.4.1 Physical Mechanisms and Phenomena that are Expected to be Involved.

Analysis and discussion of the test results are given in view of physical mechanisms and phenomena that are expected to be involved in the system and were discussed or reported in the literature (see also Chapter 1). They are:

1. Incident free field stress distribution, which is the stress field in the soil under external load with no embedded structure. The free field pressure constructs the initial loading on the embedded structure, whose response causes deviation of the interface load from the free field pressure at the same location and time.

2. The initial total pressure acting on the structure is the incident pressure, p^i plus the reflected pressure from the soil-structure boundary, p^r. It is determined by the boundary conditions at the soil-structure interface and the effect of the mechanical impedance of the soil. The mechanical impedance is a measure of the resistance of a system or medium to an applied load. In a single degree of freedom system the impedance is equal to ρc, where ρ is the density and c is the longitudinal wave velocity. As long as there is no gap between the soil and the structure, and for a plane pressure wave, the impedance gives the relation between the pressure, p^f and the velocity of the soil particles, v_{soil}:

$$p^i = p^f = (\rho c) v_{soil} \tag{2.12}$$

The reflected pressure wave and the total pressure, p, at the soil-structure interface are given by:

$$p^r = (\rho c) \cdot (v_{soil} - v_{str}) = p^f - (\rho c) v_{str} \tag{2.13}$$

$$p = p^i + p^r = 2p^f - (\rho c) v_{str} \tag{2.14}$$

where v_{str} is the velocity of the structure. (v_{str} is formally the velocity of the structure particles at the interface. For a relatively rigid roof, such as concrete, and an incident wave with a relatively long duration, such as the free field impulse, v_{str} is the actual velocity of the roof).

It is, therefore noted that this mechanism, associated with wave propagation phenomena, is dominated by the boundary velocity of the particles of the medium in which the wave propagates. When the medium is bounded by an elastic boundary its particle velocity is also the boundary velocity, unless there is a gap. In the present system, the structure constitutes a boundary for the soil particles which are resting on it until motion starts. When loaded by an impact, the roof responds by gaining velocity, which also affects the interface pressure.

Equation 2.14 implies that in the initial time of loading, when the velocity of the structure is not yet developed, the incident pressure is amplified at the soil-structure interface. When later structure velocity is developed in response to the applied load, the soil-interface pressure is affected by the interface velocity-pressure relation according to equation 2.14 and is expected to be reduced.

3. Tension waves normal to the roof plane are generated when the portion of the propagating compression impact, transmitted into the slab, arrives at the bottom face of the roof.

4. Arching in the soil is expected with developing structural displacement. By transferring the pressure from the more flexible parts of the structure to its stiffer parts, the soil interacts with the deflecting structure, mainly through its shear capacity. This mechanism is dominated by displacements of the structure and of the soil. In case of relatively large displacement of the roof center arching tends to decrease the pressure over this region and increase it over the edge. In case of rigid body settlement of the structure the DOB/span ratio decreases. Consequently the arching action over the roof is expected to decrease and the pressure at the center of the roof may increase again. The phenomenon of arching is also explained and described in Chapter 1.

5. Possible soil-structure gap over the center ("Double hit"). With sufficient

structure velocity a gap might develop between the soil particles and the moving structure. Such gap would be indicated by decrease of the interface pressure to a minimum of zero. When the center velocity decreases, the velocity of the sand above this region may again match the velocity of the roof and reload it.

2.4.2 Sequence of the Phenomena in the Response of the Soil-Structure System.

The results are examined in light of the physical mechanisms listed in the previous section and phenomena which are expected to be involved in the system response. The following observations are of the results of test number 8, 5th hit, which was performed with a clamped slab, and a DOB of 2.5 inches (Table 2-1). Results of other tests, given in Appendix D, showed similar observations.

Comparison of the pressure records over the roof center and edge to the corresponding free field records shows that after arriving at the roof level the pressure initially follows the free field behavior. The initial free field loading of the roof was indeed measured and recorded in all the tests and lasted for 0.02 to 0.05 msec ($0.15<t<0.20$ msec in figure 2-20). This period of time was observed to be insensitive neither to the two DOB which were used nor to the boundary conditions; it increased in the test with the plexiglas roof (about 0.1 msec from the beginning of loading in figure 2-18). The rise time to the peak was also relatively longer under the highest external impact in test 6, and in test 8. Accordingly, the displacements under the longer and higher center impacts were larger than in the other hits (e.g., deflection of 0.07 in (0.18 cm) in the 4th hit in test 6 versus maximum deflections of about 0.03 in (0.08 cm) under the other hits of that test, Appendix D).

No amplification of the interface pressure, relative to the free field level was observed. The velocity which is required to prevent an amplification of the incident pressure can be evaluated from setting the interface pressure, p, equal to the free field pressure, p^f in equation 2.14. The relevant properties of the soil are:

$$\rho_{soil} = 1.6 \cdot 10^{-4}\ lb\text{-}sec^2/in^4\ (1710\ KgM/m^3)$$

$$c_{soil} = \frac{DOB}{arrival\ time} = 15000\,in/\mathrm{sec}\ (381\,m/\mathrm{sec})$$

For the condition $p = p^f$ to be satisfied at a level of 100 psi (0.69 MPa), the roof velocity has to be in the order of 40 in/sec (1.02 m/sec). However, during the initial loading period the velocity of the structure was developing from zero (rest) to less than 50 in/sec (1.27 m/sec; 0.15 msec$<t<$0.2 msec in figure 2-20).

In the apparent lack of sufficient roof velocity the interface pressure readings may be explained by considering a tension wave reflected from the bottom of the roof. The velocity of an elastic wave through the roof thickness is given by equation 2.15:

$$c_L = \sqrt{\frac{E(1-\nu)}{\rho(1+\nu)(1-2\nu)}} \tag{2.15}$$

where: c_L is the longitudinal, or compressive wave velocity.

E is the concrete Young's Modulus.

ν is the concrete Poisson ratio.

ρ is concrete mass density.

The mass density of micro-concrete was $1.95 \cdot 10^{-4}$ lb-sec^2/in^4 (2084 KgM/m^4). Poisson's ratio of concrete can be assumed as 0.1 to 0.2, which in either case does not influence significantly the value of the velocity given by equation 2.15. Table 2-4 shows the wave speed values for these material properties, for Young's modulus of $2 \cdot 10^6$ psi (13790 MPa) and $5 \cdot 10^6$ psi (34475 MPa), and the corresponding time, t_T it would take for a reflected tension wave to arrive at the upper face of the roof. The time t_T is calculated according to equation 2.16, assuming that the velocity of the incident compression wave and of the reflected tension wave are the same:

$$t_T = 2\frac{h}{c_L} \tag{2.16}$$

where h is the thickness of the roof.

As can be seen in Table 2-4, from the incidence of the compression impact on the roof upper face, up to 0.01 msec are required for a tension wave to be reflected and arrive from the bottom free face of the roof. The test results show that until that time the free field pressure was still low enough and the measurements of the interface pressure were likely to have a relatively high level of noise to signal ratio. Thus, it is possible that even if it existed, an amplification may have not been detected.

A reflected tension wave might have caused a decrease of the soil-roof pressure when propagating back to the upper roof surface, and spalling at the bottom face of the roof. No spalling was observed in any of the tests, which is reasonable since the peak pressure value, measured under the highest drop of the impactor, was about 160 psi (1.1 MPa; figure 2-20). An equal tension stress wave reflected from the free bottom of the roof could be sustained by the concrete. An observation which might resemble spalling and indicate a reflected tension wave at the roof bottom, was the local detachment of the LVDT fixture at the slab center, which occurred several times (see also Table 2-2).

About 0.02 to 0.05 msec after hitting the roof both the pressure over the center and over the edge started to drop. In comparison with corresponding free field reference signals this drop was a deviation caused by the roof gaining velocity upon being hit. Therefore, it was concluded that for the first 0.05 to 0.1 msec the response of the roof involved a mechanism appropriate to wave propagation in a medium with an elastic boundary, where the velocity of the boundary affects the normal pressure acting on it. The time of initial deviation from the free field pressure is marked with "A" in the figures.

Approximately 0.1 to 0.15 msec from the initial loading of the roof, the pressure over the center continued to drop while over the roof edge it rose again and returned to the free field level (Marked "B" in figure 2-20, at t≈0.24 msec), although the edge was still moving downwards with a negative velocity (figure 2-21, t≈0.24 msec). This part of the response indicates the development of arching identified by a decrease of the normal pressure over the more flexible central part of the roof and its increase over the stiffer edge, due to relative displacement of the center. Note that in the axisymmetric geometry of this system, the arching effect is more likely to occur as a dome action in the soil. It is still referred to as *arching* because it is the usual terminology for this mechanism.

The pressure over the center dropped to zero (or maintained a moderately higher minimum in other tests), while the pressure record over the edge of the roof did not drop to zero during the first 1 to 1.5 msec of the response. This phenomenon indicates that in some cases where the pressure over the center dropped to zero, the velocity of the roof was sufficient to cause detachment of its center part from the sand above it for a period of up to 0.2 msec, as also can be seen in the impulse records (e.g., points "B" to "C" in figures 2-20, 2-21, 2-22), which show a decrease in the slope of the center impulse. The period of minimum or zero slope indicate minimum pressure, which when equal to zero can be interpreted as detachment of the soil particles from the roof. The minimum pressure over the roof center is marked "C" in the figures.

About 0.17 to 0.20 msec after the initial loading of the roof ($t \approx 0.35$ msec in figures 2-20 and 2-21), and during a period of about 0.20 msec, there was a second increase of the normal pressure over the center of the roof, while the pressure over the edge slightly decreased below the level of the free field. During this period of time the motion of the roof center was still downward (negative center velocities during $t < 0.58$ msec in figure 2-21). The amplitude of the center velocity decreased at that time, and the velocity of the sand above this region may have again matched the velocity of the roof and reloaded it. It was also possible that due to a rigid body displacement of the structure, causing the displacement of the edge of the roof, negative arching (or a decrease in the previously developed arching) was developed over it and the pressure over the center increased.

Further analysis shows that 0.3 to 0.4 msec after the arrival of the incident impact, the velocity of the roof center became positive (Figure 2-21 at $t = 0.58$ msec, marked "D" in the figures), indicating an upward motion, and the normal pressure over that part of the roof increased again in a similar, but opposite, manner to the decrease of the pressure at the beginning of the response of the structure, at t $\approx$ 0.2 msec. Here, however, the increase in the pressure was not observed in all the cases (e.g., see results of test 2, 4th hit in Appendix D).

2.4.3 Influence of the Involved Phenomena on the Soil-Structure Response.

The physical mechanisms indicated by the experimental observations, occurred at the sequence described in the previous section. Their influence on the response of the structure is evaluated by examination of the roof displacement. Inspection of the cracks of the roof slab of test 8 after the fifth hit and a recorded residual displacement of about 0.02 in (0.05 cm) of its center, indicated a state of flexural damage.

More information about the behavior of the slab is obtained from examination of typical load-deflection curves of circular micro-concrete slabs of similar thickness and span. Tests with uniform pressure were performed on slabs that were fixed to rotation and to lateral displacement at the boundary[10]. The pressure was applied with center displacement control at a slow rate of 0.0133 in/min (0.034 cm/min) and at faster rate of 0.52 in/min (1.32 cm/min), and had a rise time to peak pressure of about 900 sec and 6 sec, respectively. Additional tests were performed under pressure control, that had a high rise time of about 20 msec. The slab was simply supported to allow later convenient numerical modeling (see also Chapter 3). Figure 2-23 shows the load-deflection curves of those tests. The rise time of the first central pressure peak in test 8 (5th hit) was 0.05 msec. The pressure-time records (over the center and over the edge) were plotted with respect to the displacement-time record eliminating the common time parameter, to give the load-displacement history of that test (figure 2-23). As indicated by figure 2-23, the micro-concrete slabs in the load-displacement tests sustained a maximum load, which increased at decreasing displacement with increasing rate of loading. They also indicate that the central impact on the slab which lasted less than 0.1 msec (figures 2-20 and 2-21) would have caused more damage with a longer duration, such as that of the free field impact (figure 2-20).

This point is also demonstrated in figure 2-22 where the pressure records over the structure were integrated to give the impulses. Points "A" to "D", defined in the previous section, are marked in the figure. They show the initial increase of the load up to point "A", where the structure velocity followed by displacement (point "B") caused decrease of the load over the center roof up to point "C". During this time ("A" to "C") the slope of the impulse over the center dropped to a plateau which denotes reduction of the load.

Therefore, it is concluded that the amplification of the incident pressure wave due to the relative stiffness of the structure was prevented, by the tension wave reflected from the bottom of the slab. A downward velocity and displacement of the roof further decreased the load acting on it. Due to the reduction of the load over the central portion of the roof limited damage was suffered, and further catastrophic failure was prevented. Consequently, an important consideration would be to evaluate the capacity of the buried structure for dynamic impact loading. If that capacity is higher than the initial portion of the free field load, then the other mechanisms described above are likely to decrease the free field load so that the structure, which might have failed under a load equal to the total free field load, is left intact.

Hence, it seems that the portion of the free field impulse, acting on the structure until it decreases by the mechanisms described above, has an important effect on the response or even capacity of the structure and is a valid result, provided that the tension wave reflected from the free bottom of the slab is either low enough or can otherwise be sustained by the slab.

2.4.4 Influence of the Boundary Conditions.

The effect of the boundary conditions is illustrated by comparing the response of the clamped roof in test 3 with that of the simply supported roof in test 2. Figure 2-24 shows the external pressure under the center of the target plate, as a result of dropping the impactor from a height of 25 in (63.5 cm) in tests 2 and 3. The slabs in these tests had a similar thickness and were embedded 3 in (7.62 cm) under the target plate. Under a similar external impact (Figure 2-24) the clamped slab exhibited lower maximum displacement (Figure 2-25; the displacement curve of test

3 was shifted to allow convenient comparison).

When beginning to analyze the soil-structure interaction aspects, one notes the displacement of the roof slab, which effects the development and amount of arching, took place about 0.1 msec after the beginning of the structural response. Until that time the load was not affected by the structure boundary conditions. The effect of the boundary conditions was observed when the response of the structure became significant. The impulse records over the roof edge and center in the two cases are given in figure 2-26 and shows lower impulse over the roof center in the simply supported case, and a corresponding higher impulse over the edge (dashed and solid lines for the simply supported and clamped cases, respectively, in figure 2-26). This response indicates stronger arching over the more flexible simply supported roof. It should also be noted that although not measured, it is reasonable to assume a more concave deflection shape of the simply supported roof, which would tend to increase the more flexible zone of the roof and decrease the load over it, by arching.

It seems that on repeated hits the stiffness of the clamped slabs decreased, either by micro-cracking or by some loosening of the grip of the clamping cap. Noting that the decrease of the pressure over the roof center occurred in the first 0.1 to 0.2 msec of the structural response, it can be seen that the roof did not reach its maximum deflection at that time. As a result, the displacement of the roof center in the first 0.1 msec of the response was larger after it was hit repeatedly (figure 2-28) and consequently the central part of the slab was less loaded than in the previous hits (compare first and third hits in figure 2-29).

2.4.5 Effect of DOB.

The free field pressure under the same surface impact is expected to undergo more attenuation at deeper depth. At shallow depths of burial the relative effect of other soil-structure mechanisms become more significant. The results indicate stronger arching level at deeper DOB. Comparing test 2 and test 3, which were done at DOB of 3 in (7.62 cm) and 2.5 in (6.35 cm), it can be seen in figure 2-30, that at the time when arching occurred (after the center impulse reached a plateau) the edge to center impulse ratio was higher in test 2 where the DOB was deeper:

$$\left[\frac{I_{edge}}{I_{center}}\right|_{\substack{t=0.45\,msec\\ DOB=3''}} = \frac{0.008}{0.004} \qquad \left[\frac{I_{edge}}{I_{center}}\right|_{\substack{t=0.42\,msec\\ DOB=2.5''}} = \frac{0.011}{0.008}$$

2.5 The Value of the Results from the Small Scale Experimental System.

The results of the experiments that were performed with the small scale system have two main applications:

1. Obtaining detailed information that will enable close study of the basic mechanisms which are involved in a soil-embedded structure system.

2. Enable predictions of the response of similar larger scale systems.

As for the first application, it is sufficient to analyze the parameters and experimental records as they are. This study provides an analysis of the small scale system. Nevertheless it is important to evaluate the value of the results obtained here for the understanding and analysis of larger scale systems of structures embedded in soil.

For this reason , dimensional analysis was performed based on the theory of similitude, which is detailed in Appendix C.

Table 2-5 shows the ratios that should be used when extrapolating any variable from the small scale model system to a larger prototype system. These extrapolation rules are based on the following assumptions:

1. The geometrical scaling factor is equal to a known chosen factor, n.

2. The materials which are used in the model are similar in their mechanical and weight properties to those which are used in the prototype.

A well known conflict is introduced when similar materials are used for the prototype and for the model, and the gravitational acceleration is not scaled (e.g. by using a centrifuge)[15,23]. This causes some distortion in the model to prototype extrapolation. That distortion, however, is relatively negligible and falls within the range of other experimental errors, when the gravitational effect is minor. As demonstrated in Appendix C, if a variable in the system, "VAR", is assumed to consist of a static portion, "VAR_{st}", and of a dynamic portion, then the distortion depends on the geometrical scaling factor and on the ratio of the total amplitude of the variable to its static portion, according to equation 2.23:

$$\% \, Distortion = \frac{VAR^{true} - VAR}{VAR^{true}} \cdot 100 = \frac{100}{1 + \frac{1}{(n-1)} \cdot \frac{VAR_m}{VAR_{mst}}} \tag{2.23}$$

where: VAR^{true} is the true prototype value

VAR is the extrapolated prototype value

VAR_m is the model value (usually measured in the test)

VAR_{mst} is the static portion of the model value

In the case of a dominant dynamic portion the distortion decreases as it does when the scaling factor is low. It is also shown in Appendix C that the levels which were obtained of the pressure over the roof, and of the mid-roof displacement were larger than their corresponding static values. Hence, a possible distortion due to the unscaled gravitation is low to moderate, and the ratios given in Table 2-5 are sufficient for a model to prototype predictions based on the current system with a geometrical scaling factor as high as 60.

It should be noted, however, that the external pressure cannot be extrapolated, and that the relatively low level impact which was produced in the current system (up to 500 psi; 3.45 MPa) might not be typical of a full scale explosive impact. However, the time is scaled up by a factor of n, expanding the extrapolated prototype time to a longer, more realistic duration.

There are three more aspects which present possible difficulties in the extrapolation of the small scale system response:

1. The response of the reinforced micro-concrete in the model: The usage of this particular technique followed the recommendations of Cunningham, Townsend, and Fagundo[12] who found it suitable for modeling larger scale reinforced

concrete elements. Further confirmation was obtained in the observations of Chen et. al.[10] who tested similar small scale slabs and found their response to be similar to the response of larger scale slabs.

2. Modeling of the backfill: On one hand the use of 20-30 Ottawa sand cannot model geometrically a typical soil backfill which is used over larger scale structures. On the other hand its main properties, i.e. zero tensile strength, shear capacity, and granular structure, are assumed to be sufficient for representing the primary characteristics of such backfill.

3. Strain rate effect, and size effect[5,6] might be significant in the analysis of the response of concrete elements. This is especially important in failure initiating crack propagation in quasi-brittle materials such as concrete[11,2[illegible]]. For the reinforced concrete slabs which are considered in the present study, the rate effect was indeed observed[10] but it is assumed to have a limited influence on the extrapolation of the fundamental phenomena as observed in the model, to larger scale systems. Similarly, extrapolation is not likely to be affected by the size effect law considerations when the structure failure is dominated by yielding of the reinforcing steel. Undoubtedly, further study of these phenomena will deepen the understanding and knowledge of their influence on both the soil-structure problem, and on the model to prototype extrapolation of other experimental systems of similar nature.

Therefore, the value of the results from the small scale experimental system of the present study, lies mainly in revealing the mechanisms that are involved in its response and their influence, as discussed in the previous sections. The above discussion shows that although specific extrapolation might not be practical (and was indeed not intended), these mechanisms as analyzed here are likely to be involved in similar larger scale soil-embedded structure systems.

Table 2-1
Properties of the Micro-Concrete Slabs

Test Number	DOB (inch)	Boundary Conditions	h (inch)	ρ (%)	ρ' (%)	f'_c (psi)
1	3	Simply Supported	0.38	0.6	--	6000
2	3	Simply Supported	0.44	0.5	0.5	6000
3	3	Clamped	0.44	0.25	0.25	6000
4	3	Clamped	0.50	0.22	0.22	5000
5_a	3	Clamped	0.45	0.49	0.49	5000
5_b	2.5	Clamped	0.45	0.49	0.49	5000
6	2.5	Simply Supported	0.43	0.26	0.26	5000
7	2.5	Simply Supported	0.52	0.21	0.21	5000
8	2.5	Clamped	0.45	0.24	0.24	6500

Notes:

1. Internal radius, R = 2.50 inches.
2. $\rho = 100 \cdot A_s / s \cdot d$, in each direction, where $A_s = 9.5115 \cdot 10^{-4}$ in^2, is the cross sectional area of the #20 wire that was used, s is the spacing, and d = h - 0.06 inch.
3. $f_y = 51000$ psi.
4. 1 inch = 2.54 cm; 1 in^2 = 6.45 cm^2; 145 psi = 1 MPa.

Table 2-2
Sequence of the Impactor Hits

Test Number	Height of Drop of the Impactor (inches)									
	Hit #1	Hit #2	Hit #3	Hit #4	Hit #5	Hit #6	Hit #7	Hit #8	Hit #9	Hit #10
1	25	25	25	50	50[1]					
2	25	25	25	25	35	50[1]				
3	25	35	35[2]	35	35	50	50[3]			
4	25	25	50	50	65	65	75	75	90	90[3]
5_a	50	50	65	65	90	90[4]				
5_b	50	65	90	90[3]						
6	25	25	25	90[5]						
7	25	25	25[6]	75	75[7]					
8	25	25	25	75	90[5]					

1. LVDT and accelerometer were detached. Visible cracks at the bottom of the slab.

2. LVDT was detached. This hit was not recorded.
3. Slight cracking at the bottom of the slab.

4. The structure was excavated and no visible damage was detected. The slab was re-embedded under 2.5 inches (test 5_b).

5. Mild failure, visible cracks at the bottom of the slab.
6. LVDT was detached and the structure was excavated. Two slight radial cracks were observed. The slab was re-embedded.
7. LVDT was detached and the structure was excavated. The roof slab failed, more radial cracks were observed.

Table 2-3

Method of Data Acquisition

Information / Record	Source
Start time of the vertical velocity and displacement at roof center.	Top accelerometer output (singly and doubly integrated, respectively).
Amplitude of the vertical velocity and displacement at the roof center.	LVDT output (first derivative and direct output, respectively; time is shifted according to the above).
Start time of the whole structural vertical velocity and displacement.	Bottom accelerometer output (once and double integrated, respectively).

Note: Since the magnitudes of the rigid body velocity and displacement are less than 10% of the roof center velocity and displacement (compare test results in figures 2-15 and 2-16), the difference between the relative and absolute motion records of the roof center is not large. However, for determining the possible load-displacement (or load-velocity) relationship at the roof edge, the rigid body displacement record (bottom accelerometer) is not negligible, and even if its amplitude had relatively larger experimental errors (than the LVDT's records), important information about the start time of that displacement and its general shape (in the time domain) is provided.

Table 2-4
Wave Velocities and Propagation Time in Micro-Concrete Slabs

	$E = 2\cdot10^6$ psi		$E = 5\cdot10^6$ psi	
	$\nu = 0.1$	$\nu = 0.2$	$\nu = 0.1$	$\nu = 0.2$
c_L (in/sec)	102419	106752	161938	168790
t_T (h = 0.4")	7.8 μsec	7.5 μsec	4.9 μsec	4.7 μsec
t_T (h = 0.5")	9.7 μsec	9.3 μsec	6.2 μsec	5.9 μsec

Table 2-5
Extrapolation Ratios from a Small Scale System to a Larger Scale System

Description of the variable	Dimension	Prototype/Model ratio
Geometry variables which have a length dimension	L	n
Geometry variables which have area dimension	L^2	n^2
Variables which have dimension of force per area (e.g. pressure, bulk modulus).	FL^{-2}	1
Non-dimensional variables (e.g. strain, Poisson ratio)	--	1
Variables which have dimension of mass density	$ML^{-3} =$ FT^2L^{-4}	1
Accelerations	LT^{-2}	n^{-1}*
Velocities	LT^{-1}	1
Time	T	n

* with the exception of the acceleration of gravity (i.e., $g_m = g_p$).

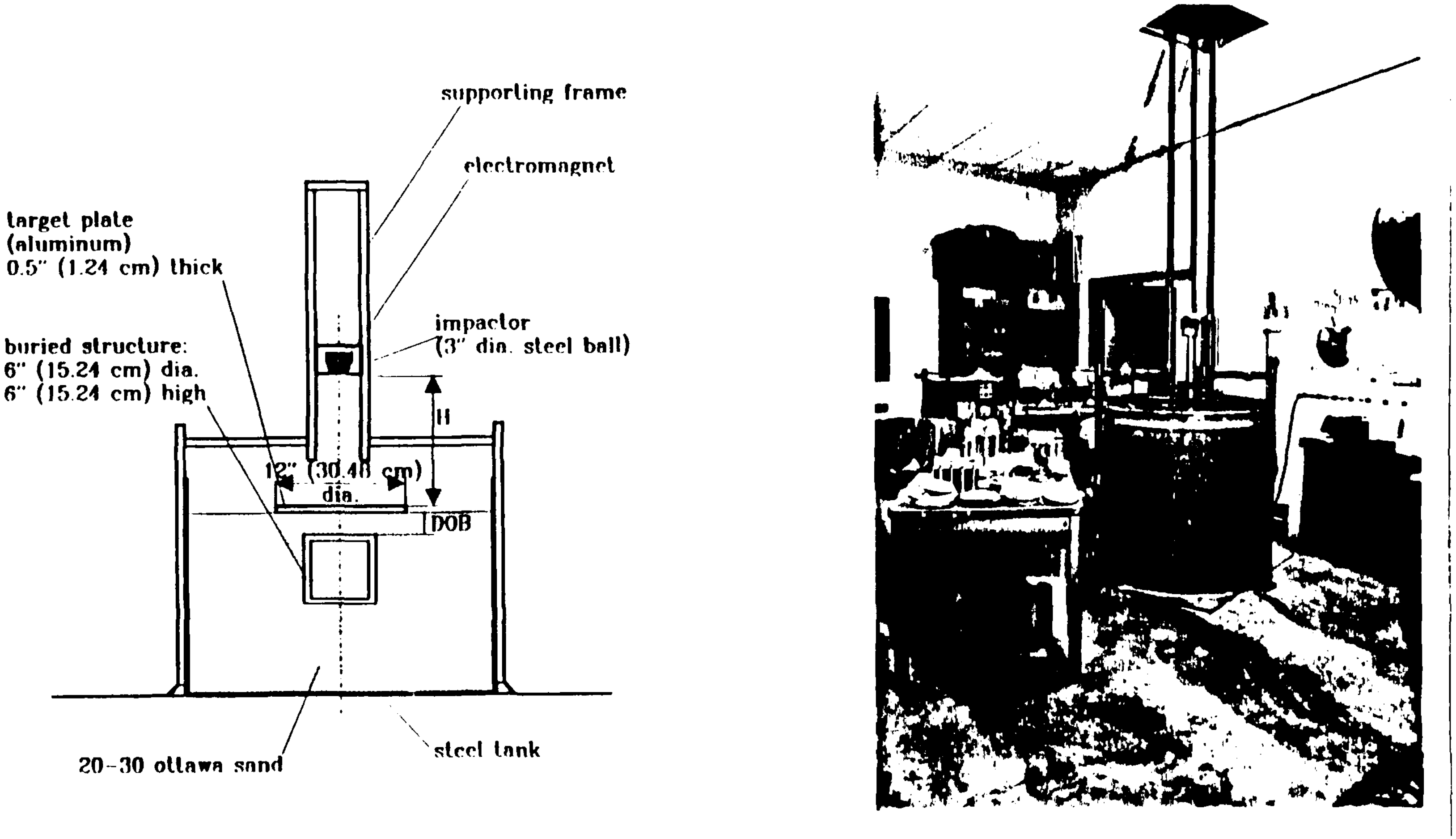
supporting frame
electromagnet
target plate
(aluminum)
0.5" (1.24 cm) thick
impactor
(3" dia. steel ball)
buried structure:
6" (15.24 cm) dia.
6" (15.24 cm) high
H
12" (30.48 cm)
dia.
DOB
20-30 ottawa sand
steel tank

Fig. 2-1: Experimental set up for a small scale model of a soil-embedded structure system.

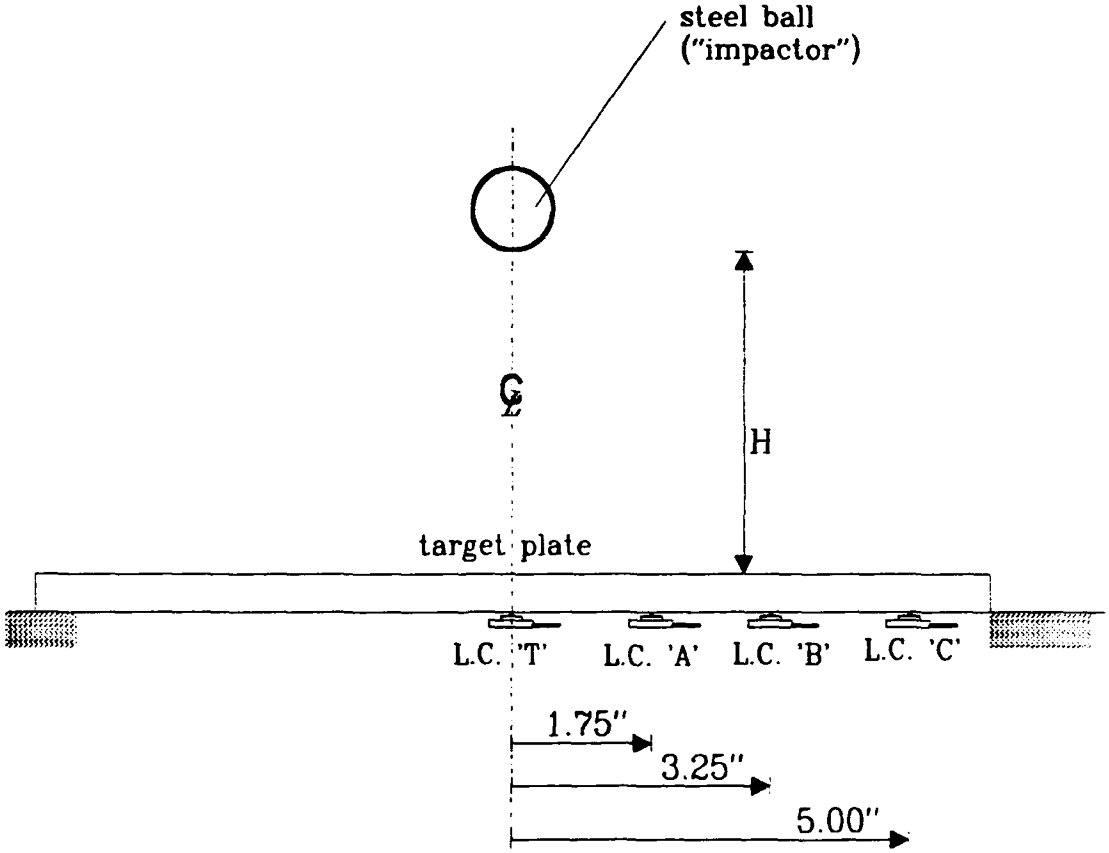
steel ball
("impactor")
℄
H
target plate
L.C. 'T'
L.C. 'A'
L.C. 'B'
L.C. 'C'
1.75"
3.25"
5.00"

Fig. 2-2: External load mesurement setup.

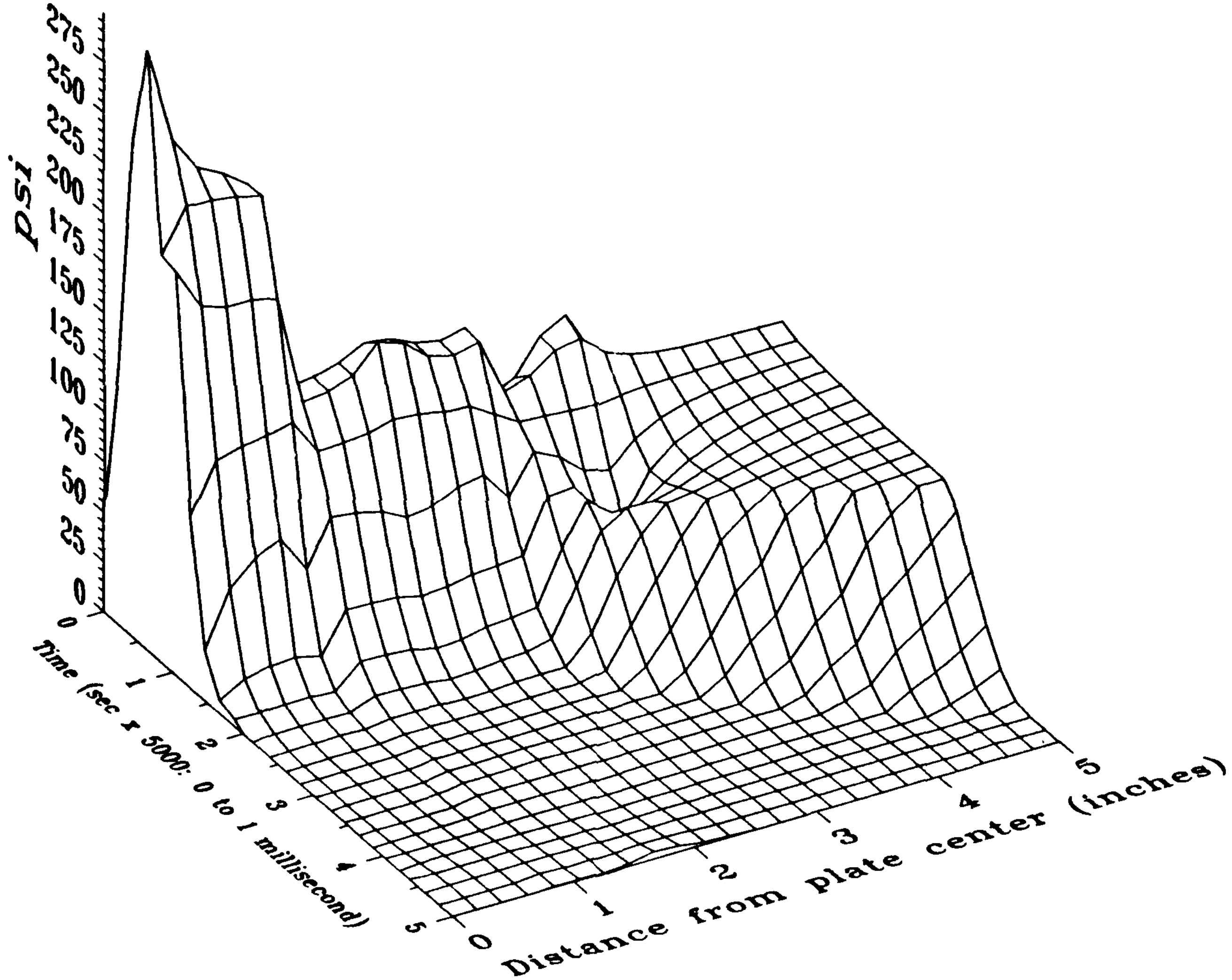

Fig. 2–3–a: Pressure distribution under the target plate (H =25 inches)

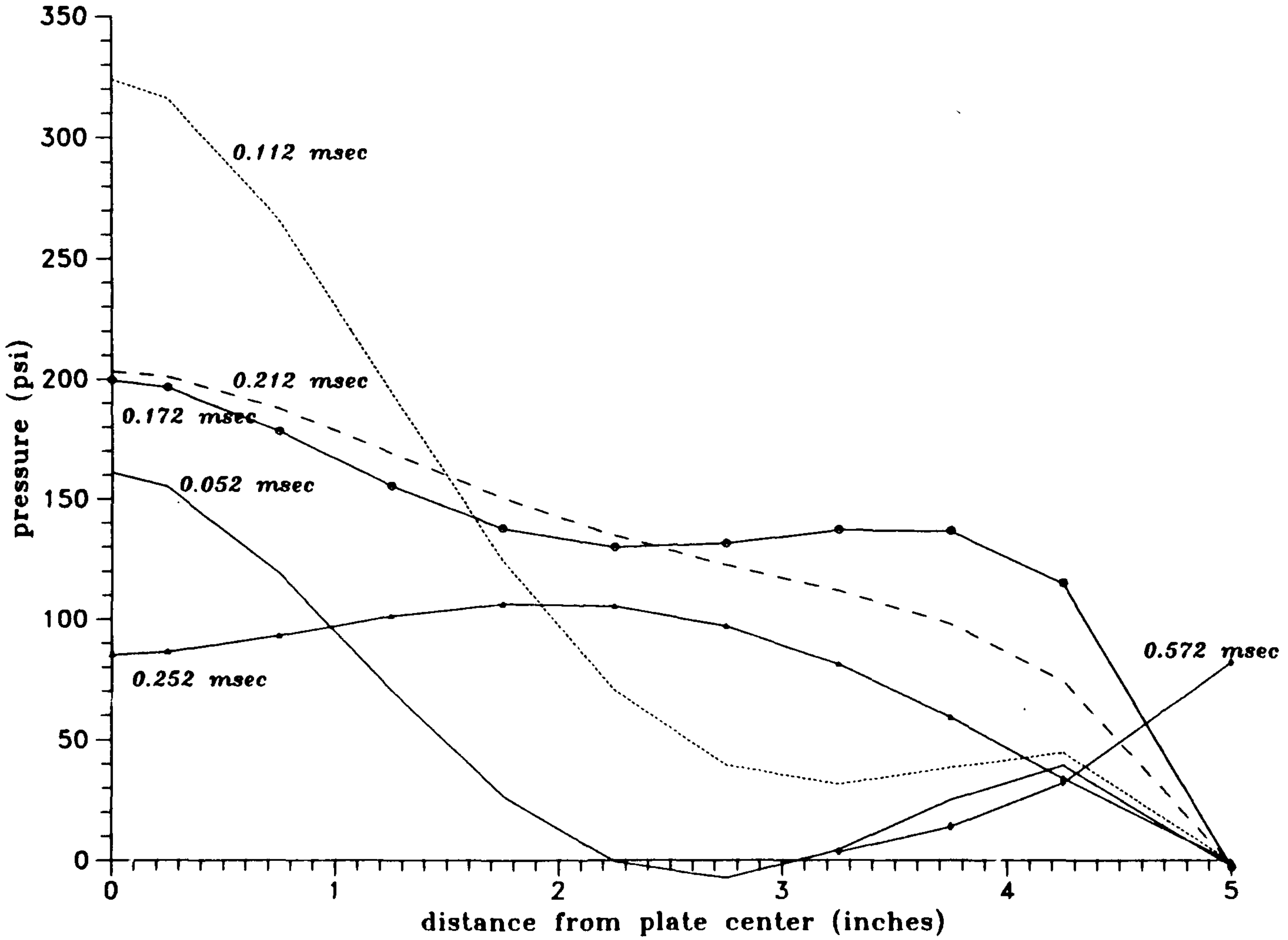

Fig. 2-3-b: Pressure distribution under the target plate (H = 25 inches).

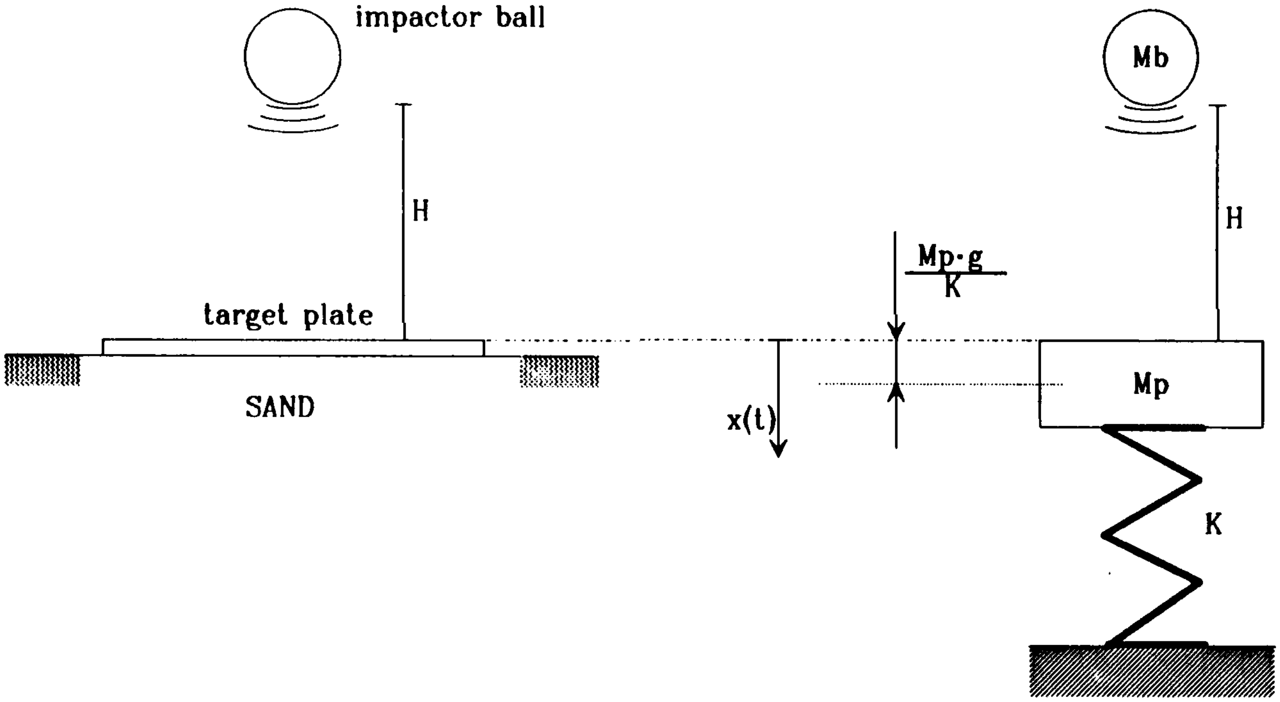
impactor ball
H
target plate
SAND
x(t)
Mp·g / K
Mb
H
Mp
K

Fig. 2-4: Equivalent SDOF system for estimation of the total load induced under the target plate.

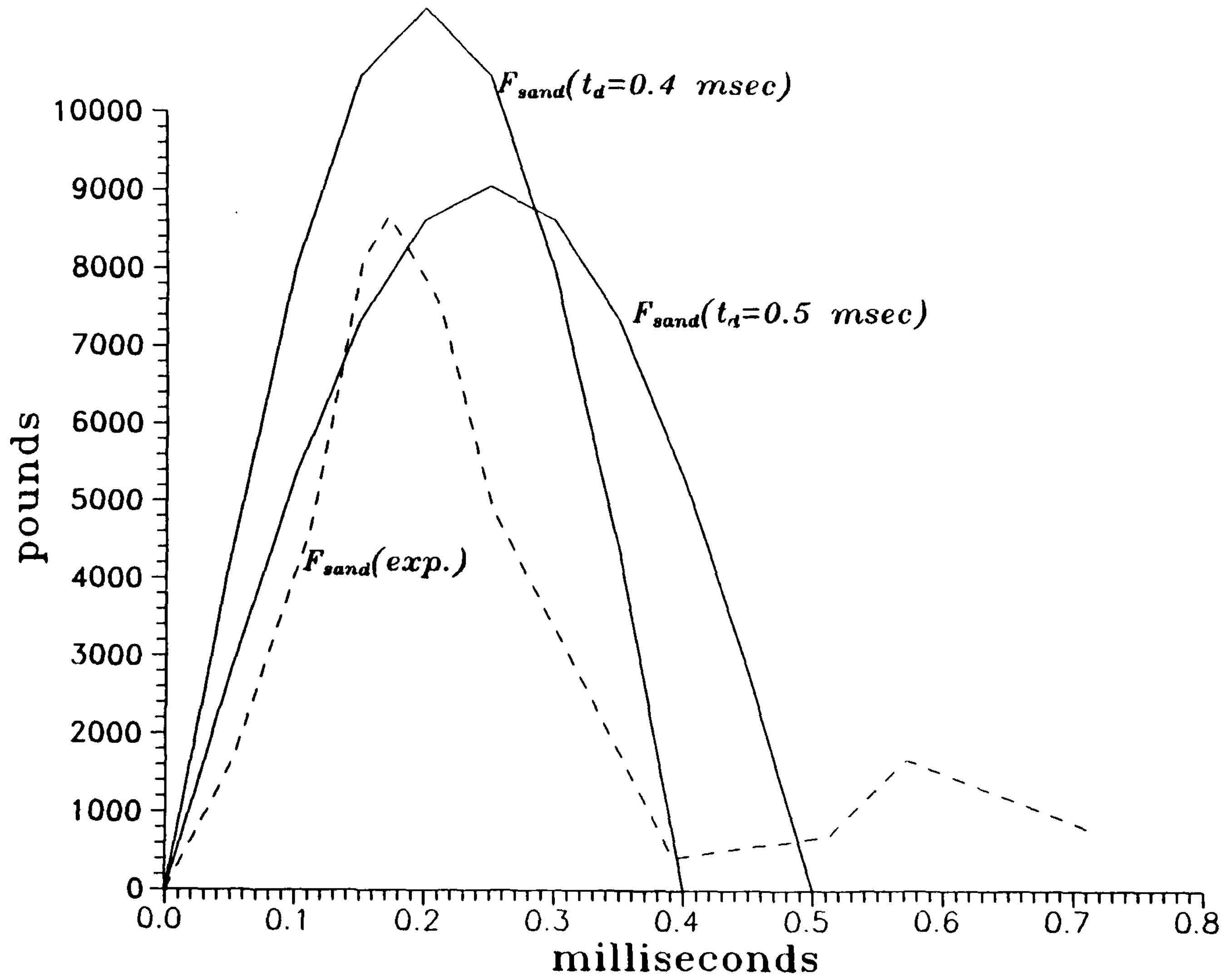

Fig. 2-5: The total force, F_{sand}, applied under the target plate (H = 25 in).

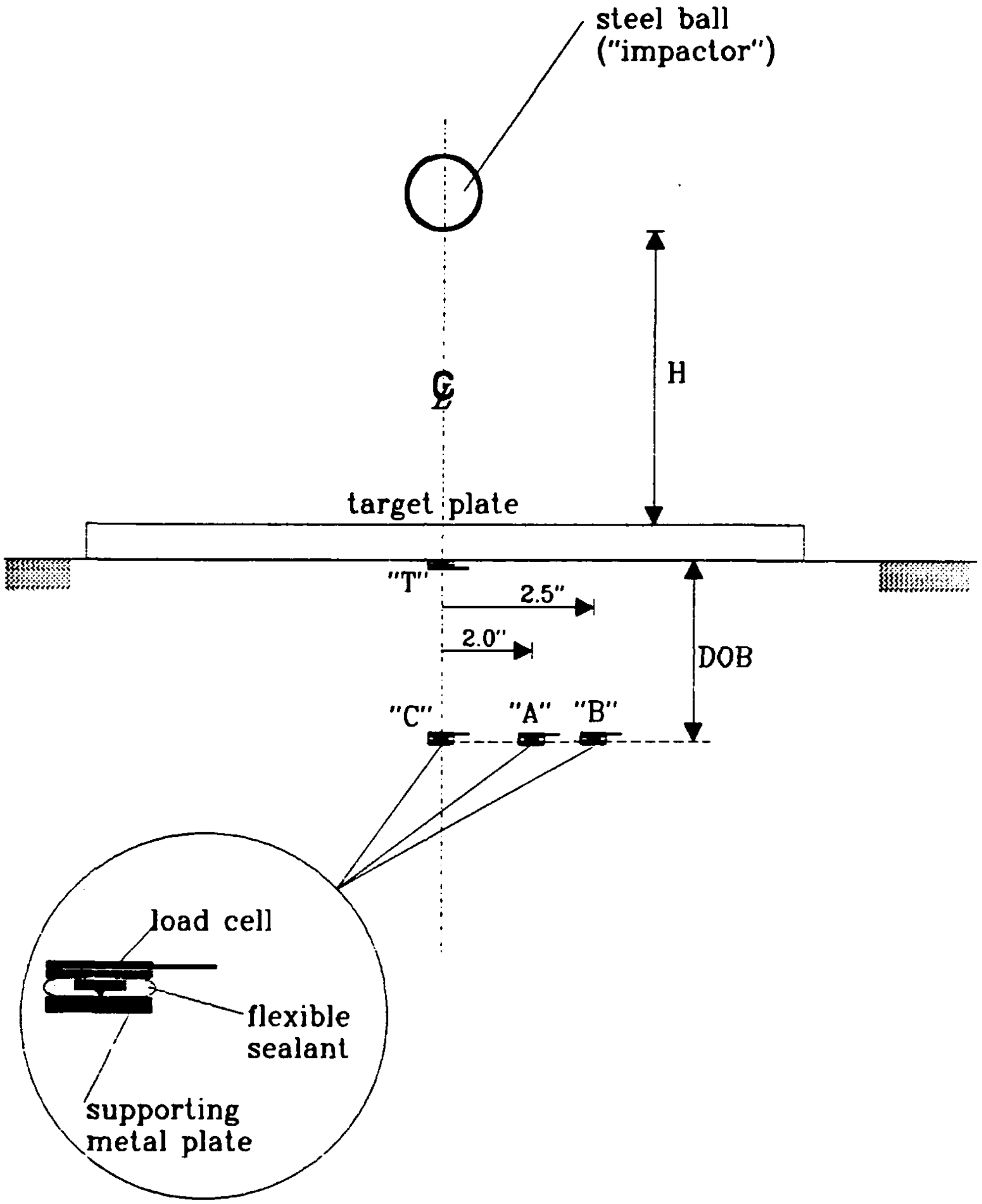
steel ball
("impactor")
℄
H
target plate
"T"
2.5"
2.0"
DOB
"C"
"A"
"B"
load cell
flexible
sealant
supporting
metal plate

Fig. 2–6: Setup for measurement of the free field vertical stress distribution.

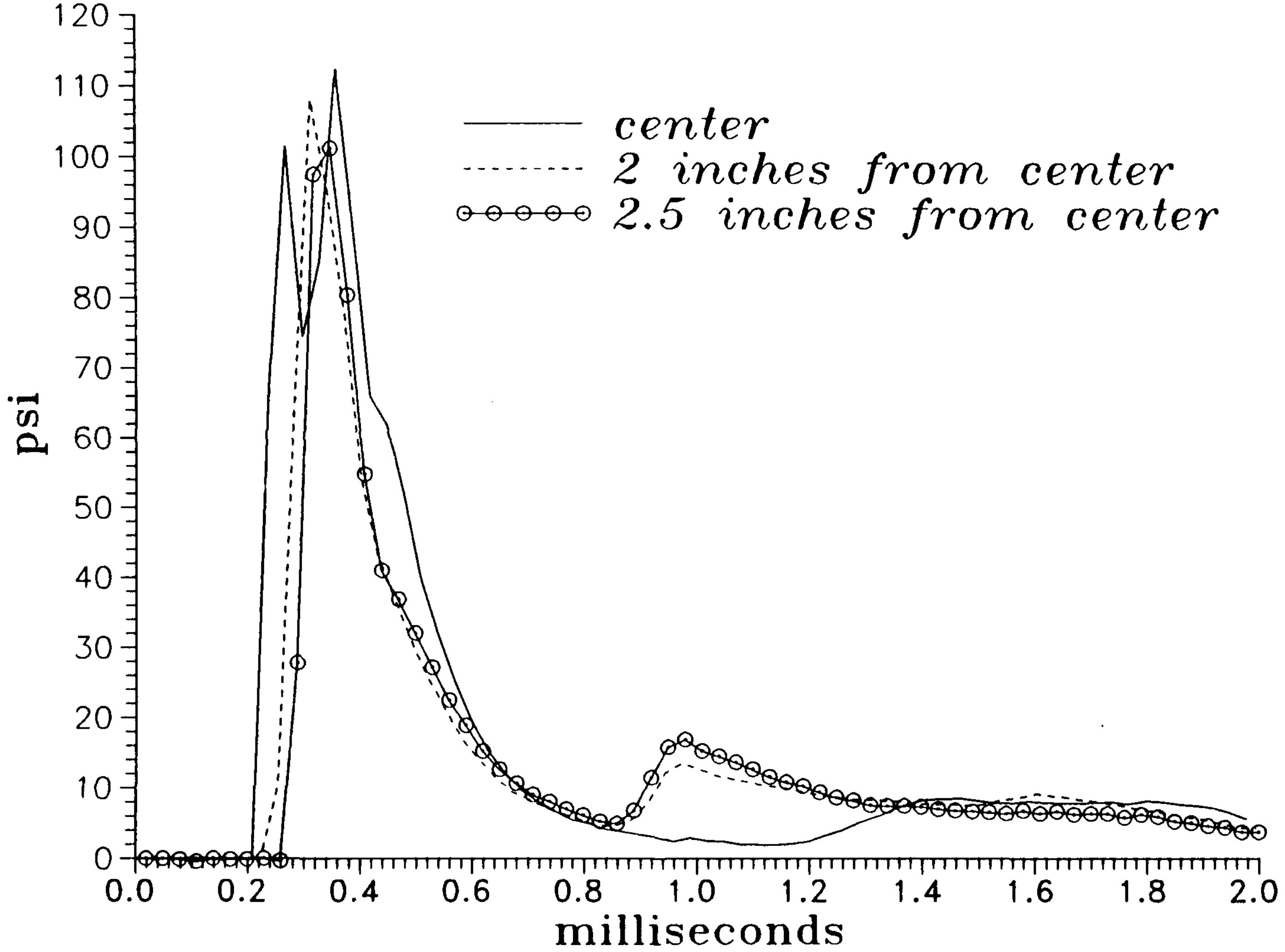

Fig. 2-7-a: Free field pressure; DOB = 3 inches, H = 25 inches.

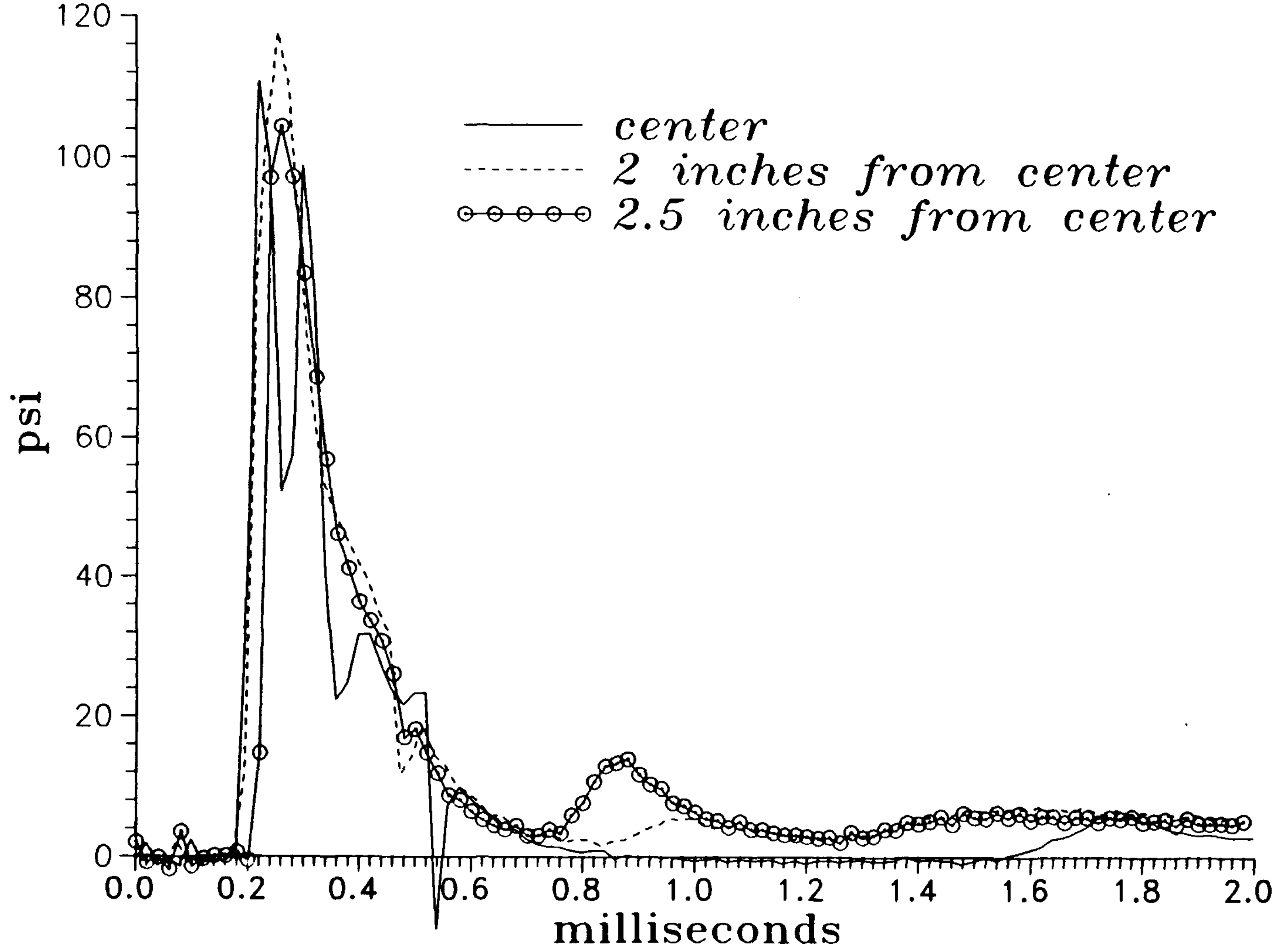

Fig. 2-7-b: Free field pressure; DOB = 2.5 inches, H = 25 inches.

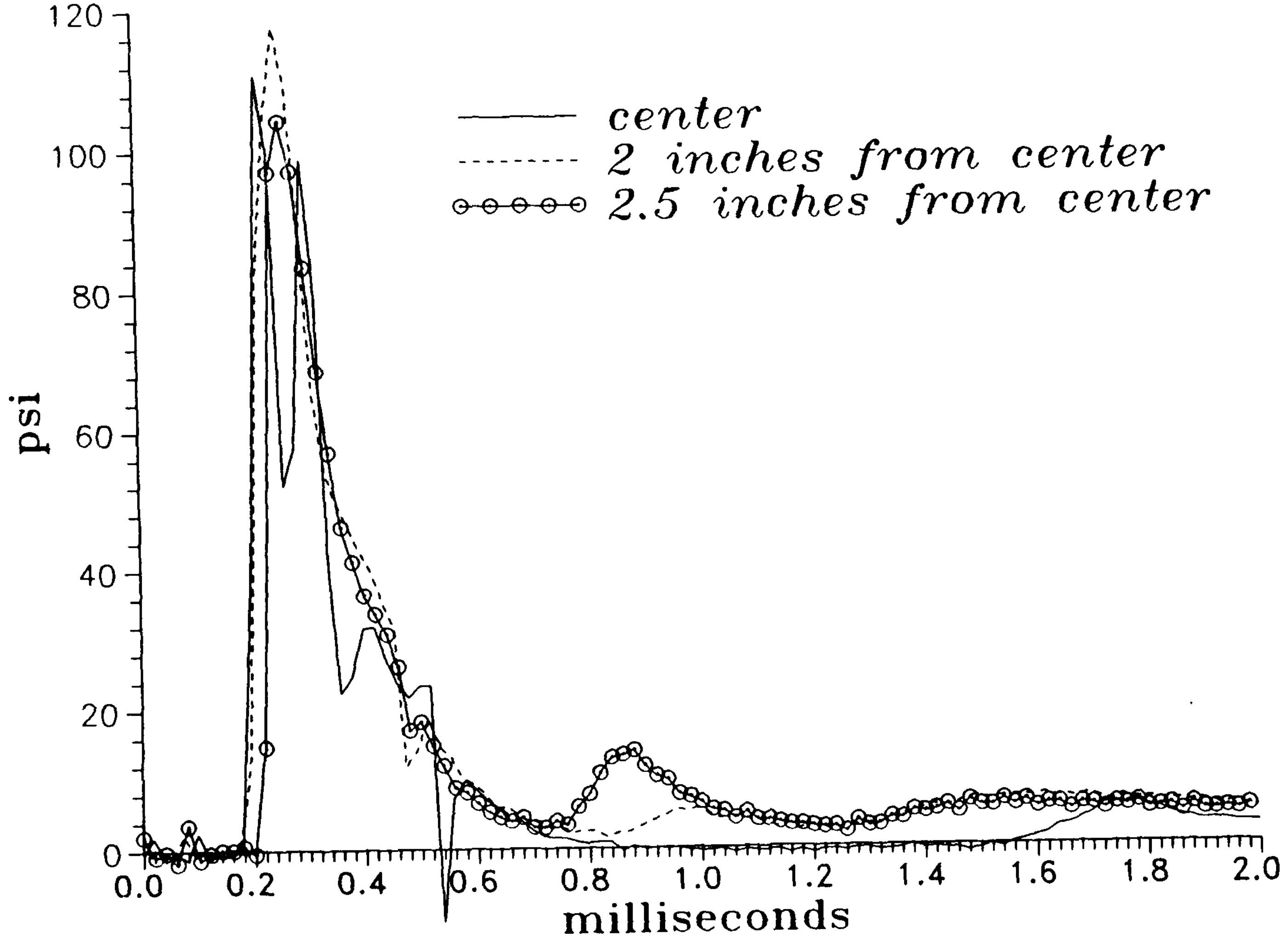

Fig. 2-7-b: Free field pressure; DOB = 2.5 inches, H = 25 inches.

Percent of Microaggregate

Sieve #	Percent sand by weight
30	
	20
50	
	70
100	
	10
100	

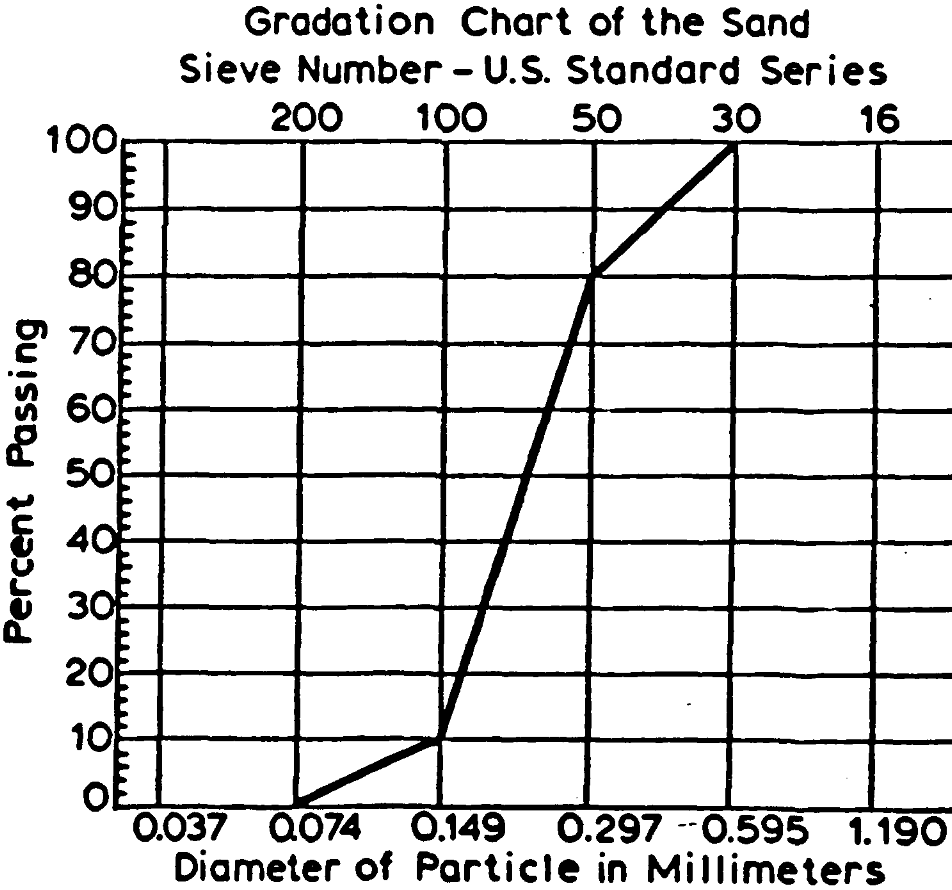
Gradation Chart of the Sand
Sieve Number - U.S. Standard Series

Fig. 2-9: Sieved portions of the sand used for the micro-concrete specimens.

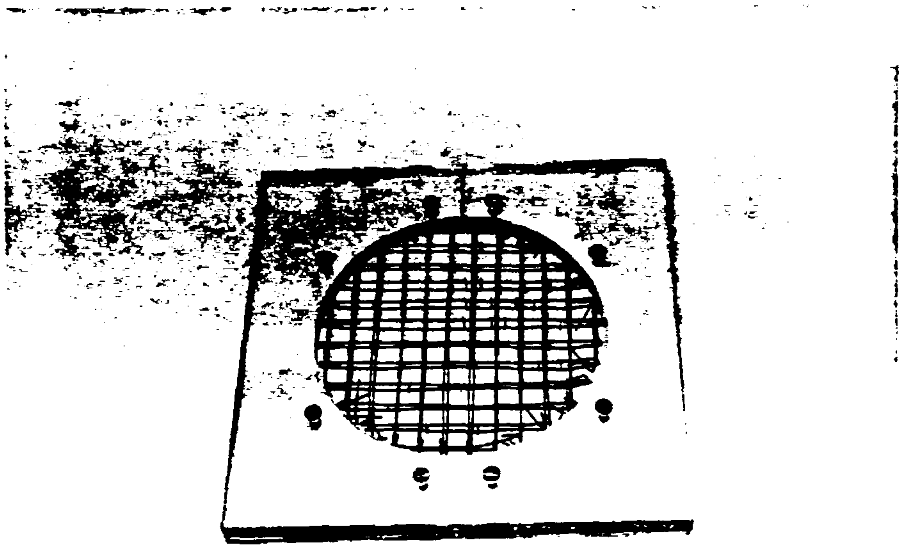

Fig. 2-10-a: Form and reinforcement ready for casting of micro-concrete slabs.

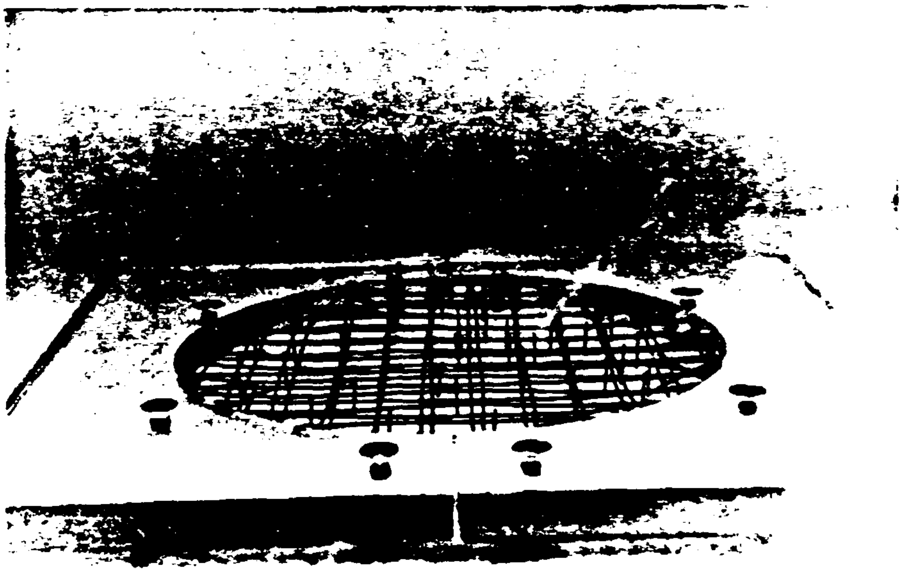

Fig. 2-10-b: Casting of micro-concrete slabs -detailed view of the double reinforcement placed in the form (The spot welded meshes are held apart with vertical spacers).

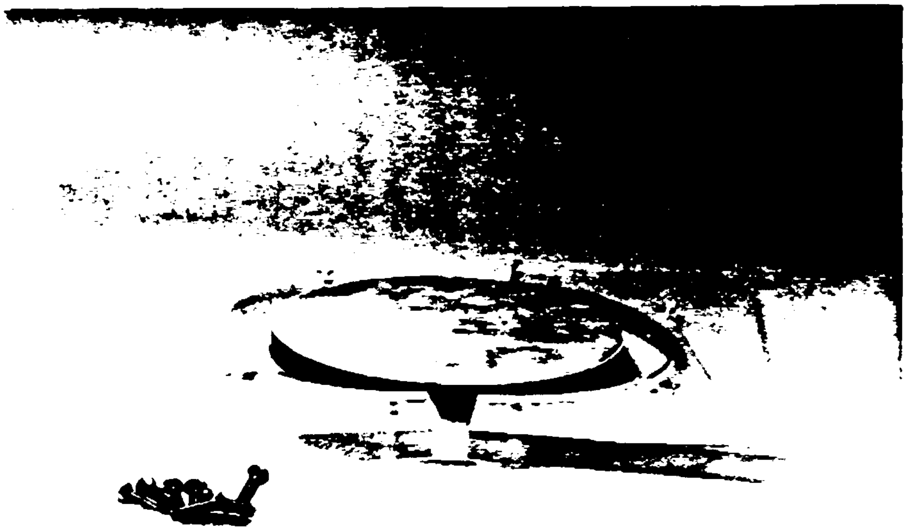

Fig. 2-10-c: Removal of the specimen from the form after casting.

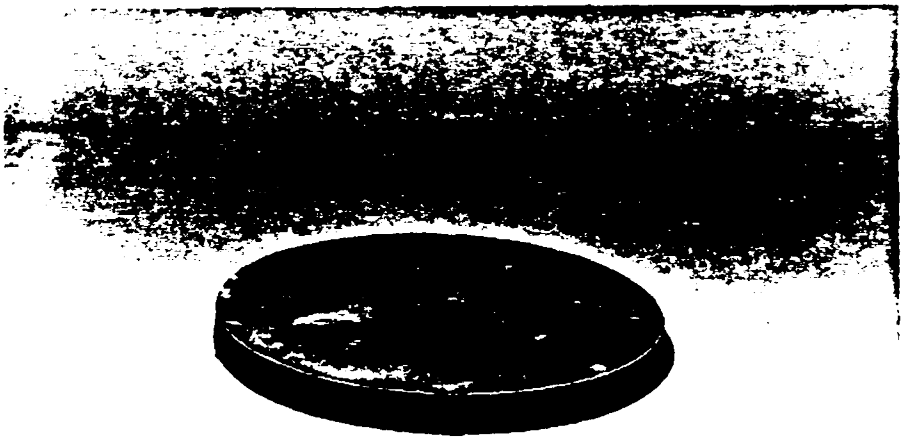

Fig. 2-10-d: Casting of micro-concrete slabs - the final product, a doubly reinforced micro-concrete slab (Actual dimensions: 0.45 inch thick, 6 inches diameter).

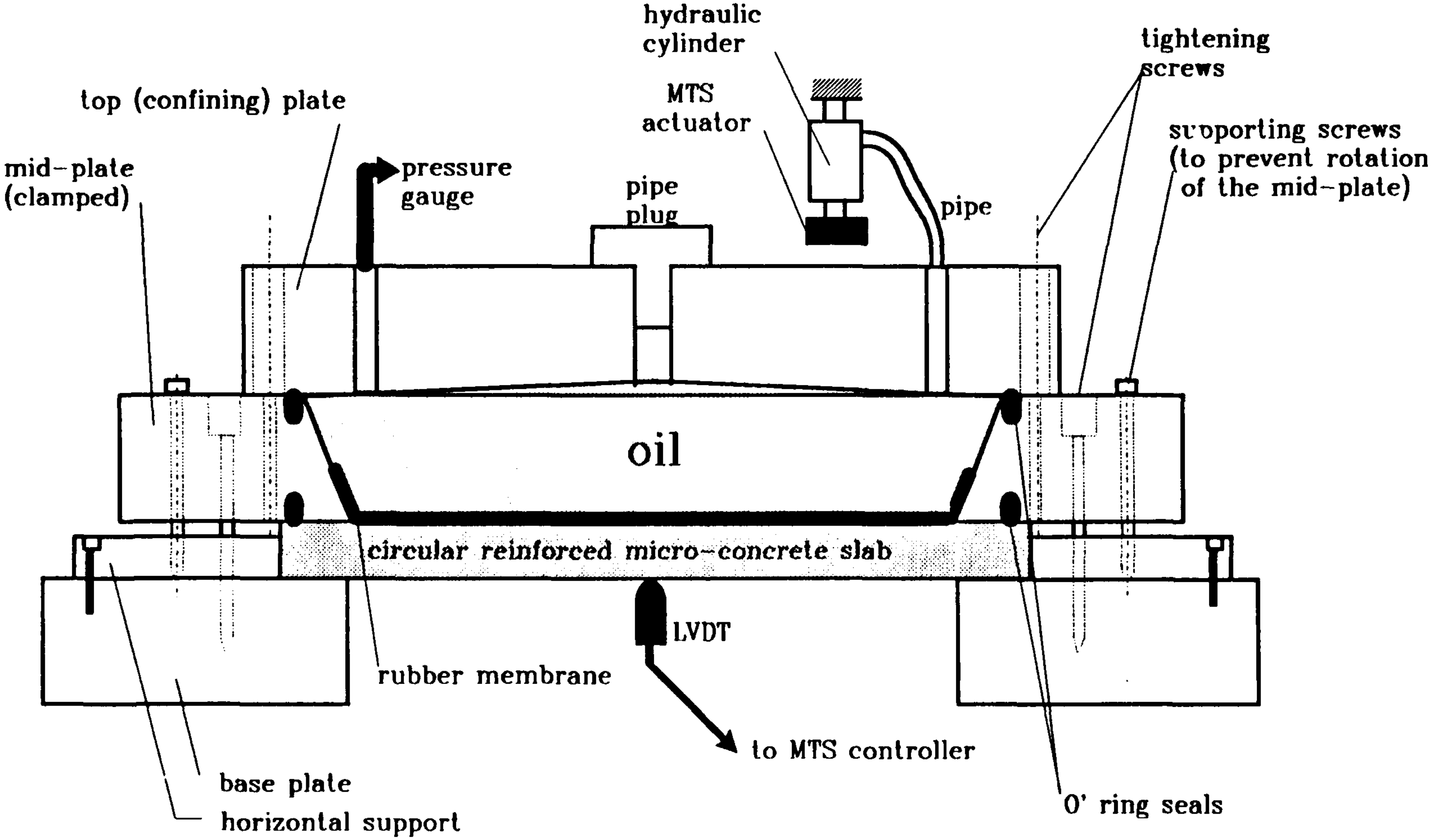
hydraulic cylinder
MTS actuator
tightening screws
top (confining) plate
supporting screws (to prevent rotation of the mid-plate)
mid-plate (clamped)
pressure gauge
pipe plug
pipe
oil
circular reinforced micro-concrete slab
LVDT
rubber membrane
to MTS controller
base plate
horizontal support
0' ring seals

Fig. 2-11: Setup for testing the micro-concrete slabs under direct uniform pressure.

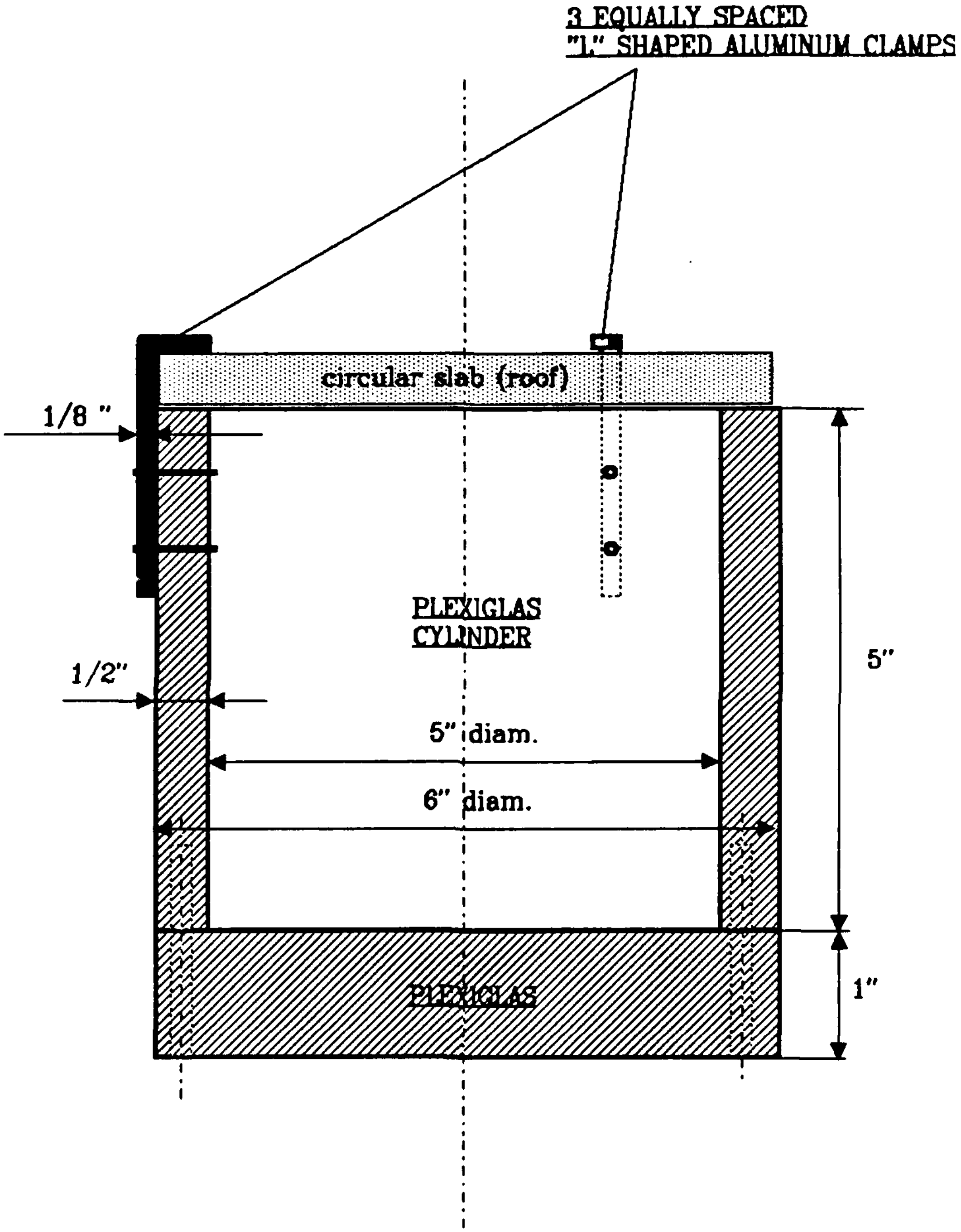
3 EQUALLY SPACED
"L" SHAPED ALUMINUM CLAMPS
circular slab (roof)
1/8 "
PLEXIGLAS
CYLINDER
1/2"
5" diam.
6" diam.
5"
PLEXIGLAS
1"

Fig. 2-12-a: Details of a structure with a SIMPLY SUPPORTED roof.

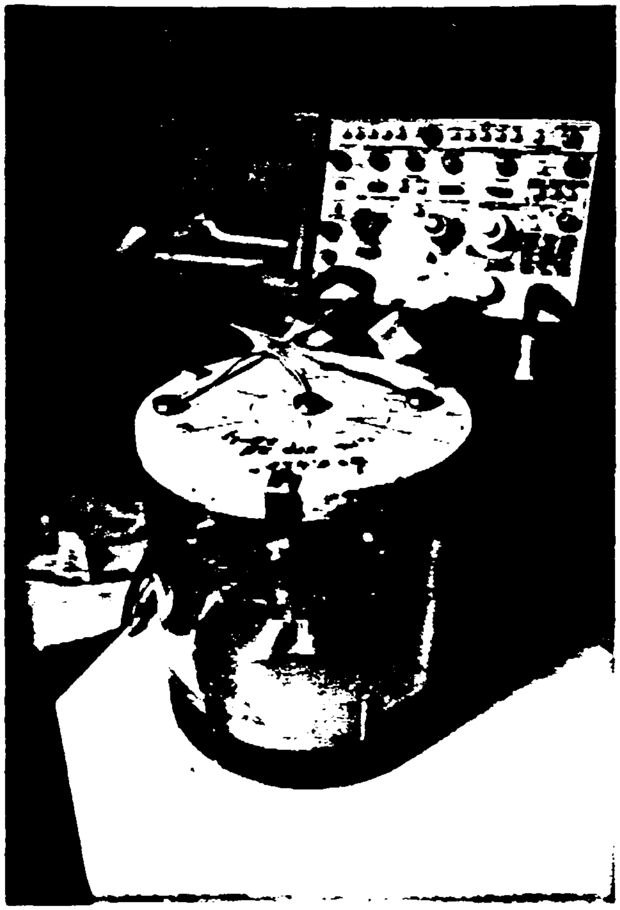

Fig. 2-12-b: Detail of the model structure with a SIMPLY SUPPORTED roof.

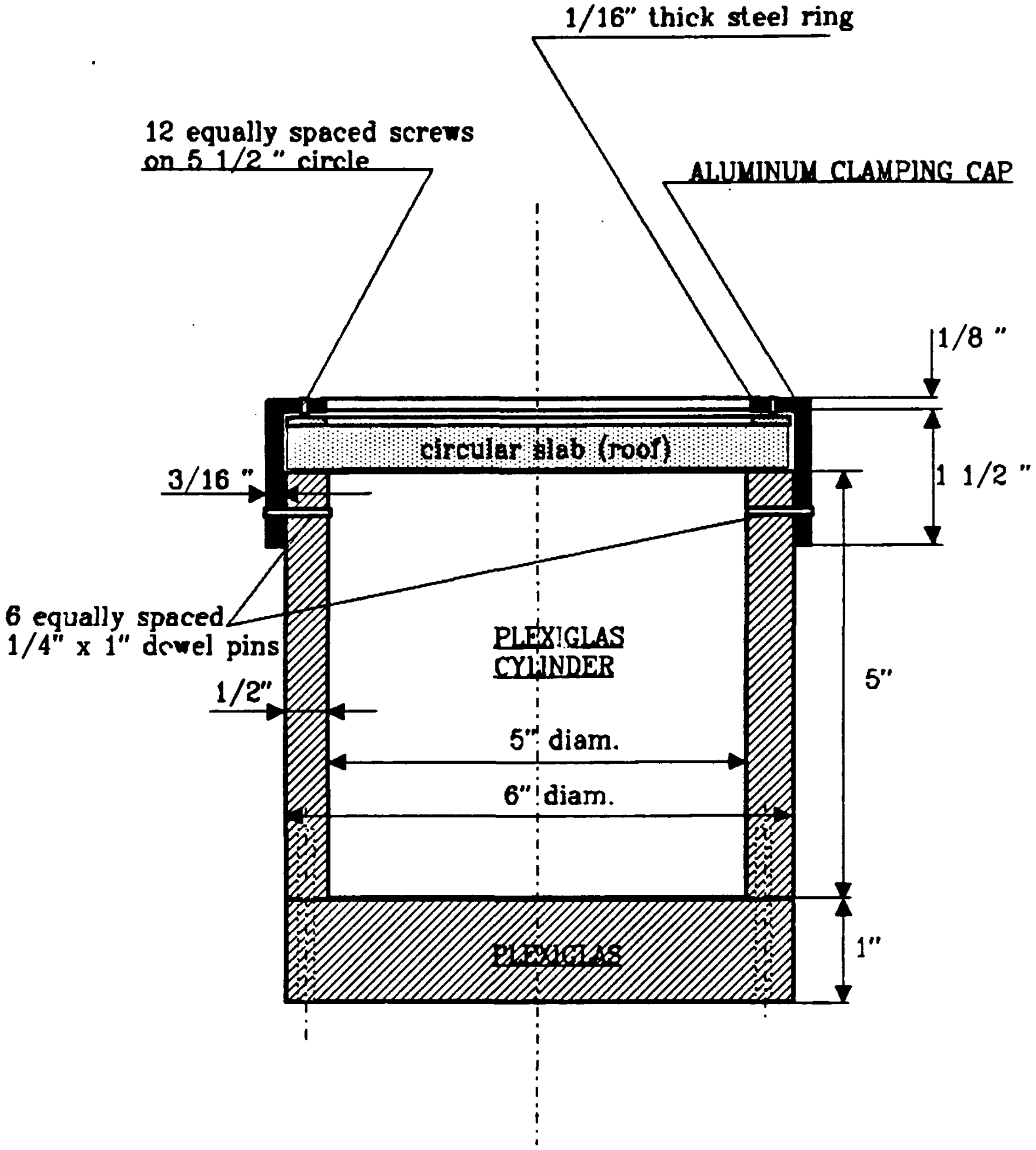
1/16" thick steel ring
12 equally spaced screws on 5 1/2 " circle
ALUMINUM CLAMPING CAP
1/8 "
circular slab (roof)
1 1/2 "
3/16 "
6 equally spaced 1/4" x 1" dowel pins
PLEXIGLAS CYLINDER
1/2"
5"
5" diam.
6" diam.
PLEXIGLAS
1"

Fig. 2-13-a: Details of a structure with a CLAMPED roof.

Fig. 2-13-b: Detail of the model structure with a CLAMPED roof.

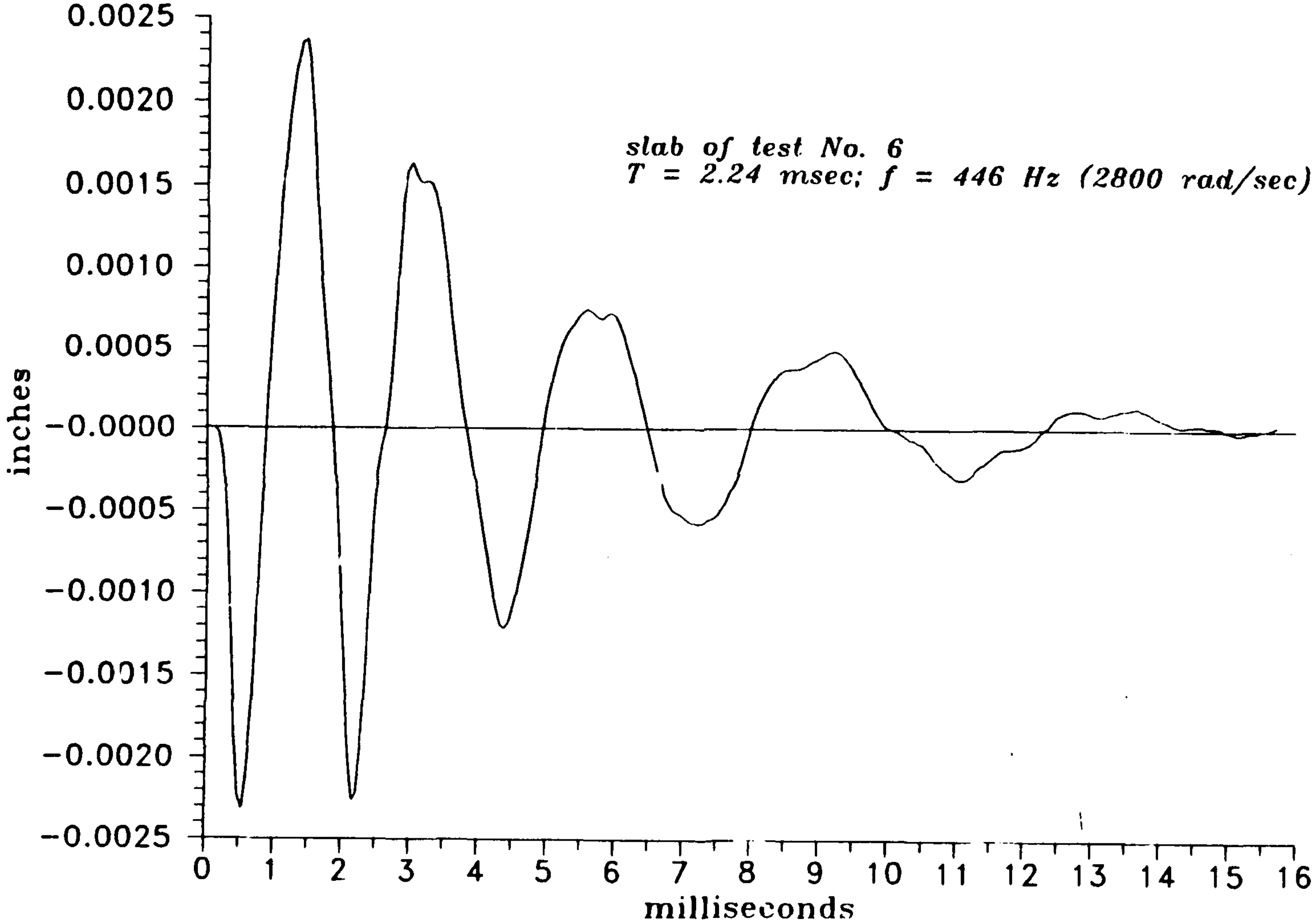

Fig. 2-14-a: Free Vibration of a simply supported slab.

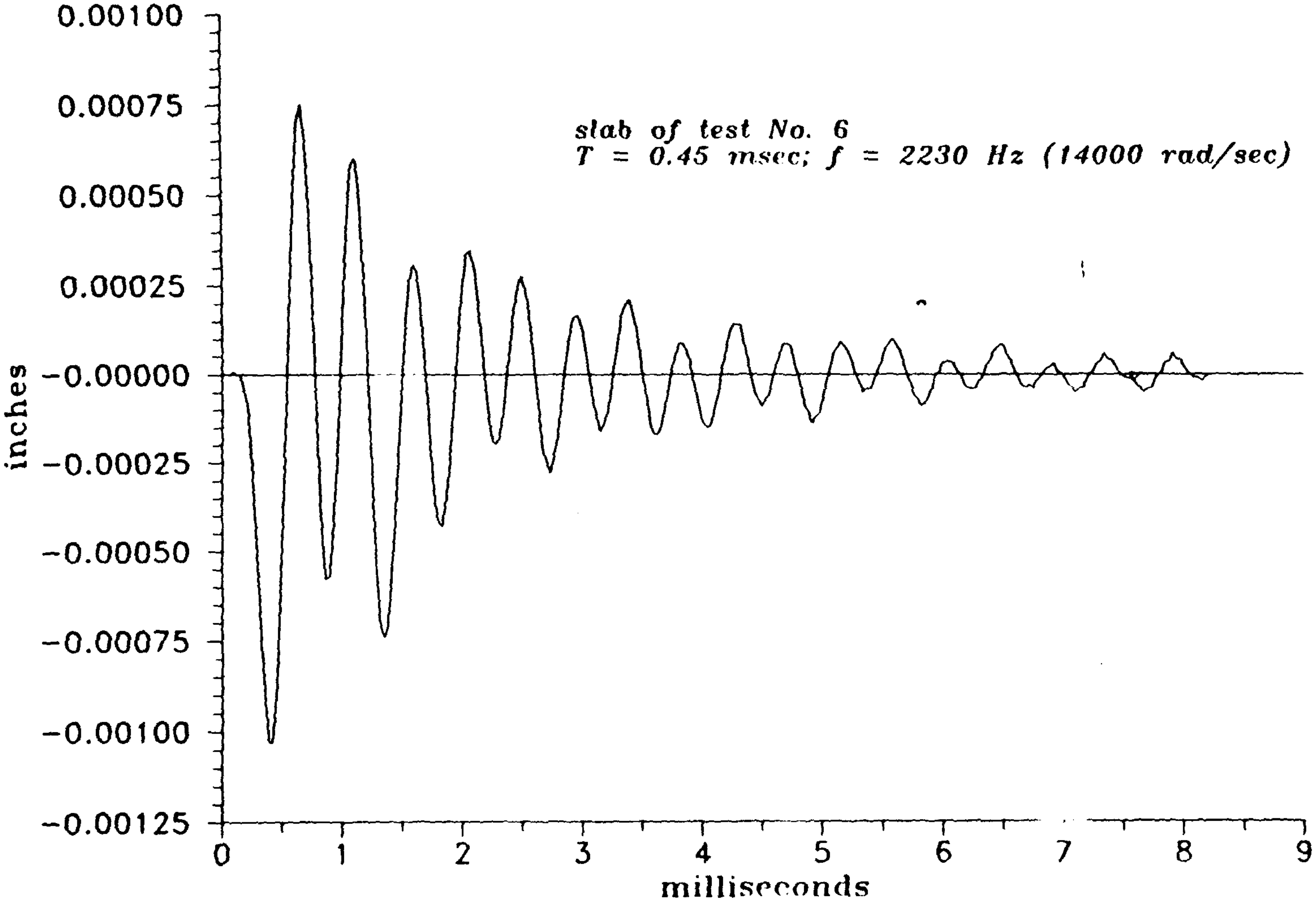

Fig. 2-14-b: Free Vibration of a clamped slab.

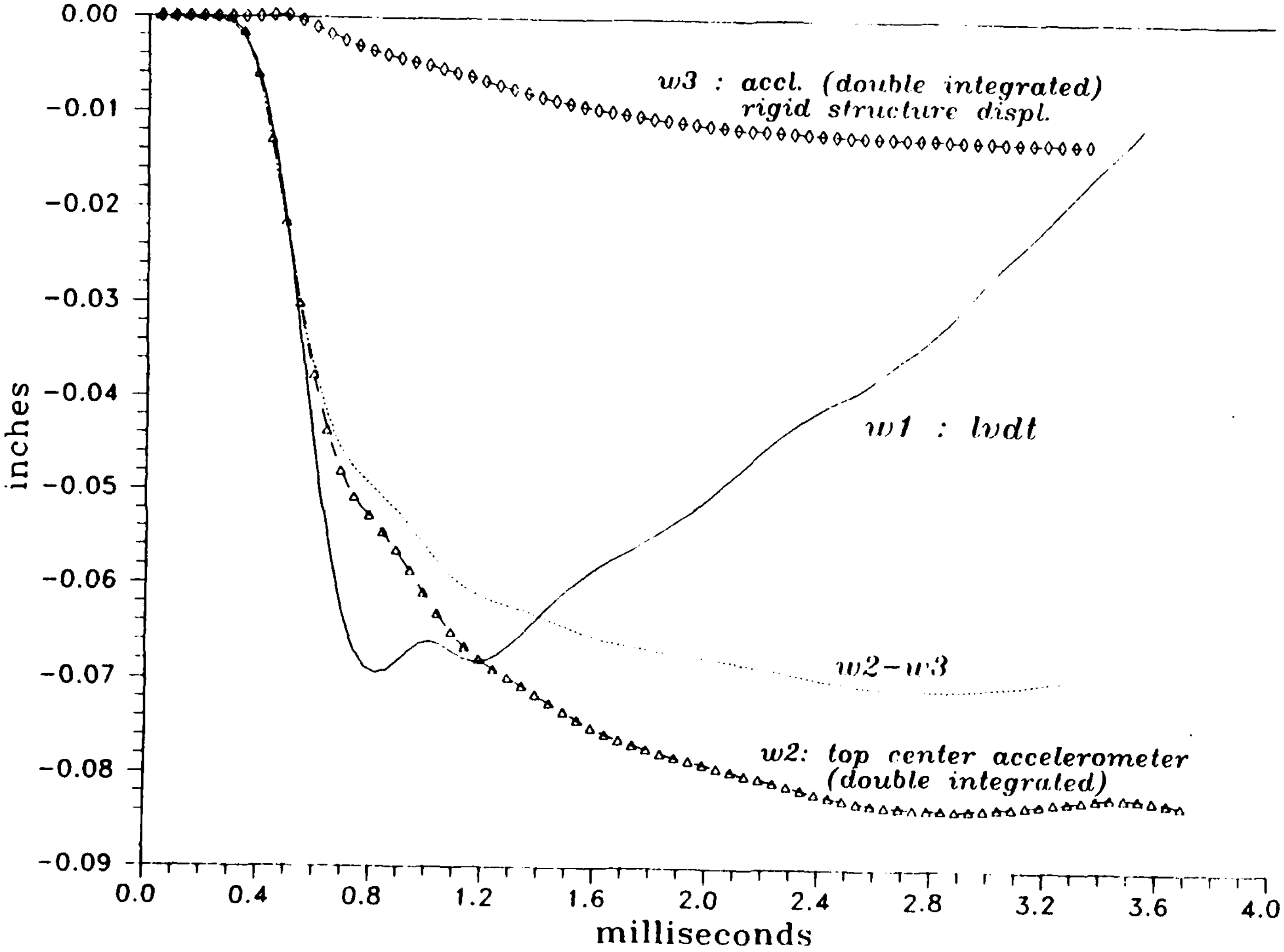

Fig. 2-15: Displacement records of the roof center and of the rigid structure (Plexiglas roof).

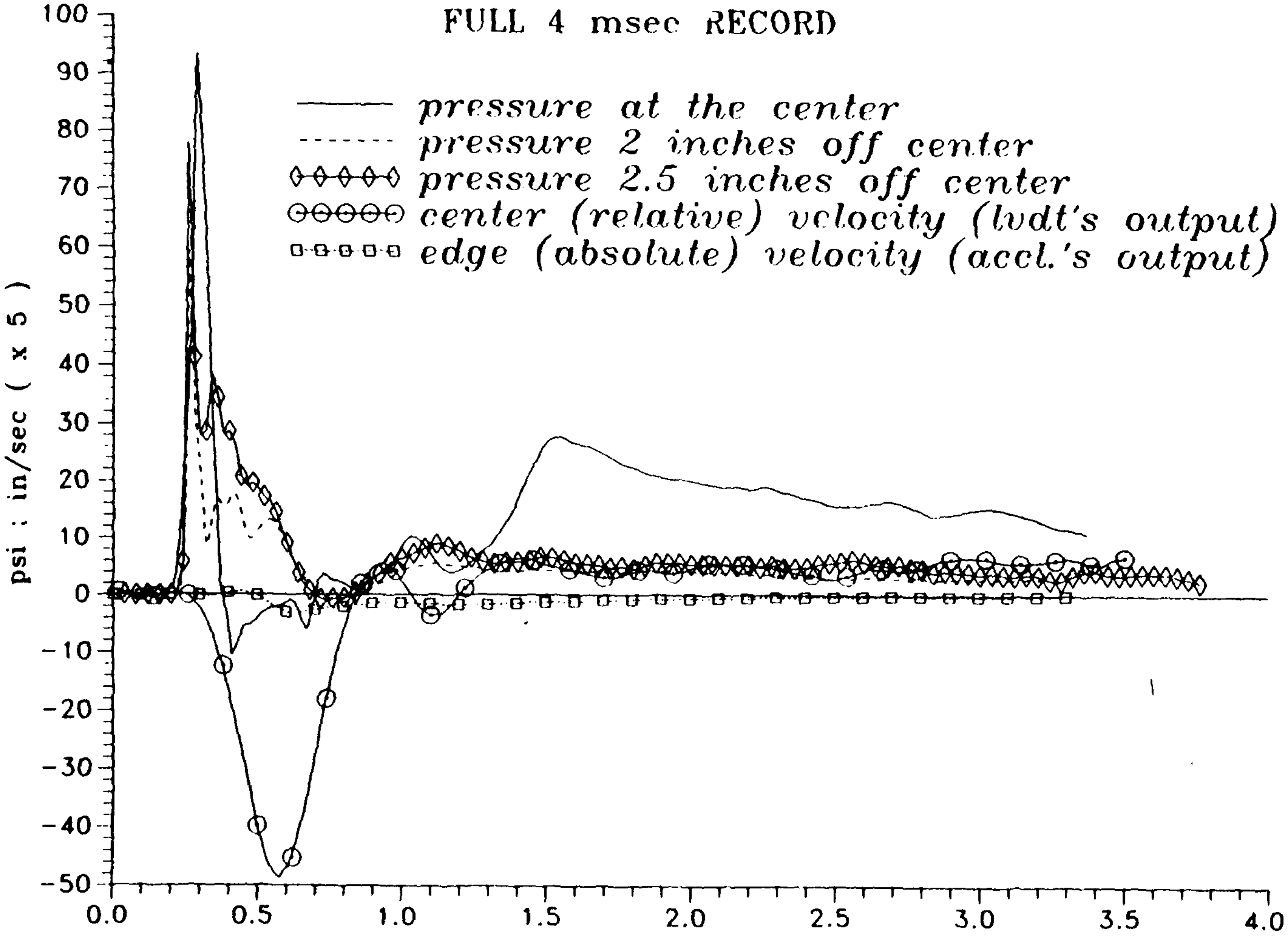

Fig. 2-16: Pressure and velocity signals of the plexiglas roof. (DOB = 3 inches, H = 25 inches)

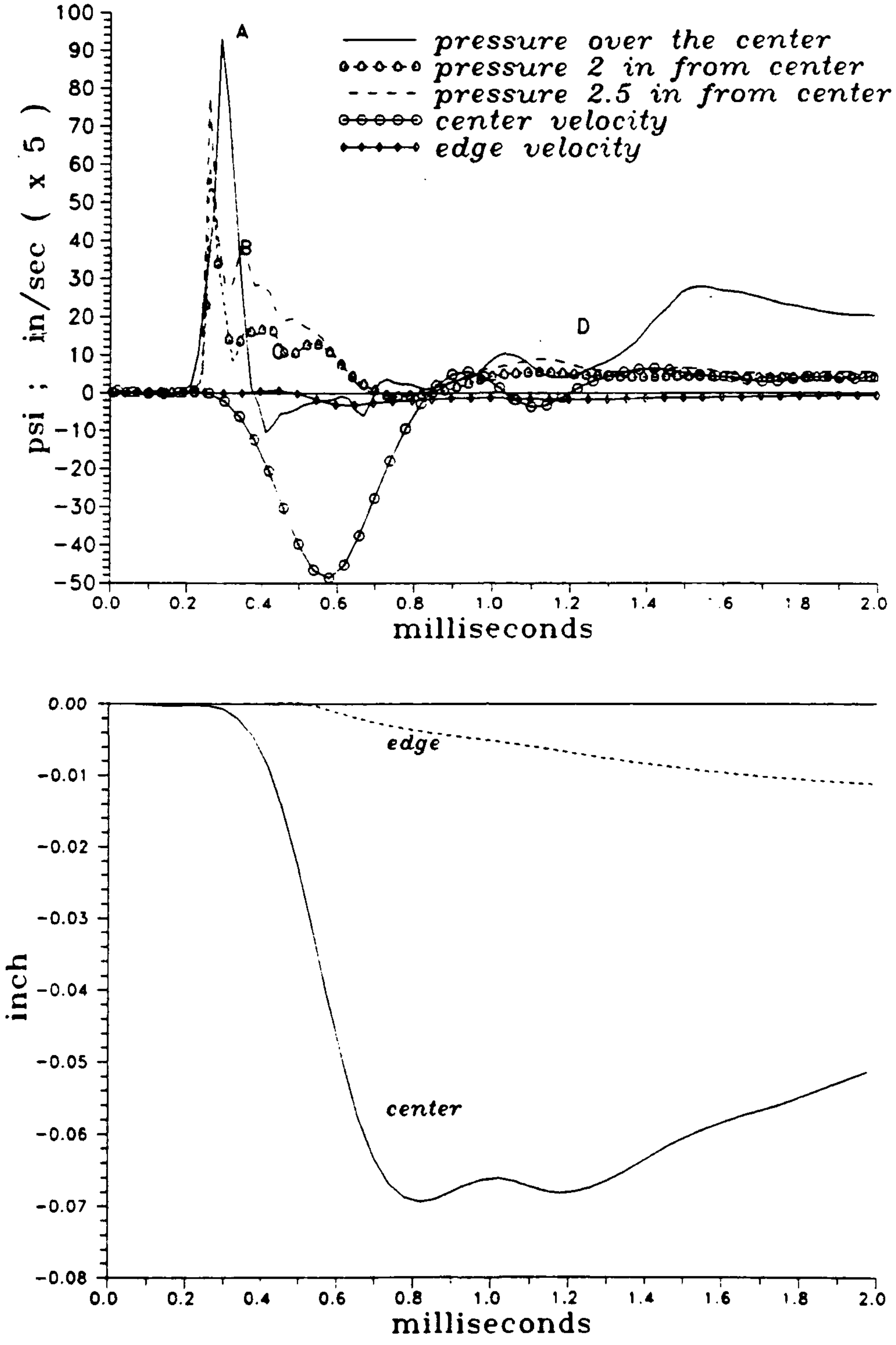

Displacements

Fig. 2-17: Response of the plexiglas roof.
(DOB = 3 in; H = 25 in)

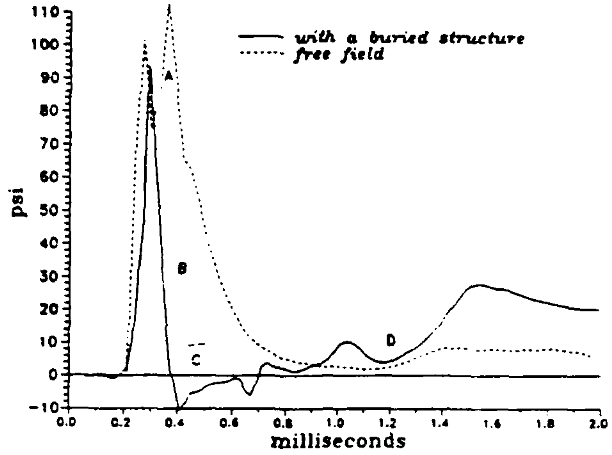

At the center.

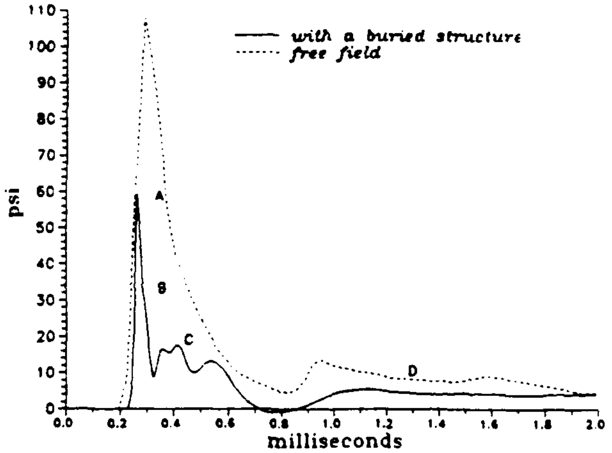

2 inches from the center.

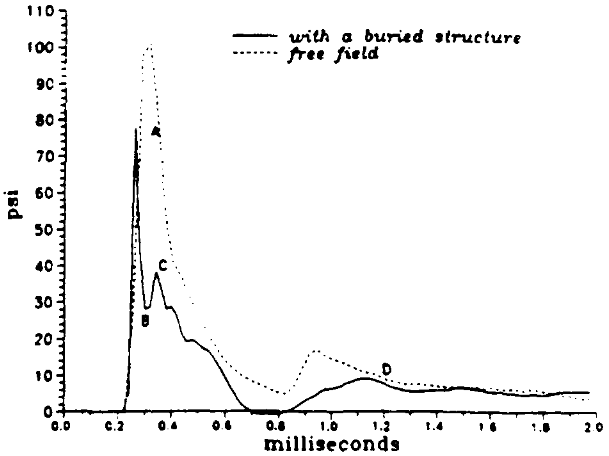

2.5 inches from the center.

Fig. 2-18: Pressure at buried roof level v.s. free field.
(Plexiglas roof; DOB = 3 in, H = 25 in)

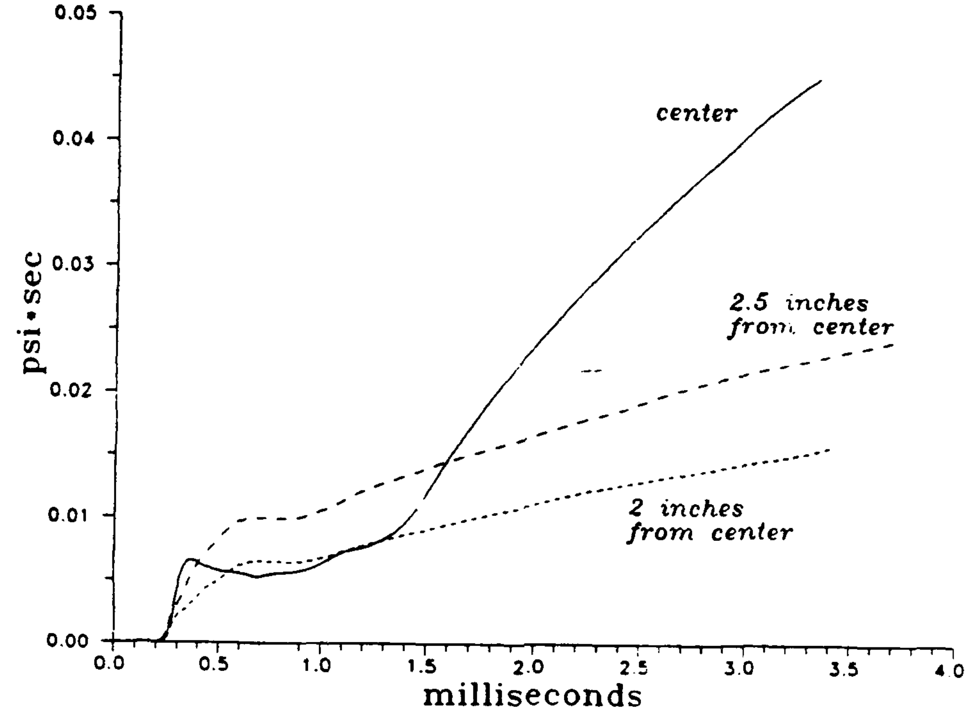

FULL 4 msec RECORD

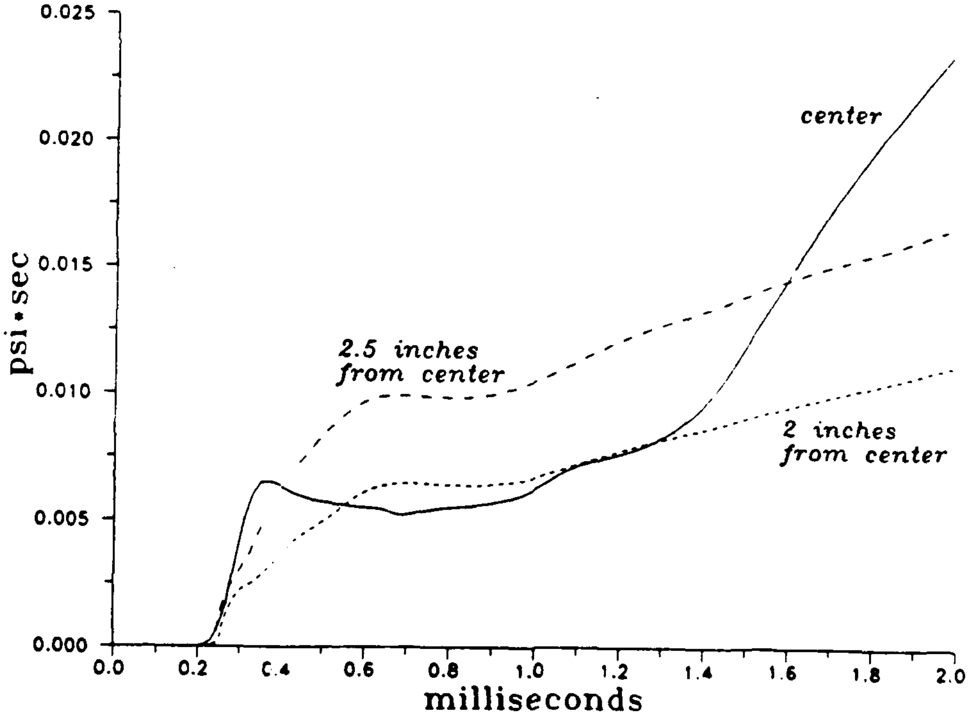

MAGNIFIED 2 msec RECORD

Fig. 2-19: Impulse records over the plexiglas roof. (DOB = 3 inches, H = 25 inches)

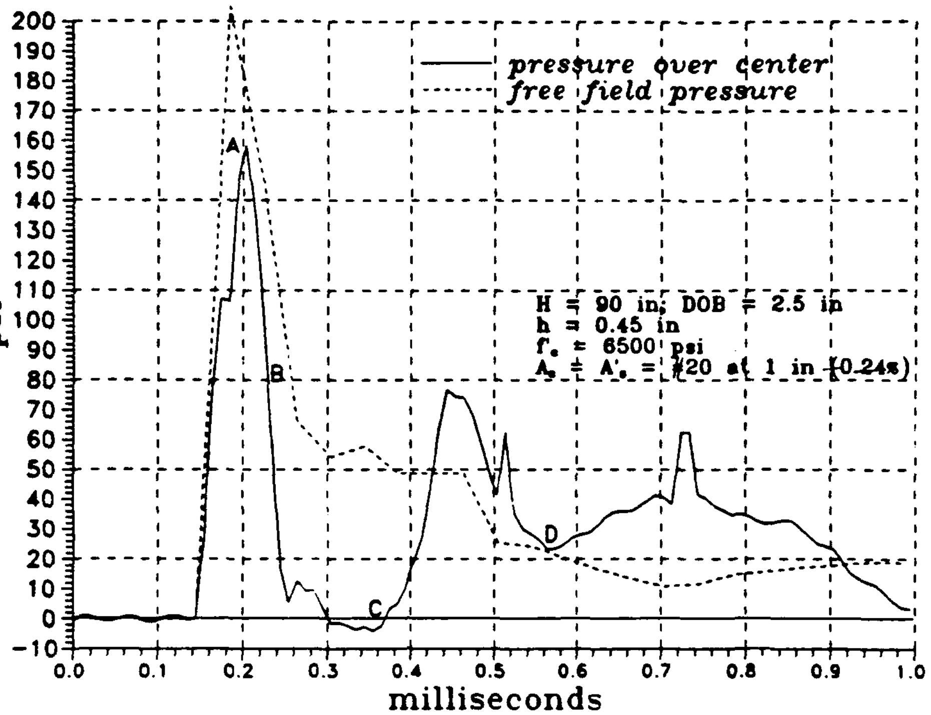

AT THE CENTER

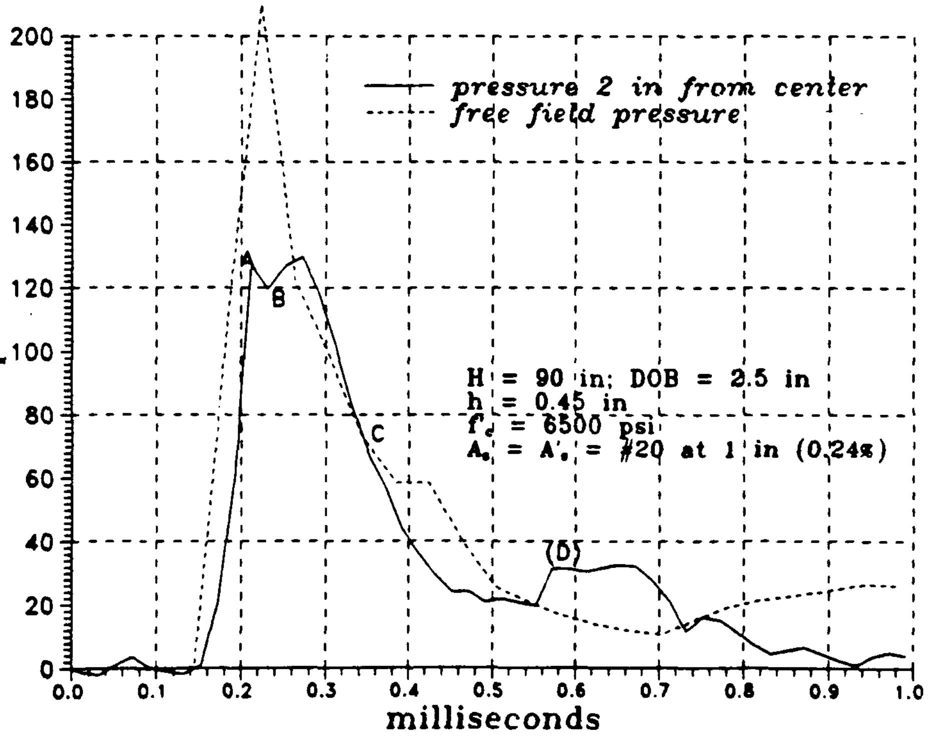

OVER THE EDGE

Fig. 2-20: Pressure over the clamped roof of test 8 (5th hit) v.s. free field.

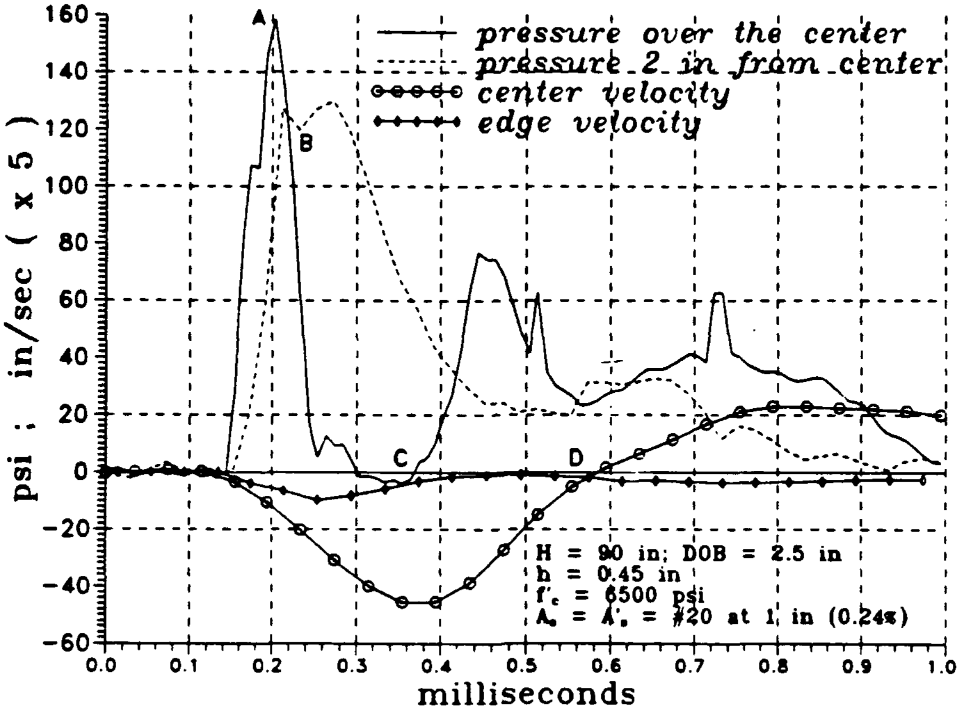

PRESSURE AND VELOCITY

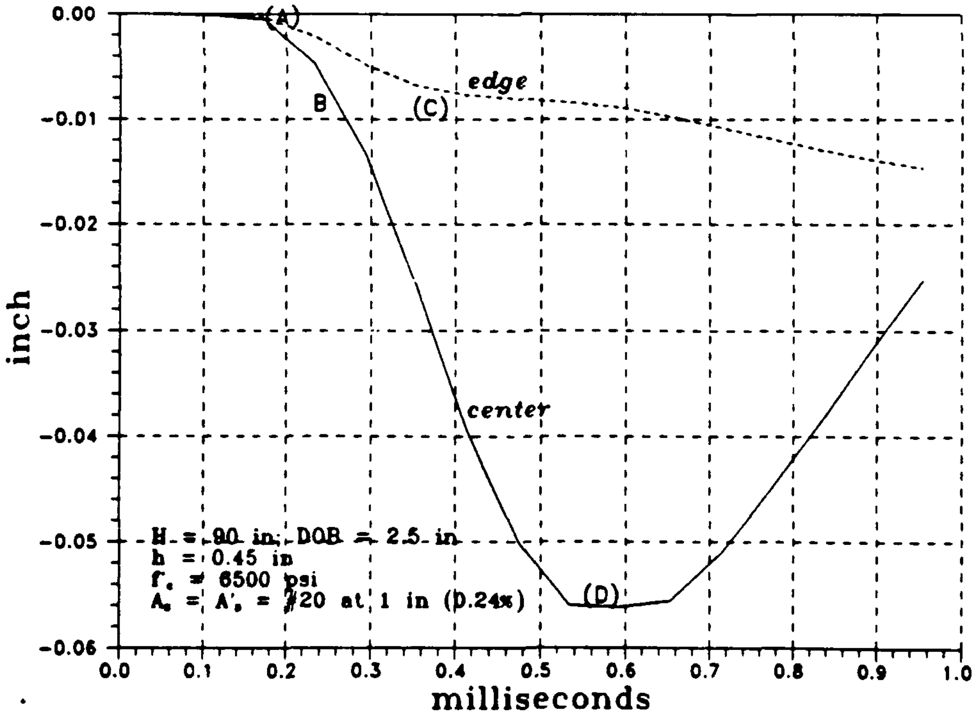

DISPLACEMENTS

Fig. 2-21: Response of the clamped roof in test 8 (5th hit).

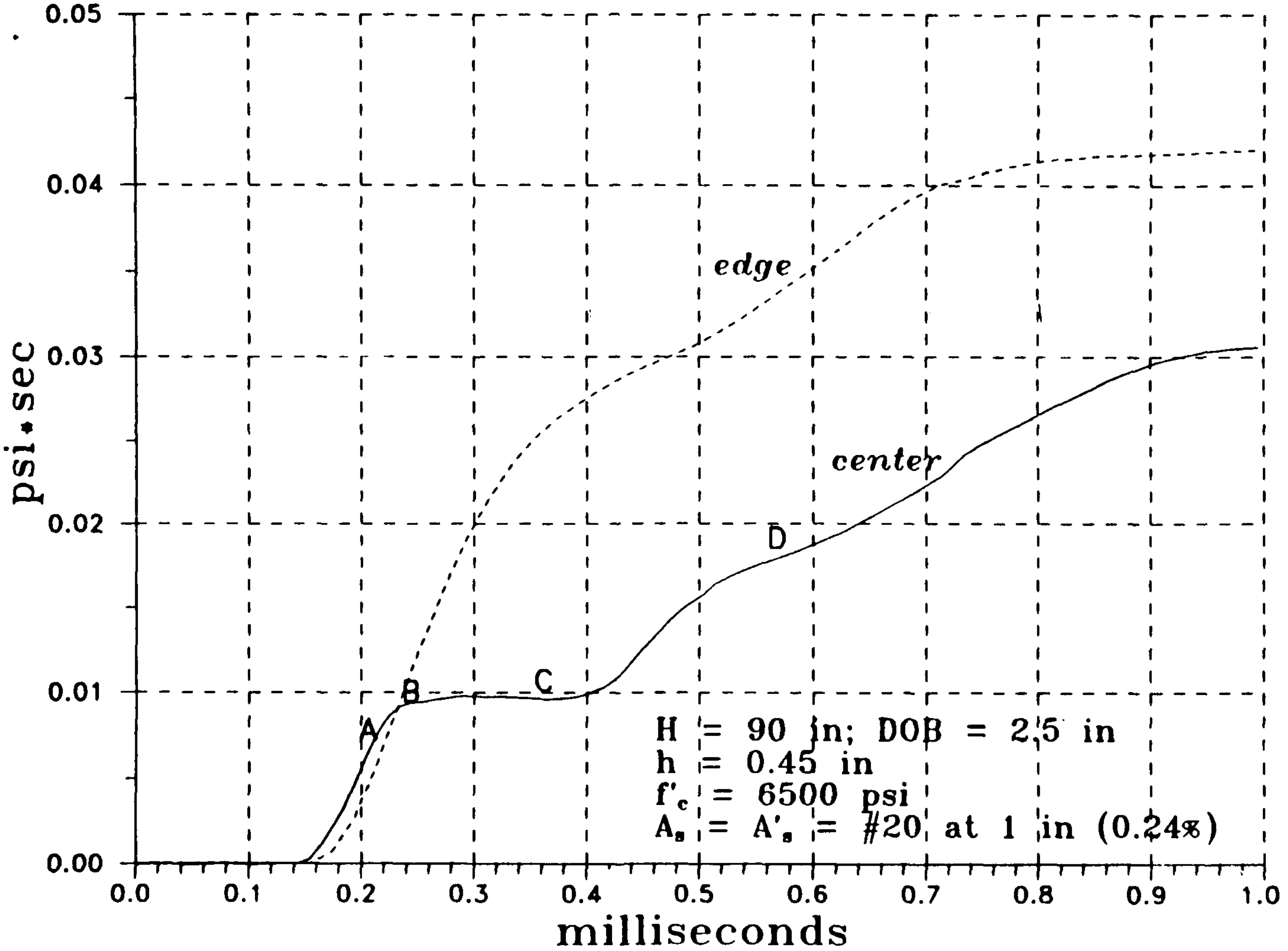

Fig. 2-22: Impulse records over the clamped roof in test 8 (5^{th} hit).

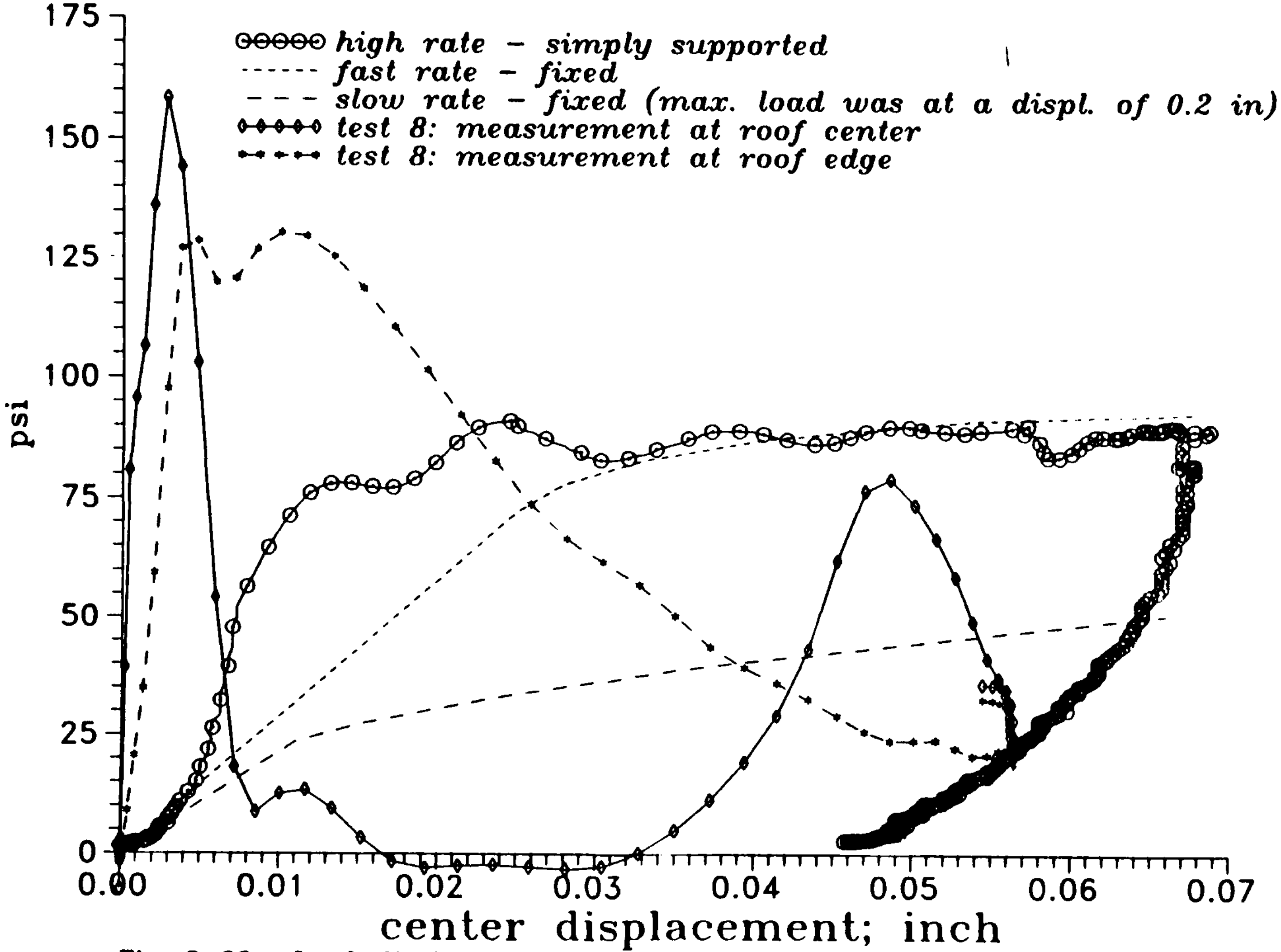

Fig. 2-23: Load-displacement curves of micro-concrete plates under pressure applied at different rates.

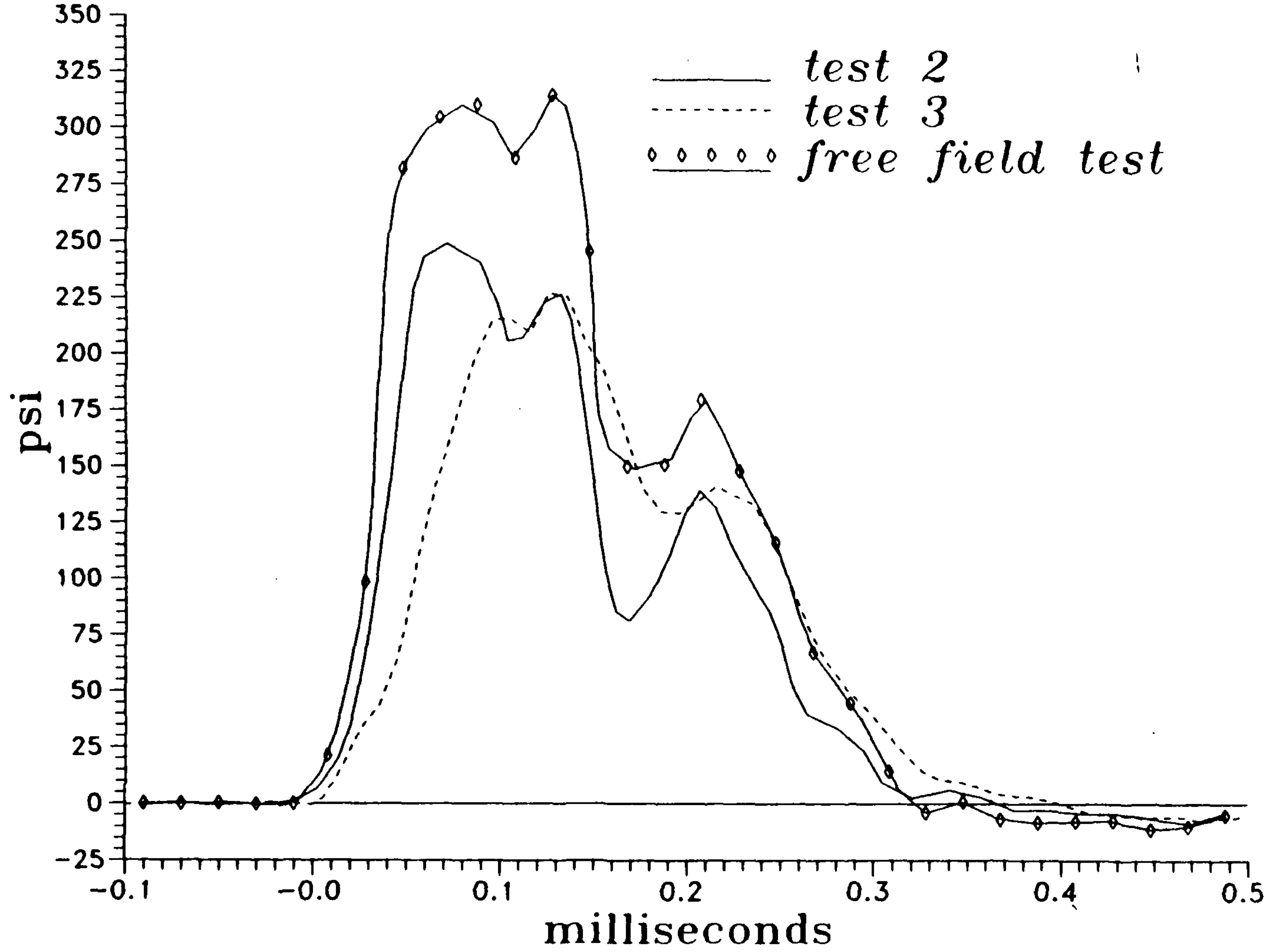

Fig. 2-24: Pressure induced under the target plate center in the tests with DOB = 3 inches (H = 25 inches).

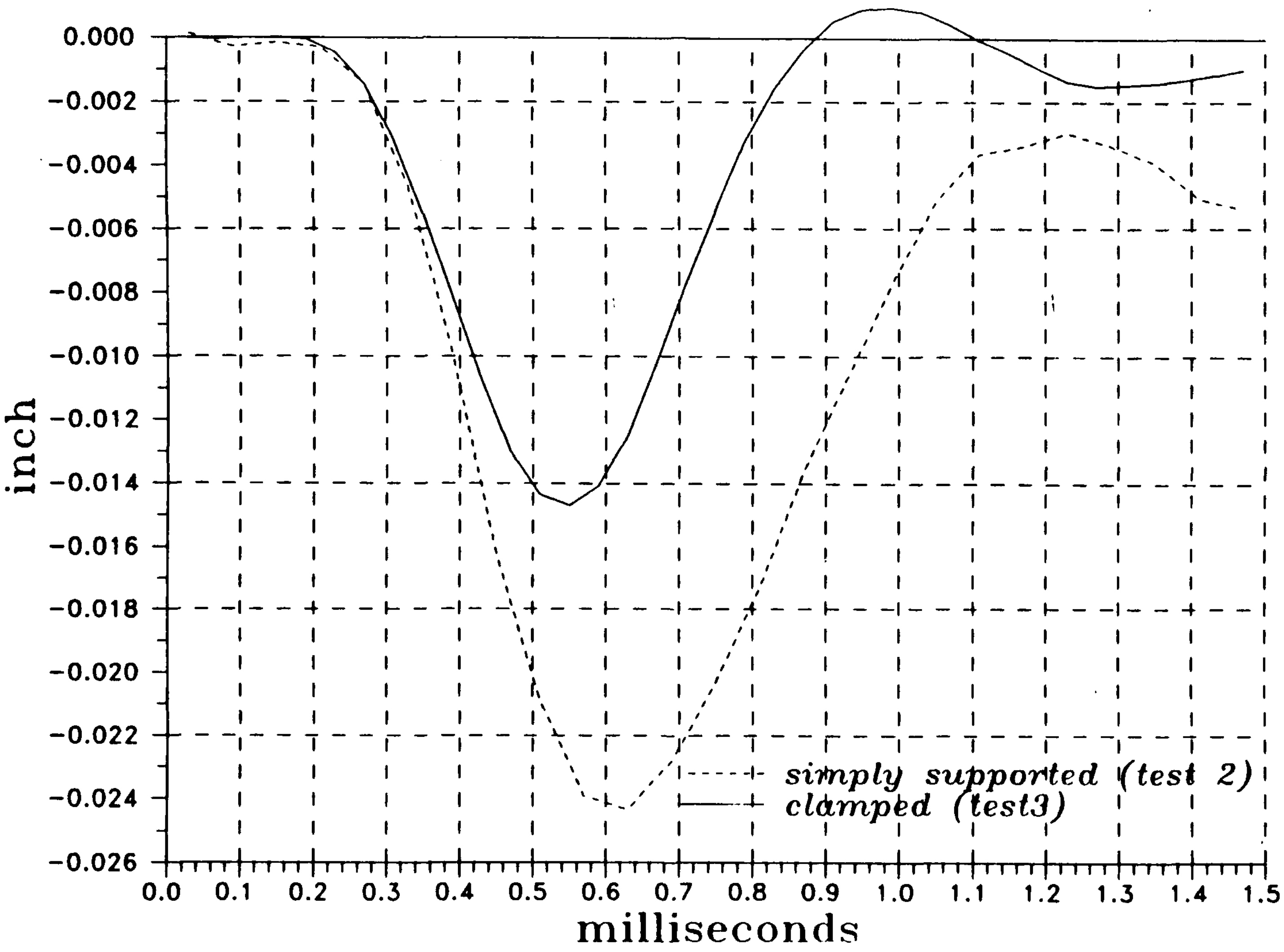

Fig. 2-25: Simply supported v.s. clamped roof - displacement of the center. (DOB = 3 in; H = 25 in)

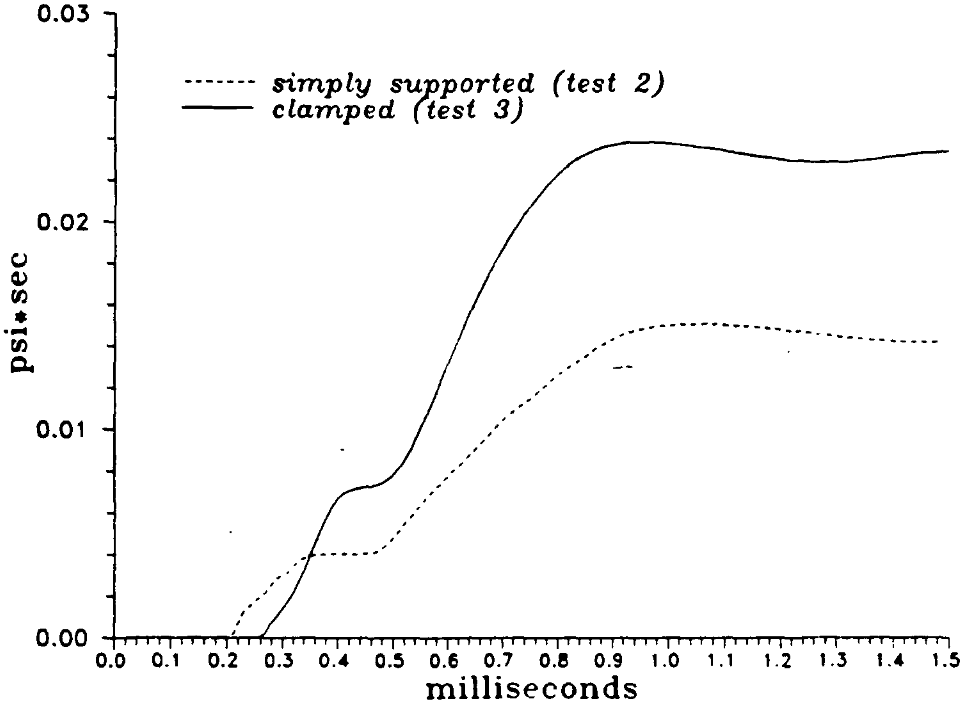

IMPULSE AT THE CENTER

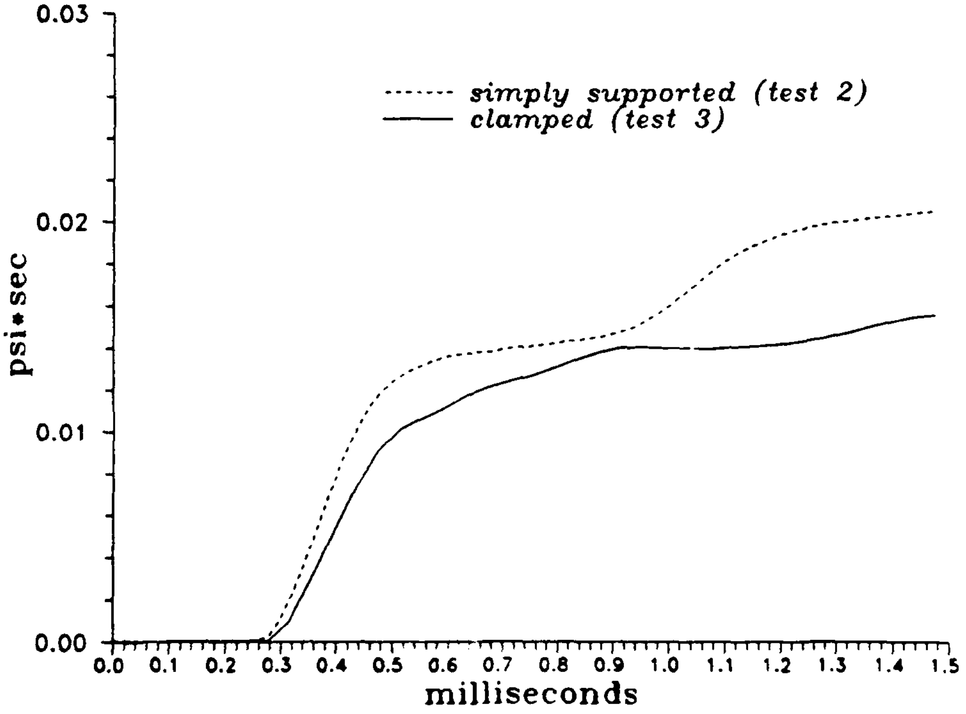

IMPULSE OVER THE EDGE

Fig. 2-26: Simply supported v.s. clamped roof - impulse records.
(DOB = 3 in; H = 25 in)

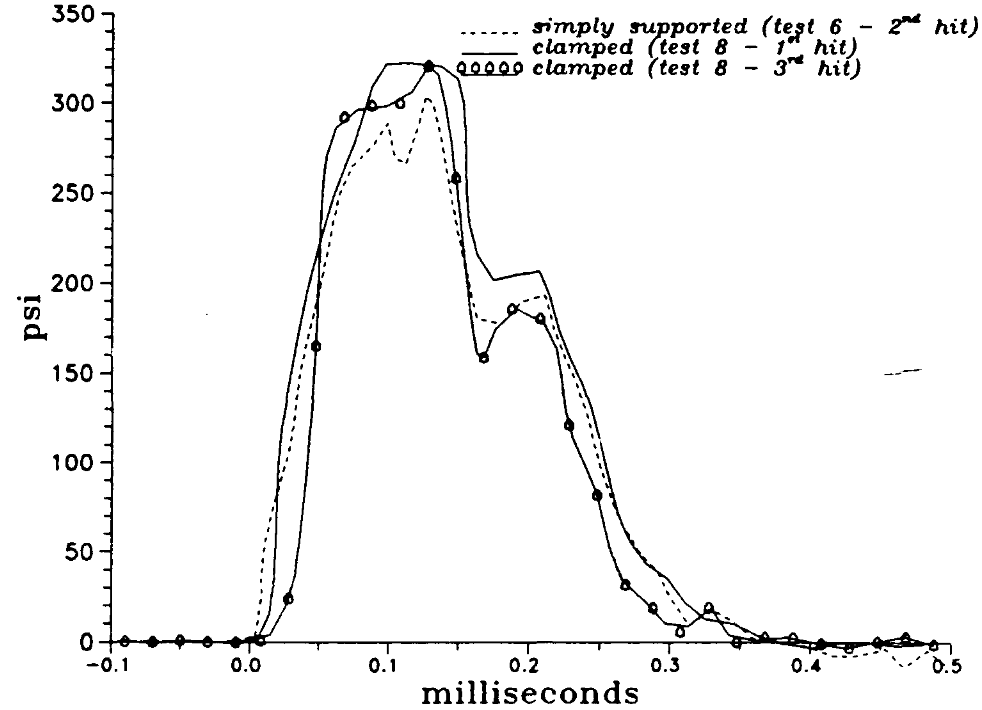

Fig. 2-27: Pressure under the target plate center - H = 25 in, DOB = 2.5 in.

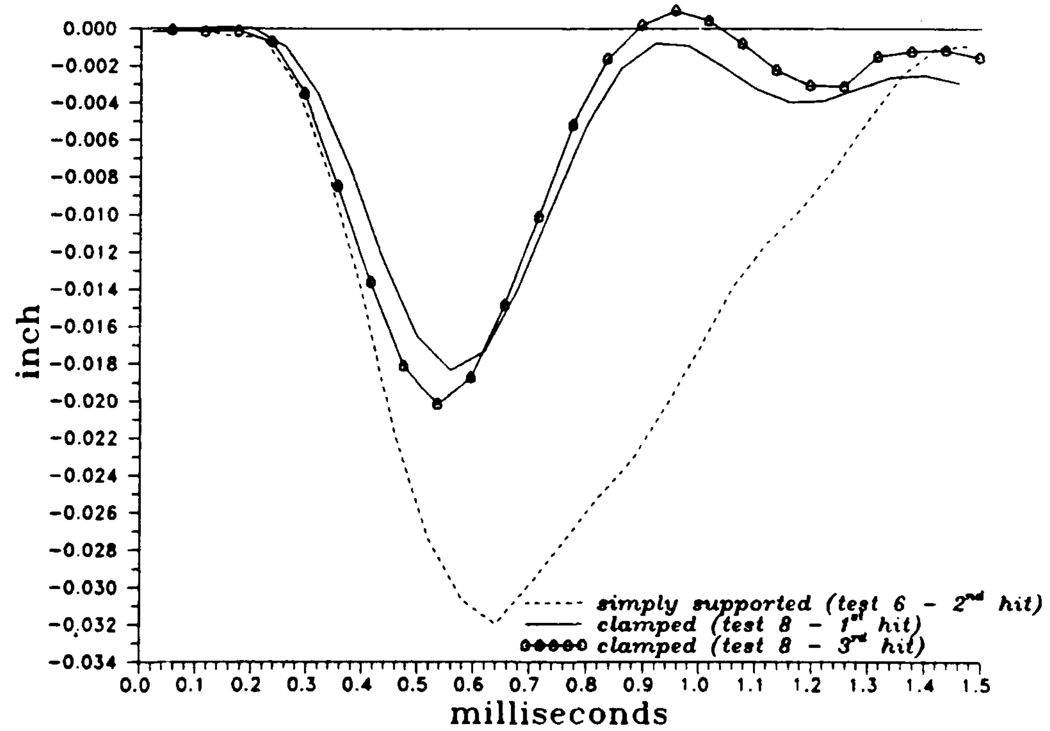

Fig. 2-28: Simply supported v.s. clamped roof - displacement of the roof center (DOB = 2.5 in; H = 25 in).

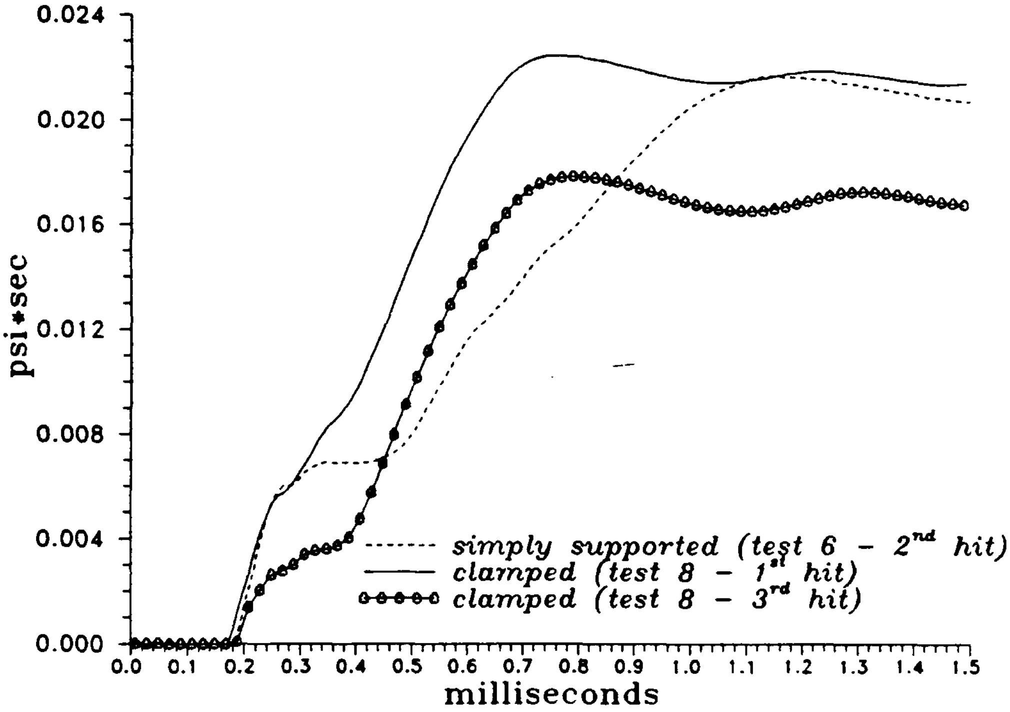

IMPULSE AT THE CENTER

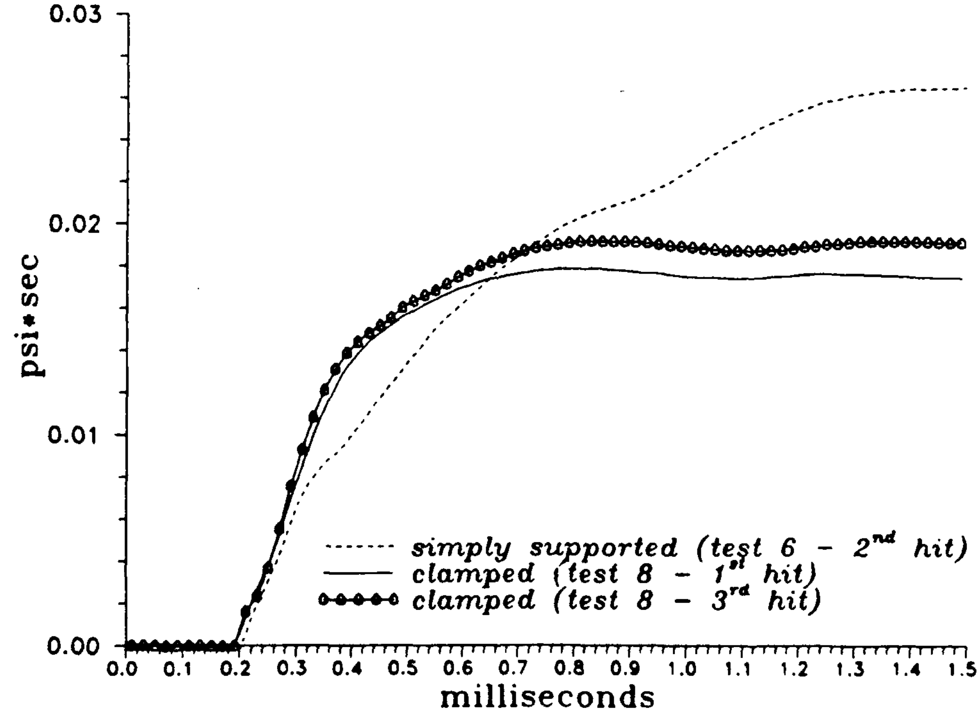

IMPULSE OVER THE EDGE

Fig. 2-29: Simply supported v.s. clamped roof - impulse records.
(DOB = 2.5 in; H = 25 in)

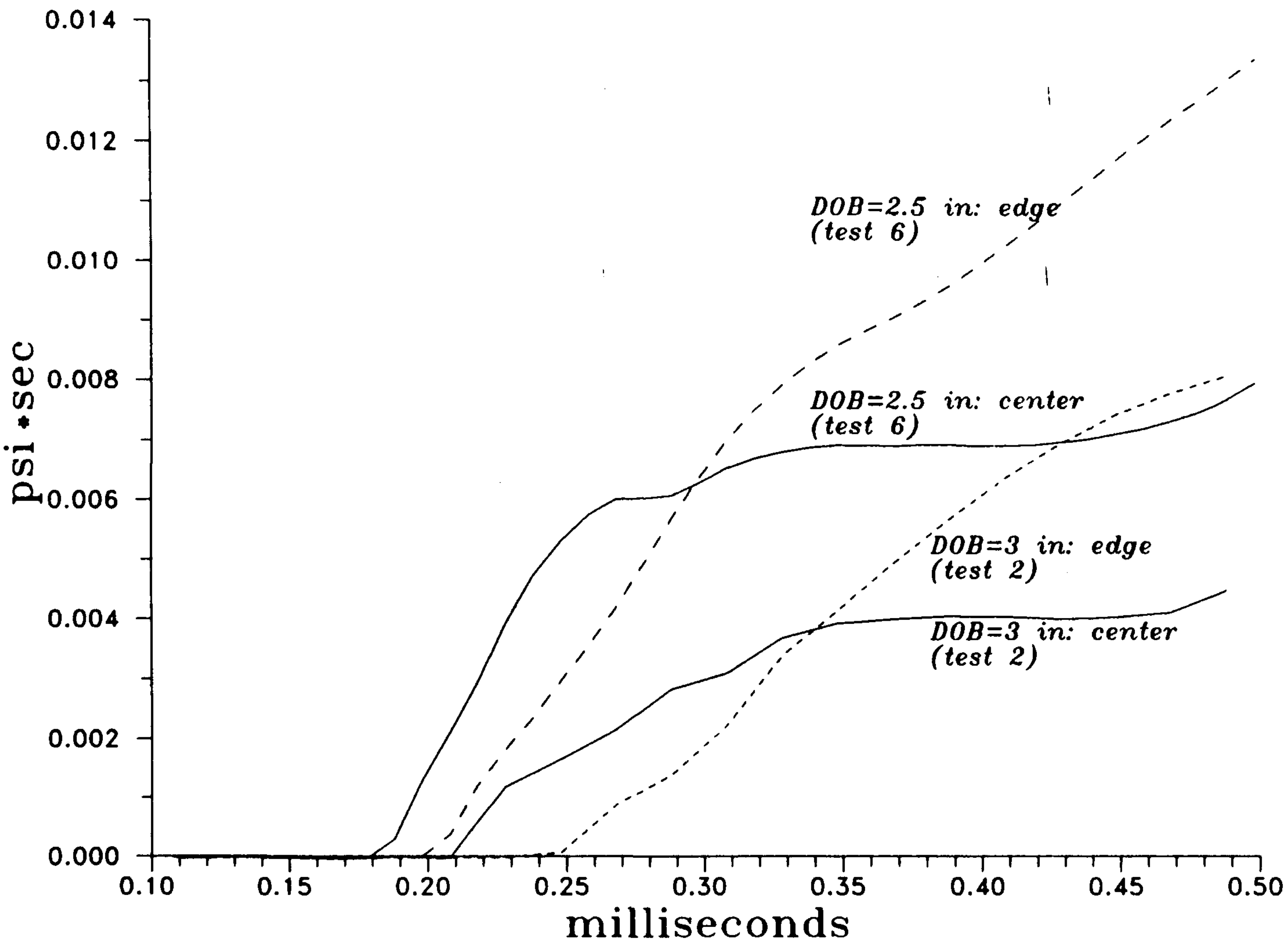

Fig. 2-30: Impulse records over roof slabs at different DOB.

CHAPTER 3

NUMERICAL ANALYSIS

3.1 Description of the Numerical Method.

Numerical analysis of the system was performed by employing a nonlinear, two dimensional dynamic finite element code, SAMSON2[36]. The program was run on an HP9000 series 300 Work-station, on an "Encore Multimax 320 machine", and on a "CRAY-2" super-computer. The numerical simulation serves as an analytical tool, supplementary to the experimental system. The axisymmetric geometry of the experimental setup allows a numerical analysis with a two dimensional model. The main features in the SAMSON2 code which were used for this part of the research are the following:

1. Explicit time integration, using a central difference method. The program automatically evaluates a maximum time step size for a stable solution. This value is usually an upper bound because it includes neither damping nor nonlinear effects.

2. Nonlinear material modeling (with a tension cutoff), which was used for the soil and for the reinforced concrete roof. The material models are discussed separately in the following sections.

3. Slide lines for modeling material interfaces. The slideline is an interface defined by the user. It separates two groups of elements, allowing each group to have different element size, such that the number of nodes on each side of the slideline is not necessarily the same. There are two possible motion relations between the nodes of each side of the slideline: A tied slideline forces one set of nodes, defined as "slave nodes", to have displacements which are dictated by the set of nodes located on the other side of the slideline, and defined as "master nodes". The other possibility is an interface such as in the soil-structure case along which, slip or separation may occur. Both types of slidelines were employed for this analysis as can be seen in the finite element meshes (e.g., figures 3-7 and 3-11). Although the slide line interface is convenient, it does, however, require input of a "capture distance", to determine if nodes on opposite sides of an interface are close enough to act together. This numerical parameter has been observed to influence the response of the system. It should be noted that during the calibration process of the code (described in the following sections) a single value of capture distance parameter was used. Thus, the numerical results are suitable for the analysis of the mechanisms of the soil-structure system but should be considered with judgement when and if used for design.

Further improvement of the numerical slideline interface feature, although beyond the scope of this research, can be useful for design and analysis of soil-structure systems which indeed include such interfaces.

The numerical study included three parts:

Calibration of the material models: The experimental results with the elastic-linear Plexiglas roof, with the reinforced micro-concrete roof, and of the free field (see Chapter 2) were used as references for the calibration of the material models. Numerical simulations of these experiments assisted in the determination of the material parameters for the soil, the structure, and for the interface between them.

Supplementary research: The data acquisition system and motion and load transducers provided rather detailed experimental results (Chapter 2). Nevertheless, some information, such as the shear stresses in the soil above the structure, or the pressure in the soil around the structure was not, or could not be measured. The numerical analysis supplemented the experimental research by providing these data as well as the necessary information to confirm some of the doubts which arose concerning the interpretation of the accelerometers readings of the absolute motion of the roof and of the whole structure.

Larger scale systems: The program was used to model with a plane geometry a larger scale experiment. The analysis, described in Chapter 4, was performed in order to examine the physical mechanisms, which were observed in the small scale system (Chapter 2). While the geometry and the material parameters of the larger scale experiment were different from those which were used in the small scale system, similar behavior was noted.

3.2 Numerical Models and Simulations.

3.2.1 External Input Load for the Soil-Structure System.

The external load was introduced through 10 "load-lines". Each "load-line" describes the pressure as a piece-wise linear function of time. The pressure under the target plate was measured in the experiments described in section 2.2.1. With the assumption of an axisymmetric spatial distribution, the loaded surface was divided into annular strips according to the location of the surface nodes in the finite element mesh (Figure 3-1). Over each annular strip, i.e. between every two loaded nodes, the pressure signal was divided into several time steps, thus simulating the actual measured load.

3.2.2 Numerical Model of Plexiglas.

The plexiglas structure was modeled by axisymmetric conical shell elements. These elements can be used in the program only with an elastic-plastic biaxial material model. According to the assumption of plane stress the stresses normal to the shell plane are zero. The following stress-strain relationships for the shell elements relate to figure 3-2:

$$\sigma_{RR} = \frac{E}{(1-\nu^2)}(\varepsilon_{RR}+\nu\varepsilon_{\theta\theta}) \tag{3.1}$$

$$\sigma_{\theta\theta} = \frac{E}{(1-\nu^2)}(\nu\varepsilon_{RR}+\varepsilon_{\theta\theta}) \tag{3.2}$$

$$\sigma_{YY} = 0 \tag{3.3}$$

$$\varepsilon_{YY} = -\frac{\nu}{(1-\nu)}(\varepsilon_{RR}+\varepsilon_{\theta\theta}) \tag{3.4}$$

The following material properties are provided by the manufacturer for plexiglas:

density	$\rho = 1.12 \cdot 10^{-4}$ lb-sec^2/in^4
Young's modulus	$E = 3.5 \cdot 10^5 - 5 \cdot 10^5$ psi
Poisson's ratio	$\nu = 0.35$

Results of the numerical simulation of the free vibration of a simply supported Plexiglas slab were compared with experimental measurements. The Plexiglas plate was modeled by five axisymmetric shell elements loaded by a short duration load at the center. A similar frequency of the mid-point vibration was obtained with an elastic modulus of $3.25 \cdot 10^5$ psi (figure 3-3).

The disadvantage of this material model is its inability to model accurately materials that are weak in tension (such as soil or concrete). This disadvantage becomes insignificant when the model is used for the elastic Plexiglas structural elements. The biaxial state of stress in the shell elements is another disadvantage, which becomes important when a transverse tension wave is likely to propagate through the thickness of the roof slab (see also 2.4.1). This disadvantage does not apply to the main part of the numerical analysis, since continuum elements were used to model the concrete roof rather than type of material model and element mentioned above.

3.2.3 Numerical Model of Sand.

Sand is a granular material, which when dry, has little or no tension capacity. It is a medium which when displaced, particularly under dynamic conditions, is not necessarily a continuum. Therefore, the geometrical modeling of sand by finite elements is a numerical constraint of the actual granular material. Figure 3-4 illustrates the assumptions fundamental to the numerical modeling of the soil.

The sand was modeled by 4-node quadrilateral continuum elements with one integration point. Its mass density was measured and found to be equal to $1.6 \cdot 10^{-4}$ lb-sec^2/in^4. The material model for the sand was the "AFWL Engineering Model" given by this code, and corrected and modified for this research. The user prescribes hydrostatic, non-linear, stress-strain relations and a yield surface, which may be enhanced according to the strain rate. The sign convention specifies compression stresses and strains as negative. Under applied loading (i.e., in compression, the volumetric strain is negative, and its absolute value increases), the volumetric stress is determined according to the volumetric strain and the prescribed loading curve. The position of the unloading curve is updated according to the minimal strain and stress during its loading history and therefore shifted horizontally, parallel to the volumetric strain axis and retains the tensile cutoff at its prescribed level. For reloading, the volumetric stress-strain follows the unloading curve. When and if the volumetric strain exceeds the minimum level ever reached during loading, the volumetric stress is determined again from the loading curve. The parameters that need to be quantified are:

Constitutive relations:

$$K = \begin{cases} K(e_v) & \textit{for loading.} \\ K(\sigma_v) & \textit{for unloading.} \end{cases} \tag{3.5}$$

$$\nu = \begin{cases} \nu(e_v) & \textit{for loading.} \\ \nu(\sigma_v) & \textit{for unloading.} \end{cases} \tag{3.6}$$

Note that $K(\sigma_v)$ for unloading, may have a "cutoff value"; i.e. $K(\sigma_v > \sigma_v^{cutoff}) = 0$ means no strength in tension, beyond a volumetric stress higher than σ_v^{cutoff}.

The failure surface (which may be enhanced according to the strain rate) is:

$$Y = \sqrt{J_2'} = Y(-\sigma_v) \tag{3.7}$$

In equations 3.5, 3.6, and 3.7:

K - bulk modulus

ϵ_v - volumetric strain (positive for expansion)

σ_v - normal pressure (positive for tension)

ν - Poisson's ratio

Y - failure surface

$(J_2')^{1/2}$ - second deviatoric stress invariant

For an axisymmetric geometry, a cylindrical coordinate system is used, and the stresses increments for each time step are:

$$\Delta\sigma_{ii} = 2\mu\left(\Delta\varepsilon_{ii} - \frac{\Delta\varepsilon_v}{3}\right) + \Delta\sigma_v\,; \qquad i = r,\, \theta,\, y \tag{3.8}$$

$$\Delta\sigma_{ry} = \mu\Delta\varepsilon_{ry} \tag{3.9}$$

where: $\mu = \frac{3}{2}K\frac{(1-2\nu)}{(1+\nu)}$ is the shear modulus.

$$\Delta\sigma_v = \frac{\Delta\sigma_{rr}+\Delta\sigma_{\theta\theta}+\Delta\sigma_{yy}}{3} = K\cdot\Delta\varepsilon_v$$ is the volumetric stress increment.

$$\Delta\varepsilon_v = \Delta\varepsilon_{rr}+\Delta\varepsilon_{\theta\theta}+\Delta\varepsilon_{yy}$$ is the volumetric strain increment.

At each time step these incremental stresses are calculated according to the volumetric strain and stress, and the current material parameters (equations 3.5, 3.6, 3.8 and 3.9). The second deviatoric stress invariant is determined by:

$$\sqrt{J_2'}=\sqrt{\frac{1}{6}[(\sigma_{rr}-\sigma_{\theta\theta})^2+(\sigma_{\theta\theta}-\sigma_{yy})^2+(\sigma_{yy}-\sigma_{rr})^2]+\sigma_{ry}^2} \tag{3.10}$$

and is compared to the corresponding failure surface level, $Y(-\sigma_v)$. If exceeded, then the stresses are modified to reduce the second deviatoric stress invariant to the failure surface level while maintaining the same volumetric stress:

$$\sigma_{ii} = \sigma_v + \frac{Y}{\sqrt{J_2'}}(\sigma_{ii} - \sigma_v) \; ; \quad i = r, \theta, y \tag{3.11}$$

$$\sigma_{ry} = \frac{Y}{\sqrt{J_2'}}\sigma_{ry} \tag{3.12}$$

3.2.3.1 Literature survey of experiments with 20-30 Ottawa Sand.

For a first approximation some experimental data with 20-30 Ottawa sand were reviewed. Then the free field experimental results (described in section 2.2.2) were used for the determination of the sand modeling. The following experimental results were gathered and reviewed in order to establish some typical constitutive relationships as well as the failure envelope for Ottawa sand:

Ko and Scott[29]. tested dense, medium-dense, and loose sand under cyclic hydrostatic compression. Their results provide the constitutive relationship and give the change of volumetric strain as a function of volumetric stress. Since the tests were performed with cyclic loading, they provide the necessary information for determining the bulk modulus, K, during loading and unloading (as a function of the volumetric strain and the volumetric stress, respectively), for loose, medium-dense, and dense Ottawa sand.

More experimental data were provided from tests done by Ueng, Tzou, and Lee[50]. They made triaxial tests with Ottawa sand. Their reported results were digitized and transformed into plots of volumetric strain and volumetric stress. Schmertmann[38] made CFS (Cohesion-Friction-Strain) tests, which indicate for dense saturated Ottawa Sand under axial compressive strain larger than 0.5%, cohesion and a friction angle of about 0.05 Kg/cm^2 (0.71 psi) and 33 degrees, respectively. They also provided the failure condition for the confining pressure at which they were conducted (2 Kg/cm^2, 28.44 psi). More data for the failure conditions (i.e. failure envelope) were taken from the experimental results reported by Ko and Scott[28], for dense, medium-dense, and loose Ottawa sand. The experiments were performed under static conditions. Selig and Vey[39] tested Ottawa sand under static and dynamic induced stresses. While the purpose of the dynamic tests was to study stress propagation and attenuation, the static tests provided the failure conditions for three confining pressures, 5, 7.5, and 12.5 psi. It was reported that in some cases the dynamic peak pressure was raised above the static strength, while for other cases it was lower. Whitman and Healy[53] also examined the response of sand to dynamic loading and reported "little, if any, strain-rate effect on the strength of dry Ottawa Sand".

3.2.3.2 Calibration of the numerical model for sand.

The free field stress distribution 3 inches under the target plate was used as a reference for the material parameters of the model. Figures 3-5 through 3-8 summarize the experimental results with Ottawa sand. They also include the actual parameters that were used to calibrate the numerical model according to the free field experimental results. The finite element mesh which was used (shown in figure 3-9) describes half of the experimental set-up (applying axial symmetry). It included 216 nodes, 176 elements, and 2 slidelines. The upper part of the mesh included elements which modeled "loose" sand, while the other elements modeled "dense" sand. The external load simulated the experimental measurements of the impact under the target plate as described in section 3.2.1. A constant Poisson's ratio of 0.25 was assumed.

Figures 3-10 through 3-12 describe the soil pressure obtained numerically versus the experimental results, under an impact generated by a drop of 25 inches. The vertical pressure is compared at 3 inches under the target plate at locations at the center line, 2 inches from the center, and 2.5 inches from the center. The soil parameters yielded numerical predictions in good agreement with the experimental measurements and they were used in the next steps of the FEM analysis.

3.2.4 Numerical Simulation of the Soil-Elastic Structure System.

The next step examined the model containing a buried structure. Figure 3-13 describes the mesh which was used to simulate the experiment which was performed with the plexiglas roof slab (section 2.2.3). It had 282 nodes, 181 elements, and 8 slideline interfaces. The Plexiglas structure was modeled with axisymmetric shell elements, section 3.2.2.. Vertical stresses over the roof as well as the motion (displacement and velocity) of the roof and of the whole structure, were computed by the finite element program, modeling the small scale experiments described previously (2.2.3). Among other parameters of the system examined was the soil-roof slideline interface. The following comparison was performed between the numerical and the experimental records: Displacement of the center of the roof, pressure at the center of the roof, and pressure over its edge, 2.5 inches from the center. The input was the load function used for the free field runs. Modeling of the sand was taken according to results obtained from the free field runs, figures 3-14 through 3-17.

The numerical calculations model well the experimental results up to about 1 msec. Then the roof center rebounded sharply upwards in the numerical model, while it maintained a lower frequency response in the experiment (figure 3-14). This behavior was reflected in the velocity record and also caused a sharp increase in the pressure records over the structure (see FEM records at $t \geq 1$ msec in figures 3-15, 3-16, and 3-17, respectively).

The runs with the Plexiglas roof combined the soil and the structure and provided optimal calibration of the capture distance value of the slide line interface between them. No friction or adhesion was introduced at this interface, and the value of the capture distance was kept unchanged in the following runs with the reinforced concrete slab as the structure roof. These runs also provided additional information to that which was obtained experimentally. As it can be seen in figure 3-14 the absolute center displacement and the displacement relative to the floor are similar. Hence, the records of the relative motion, experimentally obtained by the LVDT, are verified as representative to the motion of the roof center since the relatively smaller absolute motion of the whole structure was indicated by the accelerometers signals (see Chapter 2) as well as in the numerical results. Further numerical results of the soil-Plexiglas roof run are discussed in section 3.3.

3.2.5 Numerical Model of Reinforced Concrete.

No attempt was made to use a sophisticated material model for the concrete. The material model which was used merely applied the basic behavior of concrete, and the analysis was focused on the soil-structure interaction mechanisms which are involved. Modeling of the reinforced micro-concrete slabs was performed with the 4-node quadrilateral continuum elements for concrete, and with shell elements for steel (figure 3-18). While concrete is continuous and can be geometrically modeled by continuum elements, it is necessary to use an equivalent geometrical model for the reinforcing steel meshes. The axisymmetric shell elements represent a continuous disk equivalent to the discrete steel mesh, where the equivalence was based on equal force taken by the numerical and the actual steel. Considering a cross section of the slab at an arbitrary angle α, the internal total force taken by the steel bars over the cross section is F_x and F_y in the x and y directions, respectively (Figure 3-19). The number of steel bars in each direction over the cross section, N_x and N_y depends on the spacing, s. For an equal spacing in each direction, they are:

$$N_x = \frac{2l\sin\alpha}{s} \qquad N_y = \frac{2l\cos\alpha}{s} \tag{3.13}$$

For reinforcement bars of cross sectional area A_s, and assuming equal stress in the x and y direction ($f_{sx}=f_{sy}=f_s$), the total forces F_x and F_y are:

$$\begin{aligned} F_x &= N_x A_s f_s = \frac{A_s}{s} f_s 2l\sin\alpha \\ F_y &= N_y A_s f_s = \frac{A_s}{s} f_s 2l\cos\alpha \end{aligned} \tag{3.14}$$

The total force normal to the cross section, F_n, should be equal to the force taken by the equivalent steel disk with a thickness h_{eq}:

$$F_n = F_x\sin\alpha + F_y\cos\alpha = 2l h_{eq} f_s \tag{3.15}$$

Substituting F_x and F_y from equation 3.14 into equation 3.15, and arranging terms, the equivalent thickness for the reinforcement shell elements is obtained:

$$h_{eq} = \frac{A_s}{s} \tag{3.16}$$

The material model for the reinforcing shell elements was the biaxial elasto-plastic model with an assumed elastic modulus of $30{\cdot}10^6$ psi, and the measured yield stress, f_y, of 51000 psi (see also chapter 2). It should be noted that the shell elements were too thin to contribute significant flexural stiffness.

Because of the non-linear nature of the constitutive relations of concrete, and its relatively low strength in tension, it was also modeled by the "AFWL Engineering Model" (described in section 3.2.3) with suitable parameters for concrete. Calibration of this material model was performed with initial reference to the hydrostatic relations and failure surface based on Chen[9] and Ottosen[35]. The yield surface normalized with respect to the compressive strength, f'_c is based on the following function:

$$\alpha\left(\frac{\sqrt{J_2}}{f'_c}\right)^2 + \beta\left(\frac{\sqrt{J_2}}{f'_c}\right) + \gamma\left(\frac{I_1}{f'_c}\right)^2 + \delta\left(\frac{I_1}{f'_c}\right) - 1 = 0 \qquad (3.17)$$

where: $(J_2)^{1/2}$ is the second deviatoric stress invariant.

I_1 is the first stress invariant; $I_1 = 3\sigma_v$.

σ_v is the volumetric stress.

f'_c is the uniaxial compressive strength.

$\alpha, \beta, \gamma, \delta$ are parameters which are fitted with experimental results.

The parameter $\gamma = 0$ at failure and the other parameters which are suggested for failure conditions in the literature are 1.3, 9, and 3.2 for α, β, and δ, respectively.

The curves which were used for the analysis are shown in figures 3-20 and 3-21. They were evaluated by two separate comparisons with experimental records of micro-concrete slabs: The free vibration of the simply supported slab of test 7 (see Table 2-1) was recorded (before the test was done). The slab was numerically modeled by a finite element mesh as described in figure 3-18 with the dimensions of the slab in test No. 7. The comparison between the numerical and experimental record is shown in figure 3-22. Because of the small displacement (about 0.002 inches) the range of the strains and stresses in the slab was relatively low (maximum compressive strain of less than 0.001), and far from failure. Thus, it provided the initial parameters for the material model. Poisson's ratio was assumed to be equal to 0.2 and constant. The initial elastic modulus of micro-concrete was $\sim 1 \cdot 10^6$ psi, section 2.2.4.2. Figure 3-22 also shows the effect of the lateral restraint of the support on the response of the slab (dashed line in figure 3-22). As it can be seen the natural frequency is doubled when the support is hinged but its lateral displacement is restrained.

These model parameters were then completed and refined by using the high rate experimental results of the experiments with circular slabs that were described in section 2. The loading pressure and the experimental versus numerical record of the mid-point displacement under this pressure are given in figures 3-23 and 3-24, respectively. In figure 3-24 the numerical modeling of the reinforced micro-concrete slab with the above parameters for the "AFWL Engineering Model", was seen to be in good agreement with the experimental results. It should be noted, however, that once the concrete continuum is cracked, its finite element representation becomes less accurate. Although the material law provides a tension cut-off, a tension failure which forms a physical crack cannot be accurately modelled. Therefore, an equivalent average value was used for the tension cut-off that was lower than the actual tension capacity of the concrete. Damage or failure condition is evaluated by the strain at the reinforcing steel elements and by comparison of the slab displacement to a relevant load-displacement curve, but the extent of the damage (or failure) at very large displacements (>1/10 of the span), is not modeled. This solution was found to be satisfactory for the soil-structure modeling provided the response of the embedded structure depends mainly on early time mechanisms, which may cause later larger displacements. For the current soil-structure system it is, indeed, the early time response which is more important, and therefore the above model is adequate for its analysis.

3.2.6 Numerical Simulation of the Soil-Micro-concrete Structure System.

The element types which are described in the previous sections were used for the numerical simulation of test No. 6 (see Table 2-1), with corresponding material models. The input pressure applied at the surface under the target plate was generated under a height of drop of 25 inches. The experimental and numerical input under the center of the target plate are shown in figure 3-25. Figure 3-26 shows the finite element mesh which was employed for this analysis. The analytical results are plotted with their corresponding experimental records in figures 3-27 through 3-30. In the early-time response there is a good agreement between the analytical and experimental results. The center displacement and velocity follow their corresponding experimental records during the whole significant part of the response (figures 3-27, 3-28). As in the case of the elastic Plexiglas roof, the relative and absolute displacements are similar, indicating that the displacement of the whole structure was much smaller compared to the displacement of the roof center. The velocity record (figure 3-28) also indicates possible instability of the numerical solution at $t > 0.6$ msec, as the signal becomes relatively noisy. Such a problem might be addressed by further decrease of the time steps. However, it was not done because the time step size which was used was already small ($1 \cdot 10^{-7}$ sec) and required a long computation time. Additionally, the essential features of the early-time part of the response was already captured by the numerical solution. Accordingly, the pressure in the soil element above the roof agrees well with the corresponding experimental records up to $t \approx 0.6$ msec. Although high peaks are shown which were not measured in the experiment, they became zero at approximately the same time as in the experiment (~1.2 msec in figures 3-29, and 3-30).

3.3 Discussion of the Numerical Simulations for the Experimental Results.

The FEM analysis of the small scale system experiments enabled the parameters of the code to be calibrated, and also provided additional information, difficult to acquire experimentally. Records of vertical pressure and shear stresses in the soil, together with the vertical, transverse stresses through the micro-concrete slab mid-section, enable further examination of the mechanisms that influence its response (see Chapter 2).

3.3.1 Displacement of the Roof Slab.

The numerical displacement solution, which follows the experimental measurement during about 2 msec, also indicates that the early-time response is significant, and that the mechanisms which take place during that time, up to ~0.6 msec in the current system, are dominant in influencing the total response. These mechanisms are described in Chapter 2. At t=0.4 msec (figure 3-14) the central displacement was ~0.02 in and the strain at the reinforcing steel element at the bottom center of the slab exceeded the yielding strain, 0.0017 (E is assumed $30 \cdot 10^6$ psi for steel, and f_y = 51000 psi). The radial strain and stress in the bottom steel element were 0.0021 and 51000 psi, respectively. At t=0.6 msec the displacement at the center was 0.036 in and the radial strain in the bottom steel element was 0.0053. Referring to the load-displacement curves of similar slabs (figure 2-23), the yielding of the bottom reinforcing steel element at a central displacement of 0.02 in is reasonable, and indicates initiation of flexural damage.

3.3.2 Transverse Stresses through the Slab.

Figure 3-31 shows the transverse stresses in the slab mid-section, top, middle, and bottom elements, during the first 0.4 msec of the slab response. It can be seen that as the incident pressure wave propagated through the thickness of the slab it attenuated and reached a minimum level at the bottom element. Considering the fact that the stresses in the quadrilateral elements are calculated at their one mid-integration point, it is understood that there is some non-zero vertical stress in the slab bottom element, and that its relatively low value agrees well with the natural boundary condition of zero vertical stresses at the free bottom of the slab. This boundary condition can be satisfied by a reflection tension wave from the free bottom of the slab.

As the slab center starts to gain velocity, just before t=0.2 msec, the vertical stress at the top of the slab reaches its peak and begins to drop, while at the same time maintaining a steady minimum level at the bottom (figure 3-31). The stresses at the soil above the slab also start to decrease at the same time (figure 3-29).

3.3.3 Soil-Structure Displacements.

One of the purposes of using the slideline interface feature in the numerical model was to examine the relative motion of the soil-structure. However, due to the incorporation of the capture distance parameter, this part of the analysis, might not be reliable. Figure 3-32 describes the displacement of two nodes 0.5 inches from the center, located on opposite sides of the sand-roof interface. There appear to be some gaps between the "sand node" and the "roof node"; however they are of the order of 10^{-4} inch. This difference is more likely to be a numerical gap rather than to represent a physical one. Therefore, as in the experimental observations, a zero stress was assumed at the soil element above the structure to represent a possible physical gap.

3.3.4 Shear Stresses in the Soil above the Structure.

Figures 3-33 and 3-35 show the early time shear stresses in the soil at the level above the Plexiglas and the micro-concrete roofs, respectively. Note that the clear span of the Plexiglas roof was 2.75 inches while that of the micro-concrete roof was 2.5 inches. From these figures it can be seen that at a time of 0.3 to 0.4 msec relatively high shear stresses developed on the sides of the structure. Comparing figures 3-33 and 3-35 with figures 3-16 and 3-29, that time is seen to be when the pressure over the center of the roof was decreasing and reached its lower zero value. In the case of the micro-concrete roof the pressure over the roof edge peaked at 0.3-0.4 msec (figure 3-30) and over the Plexiglas roof it peaked for the second time after previously having decreased (figure 3-17). These observations support the interpretation of the experimental results, that arching develops in the soil over the structure after the first peak of the pressure has already loaded the structure. The shear stresses over the wall of the structure coincide with an arch action at which support there is a relatively high shear. (In the axisymmetrical case there is actually a dome action analogous to the arch action which in the following text is referred to as *arch action*.). In the soil above the walls of the structure there is a transition from a relatively low level of vertical stresses to a zone of high vertical stresses, either above, or adjacent to the stiffer support of the structure. The location of these zones might differ according to the stiffness of the roof and to the foundation stiffness, which affects the deflection of the whole structure. The change of sign of the shear stresses in this zone is associated with a lateral displacement of the sand located within the high pressure zone, on both sides of the roof. From figures 3-33 and 3-35 it can be seen that while this region was located on both sides of the Plexiglas structure, ~3 inches from the center (in figure 3-33), in the case of the stiffer concrete roof it was above the walls, ~2.5 inches from the center (in figure 3-35).

The arch, or dome action in the soil at $t > 0.35$ msec is also demonstrated in figures 3-34 and 3-36, which show the vertical pressure distribution above the Plexiglas and the concrete roof level, respectively. A concentration of vertical stresses in the soil above the relatively stiffer wall area indicates the formation of arch action over the deflecting center area of the structure.

3.3.5 Effect of the Boundary Conditions.

The case of test No. 6 in which the roof was simply supported, was simulated with a clamped type of support: Additional Plexiglas shell elements attached to the concrete element at the bottom edge and to the top Plexiglas wall element increased the bending stiffness at the support. Figure 3-37 shows the center displacement of the roof in the two cases. The clamped roof (solid lines in figure 3-37) reached a peak deflection of about 85% of that of the simply supported roof at about the same time. Although the smaller displacement of the clamped roof is expected, the relatively small difference in the deflection indicates either that the clamping model was not very effective or that plastic hinges developed at the slab edges at an early time of the response. In either case the soil pressure records over the roof (figures 3-38 and 3-39) show the same response during the first peak with higher pressure over the clamped roof center in the later time part of the response. This observation indicates an influence of the boundary conditions on the arching action in the soil over the structure. However, because arching takes place at a later-time of the response (after the first peak), its effect is significant only if the structure sustains the early-time peak loading by causing further reduction of the load.

3.3.6 Effect of the Soil-Structure Interface Properties.

In the numerical analysis, which was described in the previous sections, sliding was allowed along the soil-structure interface. A similar run was performed with fixity at the soil-structure interface. The results are shown in figure 3-40 through 3-42. The effect of the properties of the interface is displayed by a smaller deflection of the roof and by corresponding smaller load over the roof center in the fixed case (solid line versus dashed line in figures 3-40 and 3-41). It can be seen in figure 3-41 that the load over the center of the roof increases to the same peak in both cases, but drops faster in the case of a fixed interface. At $t > 0.3$ msec the load over the edge in the fixed case is higher than that in the case of free sliding interface (solid versus dashed lines in figure 3-42). These observations indicate an earlier development of soil arching when the soil-structure interface is less compliant. The arch action is caused by the deflection of the structure, and by the soil shear capacity and is enhanced by increasing the friction between the soil and the structure. It should be noted, though, that this indication must be further investigated for two main reasons:

1. While the soil-structure interface friction may allow earlier development of arching in the soil, it also loads the structure with shear stresses at its interface. The above numerical result should be followed by further experimental study of the structure response to increased interface shear stresses.

2. Since the interface model involves a numerical parameter of capture distance this result indicates a qualitative trend, which must be verified and quantified by further experimental research and improvement of the numerical modeling of the soil-structure interface.

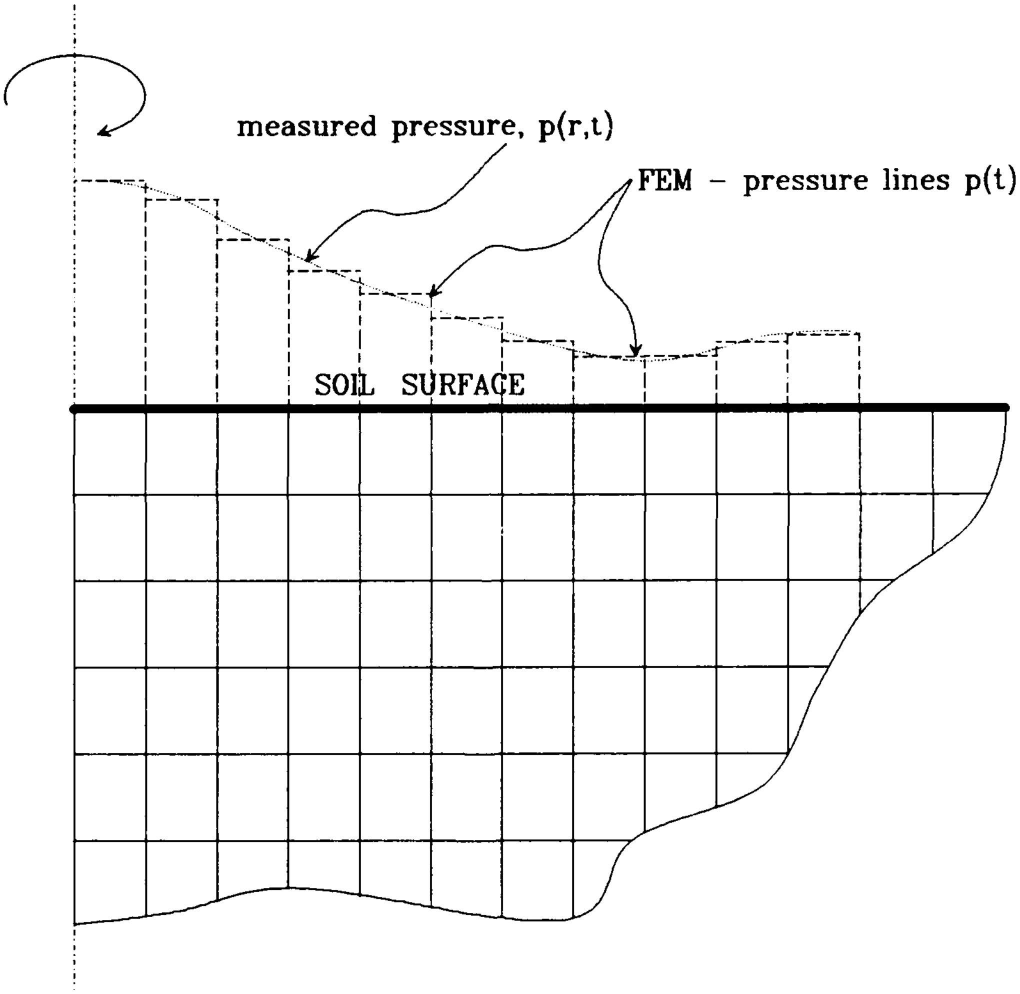
measured pressure, p(r,t)
FEM - pressure lines p(t)
SOIL SURFACE

Fig. 3-1: Input of external pressure in the finite element analysis.

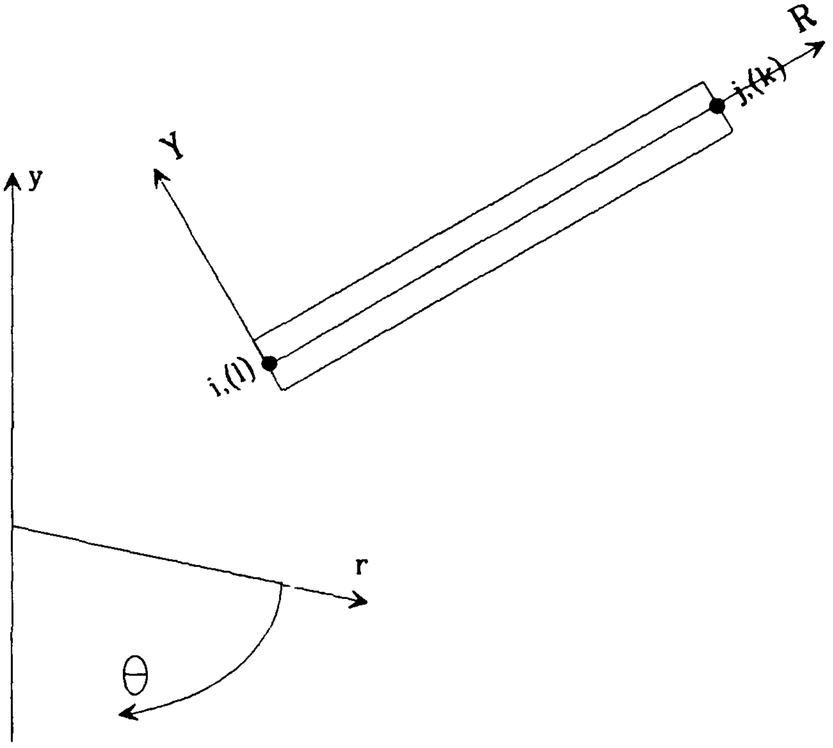

Fig. 3-2: Axisymmetric shell element.

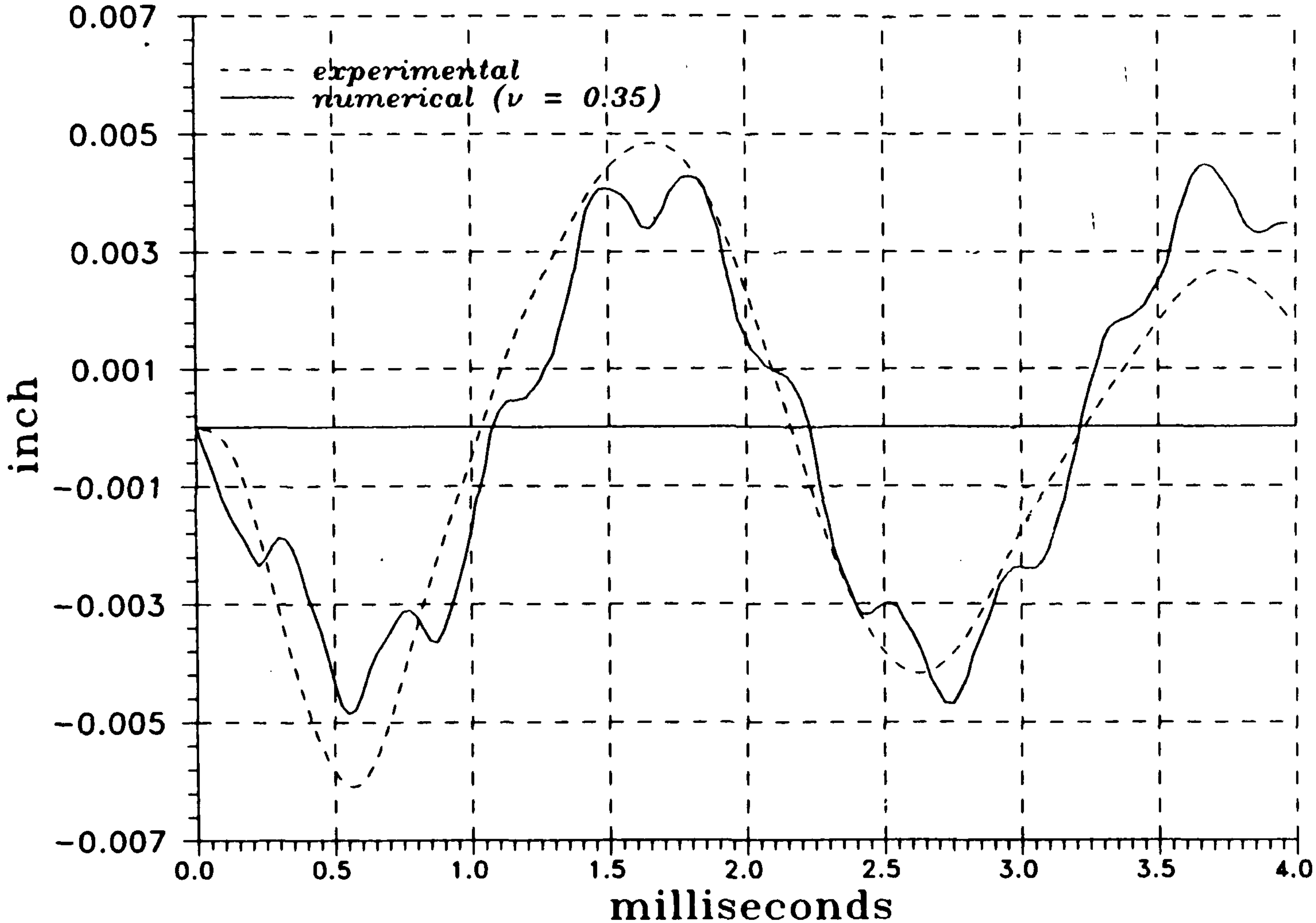

Fig. 3-3: Free vibration of a simply supported PLEXIGLAS slab.
(Displacement of the slab center; $E = 3.25 \times 10^5$ psi, $h = 0.235$ inch)

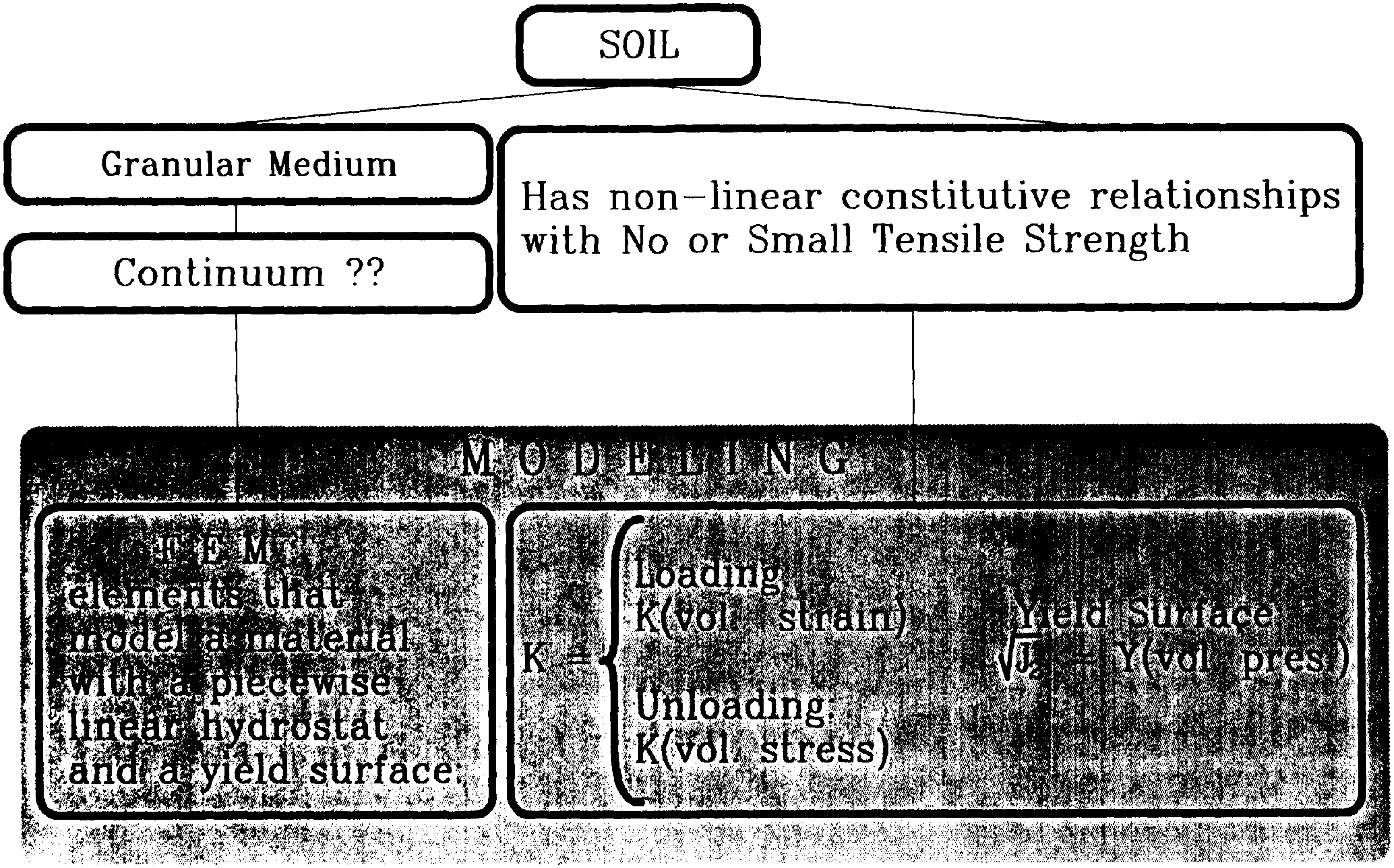
SOIL
Granular Medium
Continuum ??
Has non-linear constitutive relationships with No or Small Tensile Strength
MODELING
[illegible] FEM elements that model a material with a piecewise linear hydrostat and a yield surface:
K = Loading K(vol. strain)
Unloading K(vol. stress)
Yield Surface
$\sqrt{J_2} = Y(\text{vol. pres.})$

Fig. 3-4: Numerical modeling of soil.

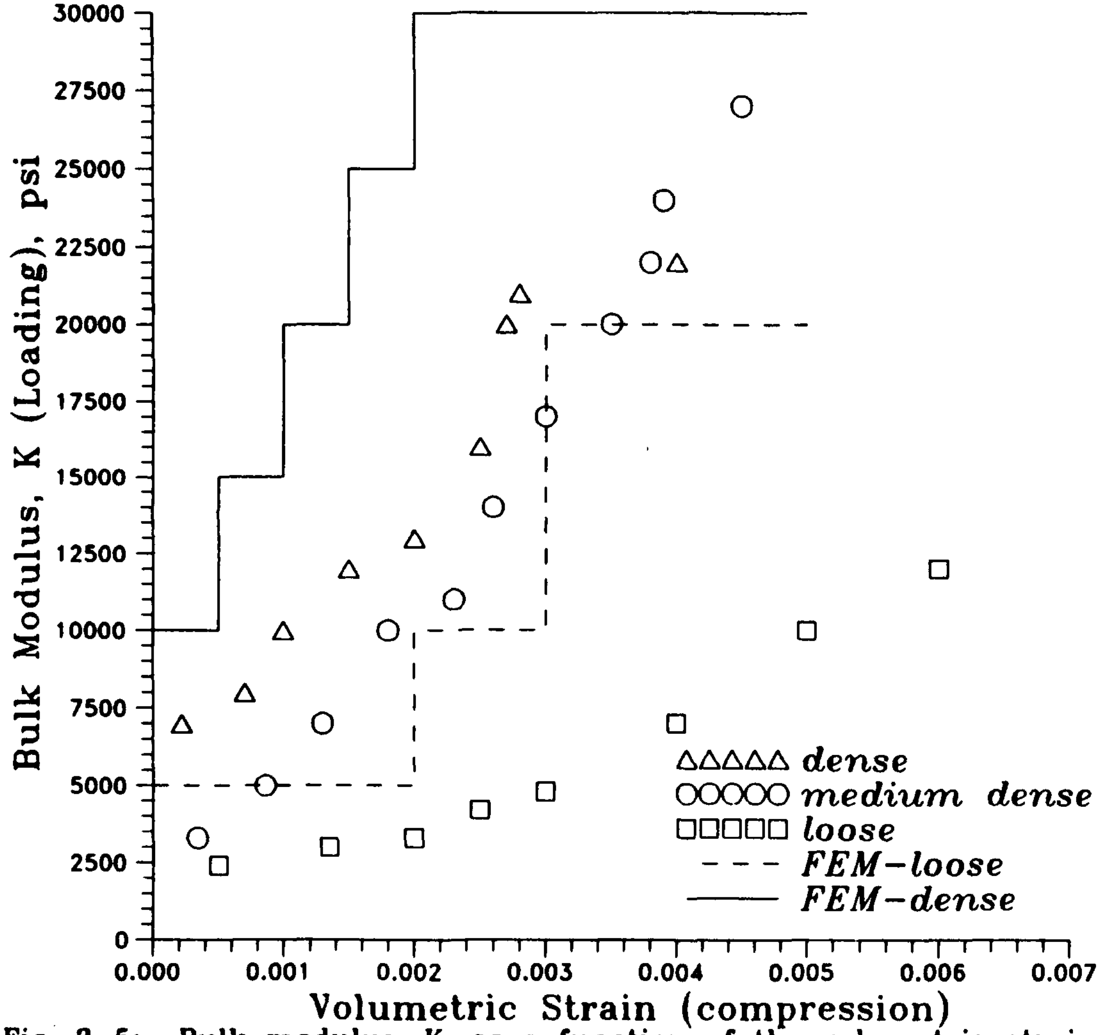

Fig. 3–5: Bulk modulus, K, as a function of the volumetric strain, ε_v, during loading of Ottawa sand – experimental measurements(28,29,38,39,50,53) and actual values used for the FEM analysis.

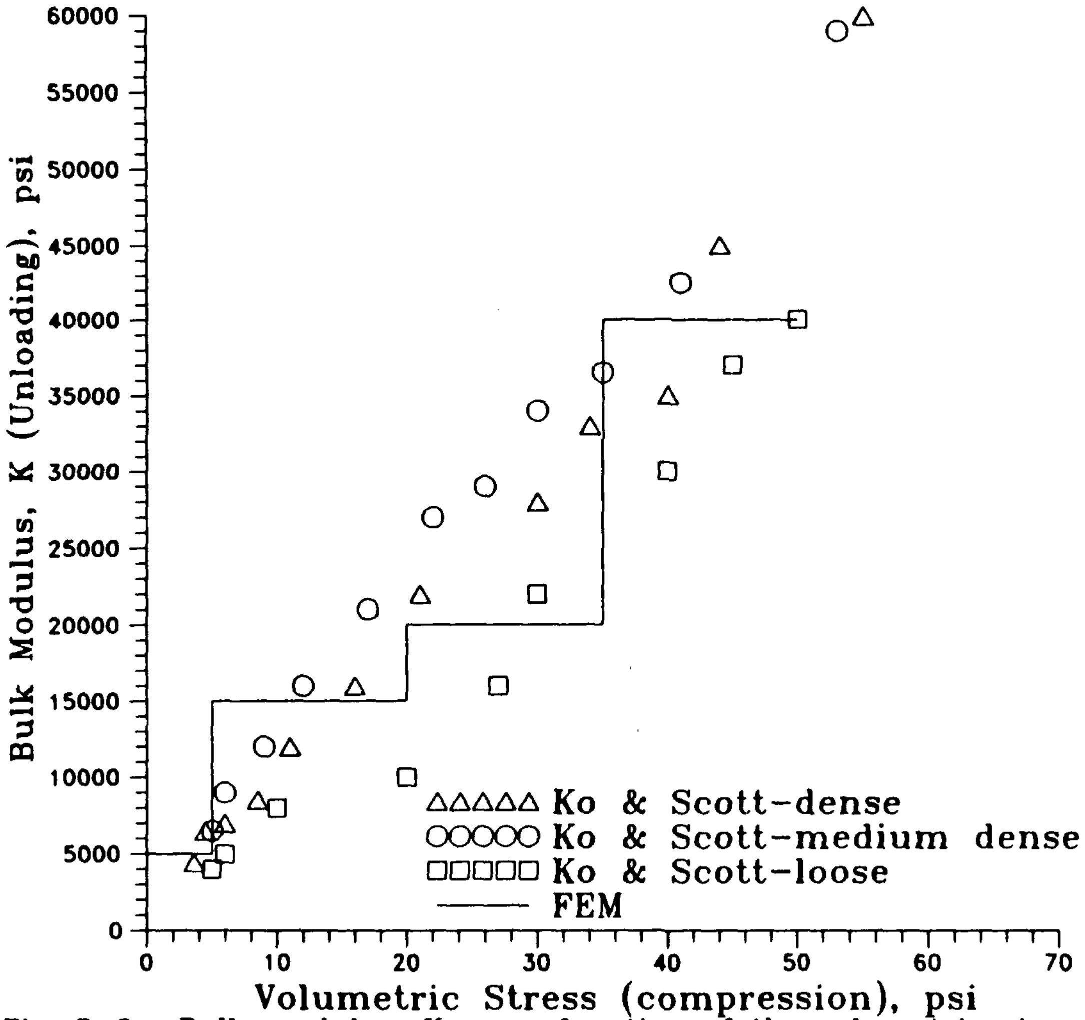

Fig. 3-6: Bulk modulus, K, as a function of the volumetric stress, σ_{v}, during unloading of Ottawa sand - experimental measurements(28,29,38,39,50,53) and actual values used for the FEM analysis.

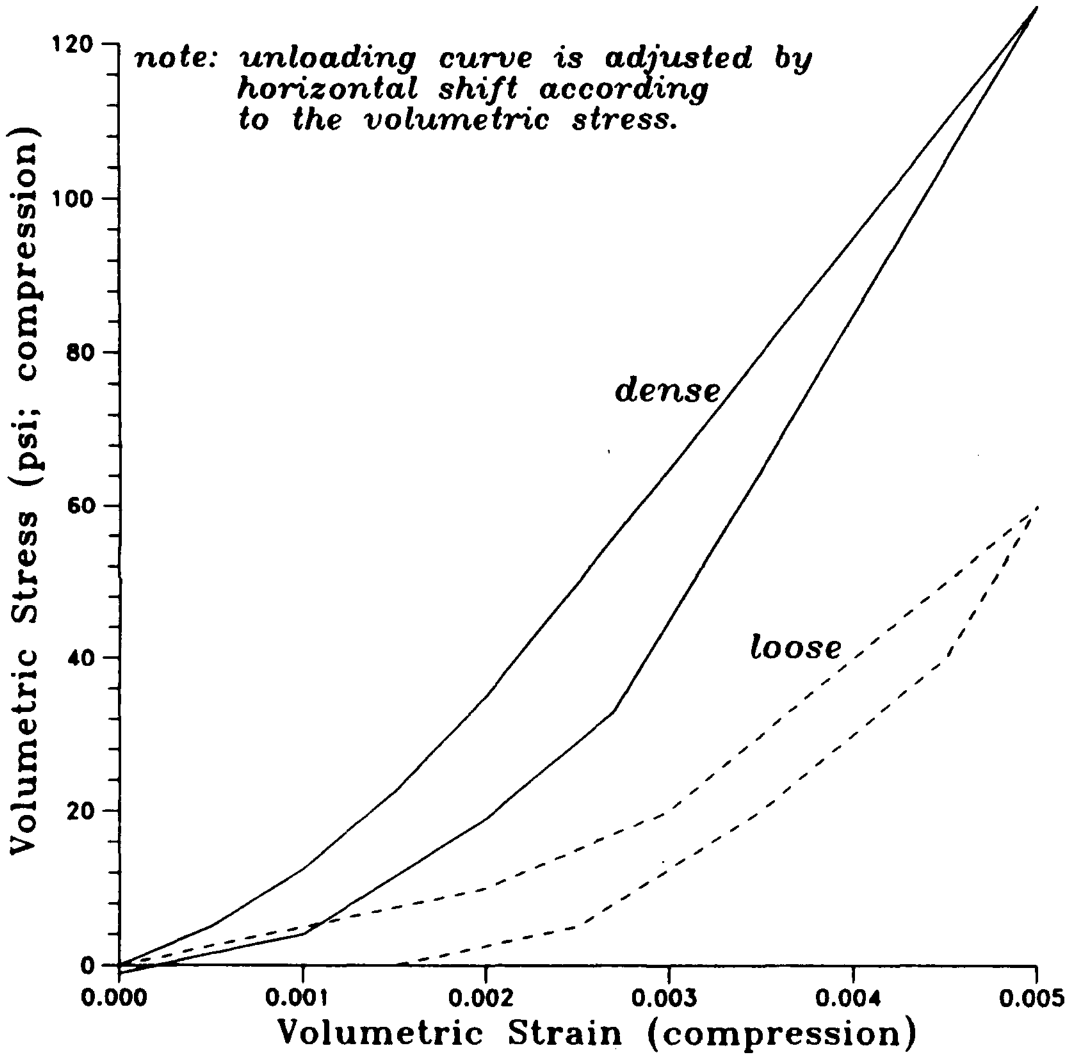

Fig. 3-7: Loading and unloading curves for numerical modeling of Ottawa sand.

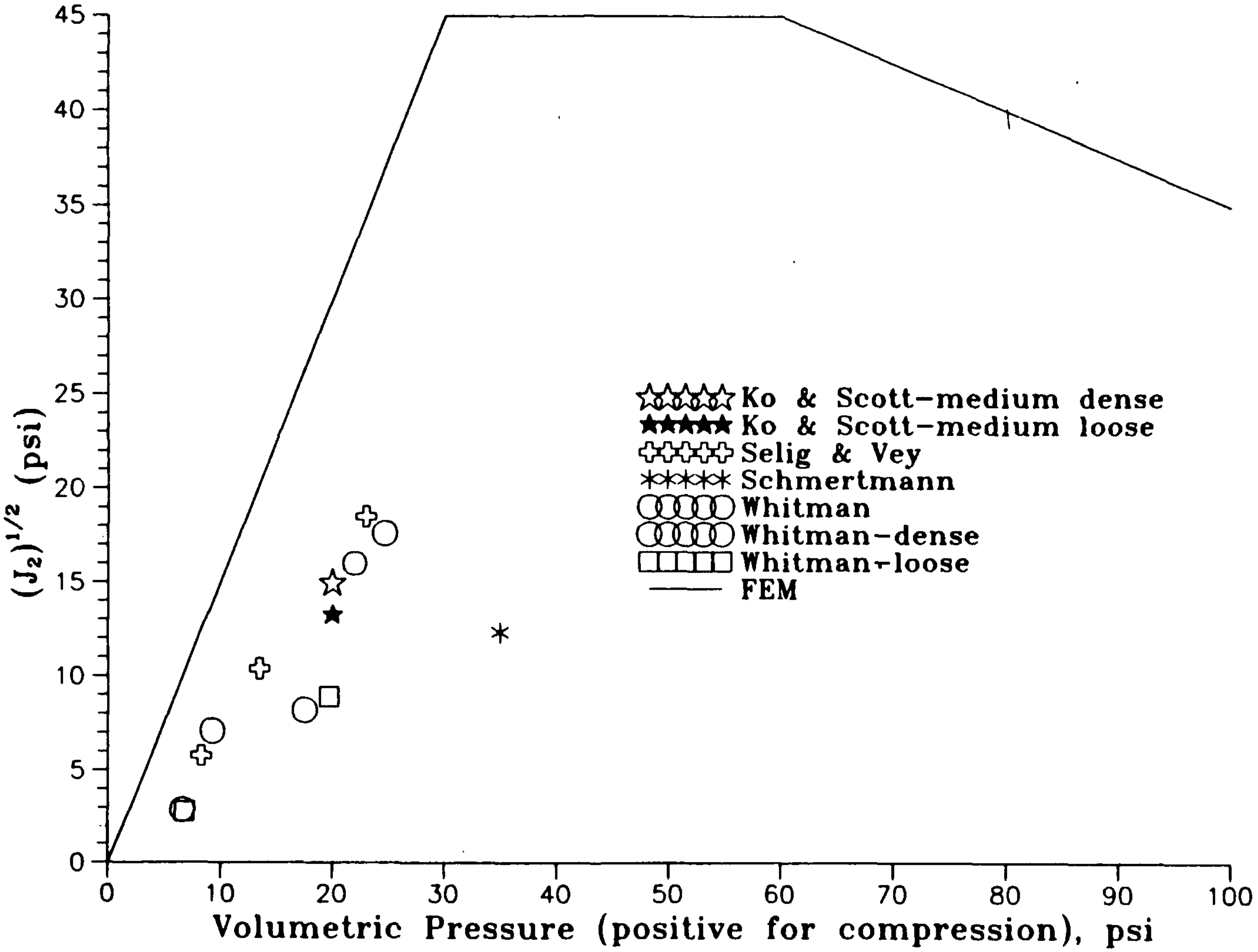

Fig. 3-8: Yield surface for Ottawa sand - experimental measurements and actual values used for the FEM analysis

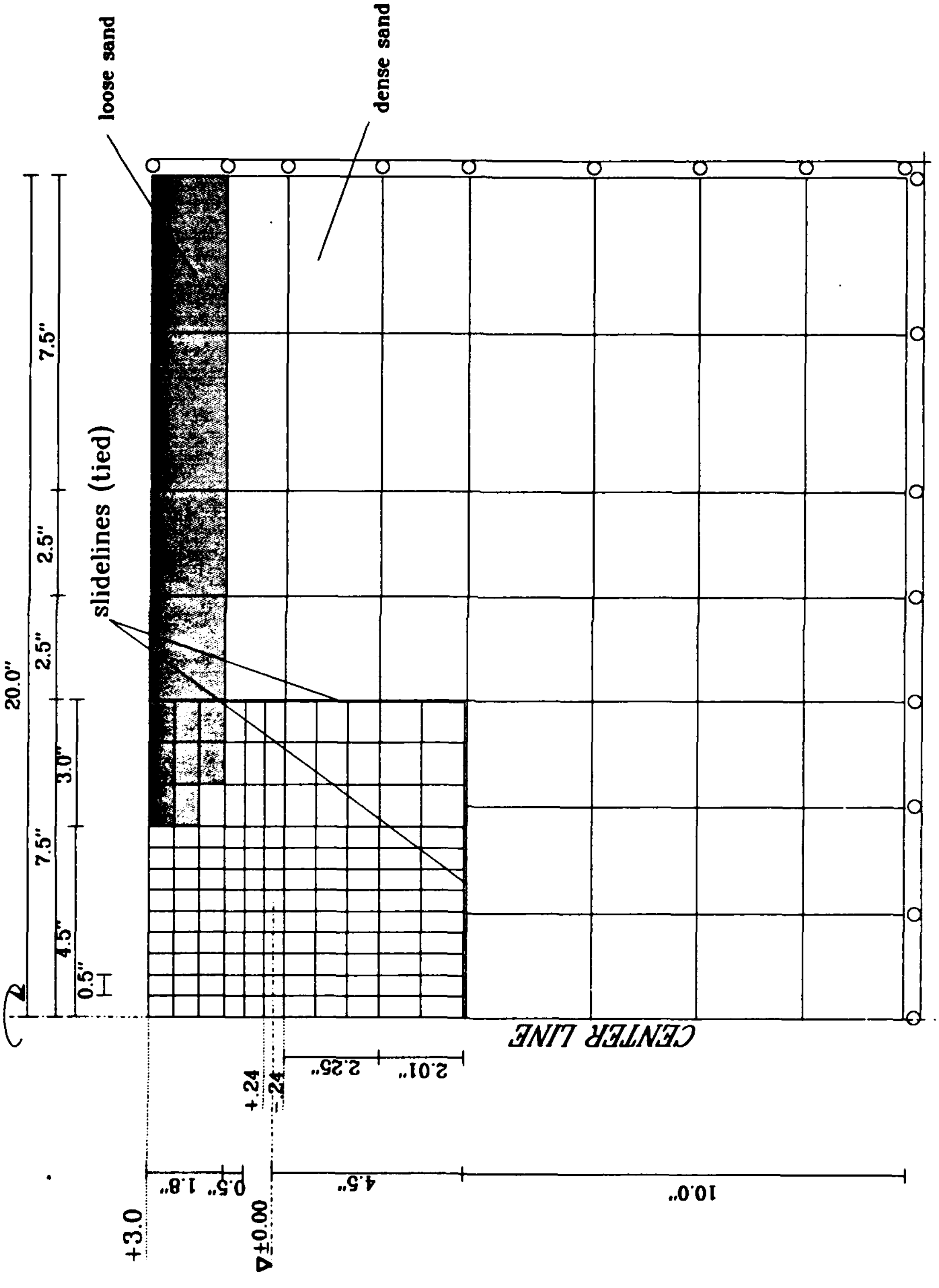
loose sand
dense sand
slidelines (tied)
20.0"
7.5"
2.5"
2.5"
3.0"
7.5"
4.5"
0.5"
CENTER LINE
2.25"
2.01"
+.24
-.24
+3.0
∇±0.00
0.5"
1.8"
4.5"
10.0"

Fig. 3-9: Finite element mesh for numerical modeling of the free field.

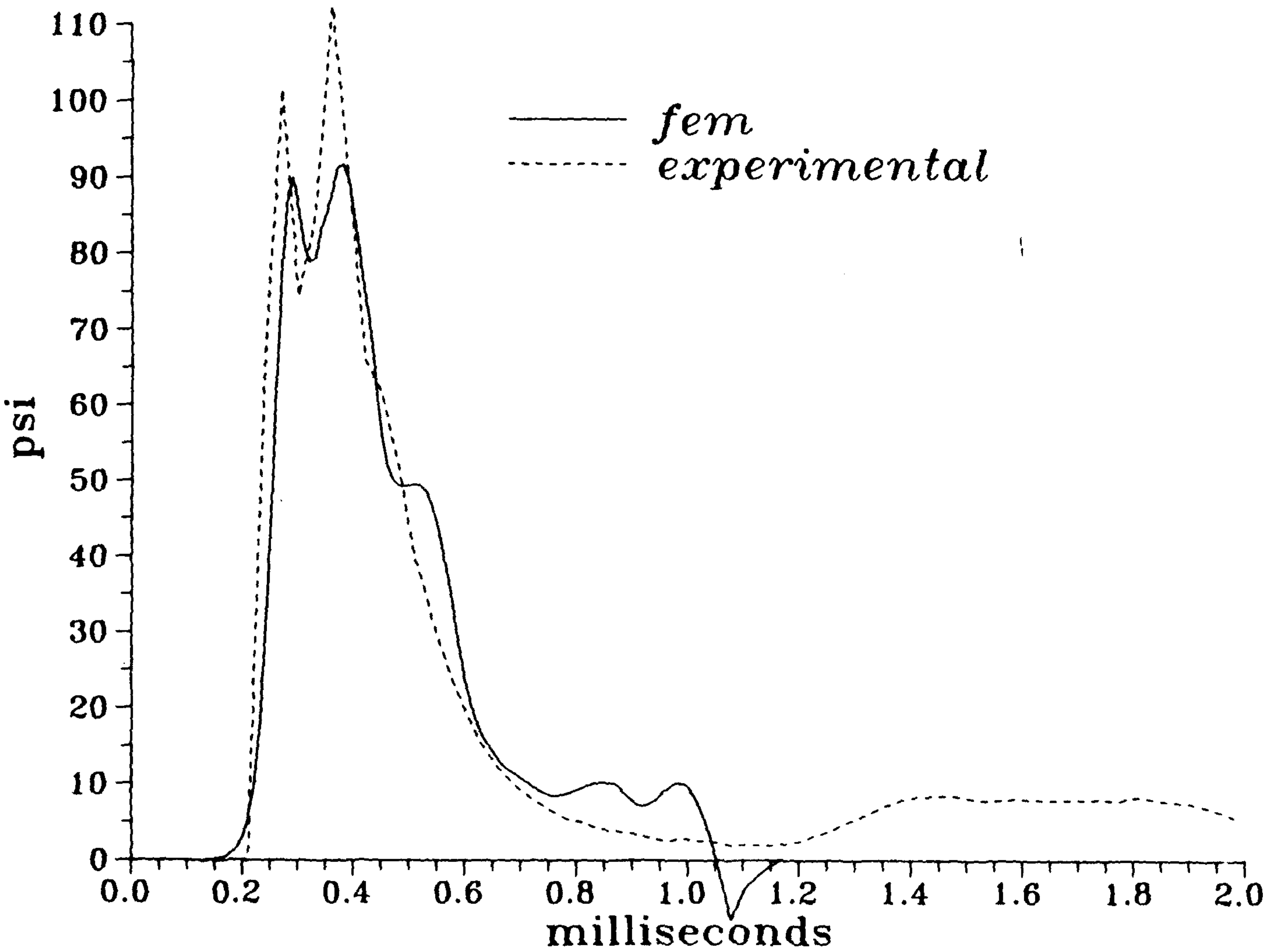

Fig. 3-10: Free field pressure at the center – numerical v.s. experimental results (DOB = 3 inches; H = 25 inches).

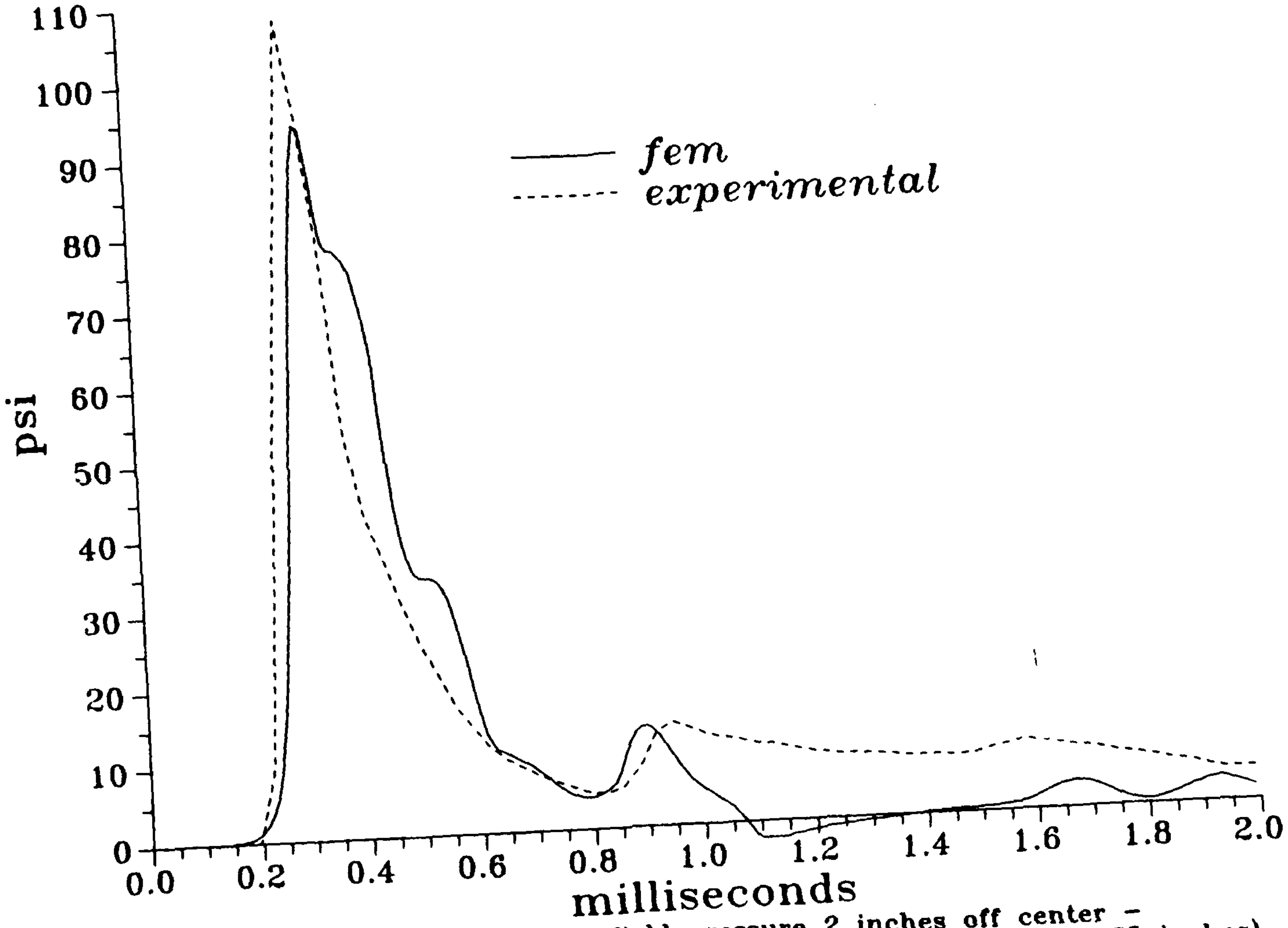

Fig. 3-11: Free field pressure 2 inches off center – numerical v.s. experimental results (DOB = 3 inches; H = 25 inches).

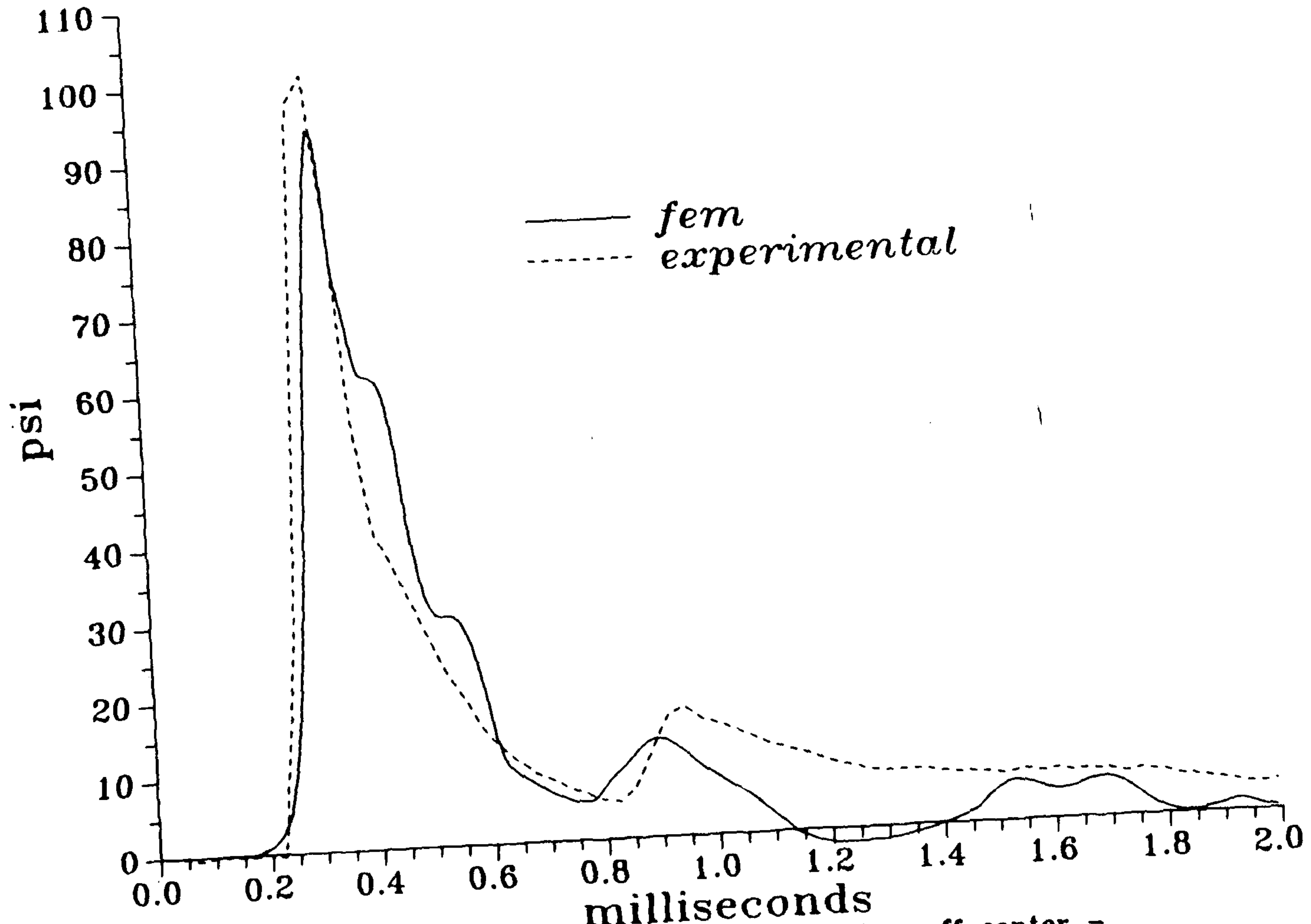

Fig. 3-12: Free field pressure 2.5 inches off center – numerical v.s. experimental results (DOB = 3 inches; H = 25 inches).

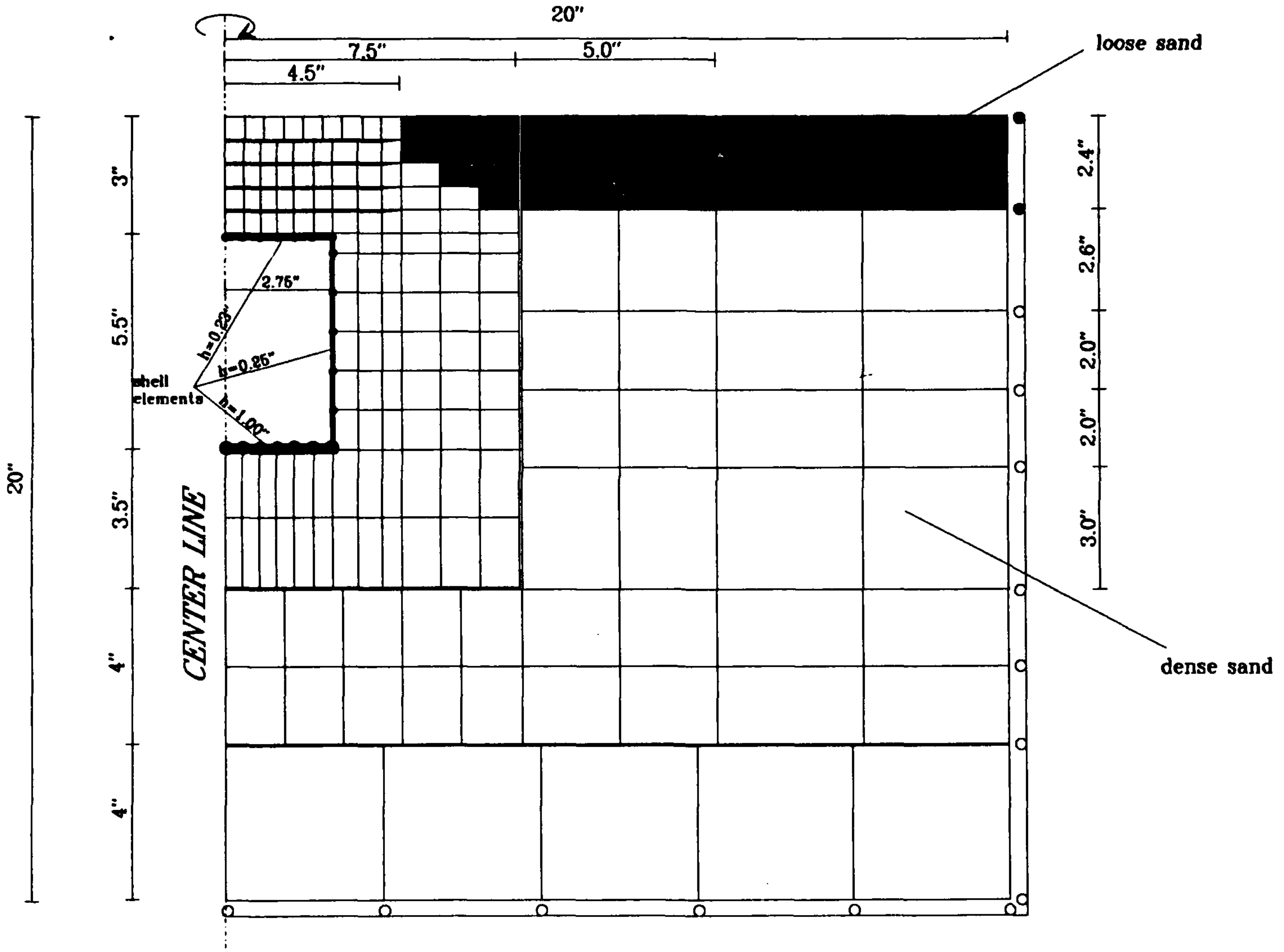
20"
7.5"
5.0"
4.5"
loose sand
2.4"
2.6"
2.0"
2.0"
3.0"
dense sand
3"
5.5"
3.5"
4"
4"
20"
2.75"
h=0.23"
h=0.25"
h=1.00"
shell elements
CENTER LINE

Fig. 3-13: Finite elements mesh for numerical modeling of the soil-elastic structure system.

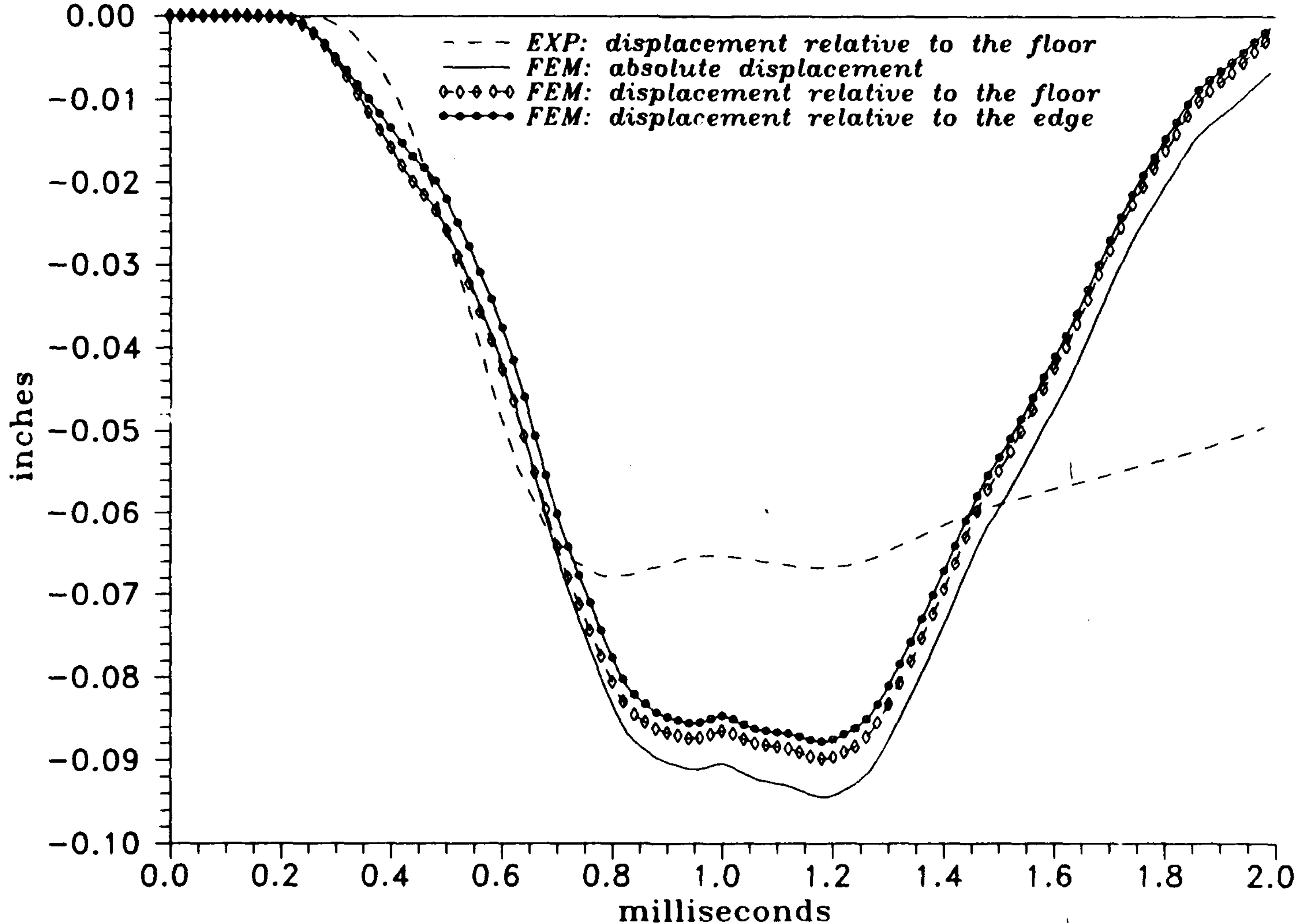

Fig. 3-14: Displacement of the roof center - FEM analysis v.s. experimental results (Plexiglas roof; DOB = 3 inches; H = 25 inches).

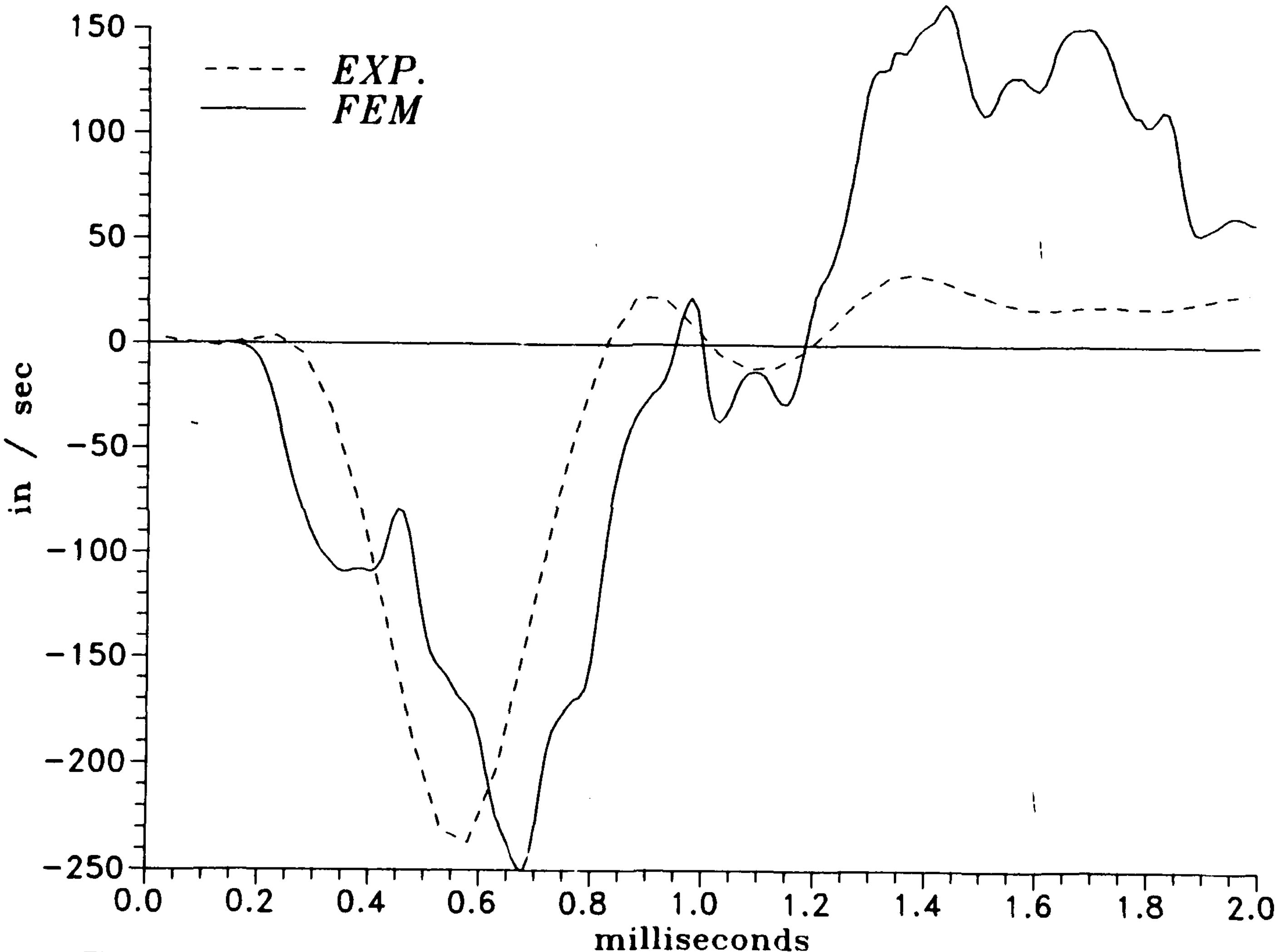

Fig. 3-15: Velocity of the roof center - FEM analysis v.s. experimental results (Plexiglas roof; DOB = 3 inches, H = 25 inches)

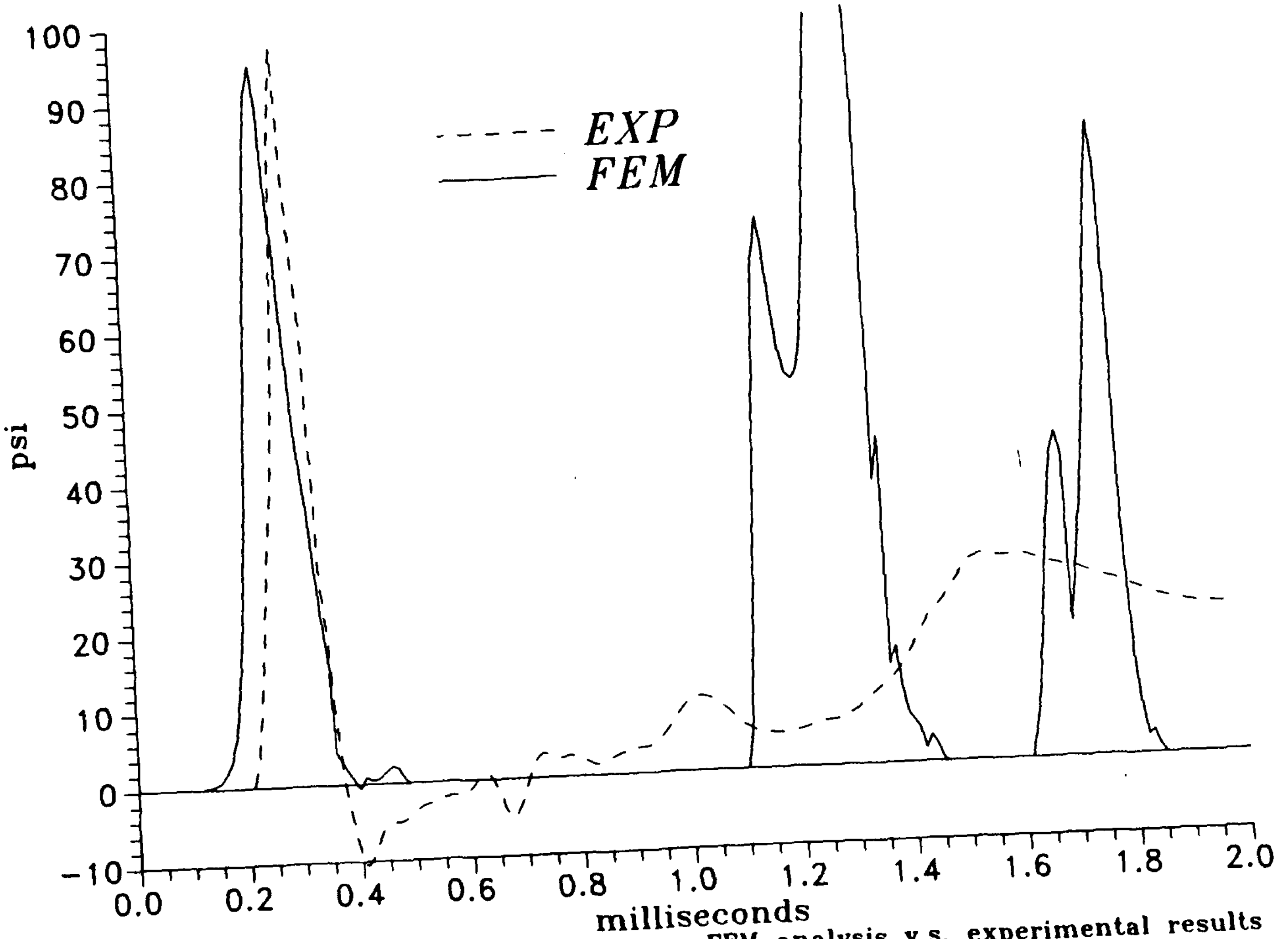

Fig. 3-16: Pressure at the roof center - FEM analysis v.s. experimental results (Plexgiglas roof; DOB = 3 inches, H = 25 inches)

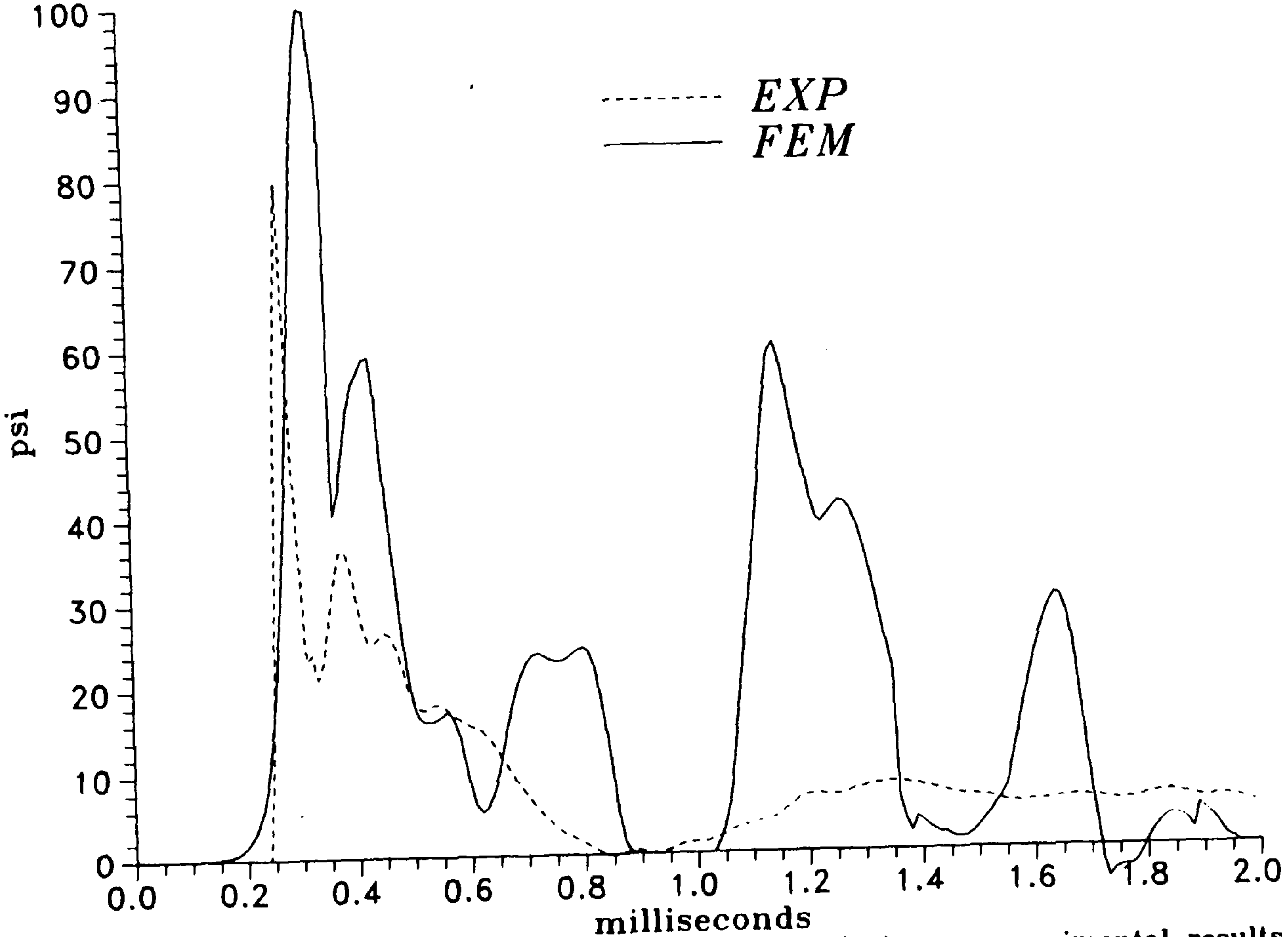

Fig. 3-17: Pressure over the roof edge - FEM analysis v.s. experimental results (Plexiglas roof; DOB = 3 inches, H = 25 inches)

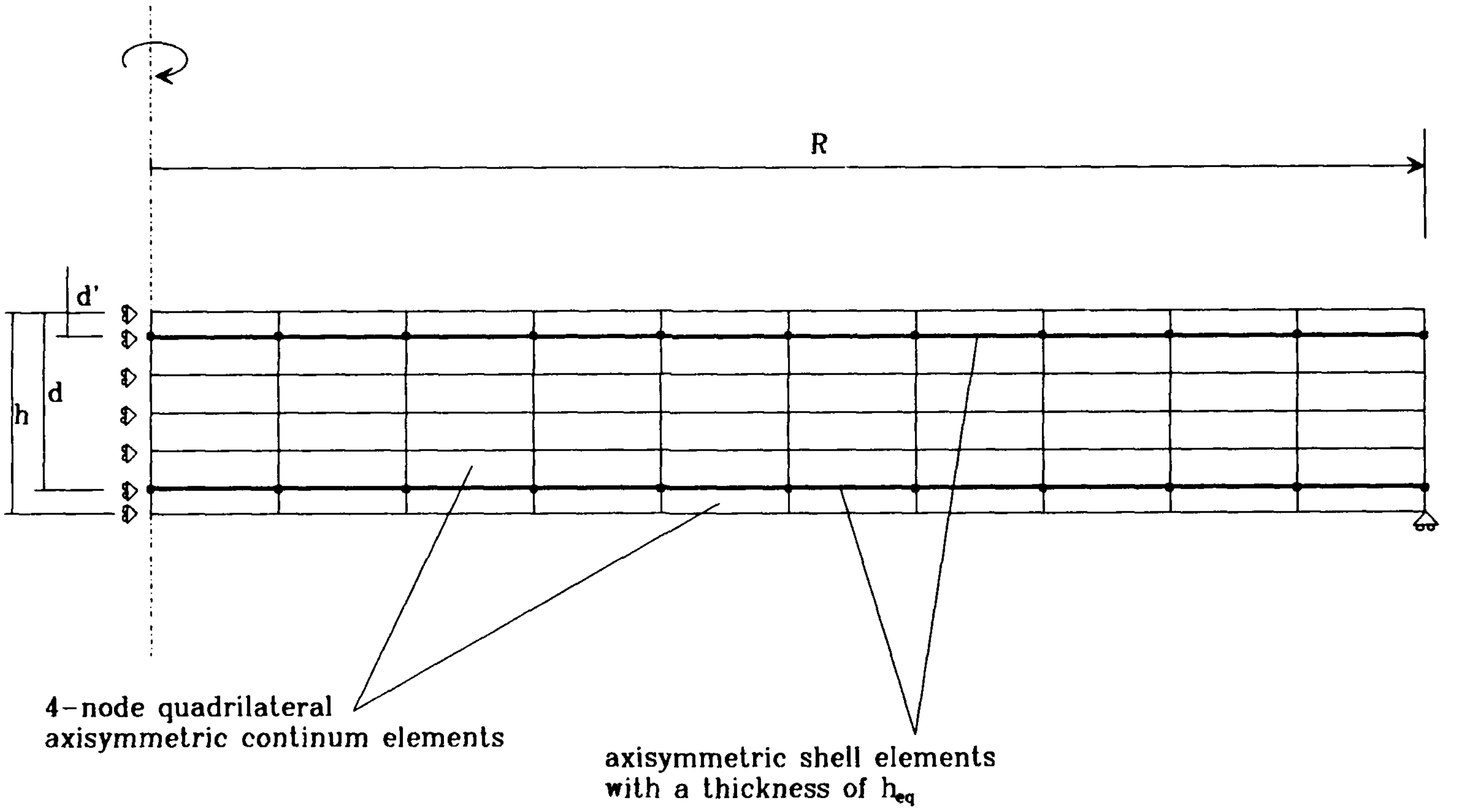
R
d'
d
h
4-node quadrilateral
axisymmetric continum elements
axisymmetric shell elements
with a thickness of h_{eq}

Fig. 3-18: Finite elements mesh model of a simply supported circular reinforced concrete slab.

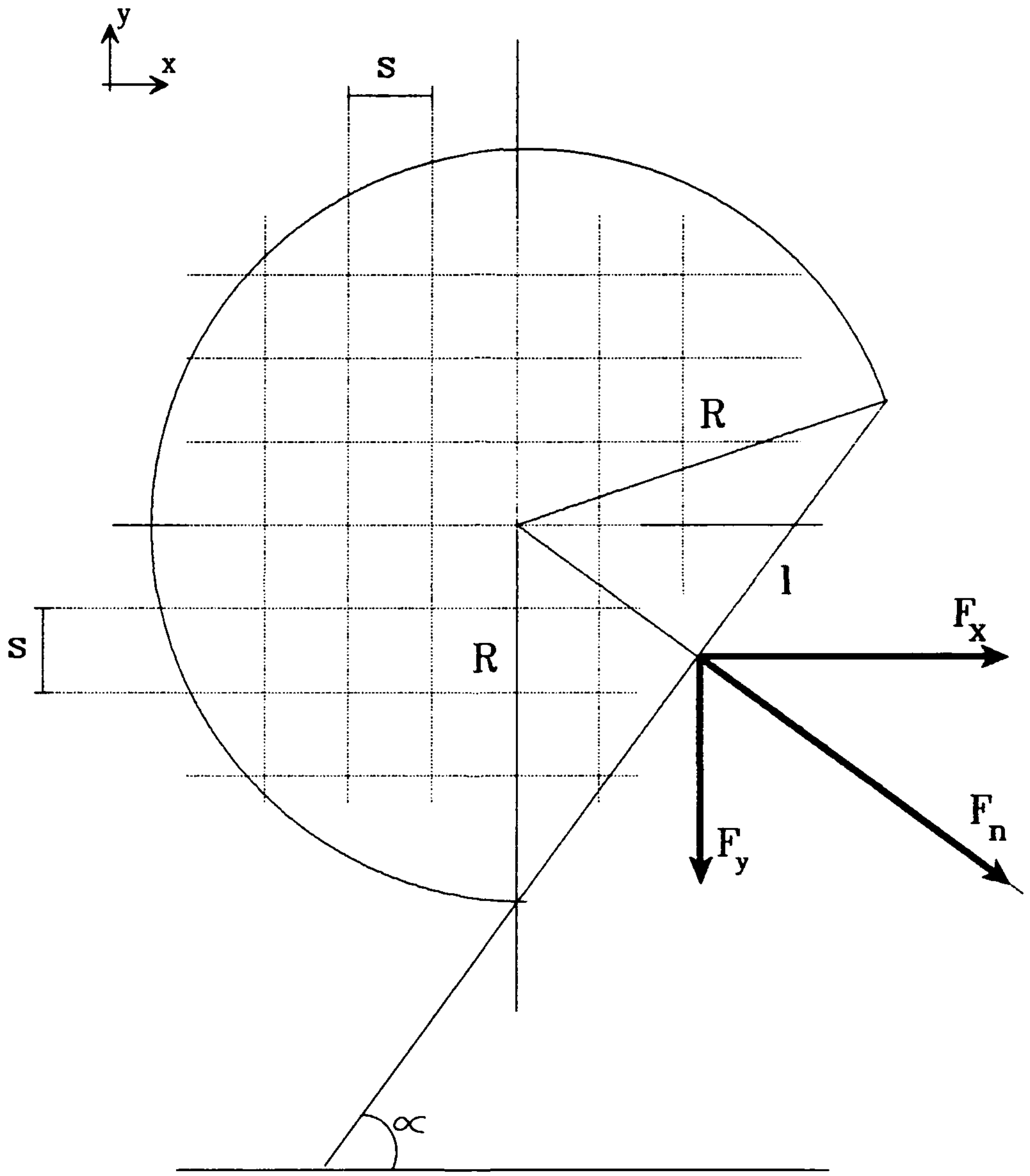
y
x
s
R
l
F_x
s
R
F_y
F_n
∝

Fig. 3-19: Forces of the reinforcing bars at an arbitrary cross-section.

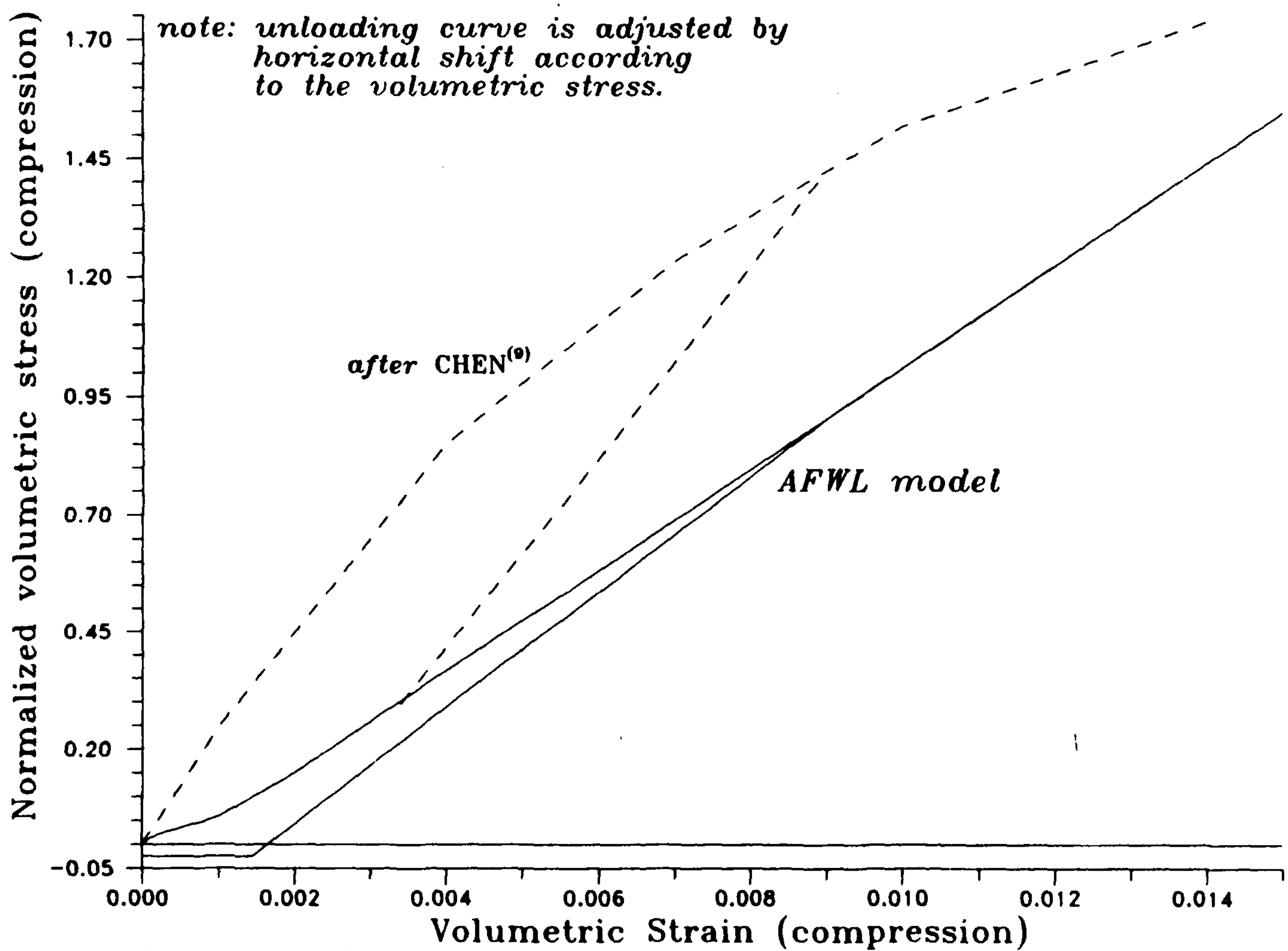

Fig. 3-20: Normalized loading and unloading curves for numerical modeling of micro-concrete. (Normalized stress = σ_v/f'_c)

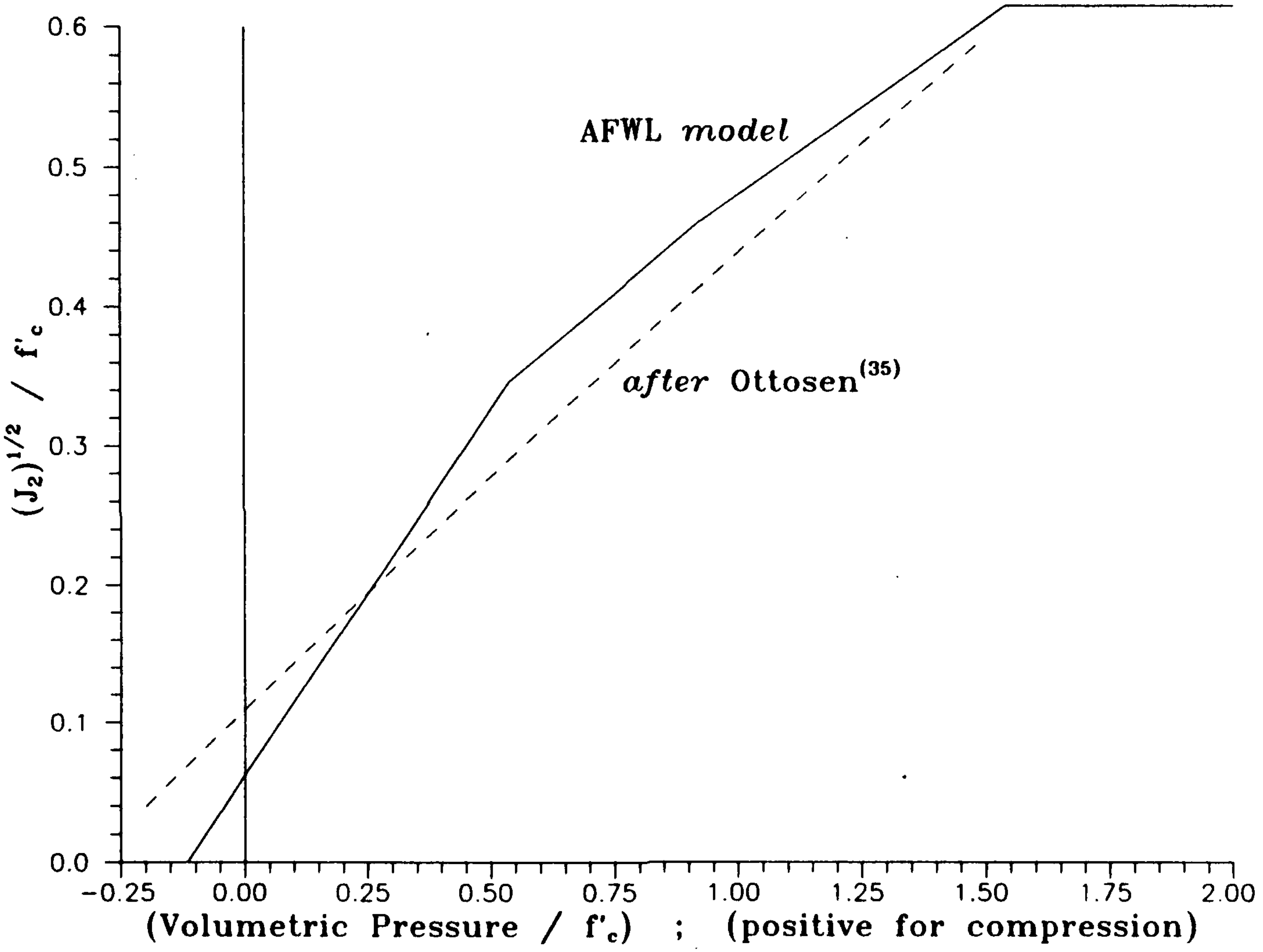

Fig. 3-21: Yield surface for the numerical modeling of micro-concrete.

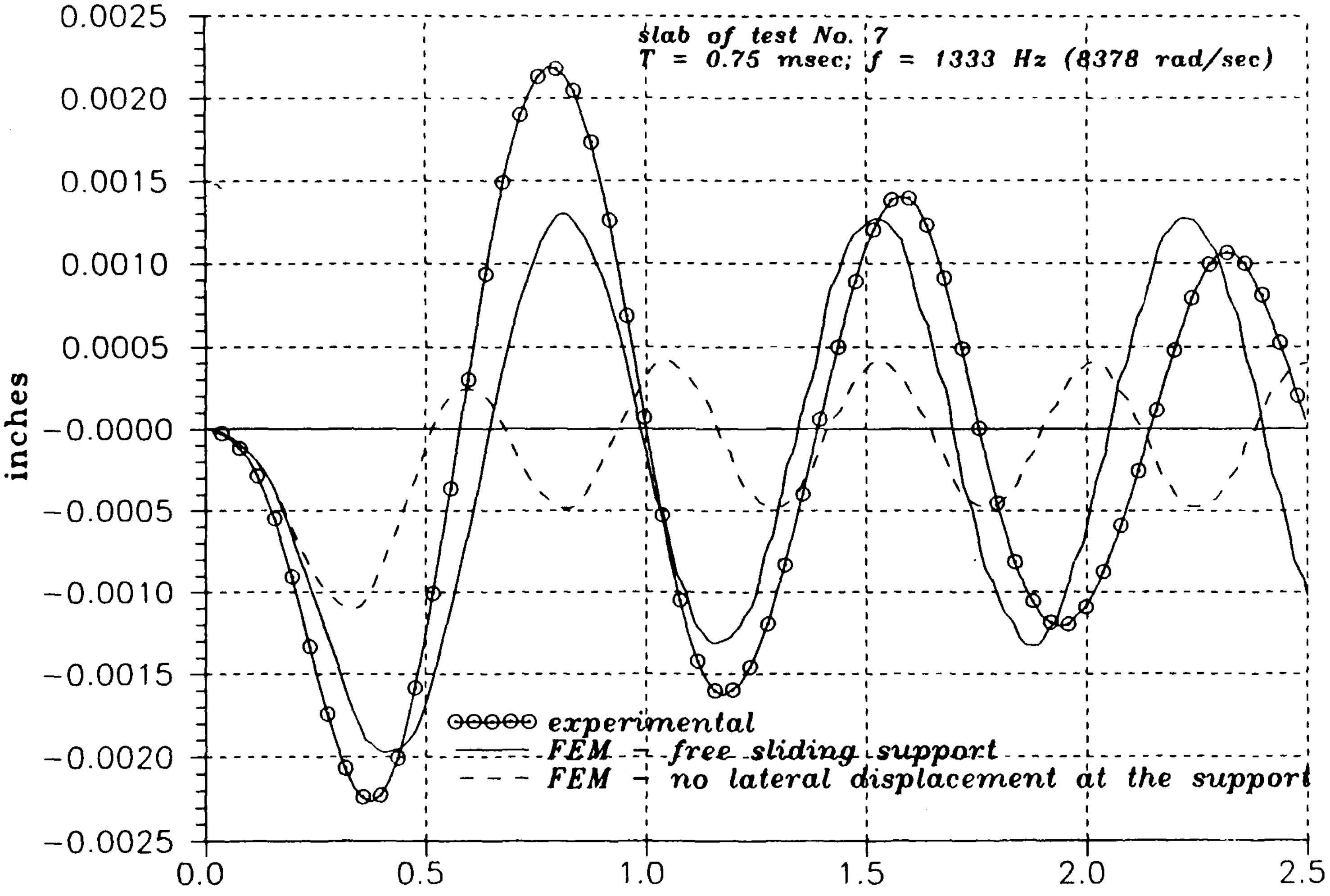

Fig. 3-22: Vibration of a simply supported micro-concrete slab.

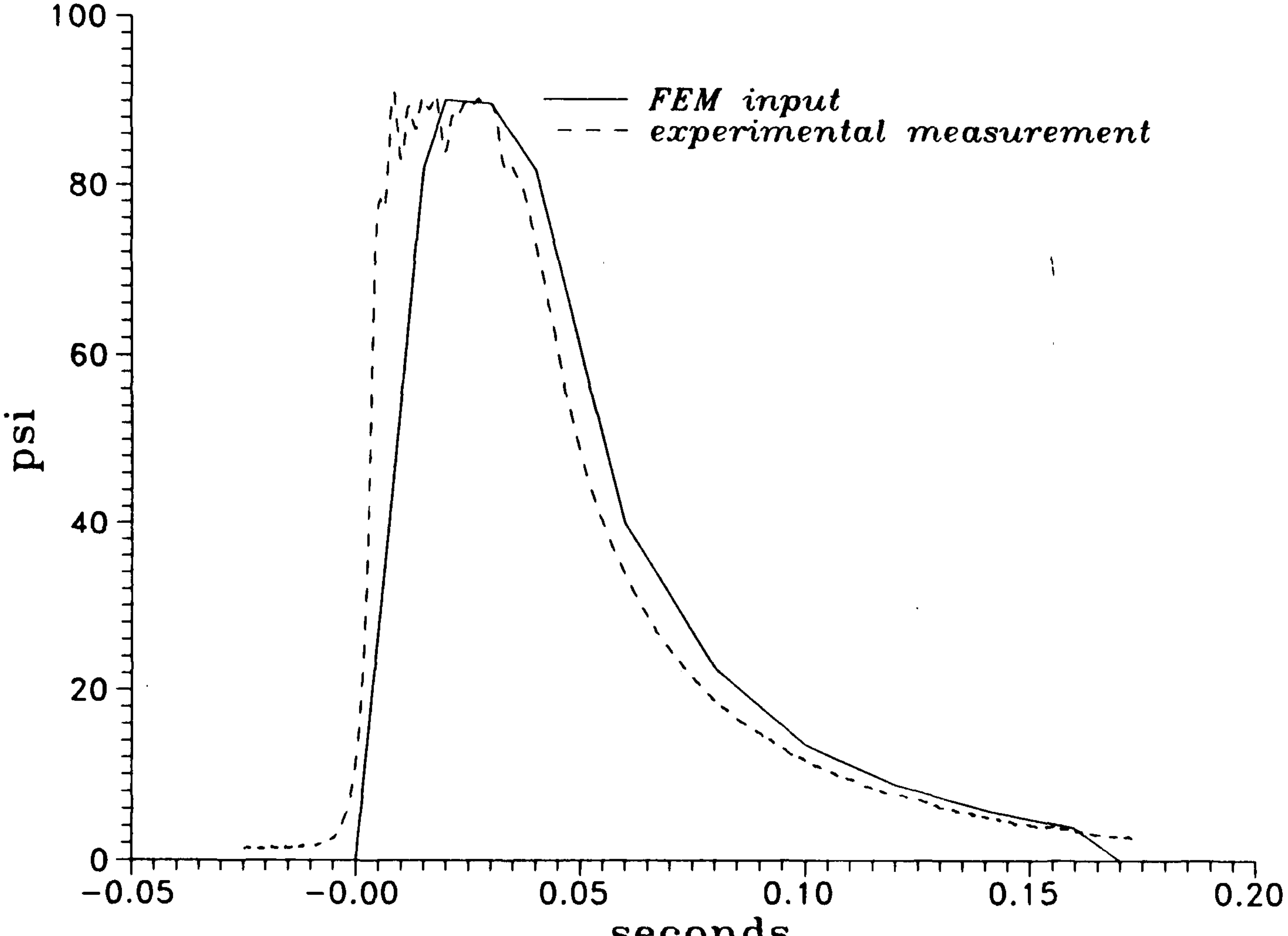

Fig. 3-23: Time record of the uniformly distributed high rate pressure over a micro-concrete slab.

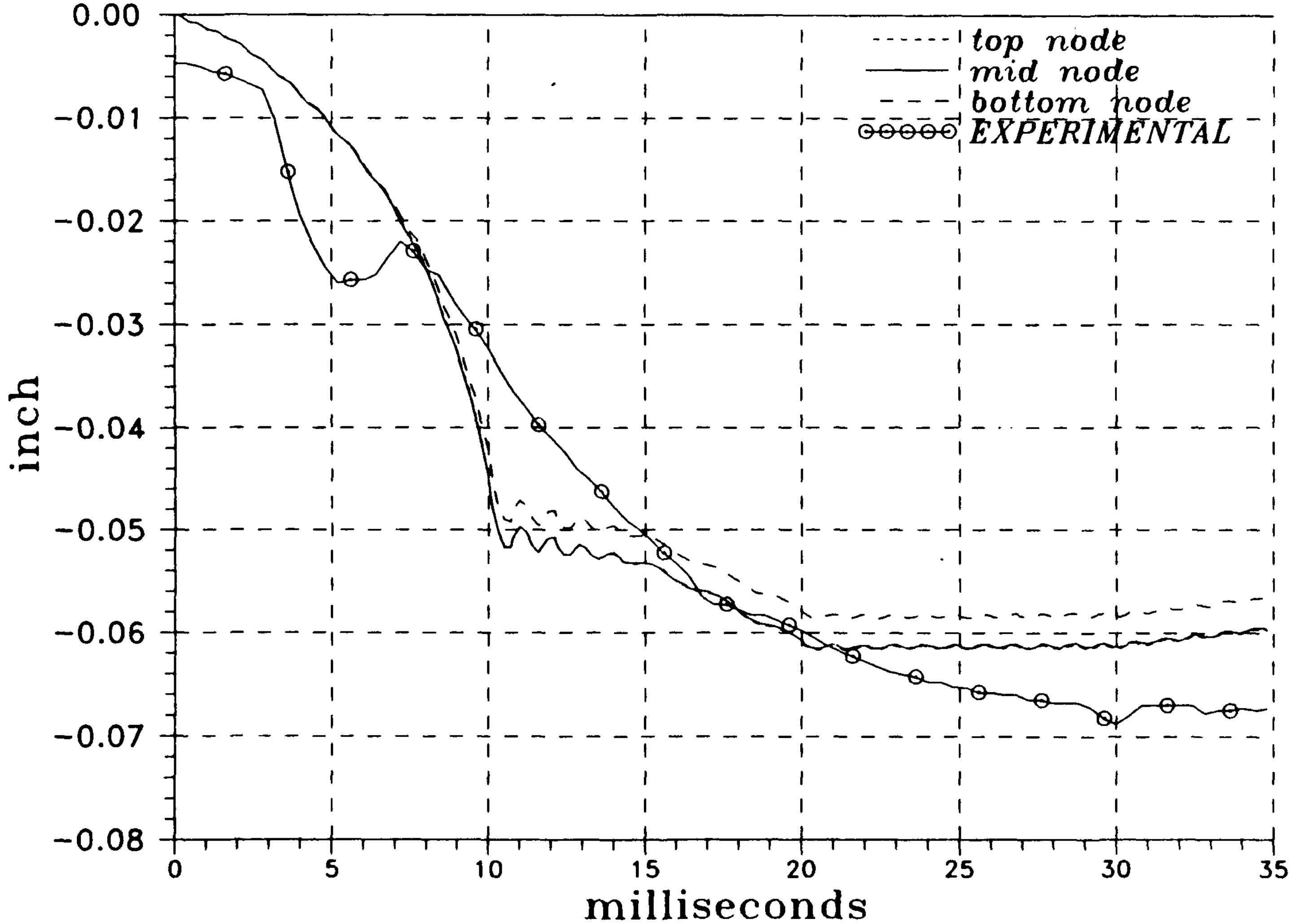

Fig. 3-24: Mid-point displacement of a micro-concrete slab under a high rate, uniformly distributed pressure (f'_c = 6500 psi, ν = 0.2, h = 0.47 inch)

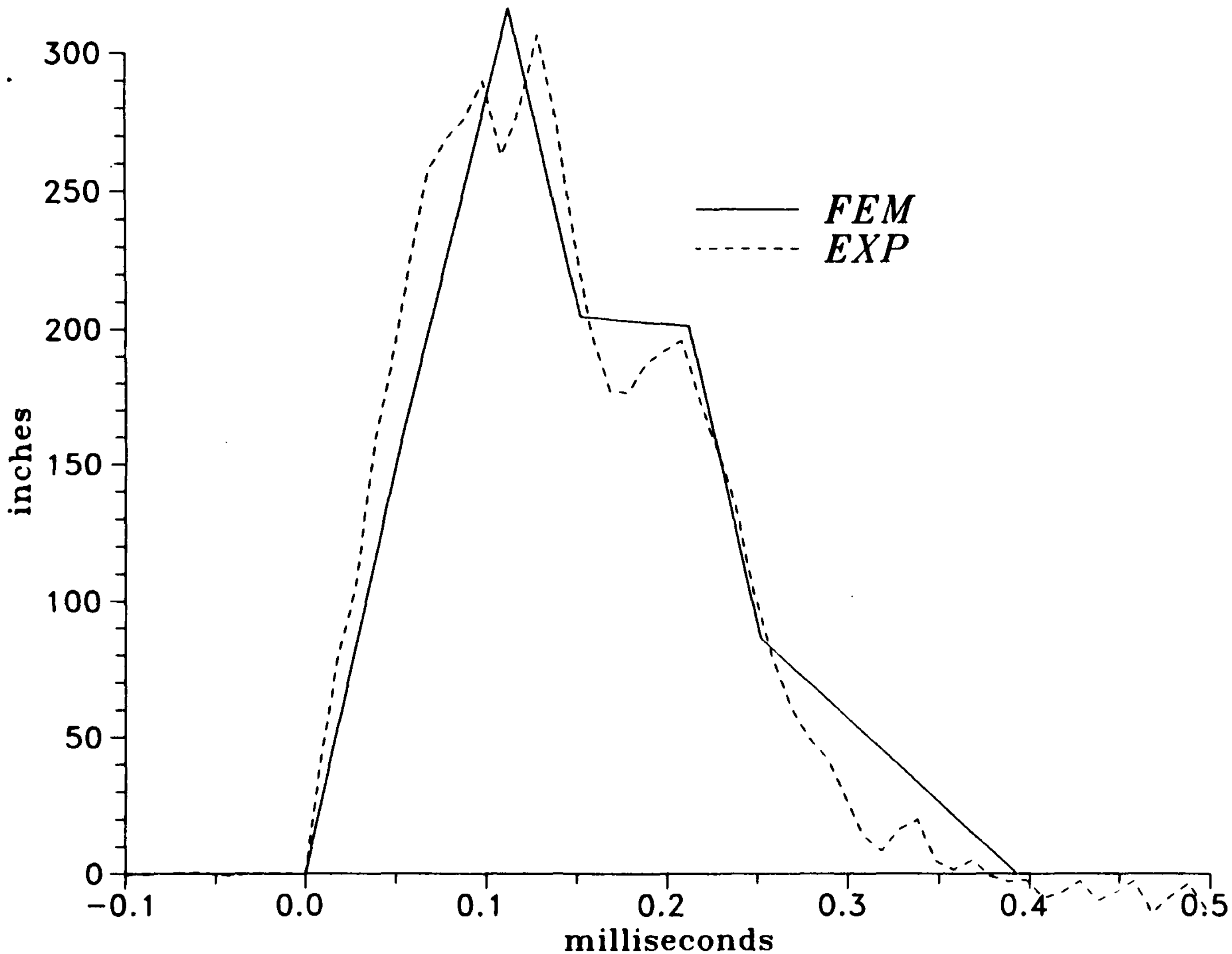

Fig. 3-25: FEM analysis of test 6, 2nd drop:
Pressure input under the center of the target plate.

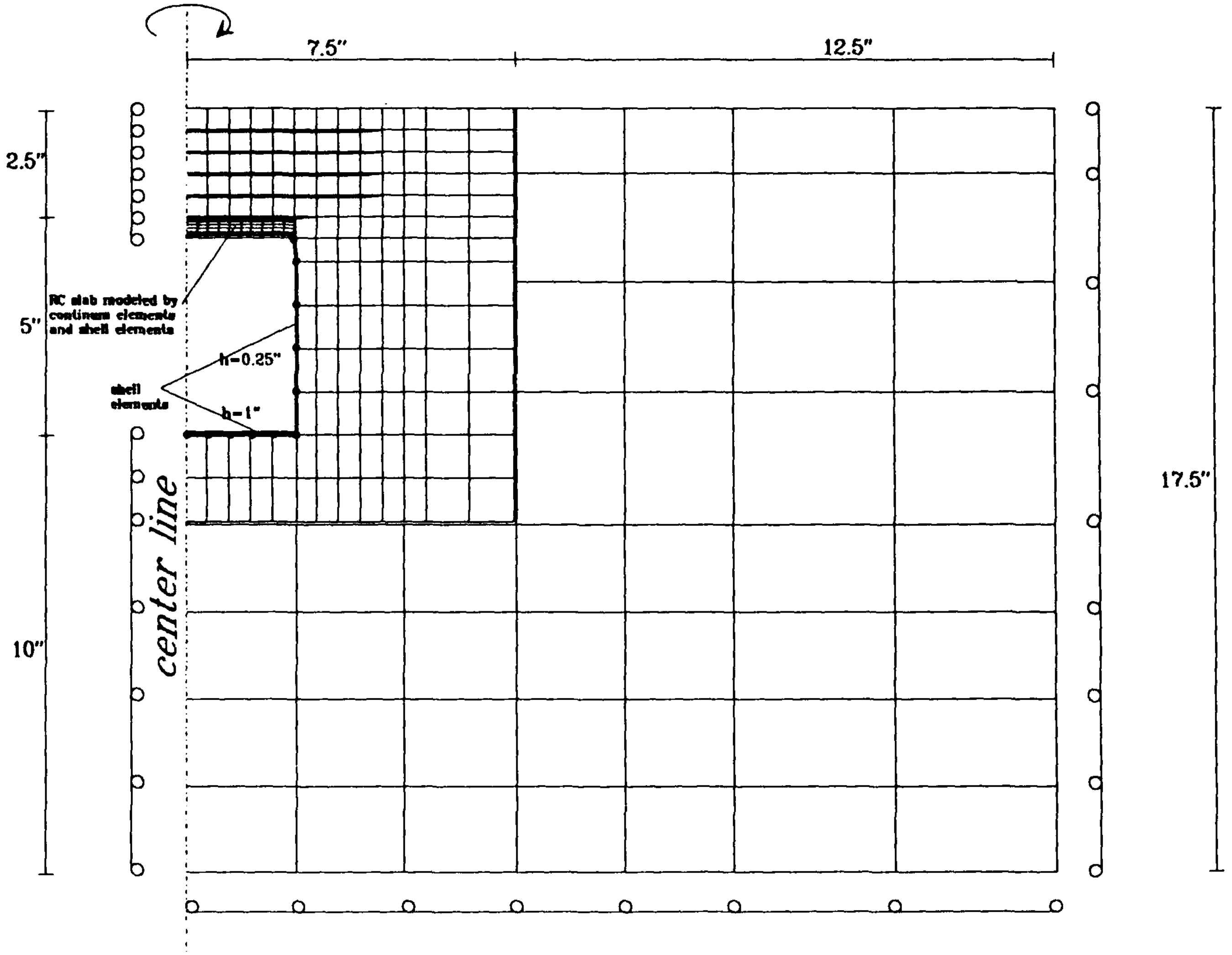
7.5"
12.5"
2.5"
5"
10"
17.5"
RC slab modeled by continuum elements and shell elements
h=0.25"
h=1"
shell elements
center line

Fig. 3-26: Finite element mesh for modeling of test No. 6.

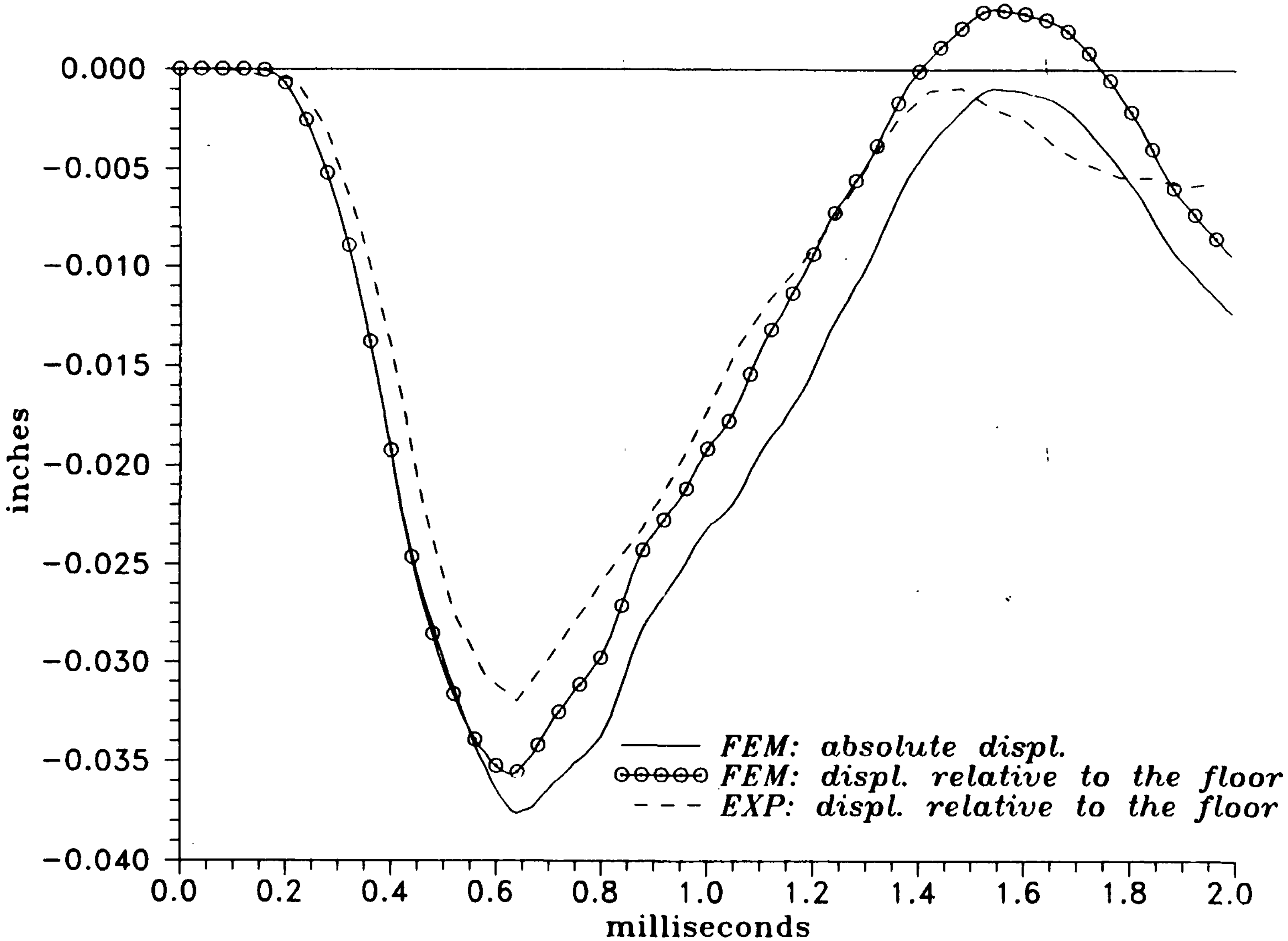

Fig. 3-27: FEM analysis v.s. experimental results (test 6, 2nd drop): Displacement of the roof center

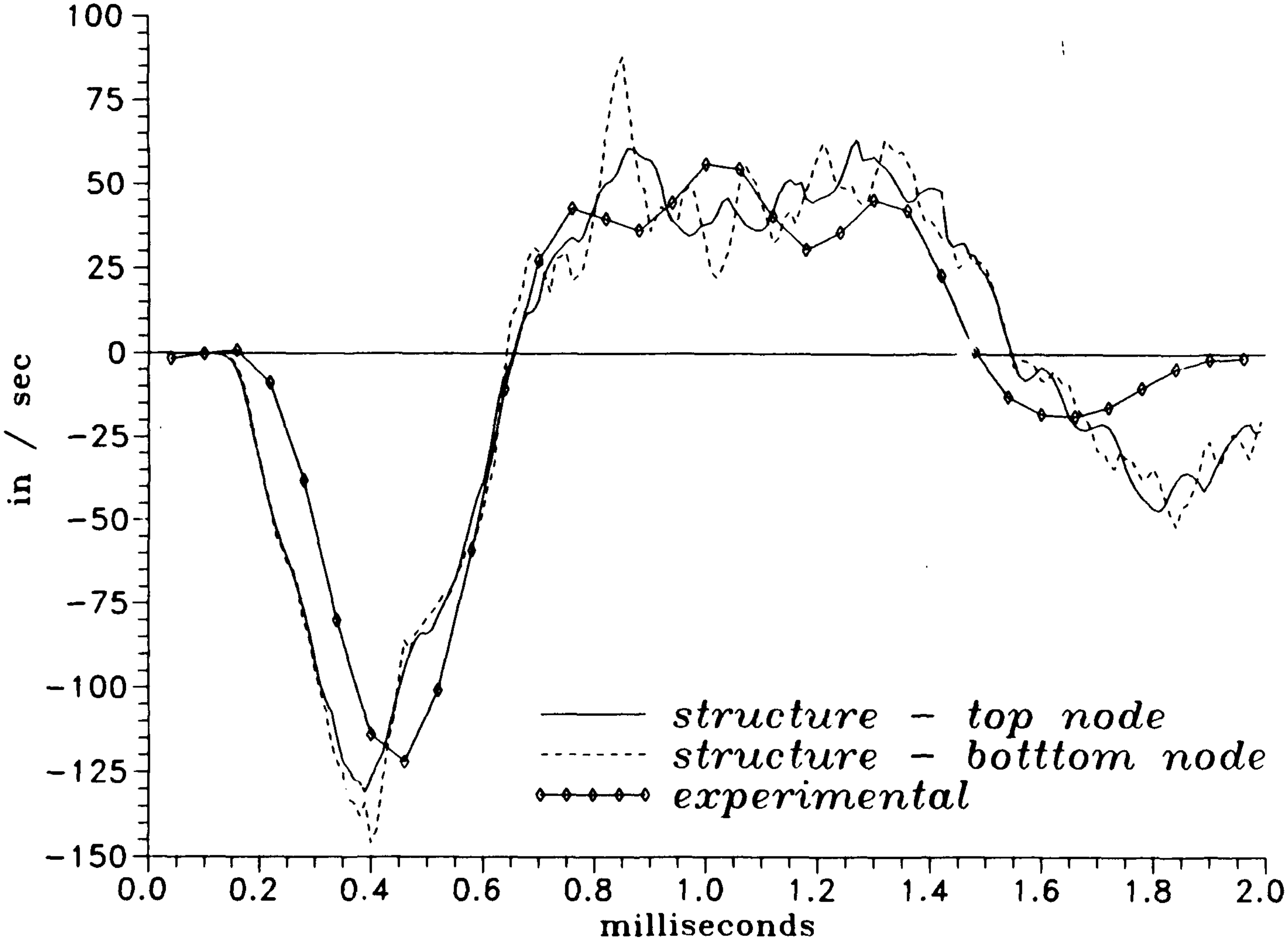

Fig. 3-28: FEM analysis v.s. experimental results (test 6, 2nd drop): Velocity of the roof center.

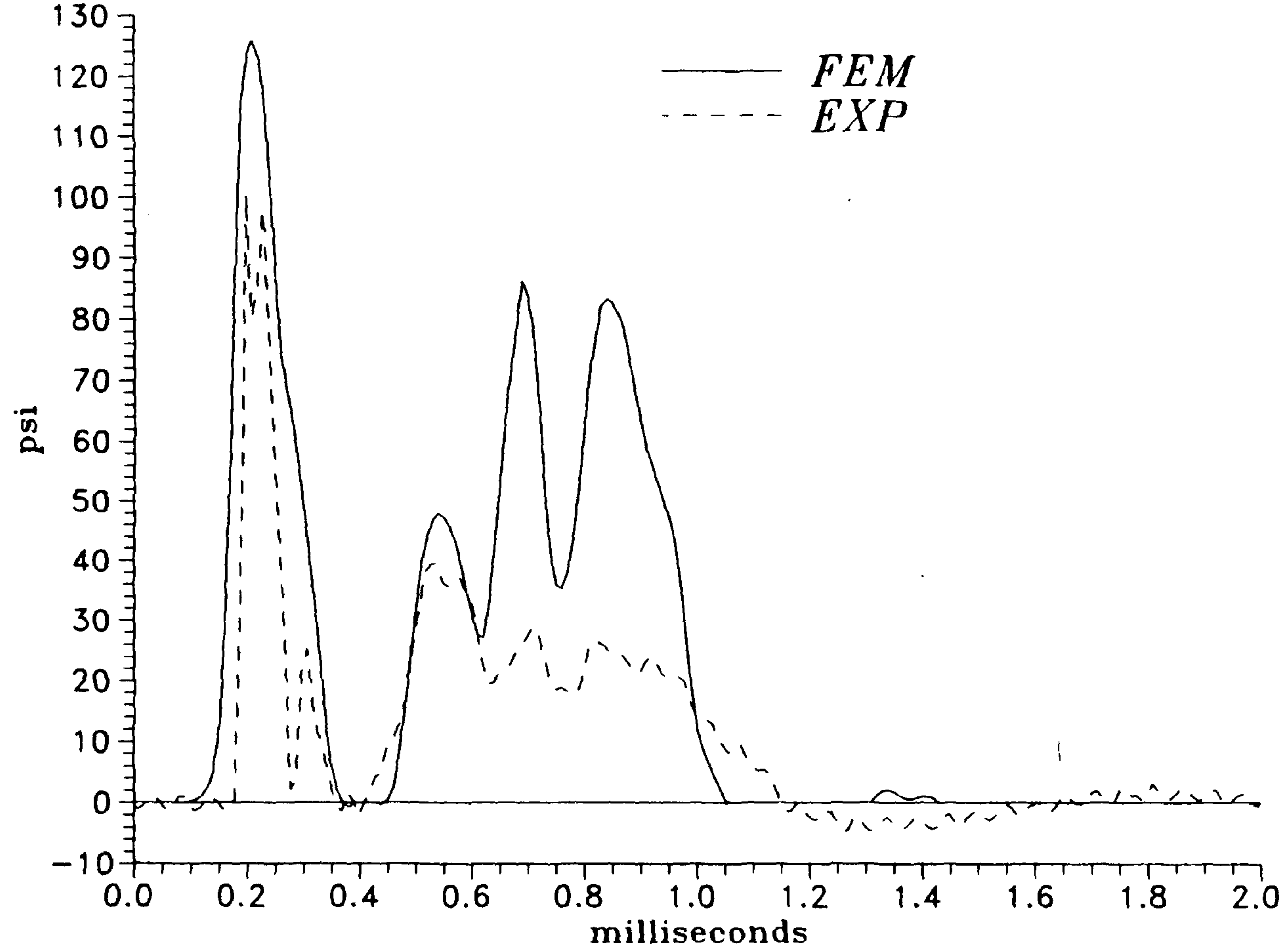

Fig. 3–29: FEM analysis v.s. experimental results (test 6, 2nd drop). Pressure at the CENTER of the roof

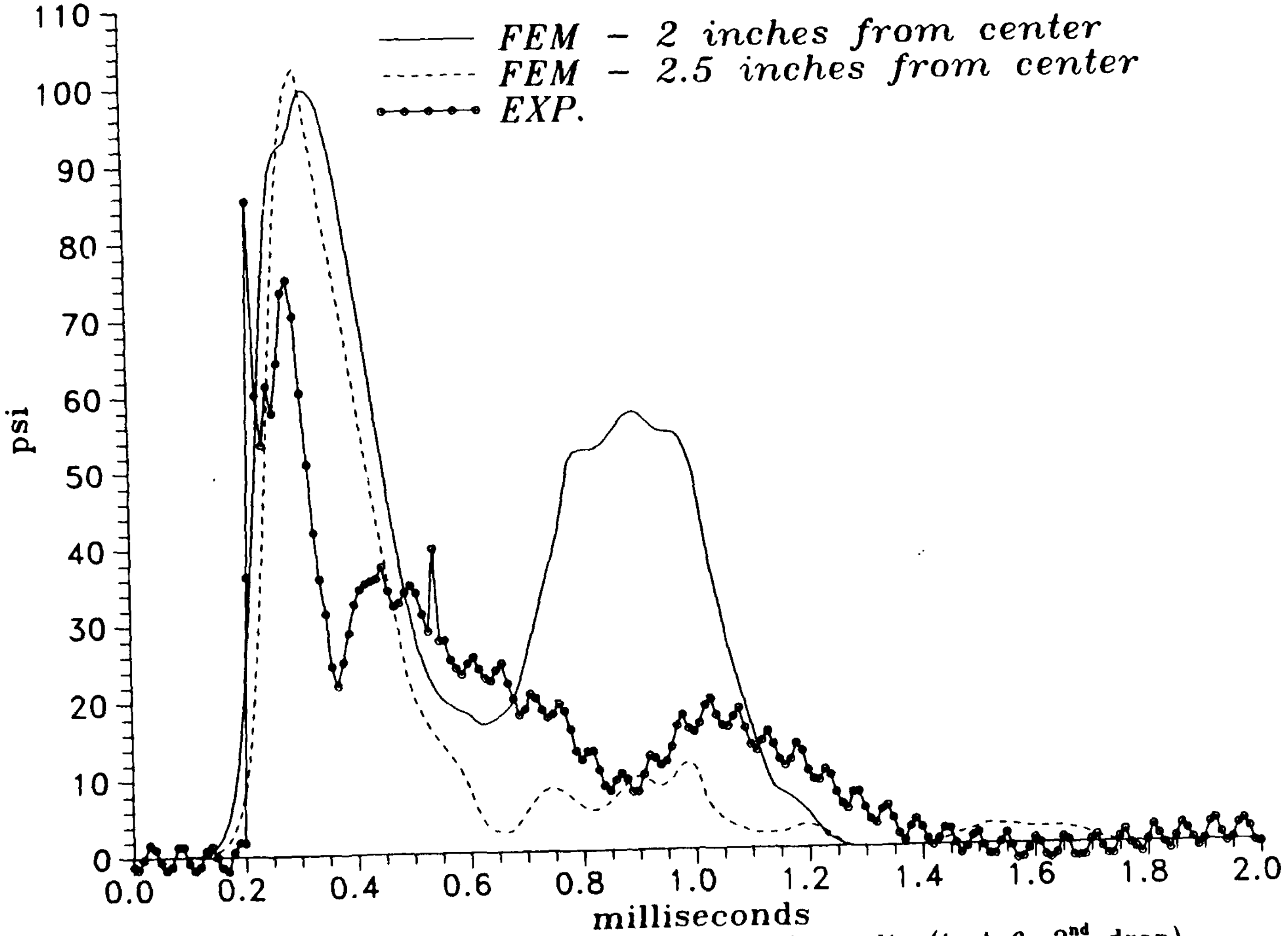

Fig. 3–30: FEM analysis v.s. experimental results (test 6, 2nd drop). Pressure over the EDGE of the roof

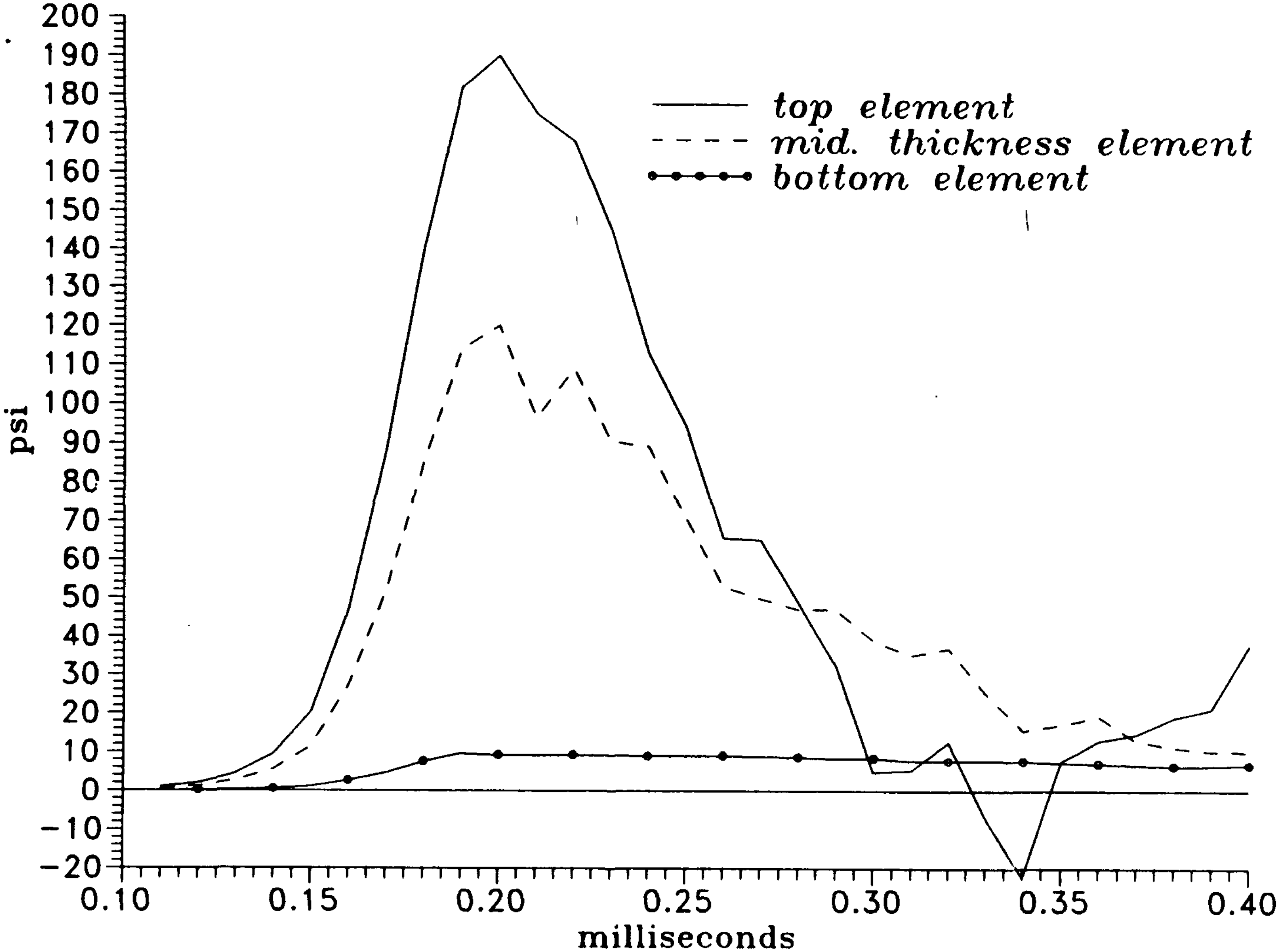

Fig. 3-31: Vertical (transverse) stresses in the slab center (Numerical analysis of test 6, 2^{nd} drop; free sliding at soil-structure interface).

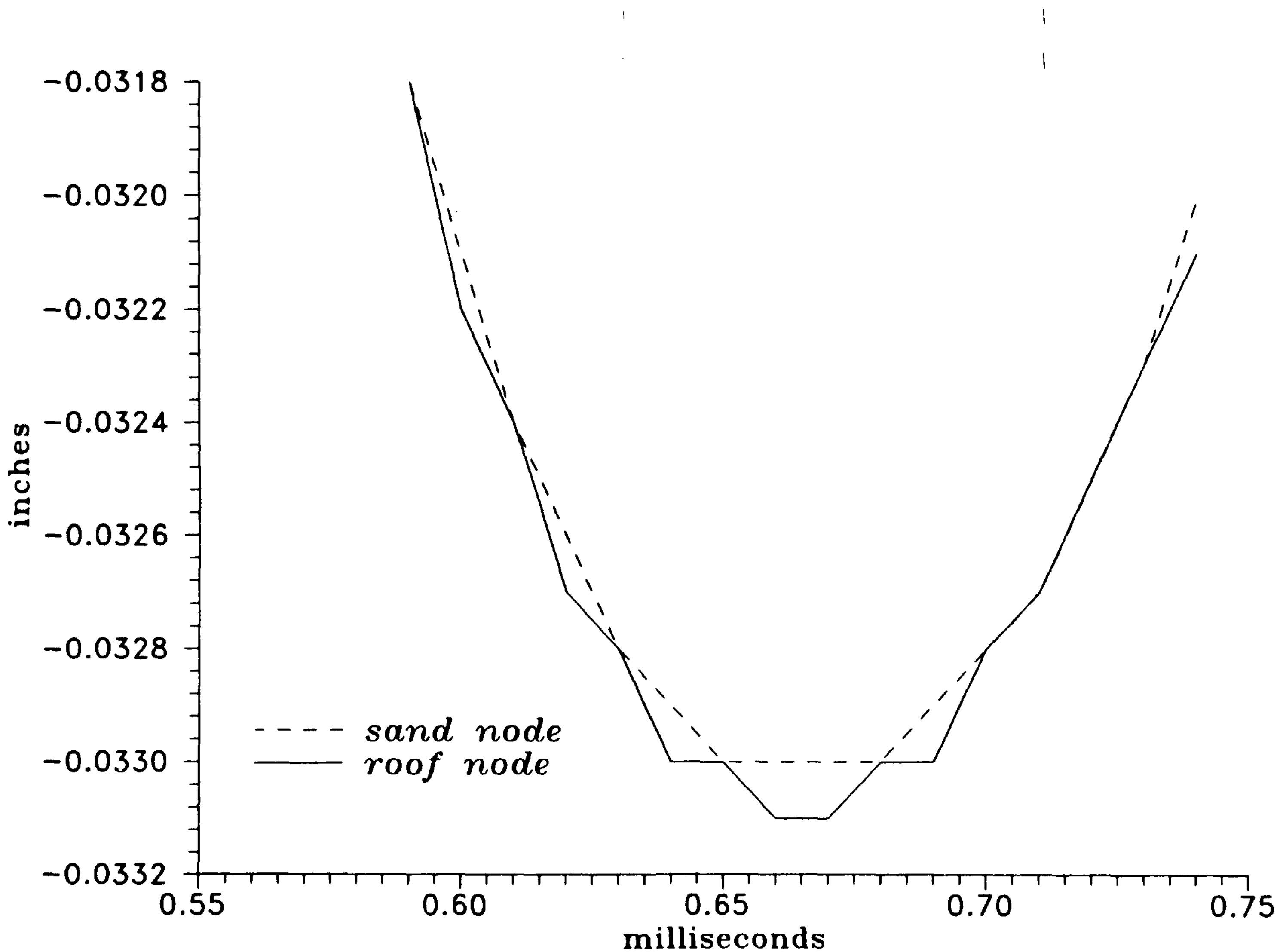

Fig. 3-32: Vertical displacements at the sand-roof interface, 0.5 inch from center (Simulation of test 6, 2nd drop).

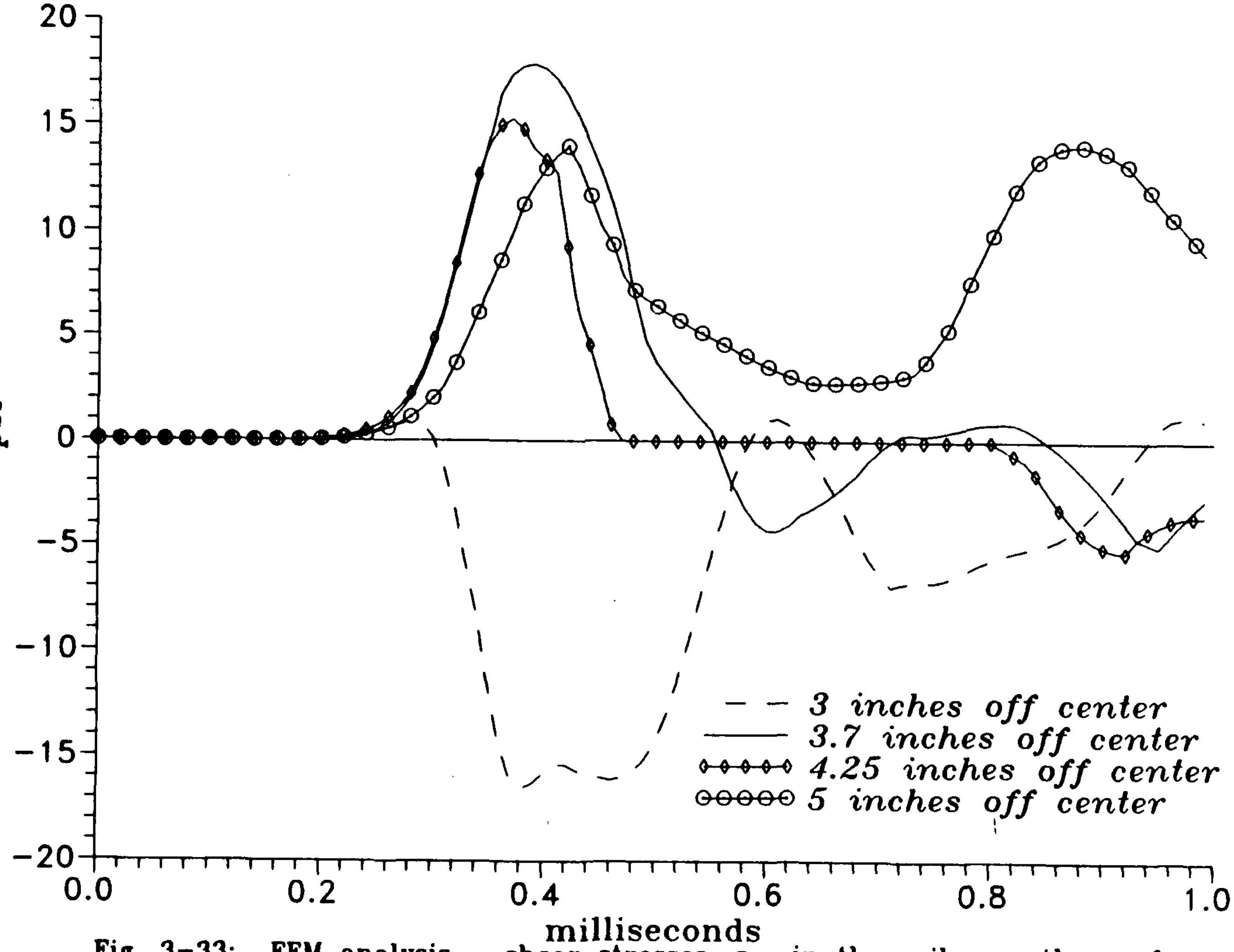

Fig. 3-33: FEM analysis – shear stresses, τ_{ry}, in the soil over the roof. (Plexiglas roof; DOB = 3 inches, H = 25 inches)

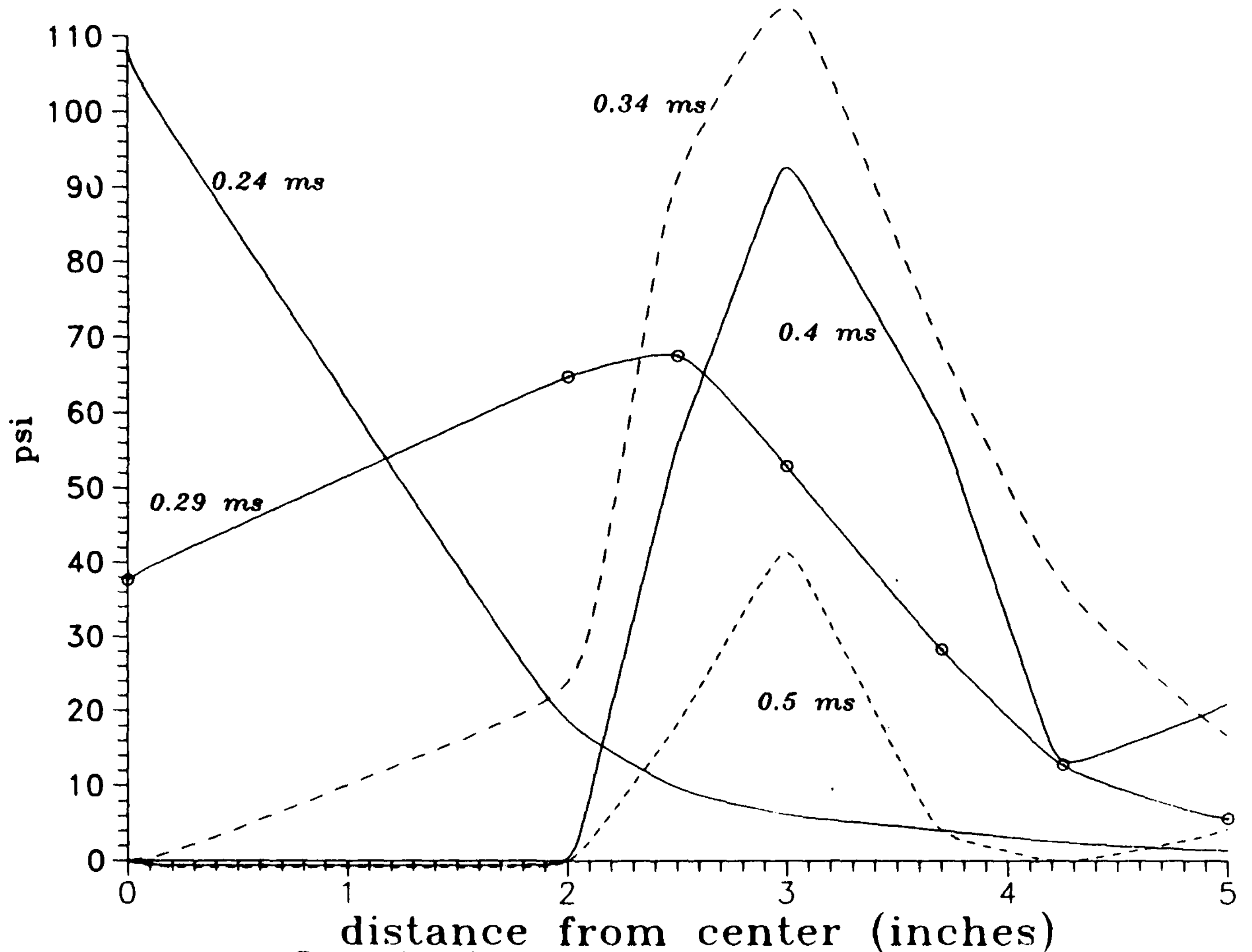

Fig. 3-34: Pressure distribution above the roof level.
(Numerical analysis; Plexgiglas roof; DOB = 3 inches, H = 25 inches)

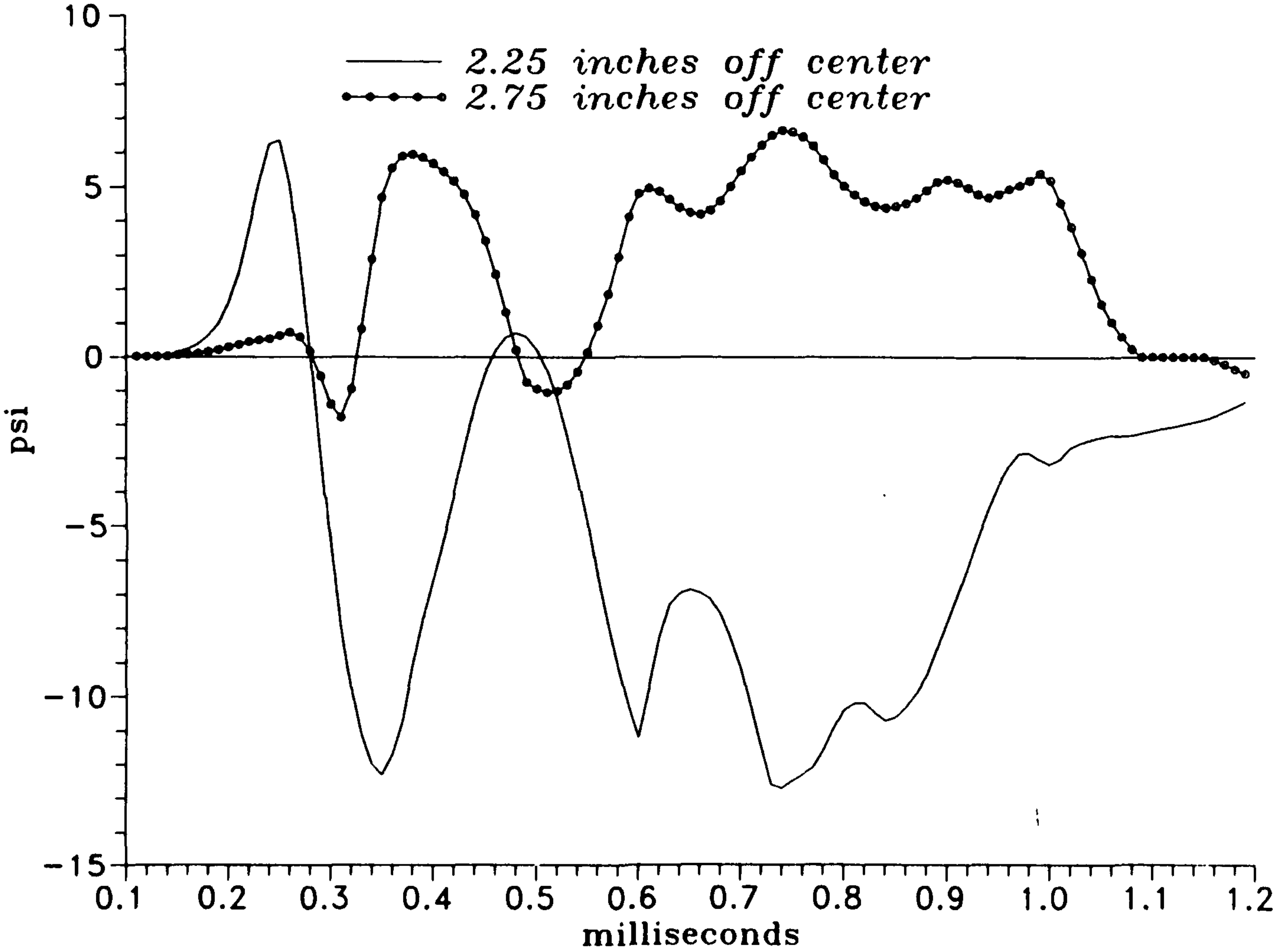

Fig. 3-35: Shear stresses, τ_{ry}, in the soil elements over the roof. (Free sliding at the roof-sand interface; Simulation of test 6, 2^{nd} drop).

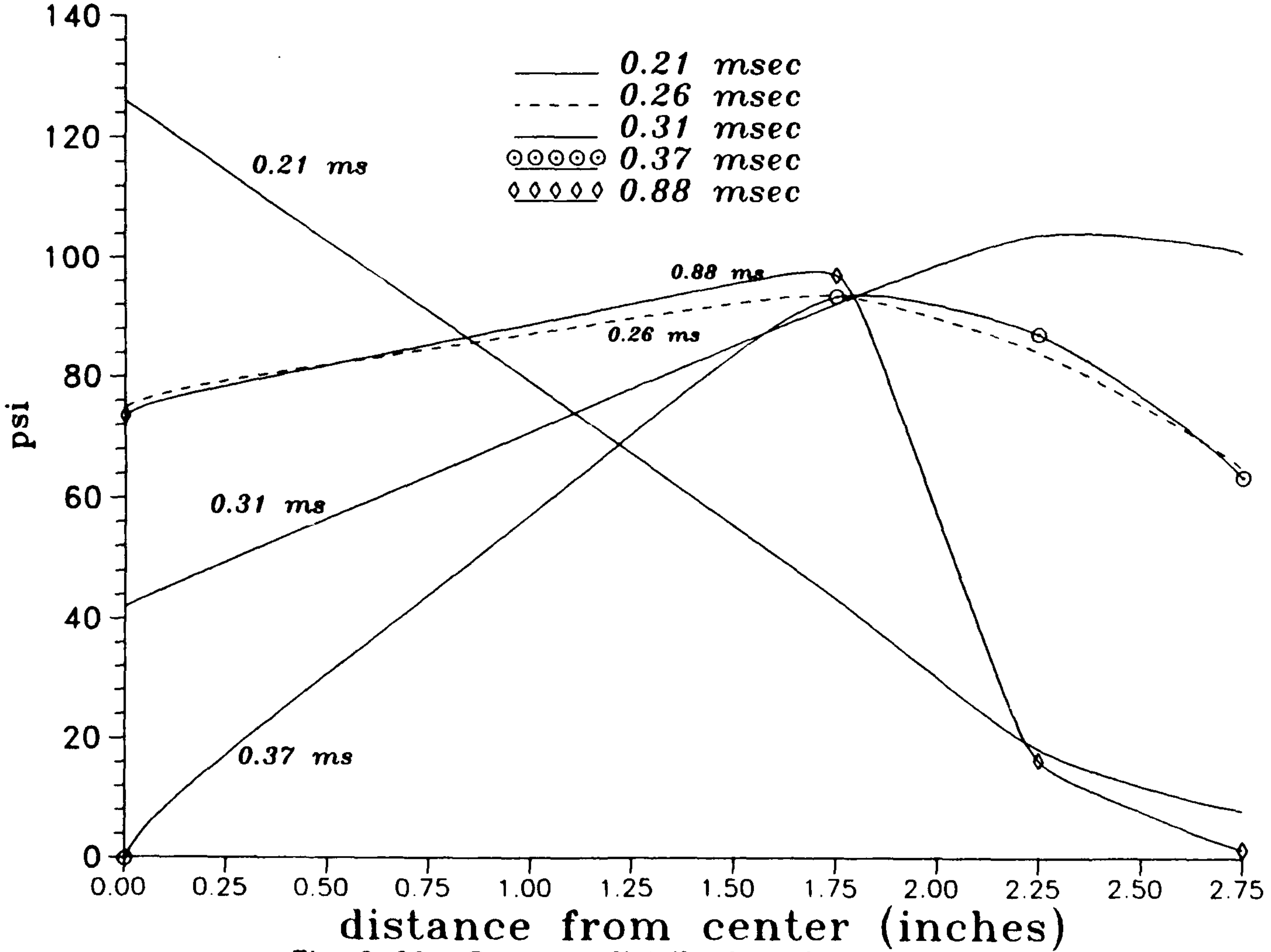

Fig. 3-36: Pressure distribution above the roof level. (Numerical analysis of m.c. roof, test 6, 2nd hit)

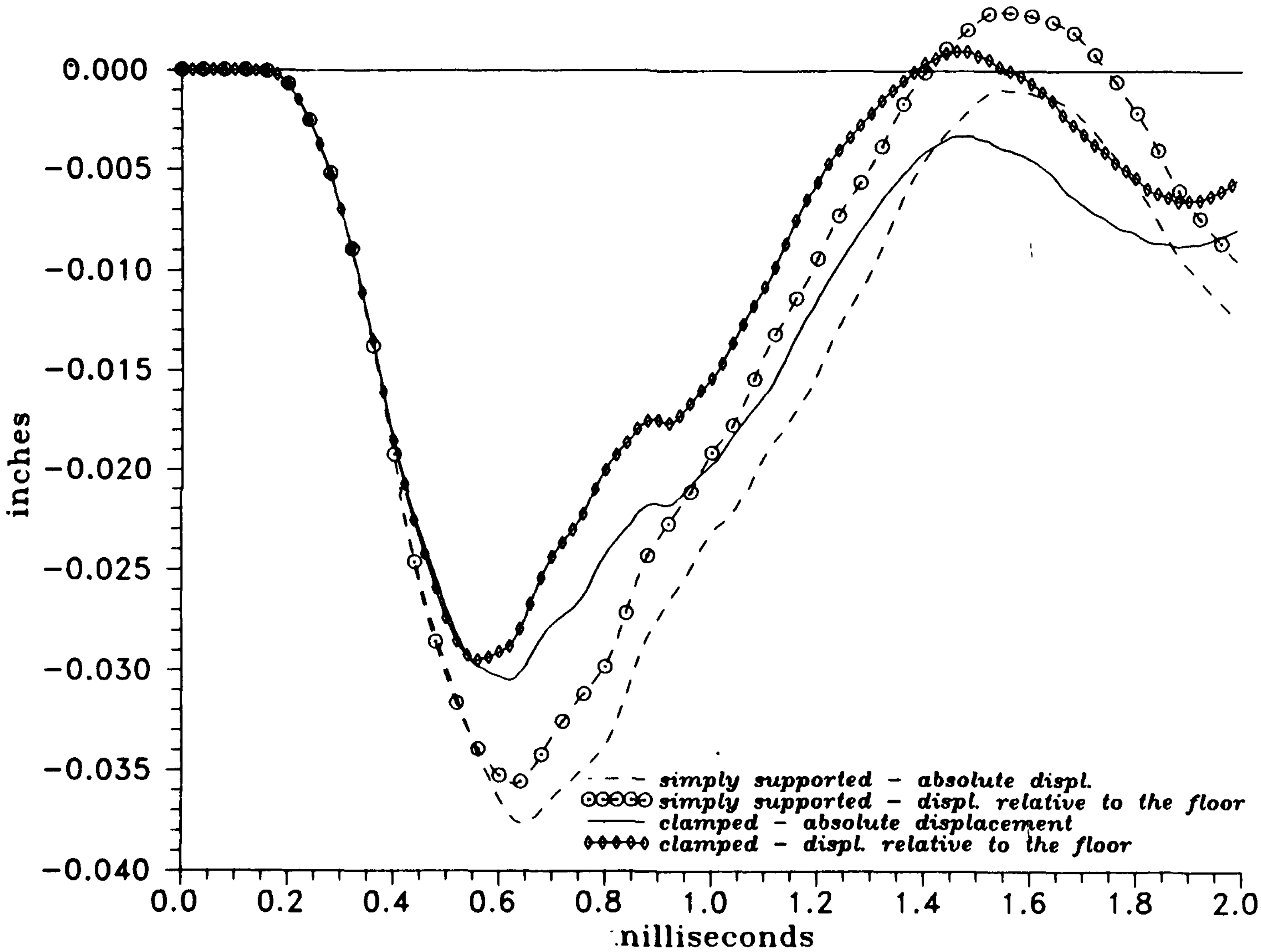

Fig. 3-37: Numerical analysis of a simply supported v.s. clamped micro-concrete roof - center displacement.

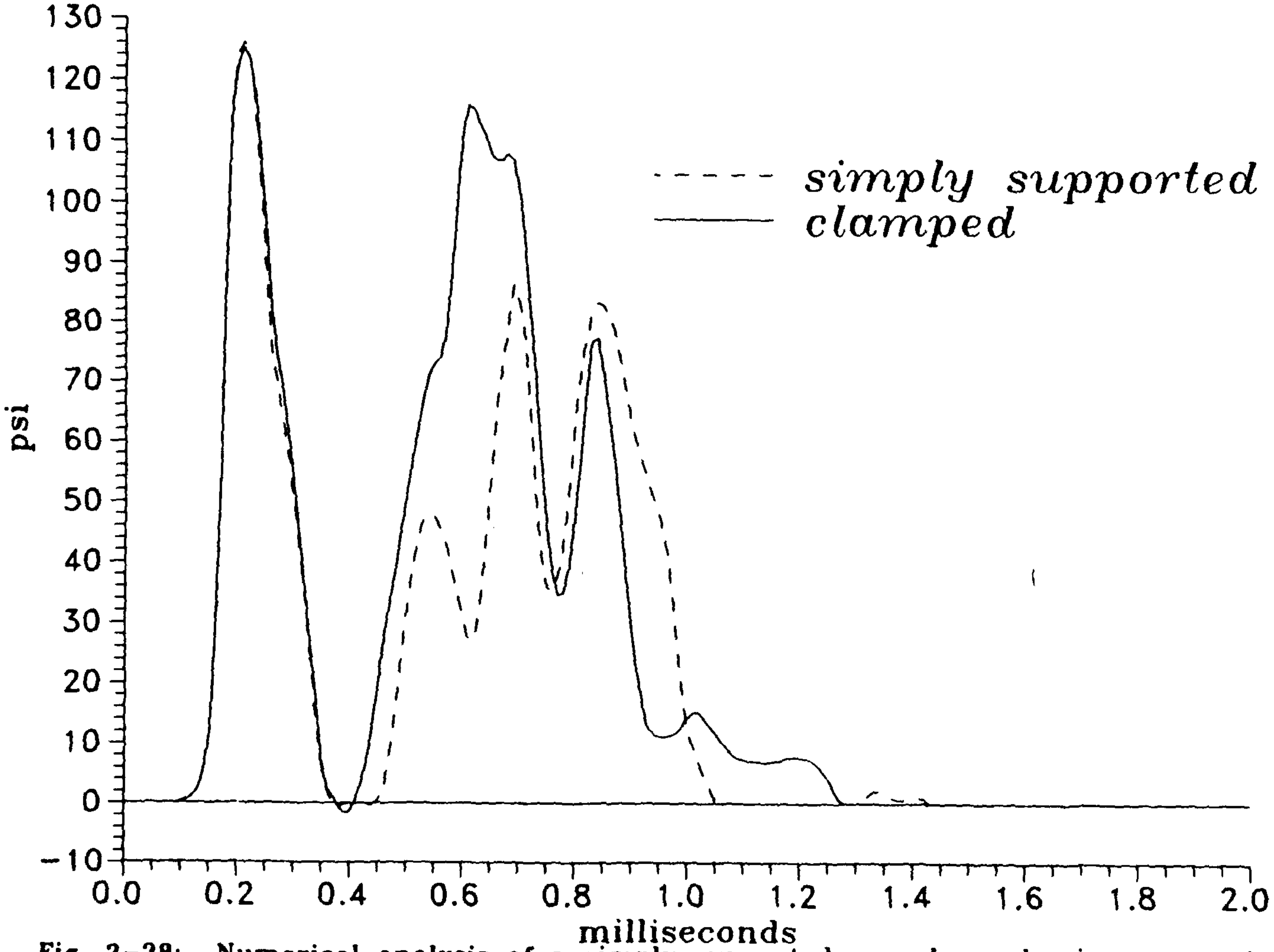

Fig. 3–38: Numerical analysis of a simply supported v.s. clamped micro-concrete roof – vertical pressure at the CENTER of the roof.

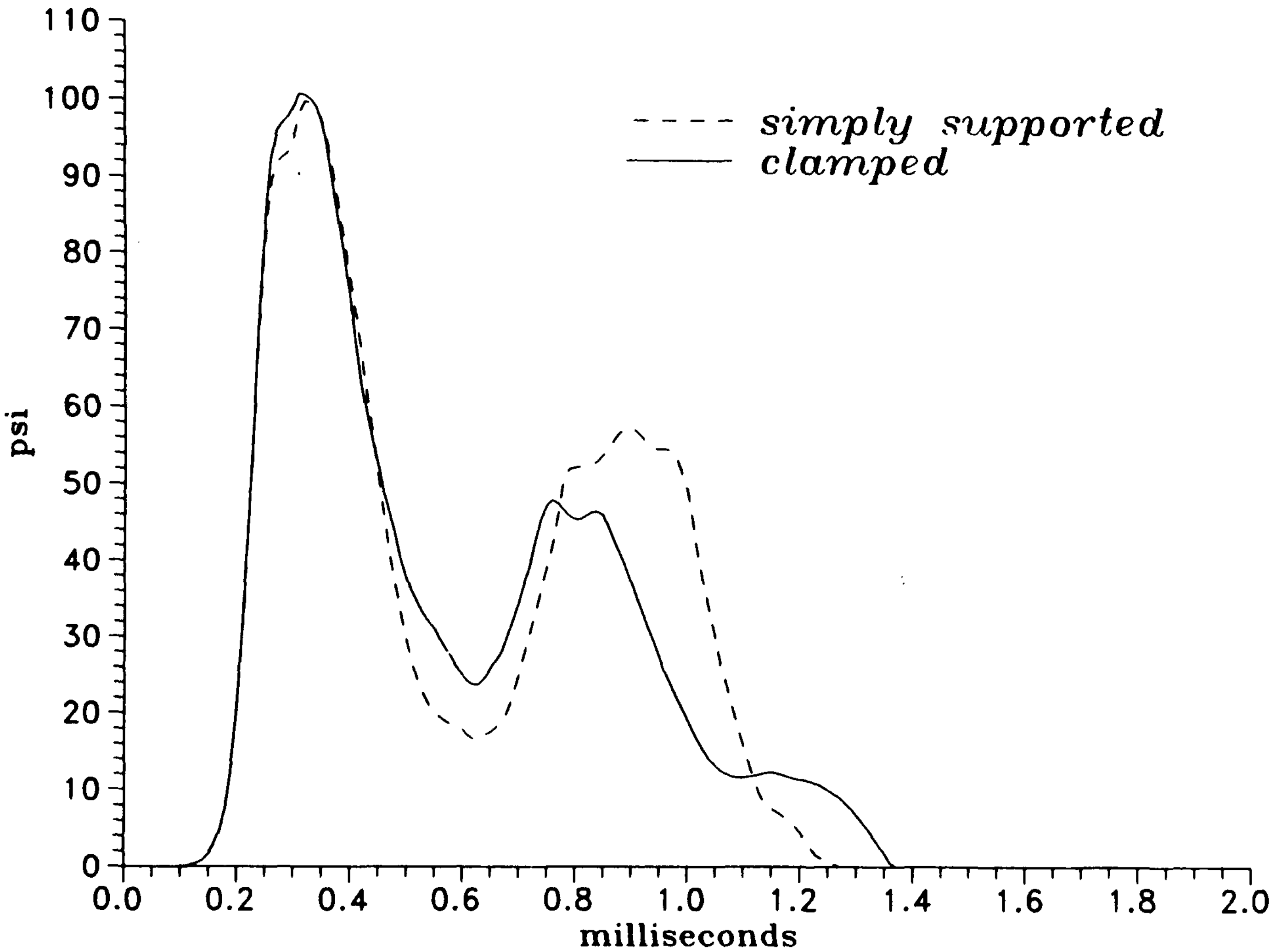

Fig. 3-39: Numerical analysis of a simply supported v.s. clamped micro-concrete roof – vertical pressure over the EDGE of the roof.

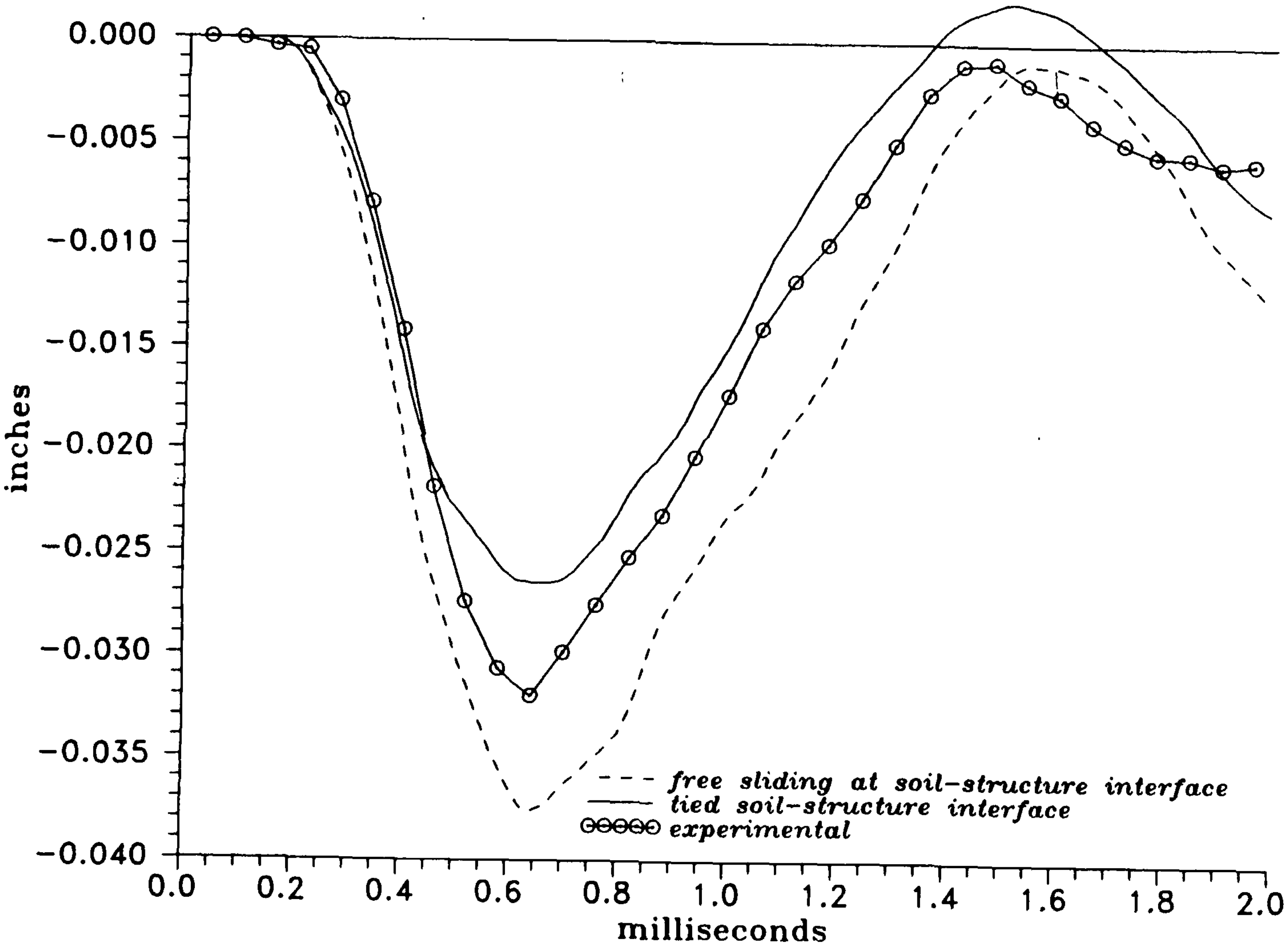

Fig. 3-40: FEM analysis of test 6, (2^{nd} drop) - effect of the soil-structure interface properties on the displacement of the roof center.

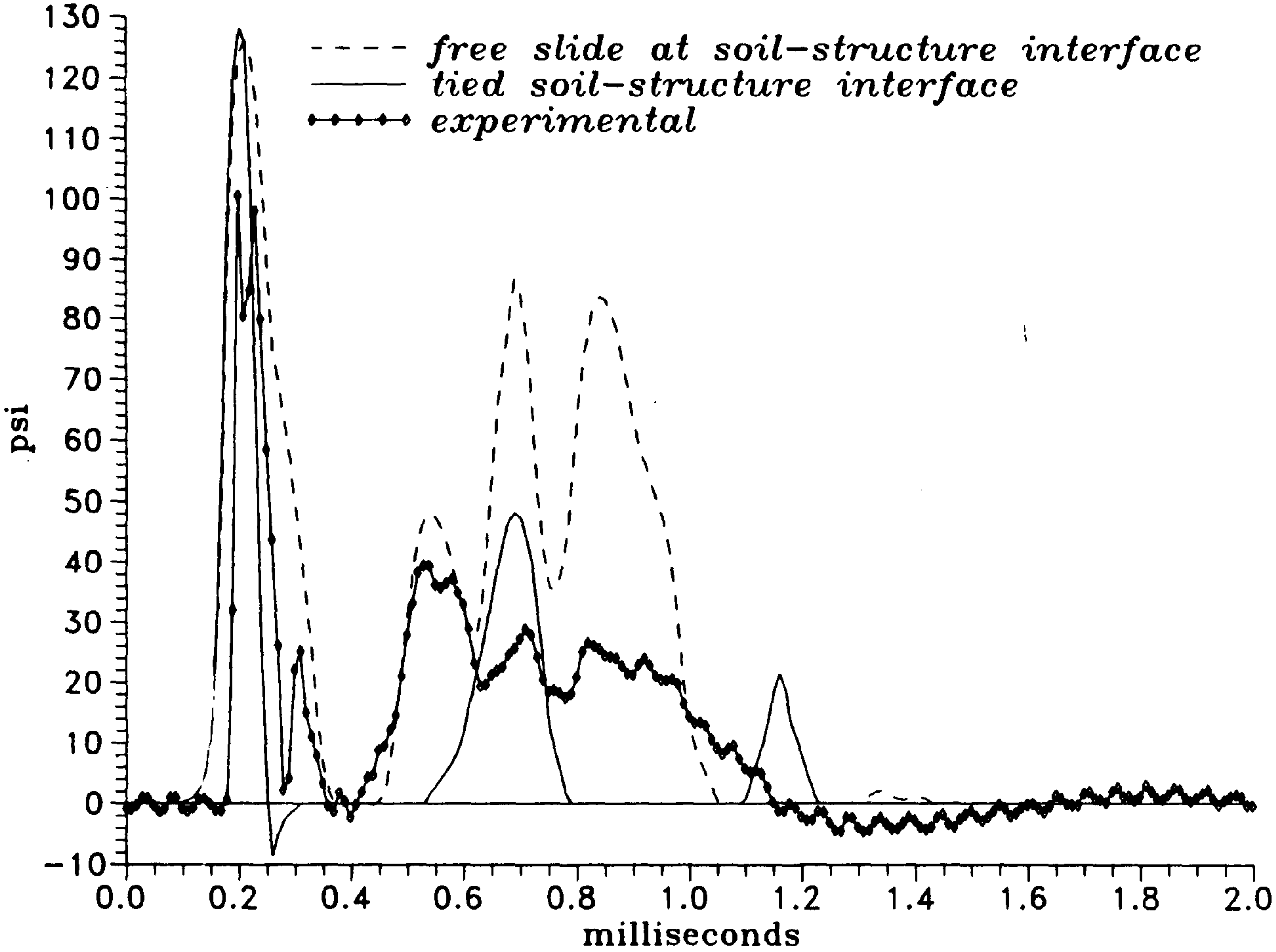

Fig. 3-41: FEM analysis of test 6, (2nd drop) − effect of the soil−structure interface properties on the vertical pressure at the roof center.

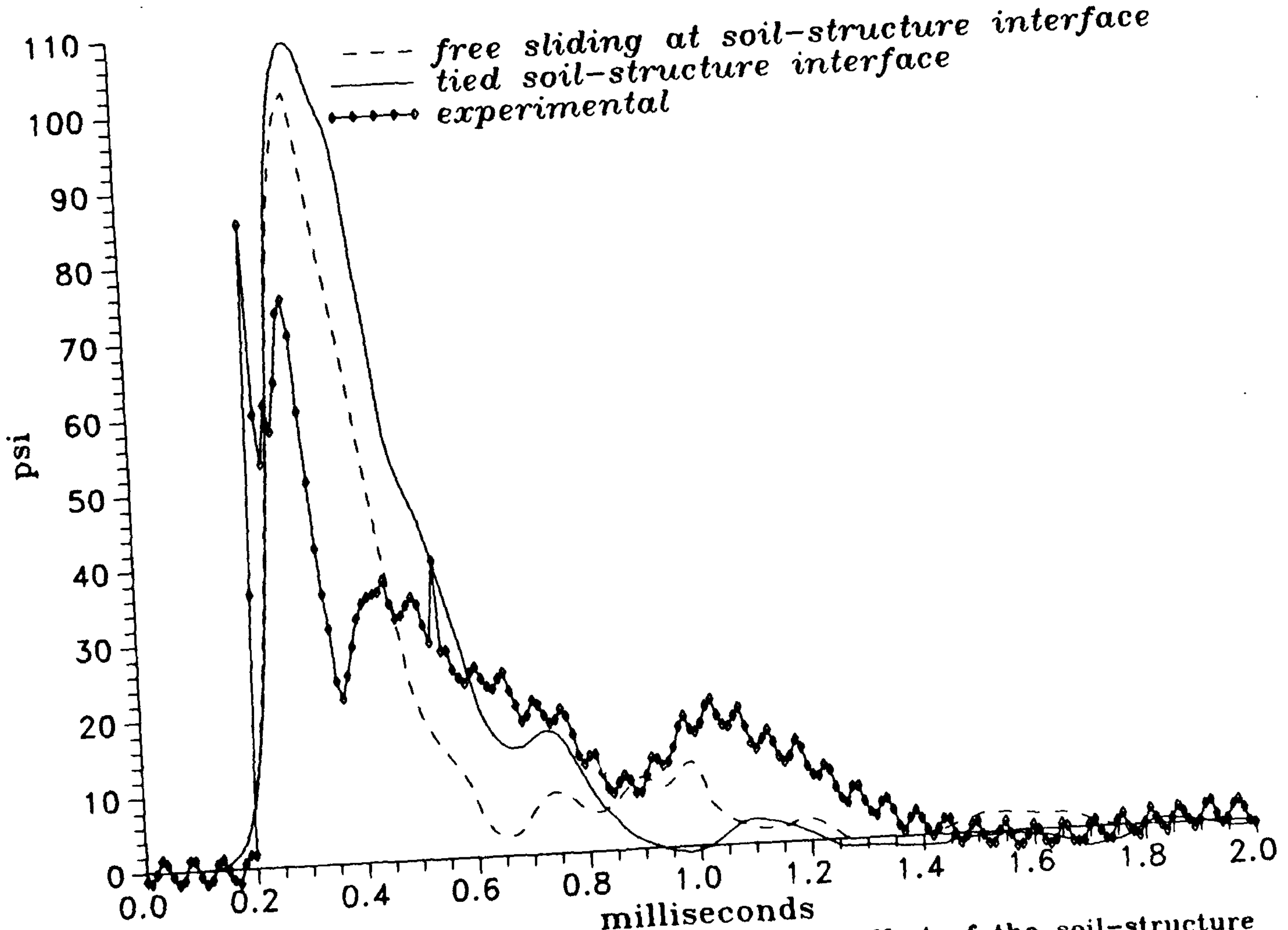

Fig. 3–42: FEM analysis of test 6, (2nd drop) – effect of the soil–structure interface properties on the vertical pressure over the edge of the roof.

CHAPTER 4

SIMULATION AND ANALYSIS OF A LARGER SCALE SYSTEM

The finite element program, which is described in Chapter 3, was employed for the numerical analysis of a soil-embedded structure system of different geometry, larger scale and with higher external load.

4.1 The Reference System and its Numerical Model.

4.1.1 Description of the Soil-Structure System.

For this purpose, an experiment conducted by Kiger, Eagles and Baylot[27] was used as a reference. They performed a series of tests with a massive post-tensioned concrete reaction structure that clamped its roof slab structural elements for rotation as well as lateral displacement and was designed to ensure one way action of the test slabs. The reinforced concrete slabs were 2.9 inches thick, and had a clear span of 24 inches together with a 0.5% tension and compression reinforcement with 0.5 inch cover. Test number 4 of this series was performed with a dynamic external load and sand backfill, and is numerically simulated here. The structure was buried at a shallow DOB equal to half of the roof span (i.e., 12 inches), and subjected to an external high explosive blast simulating a nuclear weapon. The experiment report has the following information for the materials:

1. Concrete was reported to have an average 28-days compressive strength of 6900 psi and modulus of elasticity equal to $4.56 \cdot 10^6$ psi.

2. Reinforcement was made of small-diameter deformed wire, 0.177 inch diameter with an average yield strength of 90200 psi.

3. Backfill of test number 4 was a locally available sand called Reid-Bedford model sand. Its average mass density was $1.53 \cdot 10^{-4}$ lb-sec^2/in^4.

4.1.2 Numerical Modeling of the Soil-Structure System.

4.1.2.1 Geometrical modeling.

Figure 4-1 describes the geometrical modeling of the reference system by a finite element mesh, which represents half of the system by symmetry and assuming plane strain. To simplify the calculations, only the roof slab is modeled, while the supporting structure is represented by lateral and vertical restraint at the structure bottom edge node and a lateral restraint at its upper edge node. Plane continuum elements were used for modeling the sand and the concrete; and bar elements were used to model the reinforcement. The area of the bar element was determined by analysis similar to that described in Chapter 3. Requiring equal force to be taken by the numerical reinforcement model and by the actual reinforcing mesh, leads to an equivalent numerical reinforcement area per bar element, $A_{s,eq}$:

$$A_{s,eq} = \frac{F_{steel}}{f_s} = \frac{A_{s,actual} f_s}{f_s} = \rho \cdot 1'' \cdot d = \frac{0.5}{100} \cdot 1 \cdot 2.44 = 0.012 \frac{in^2}{in} \tag{4.1}$$

4.1.2.2 Material modeling.

In this example the materials which are included in the system, reinforced concrete and sand, are similar to those of the smaller scale system. Therefore, the material law which was used to model the sand and the concrete was the "AFWL Engineering Model", described in the previous chapter. The steel was modeled by a uniaxial stress material law with parameters suitable to the actual steel wires used in the experiment (see section 4.1.1). The parameters used for the "AFWL Engineering Model" are shown in figures 4-2 to 4-5 and are not the same parameters which were used for the small scale system but were evaluated as follows:

1. The load on the system was much higher than the low impact generated by the drop of the impactor steel ball (peak of 3300 psi versus 600 psi, respectively). Therefore, the constitutive relationships in the high stress range of the soil had to be evaluated on the basis of typical stress-strain relationship of granular soils, as suggested by Lambe and Whitman[31] (see figures 4-4 and 4-5): For stresses up to about 2000 psi, the stress-strain curves are concave upward, as the soil undergoes what is called "locking". Starting at about 2000 psi, the stress-strain curve begins to develop a reverse curvature and becomes concave to the strain axis. During this

stage, sand particles fracture and permit tighter packing which again makes the stress-strain curve concave at high stresses and strains. Fracturing of the sand particles becomes important when the stresses exceed 5000 psi.

The initial parameters of the curve are similar to those shown in figure 3-5 for loose Ottawa sand and were based on the arrival time of the pressure wave as reported in the actual test. Poisson's ratio was assumed to be 0.25 (as for the Ottawa sand).

2. The concrete parameters shown in figures 4-2 and 4-3 were based on the same principles at those used for the modeling of the micro-concrete[9,35] with the reported initial Young's modulus of $4.56 \cdot 10^6$ psi. The failure surface (figure 4-3) was based on the reported compressive strength of 6900 psi. Poisson's ratio was assumed to be 0.2.

4.1.2.3 Load modeling.

Because of the nature of the explosive charge used, the load was assumed to be uniformly distributed. The pressure signal, as recorded and reported, was digitized (from Ref. 27) and used as an input at the top surface of the finite element mesh. Figure 4-6 shows the time record of the input pressure.

4.2 Results.

The results of the numerical analysis which was performed with the parameters described in section 4.1.2 are discussed here. They are compared with the experimental records which were reported in Ref. 27 and further analyzed in view of the conclusions drawn from the small scale system experiments (Chapters 2 and 3).

4.2.1 Comparison of the Numerical and Experimental Results.

Figure 4-7 shows the displacement record of the mid-roof. Both the numerical and experimental records indicate failure of the roof slab. The numerical curve is different from the experimental in the time of its initial response and in its maximum deflection. While the numerical analysis shows a mid-point deflection which starts at $t \approx 0.5$ msec, the experimental curve shows no apparent deflection up to about 1 msec later (i.e. $t \sim 1.5$ msec). Both reach a 1 inch deflection within about 2.5 msec (from the time deflection started), but while the experimental gage measured a maximum deflection of about 3 inches, the numerical record showed a maximum displacement of about 1 inch. These differences should be judged in view of the notes which were reported (Ref. 27): The gage which was used for the displacement measurements was reported to be insensitive to deflections occurring in the millisecond range which explains the difference in the response time between the numerical and the experimental record (see also in Appendix B a similar observation about the LVDT gage in the small scale system). Furthermore, it was reported that in the experiment the gage probe bent and the gage failed. Moreover, failure at very large displacements is not modelled well in the analysis, as noted in section 3.2.5. Direct loading of a similar slab was tested prior to the dynamic experiment[27] and reported to cause failure at a center displacement of about 0.25 in. The load-deflection curve which was reported (insert in figure 4-7) was obtained under static loading. This indicates that although the numerical model may not predict the actual total displacement at failure, it shows a deflection higher than 0.25 in, accompanied by yielding of the steel elements, which implies flexural damage ($\epsilon_{steel} > \epsilon_{yield}$ at t=0.78 msec and at t=2.5 msec at the support and the center, respectively).

The experimental normal pressure at the soil-structure interface is compared to the vertical stress in the elements above the roof in figures 4-8 to 4-11. The pressure gage which was located at the roof center showed an initial spike in front of the main peak of the pressure signal (not shown in figure 4-8) and the gage was reportedly broken very early in the test. Thus the earlier numerical arrival time at the center is reasonable, and its peak agrees well with the experimental one. Over the rest of the slab roof there is reasonably good agreement between the numerical and the experimental pressure records during the main first peak of the loading (figures 4-9, 4-10, and 4-11). The relatively higher secondary peak in the numerical result may be due to the difference between the actual supporting structure and its numerical modeling. While the actual structure was embedded in the backfill and probably underwent some rigid body displacement (not recorded in the experiment), it was modelled in the finite element mesh by a rigid support (figure 4-1). Hence, possible later time displacement of the whole structure might have caused arching in the sand above it which reduced the total loading over the supports of the deflecting structure. In the model, however, such displacement was not possible, therefore the higher vertical pressure over the rigid support during 1.5 msec<t<3 msec.

4.2.2 Discussion.

As in the case of the small scale system, the experimental results are limited to the number and capability of the measuring equipment. The numerical finite element analysis, after careful calibration, can provide further information usually difficult to obtain in the experiment.

Figure 4-12 shows the vertical transverse stresses across the mid-section of the roof together with the soil vertical pressure above it. While at the interface the vertical stress is similar to the soil pressure, it drops to a minimum level at the bottom of the slab where the natural boundary condition requires zero normal pressure. This is similar to the numerical results of the small scale system (see also 3.3.1). At t~0.6 msec the roof center starts to gain velocity (figure 4-13) and the pressure in the soil above it starts to drop. This pressure-velocity early time dependency was observed also in the small scale system (Chapters 2 and 3) and seems to dictate, together with the free field pressure level, the subsequent total response of the roof.

The numerical stress distribution over the roof is plotted in figure 4-14. It is interesting to see that the initial pressure peaks uniformly over the entire roof while it is lower in the soil adjacent to the roof (t=0.7 msec in figure 4-14 and t=0.65 msec in figure 4-15). Then, within only 0.1 msec the normal pressure drops sharply over the roof center, while the drop over the support (located 12 inches from the center) is much milder, and in fact remains higher than the free field level in the soil adjacent to the structure (at a distance of 15 inches from the center in figure 4-14 and at t~1 msec in figure 4-15). The initial increase of the pressure over the roof is typical of a rigid boundary effect on an incident pressure wave. Although the pressure dropped rapidly, this initial increase of the pressure was not observed in the small scale system, and the difference between the initial response of the two systems can be explained by the difference in the external load. The high explosive charge in the larger scale experiment generated a higher level of pressure than the small scale system and also had a shorter rise time to its peak. Therefore, while the initial load level in the small scale system was still relatively low when the structure began to respond, it was significantly higher in the larger scale system.

In spite of this difference, the rest of the response resembles that of the small scale system. This is demonstrated in figure 4-15 where the numerical results for the pressure and motion of the roof were plotted with the experimentally reported free field pressure (assumed uniformly distributed). Points "A" and "B", which were defined by the observations of the small scale system results (Chapter 2, section 2.4), are also identified here: As the velocity of the roof center develops, the center load decreases and keeps dropping while the pressure over the support increases at t=0.8 msec (point "B") above the reference free field level, indicating the development of arching. More evidence for this mechanism is shown in figure 4-15, where the shear stresses in the soil above the structure are plotted. Similar to the results of the small scale system, the arching action is indicated here by the development of relatively high shear stresses in the soil element over the supports (see also section 3.3.3).

The development of arching in this case, at t≈1 msec, occurred when cracking had already developed near the support and started to develop at the center (center deflection of ~0.2 in in figure 4-7), and is another example of the conclusions that can be drawn from the small scale experiment (Chapter 2) that the early-time response in a soil-embedded structure systems is dominant. The zero to peak portion of the free field incident wave at the structure level hits the structure, and is even amplified until a tension wave is reflected from the bottom free surface of the structural element (within about 0.01 to 0.7 msec in concrete slabs up to 100 in thick). If the structure can sustain this portion of the load, then the rest of the mechanisms which are involved in the system are important for further release of the load off the structure, or maintaining a mild degree of damage in a worse case.

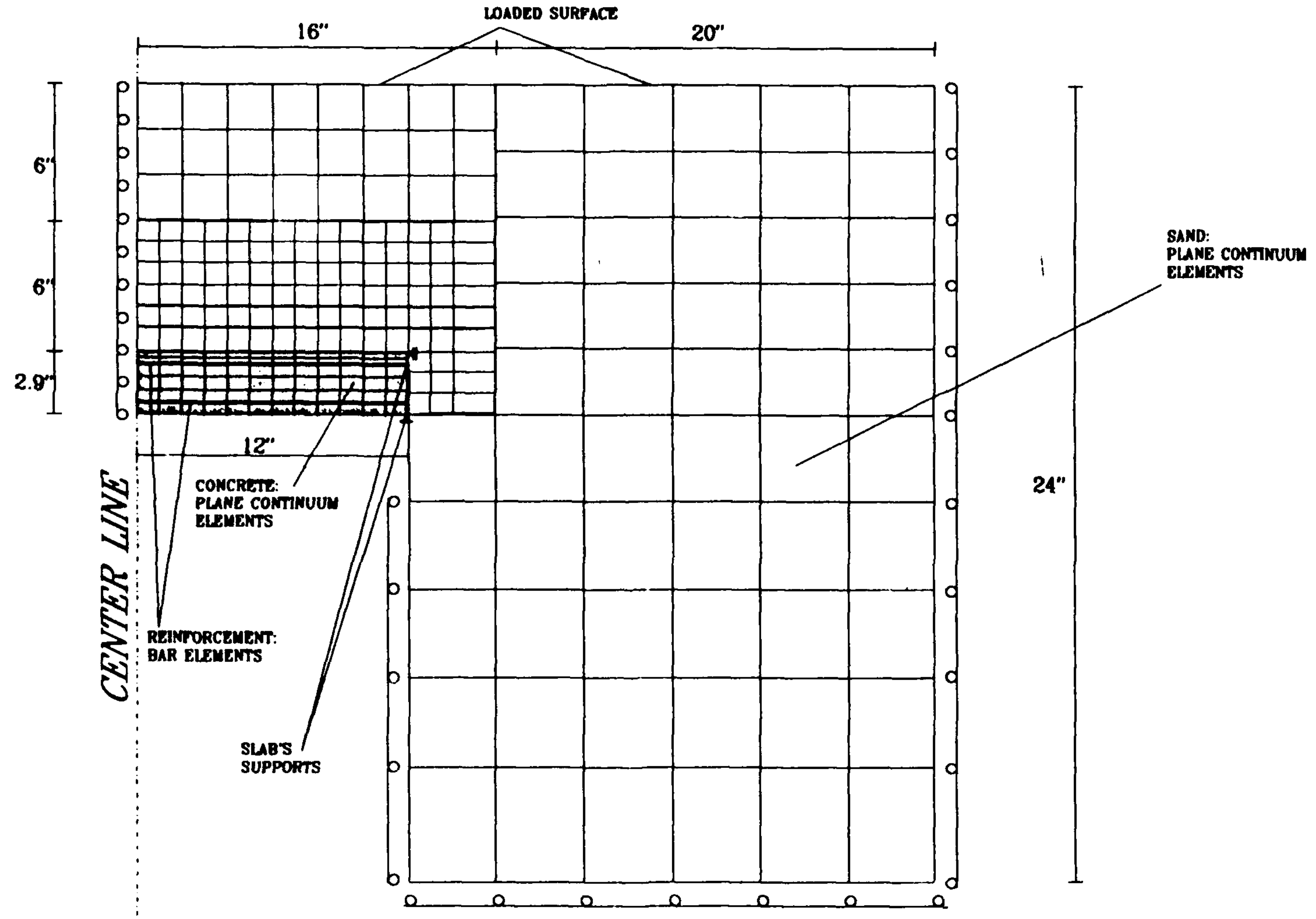
LOADED SURFACE
16"
20"
6"
6"
2.9"
12"
24"
SAND:
PLANE CONTINUUM
ELEMENTS
CONCRETE:
PLANE CONTINUUM
ELEMENTS
REINFORCEMENT:
BAR ELEMENTS
SLAB'S
SUPPORTS
CENTER LINE

Fig. 4-1: Finite element mesh for the numerical modeling of the test which was performed by Kiger, Eagles, and Baylot.[27]

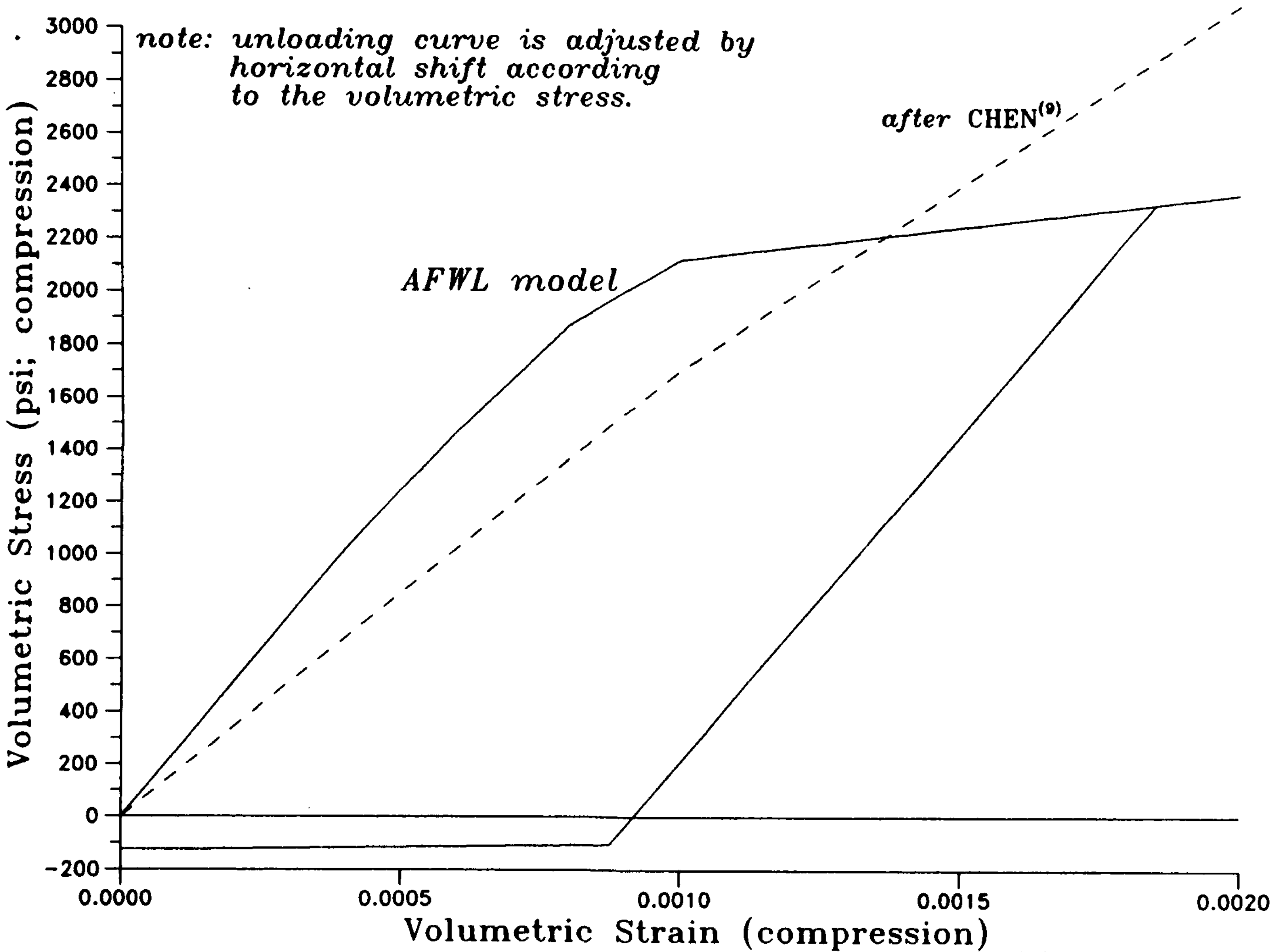

Fig. 4-2: Numerical modeling of a larger scale test[27] – Loading and unloading curves of concrete.

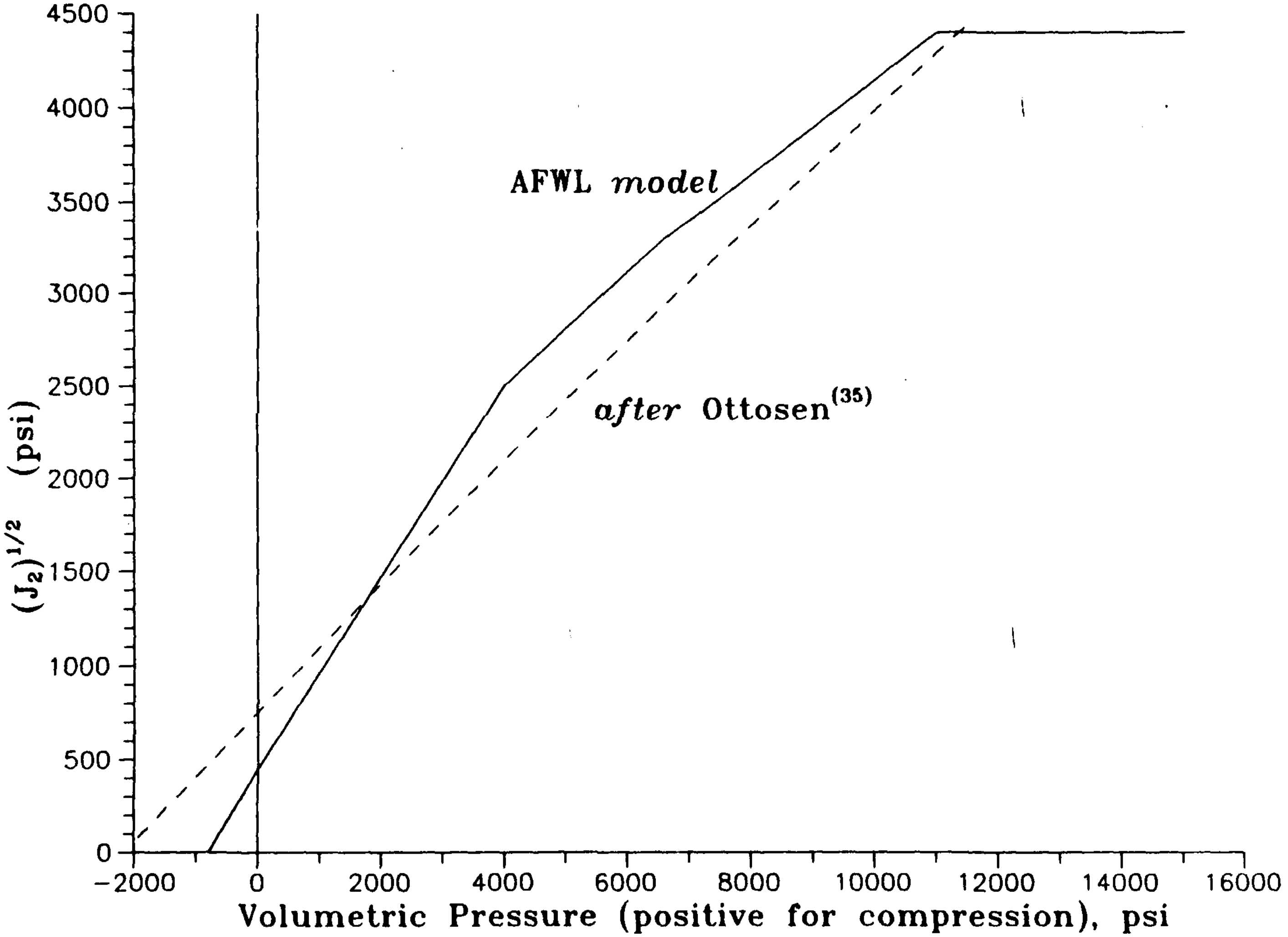

Fig. 4−3: Numerical modeling of a larger scale test[27] − Yield surface of concrete.

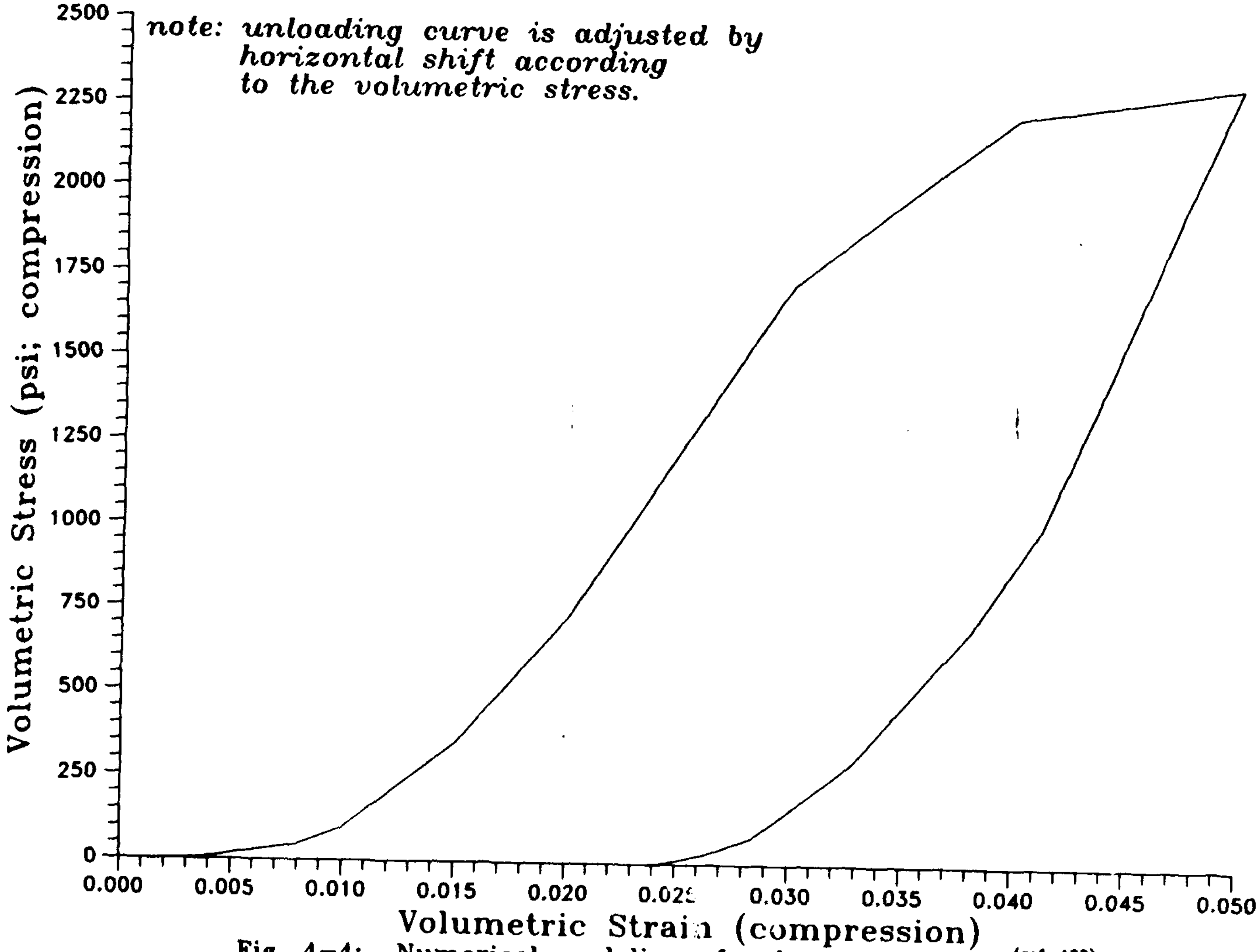

note: unloading curve is adjusted by horizontal shift according to the volumetric stress.

Fig. 4-4: Numerical modeling of a larger scale test(ref. 100) – Loading and unloading curves of the sand.

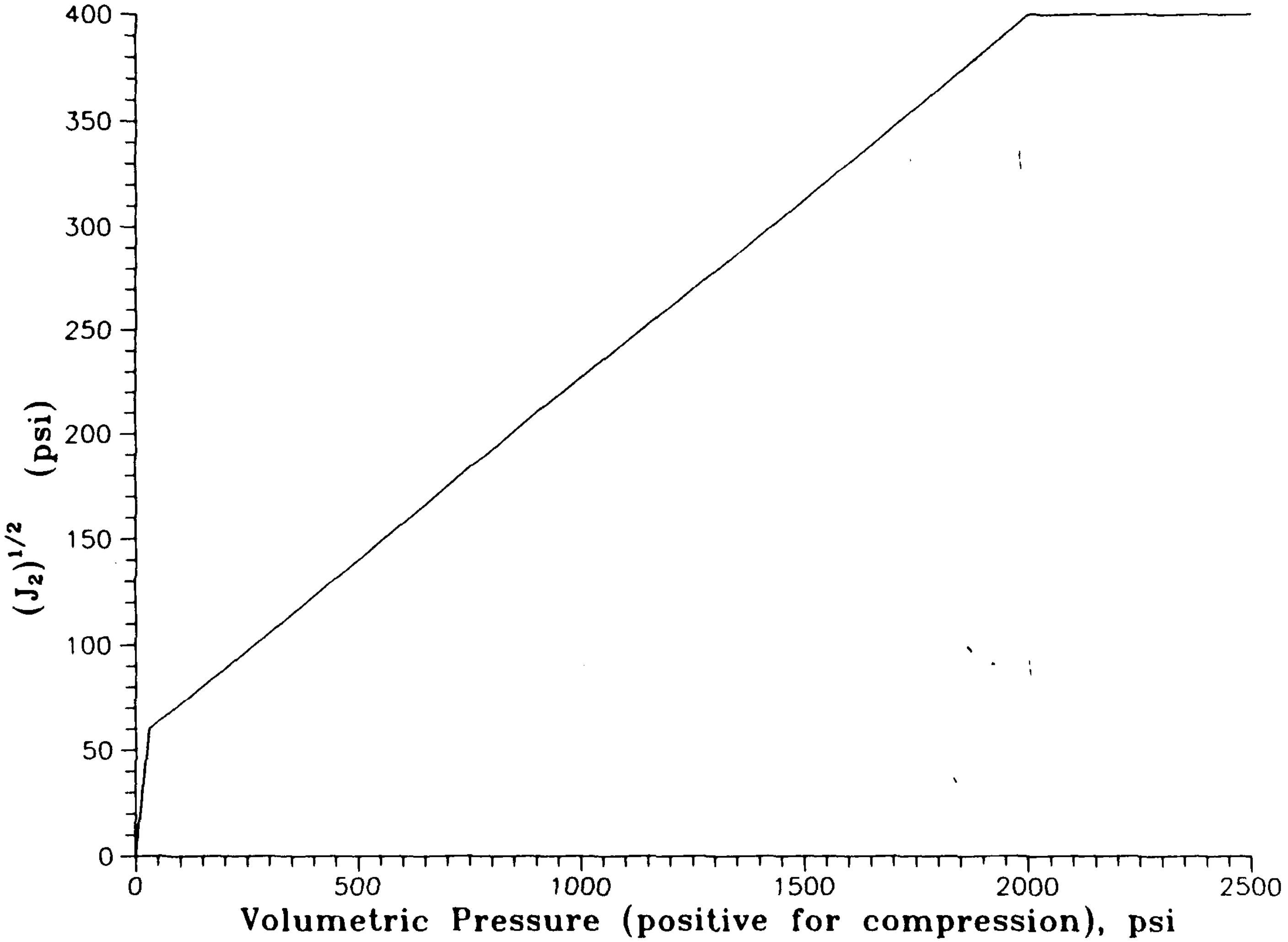

Fig. 4-5: Numerical modeling of a larger scale test[ref. 100] – Yield surface of the sand.

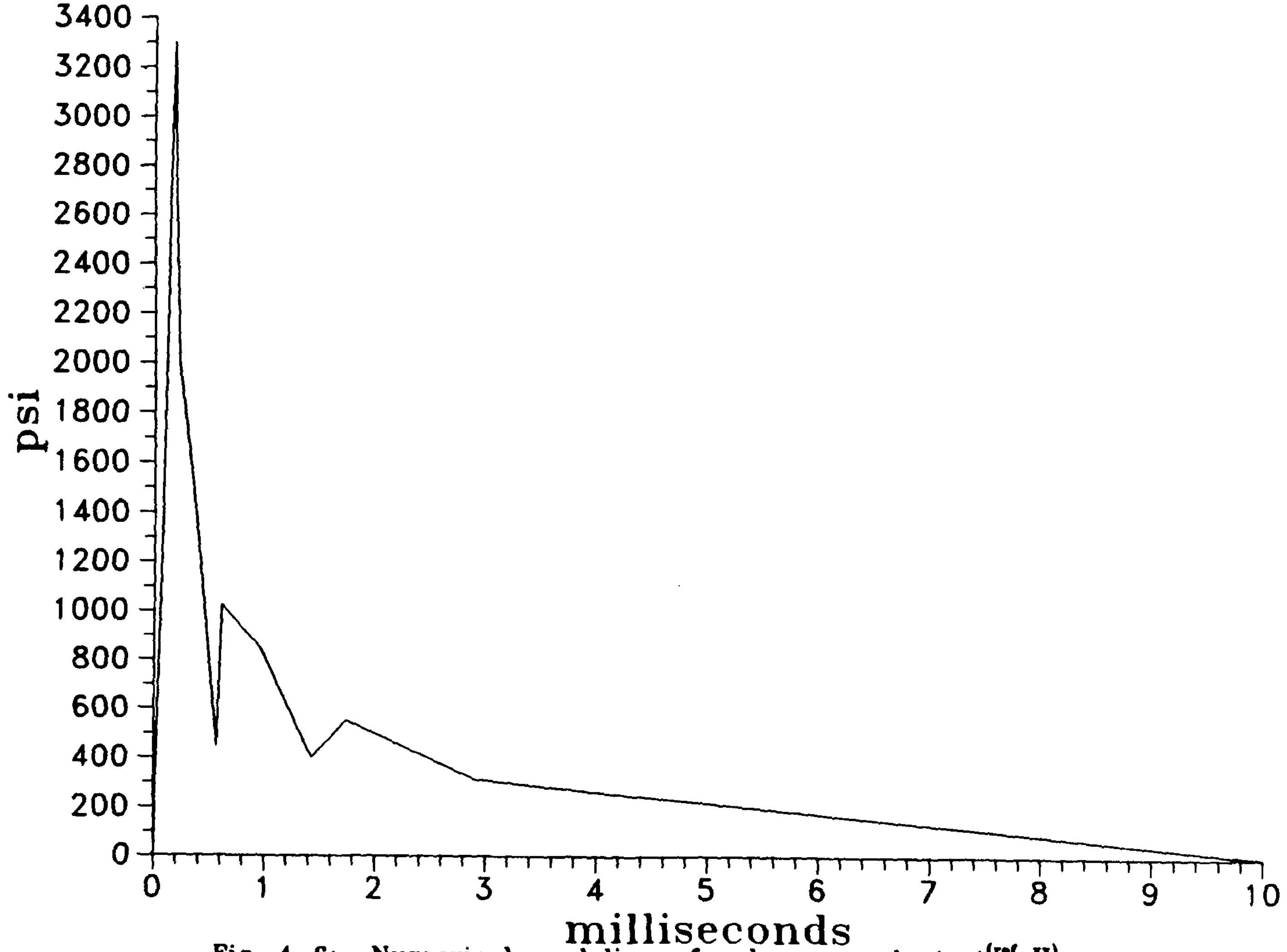

Fig. 4–6: Numerical modeling of a larger scale test(ref. xx) –
Input pressure at the surface (assumed uniformly distributed).

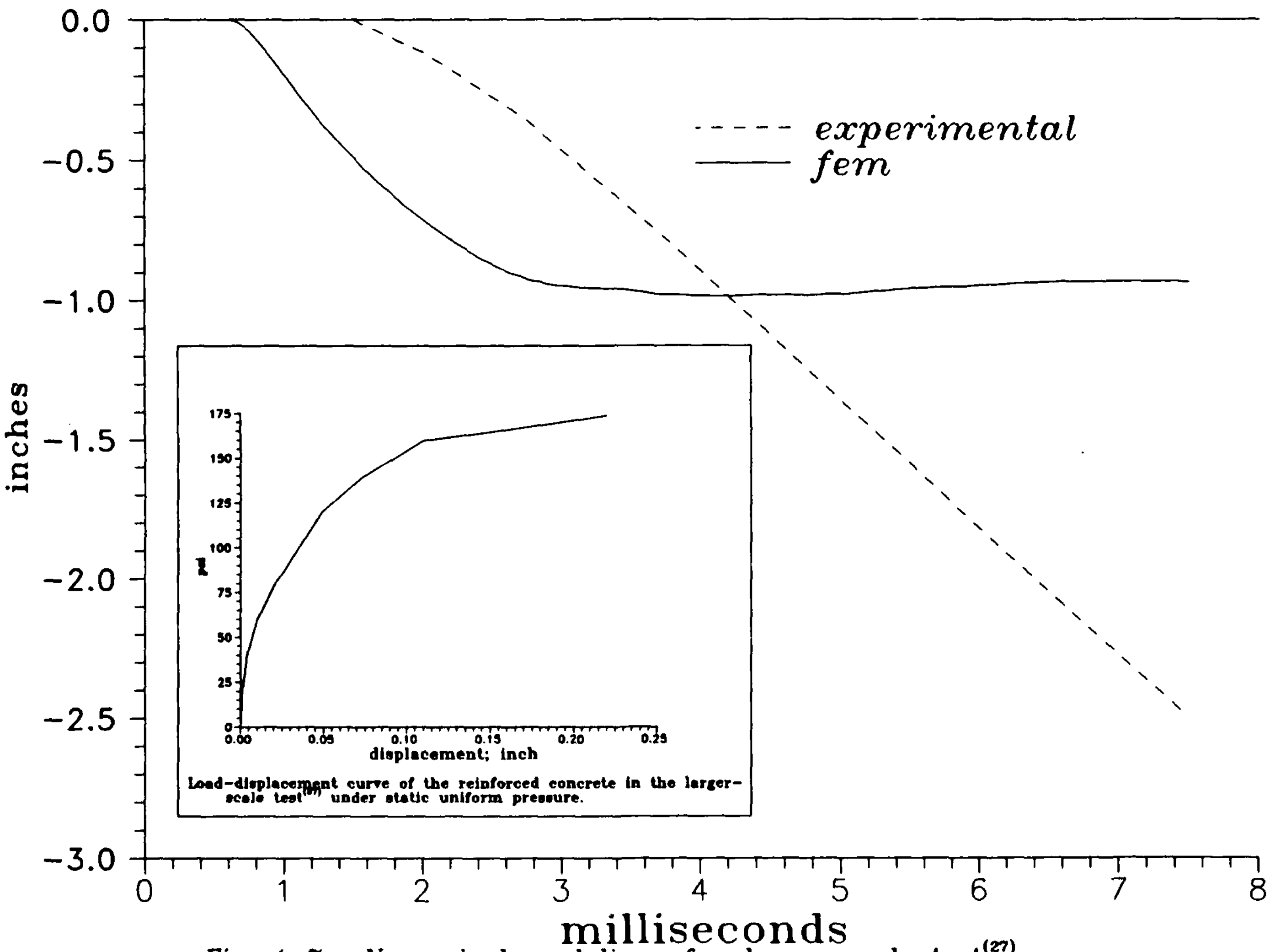

Fig. 4-7: Numerical modeling of a larger scale test(27) – Displacement of the roof center.

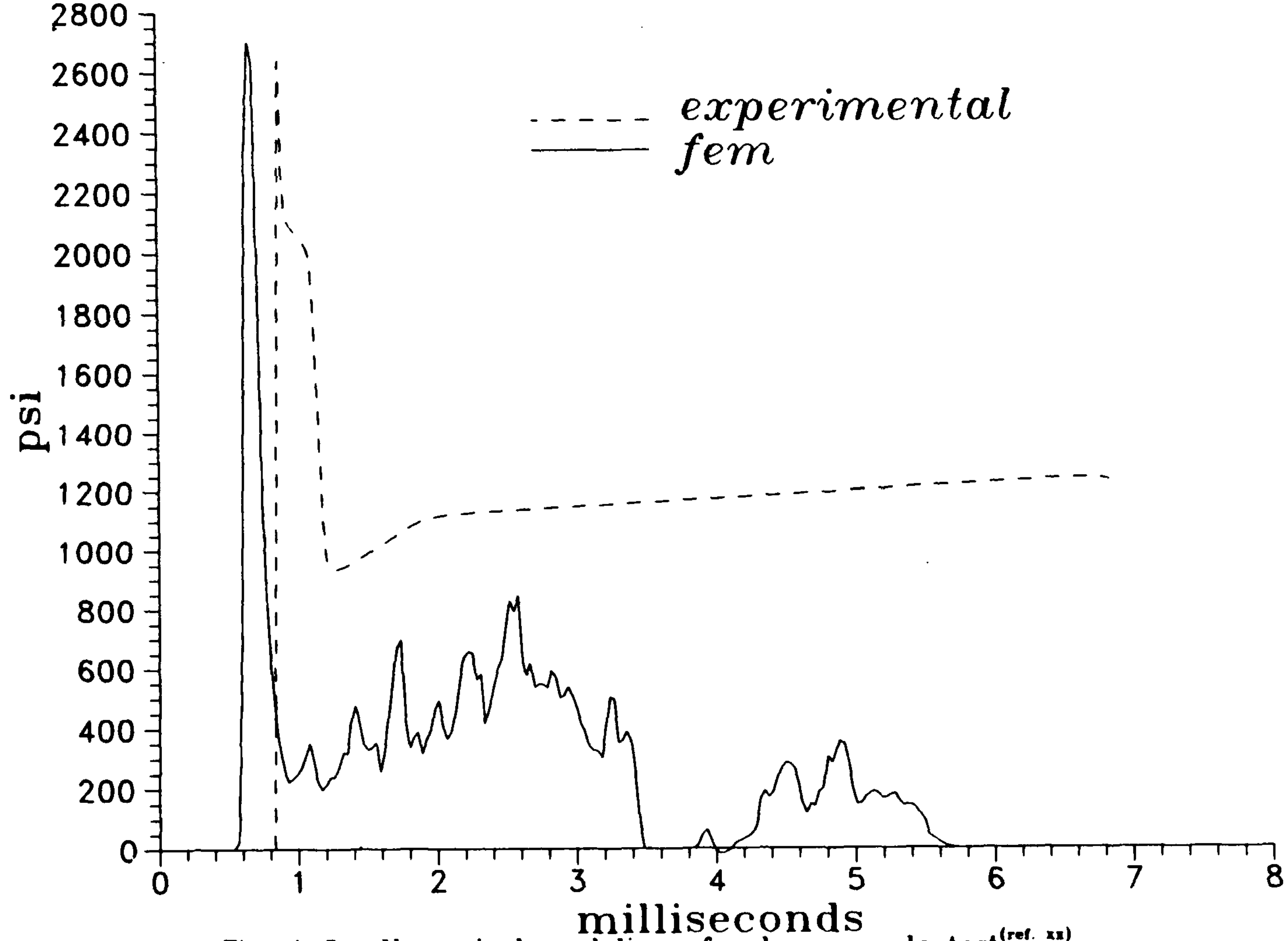

Fig. 4-8: Numerical modeling of a larger scale test[ref. xx] – Pressure at the center.

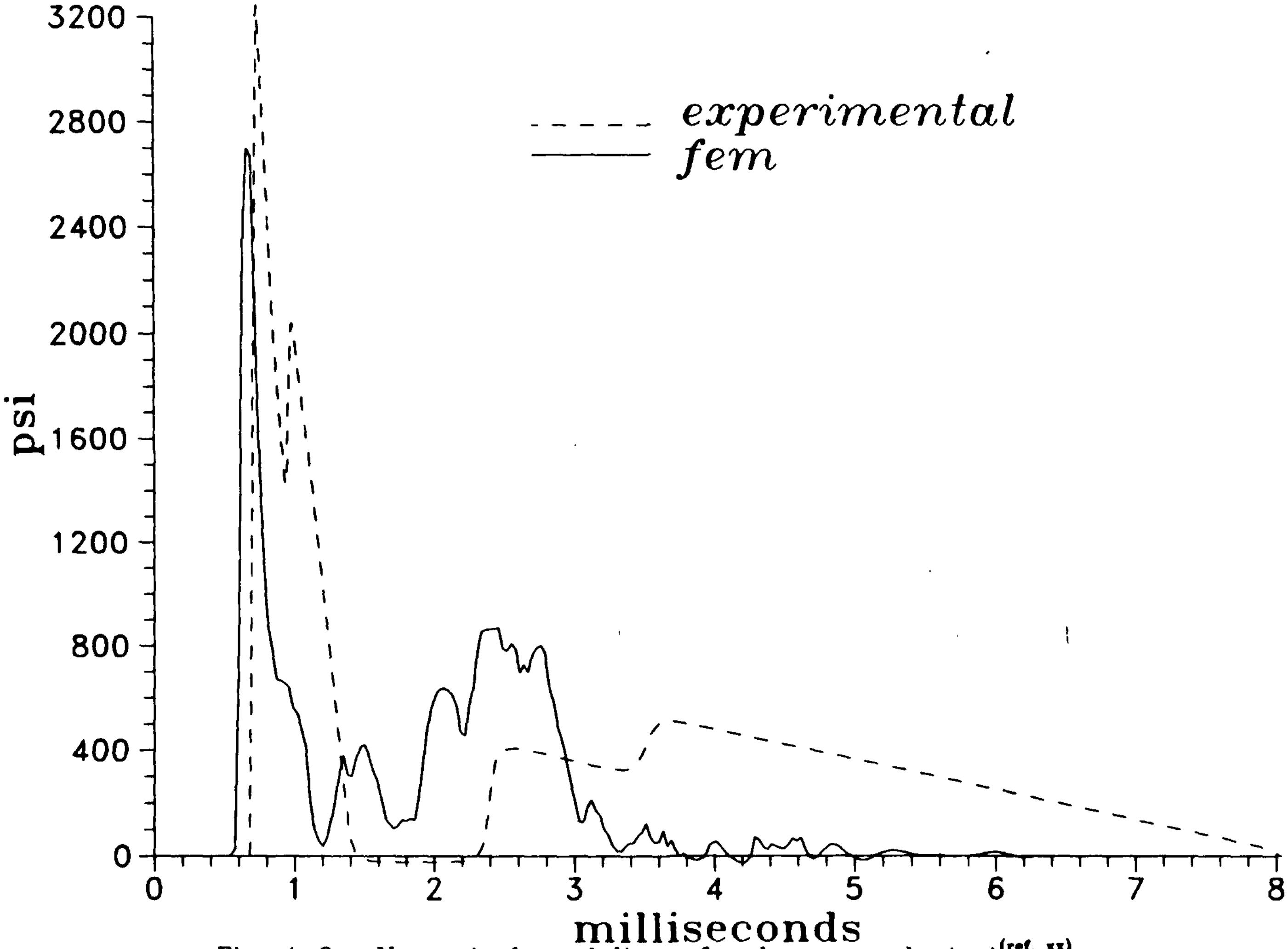

Fig. 4-9: Numerical modeling of a larger scale test(ref. xx) – Pressure over the roof 7 inches from the center.

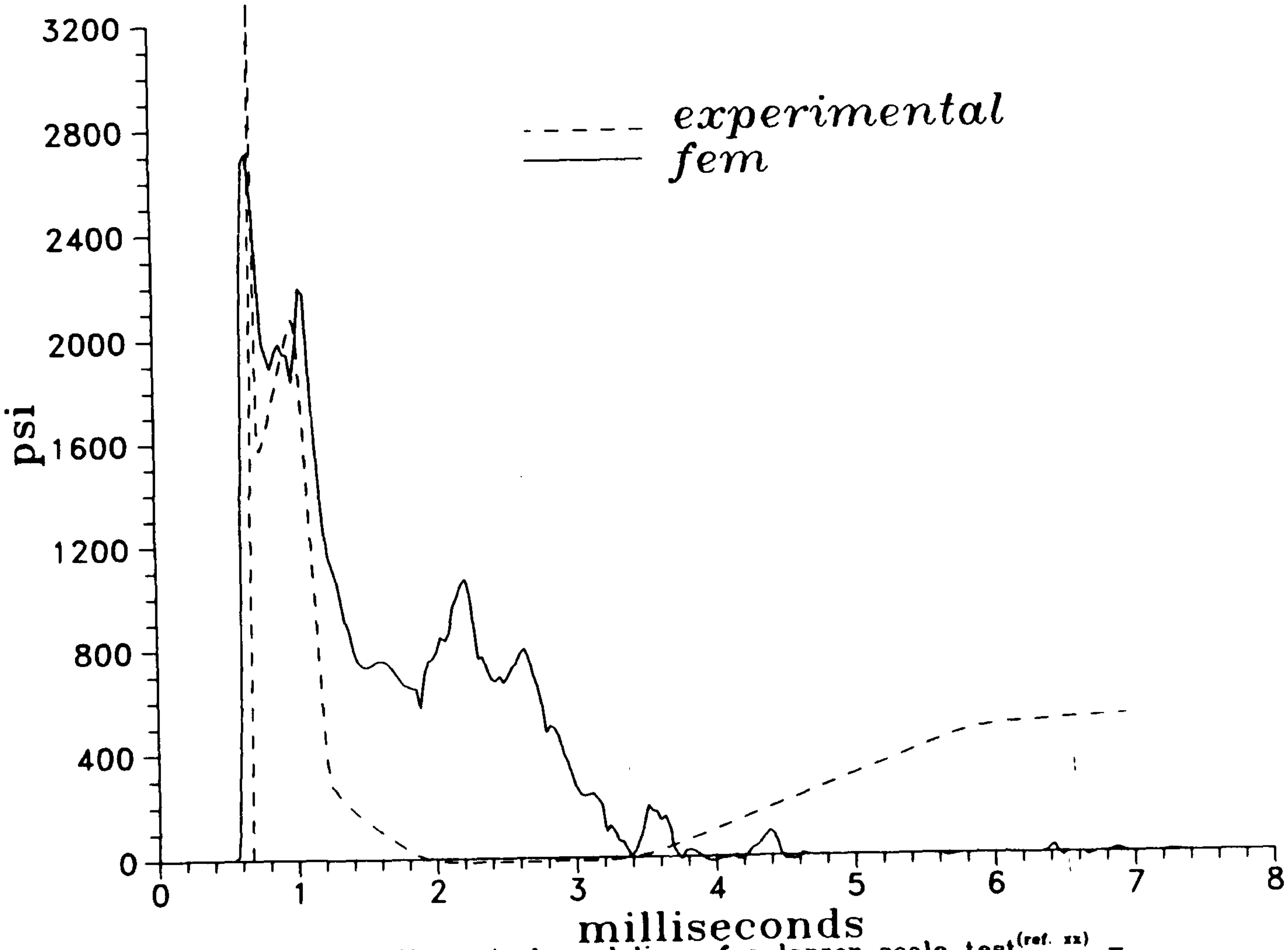

Fig. 4-10: Numerical modeling of a larger scale test(ref. xx) – Pressure over the roof 11 inches from the center.

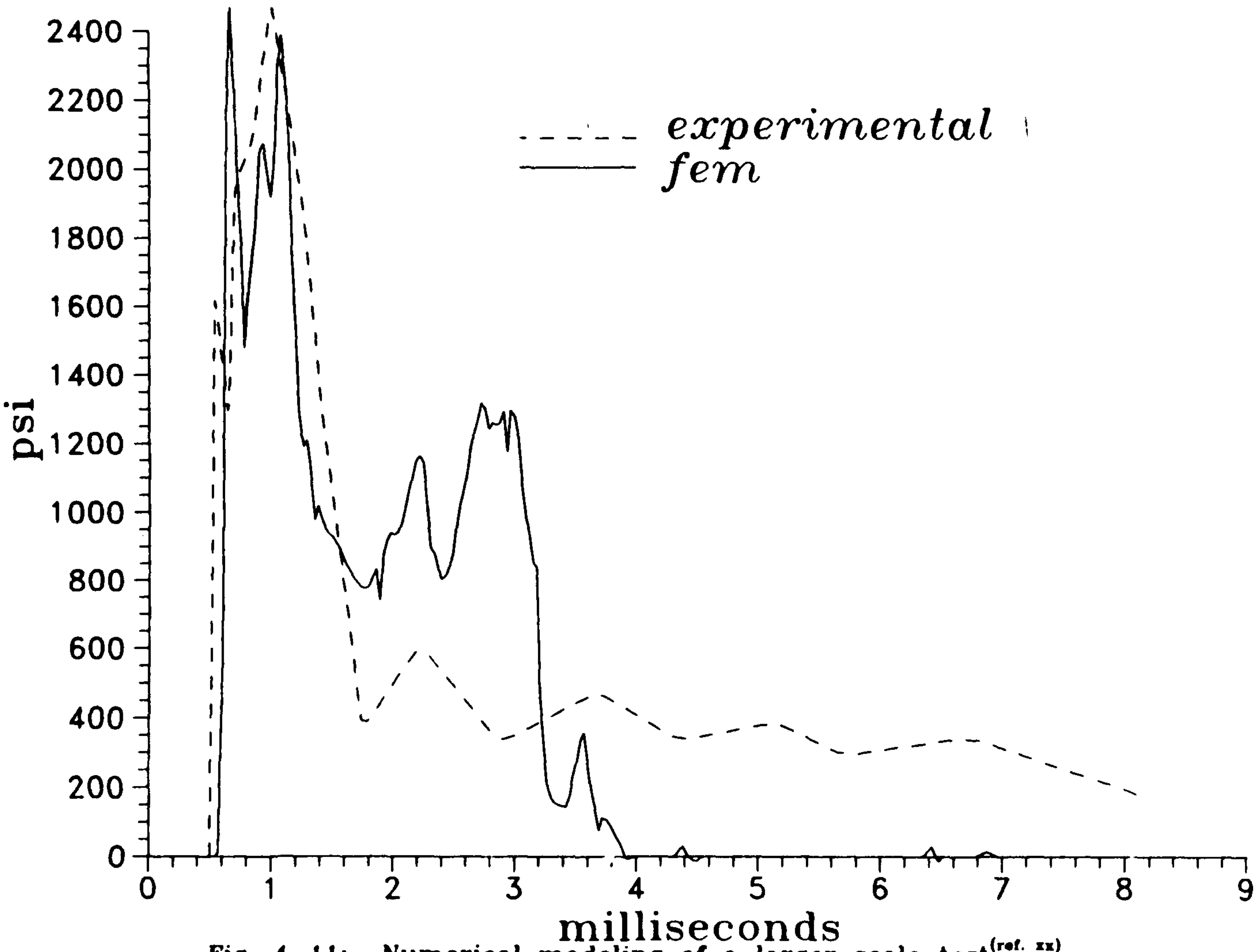

Fig. 4-11: Numerical modeling of a larger scale test$^{(\mathrm{ref.\ xx})}$ – Pressure over the support of the roof.

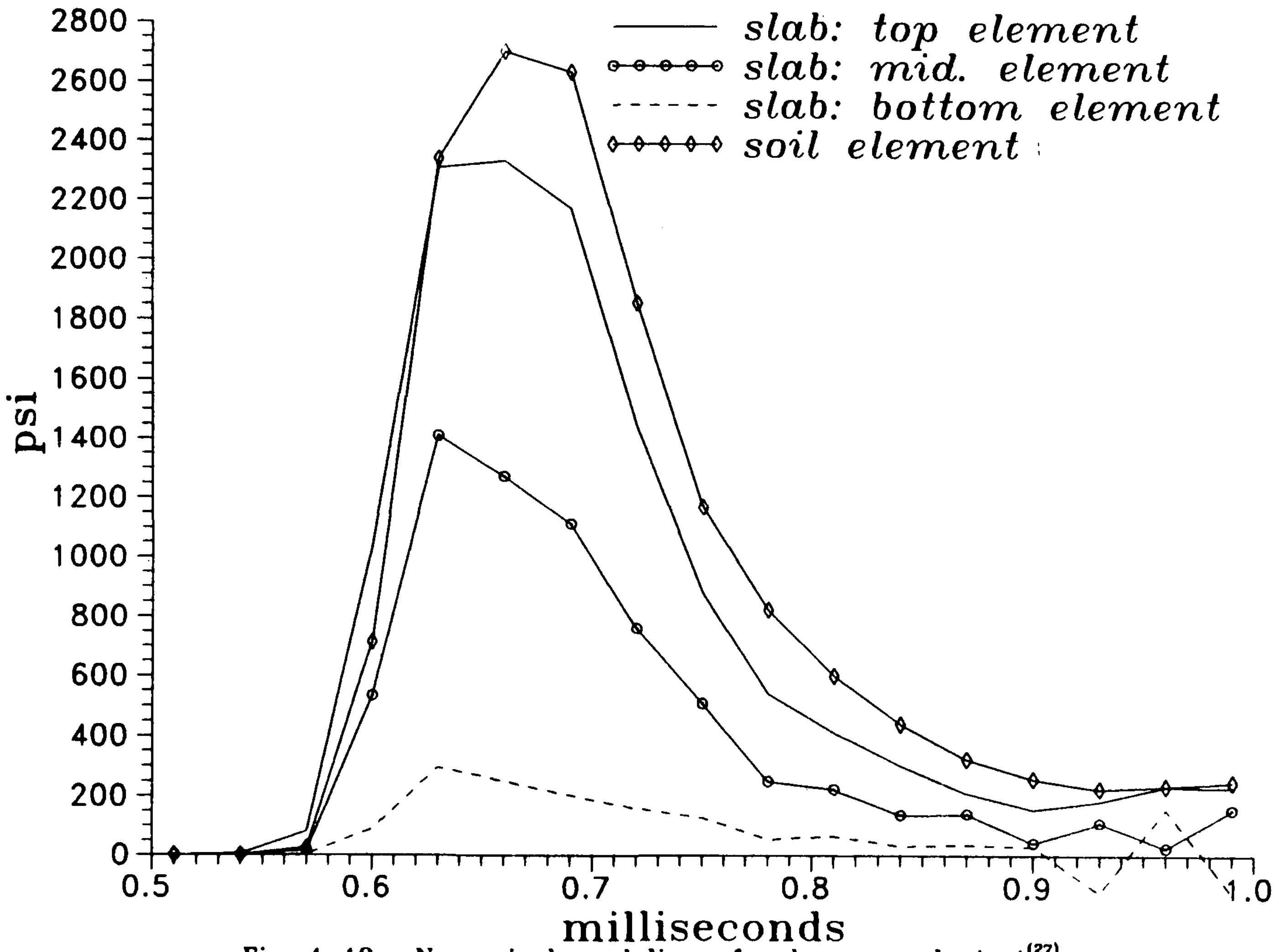

Fig. 4-12: Numerical modeling of a larger scale test(27) – Vertical (transverse) stresses across the roof center cross-section.

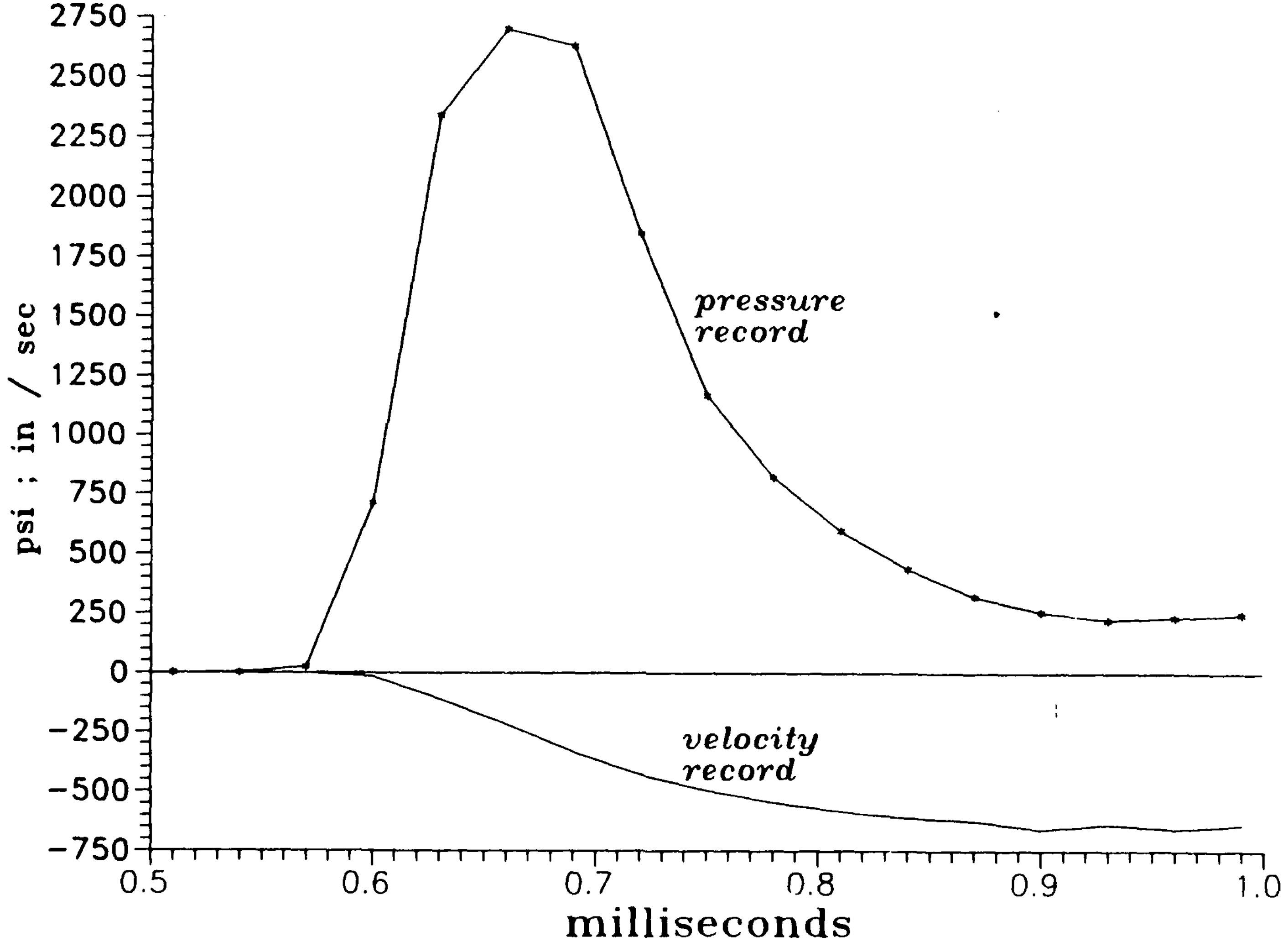

EXPANDED RECORD OF INITIAL 1/2 msec.

Fig. 4-13: Numerical modeling of a larger scale test(ref. xx) – Pressure and velocity at the roof center.

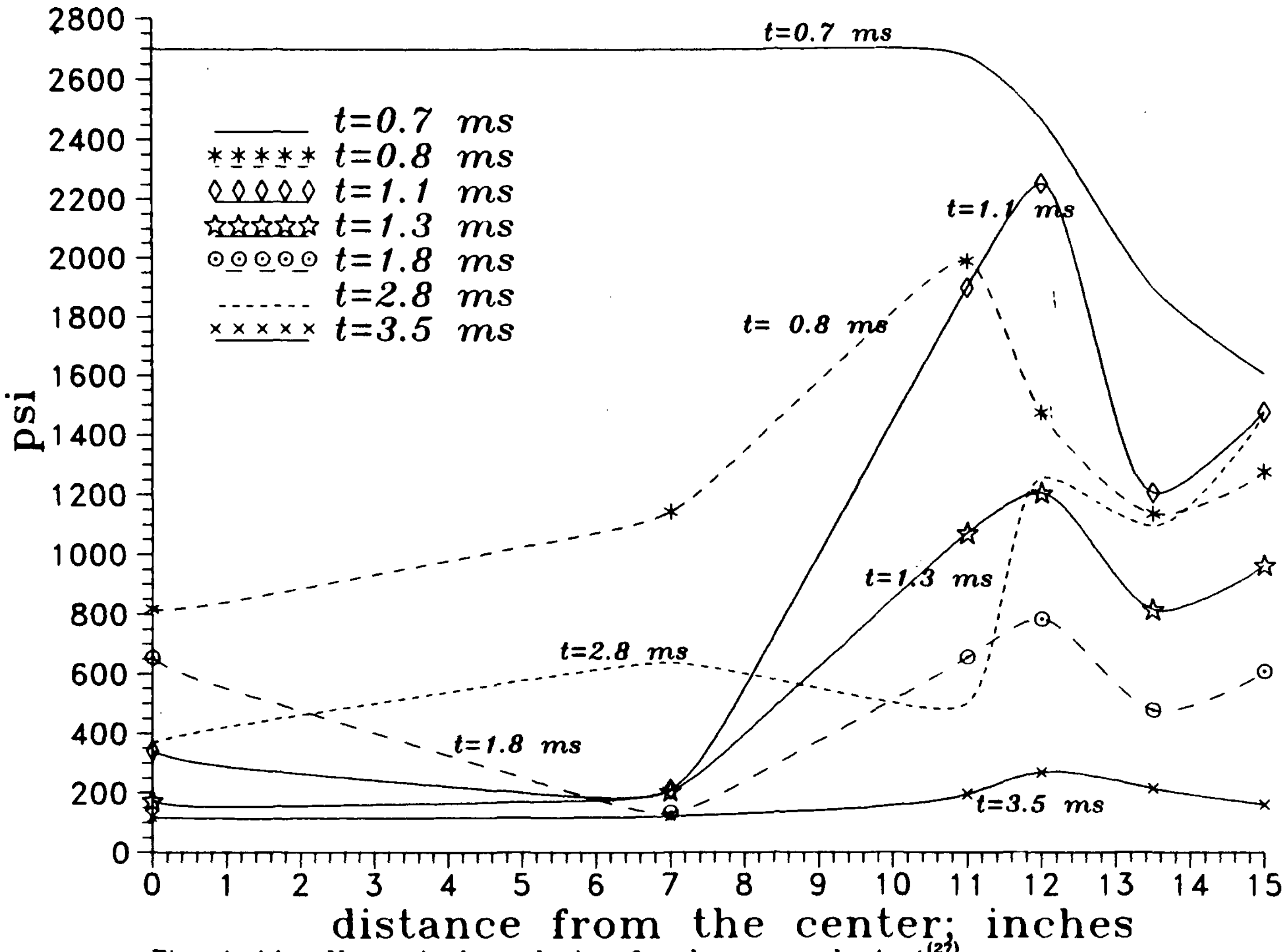

Fig. 4-14: Numerical analysis of a larger scale test[27]–
– Pressure distribution over the roof.

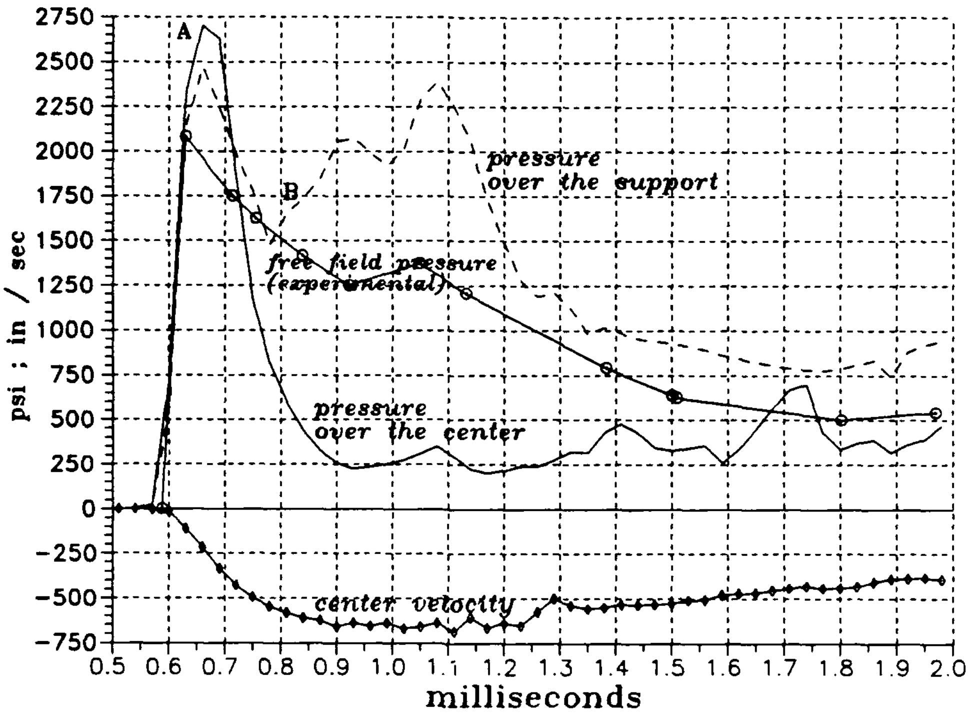

EXPANDED RECORD OF THE INITIAL 2 msec.

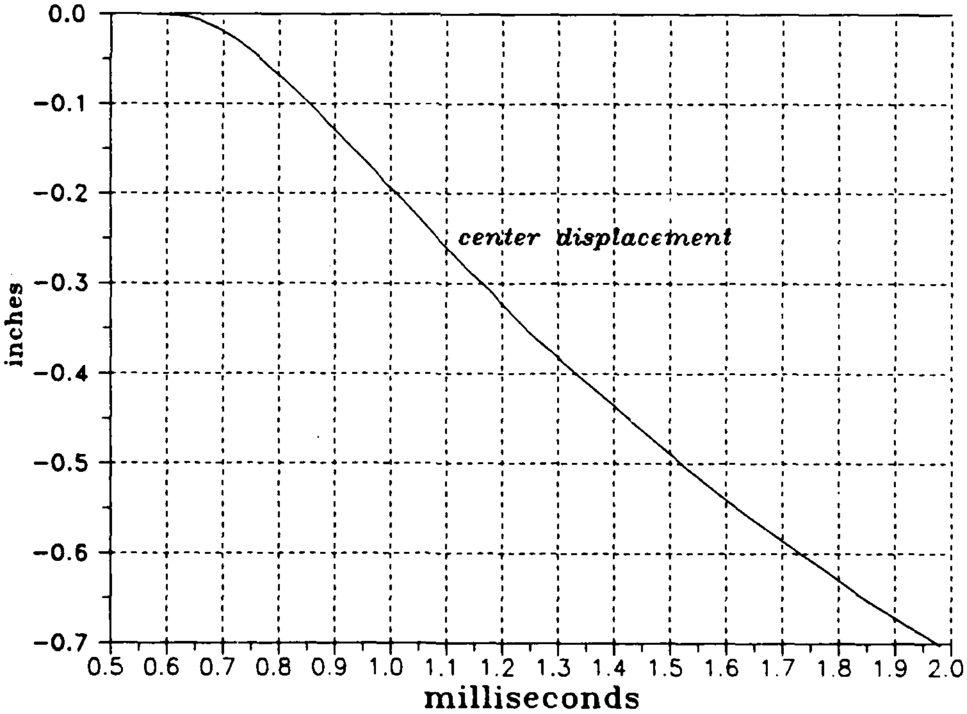

EXPANDED RECORD OF THE INITIAL 2 msec.

Fig. 4-15: Numerical modeling of a larger scale test(37) – Pressure over the roof and motion records of the roof center.

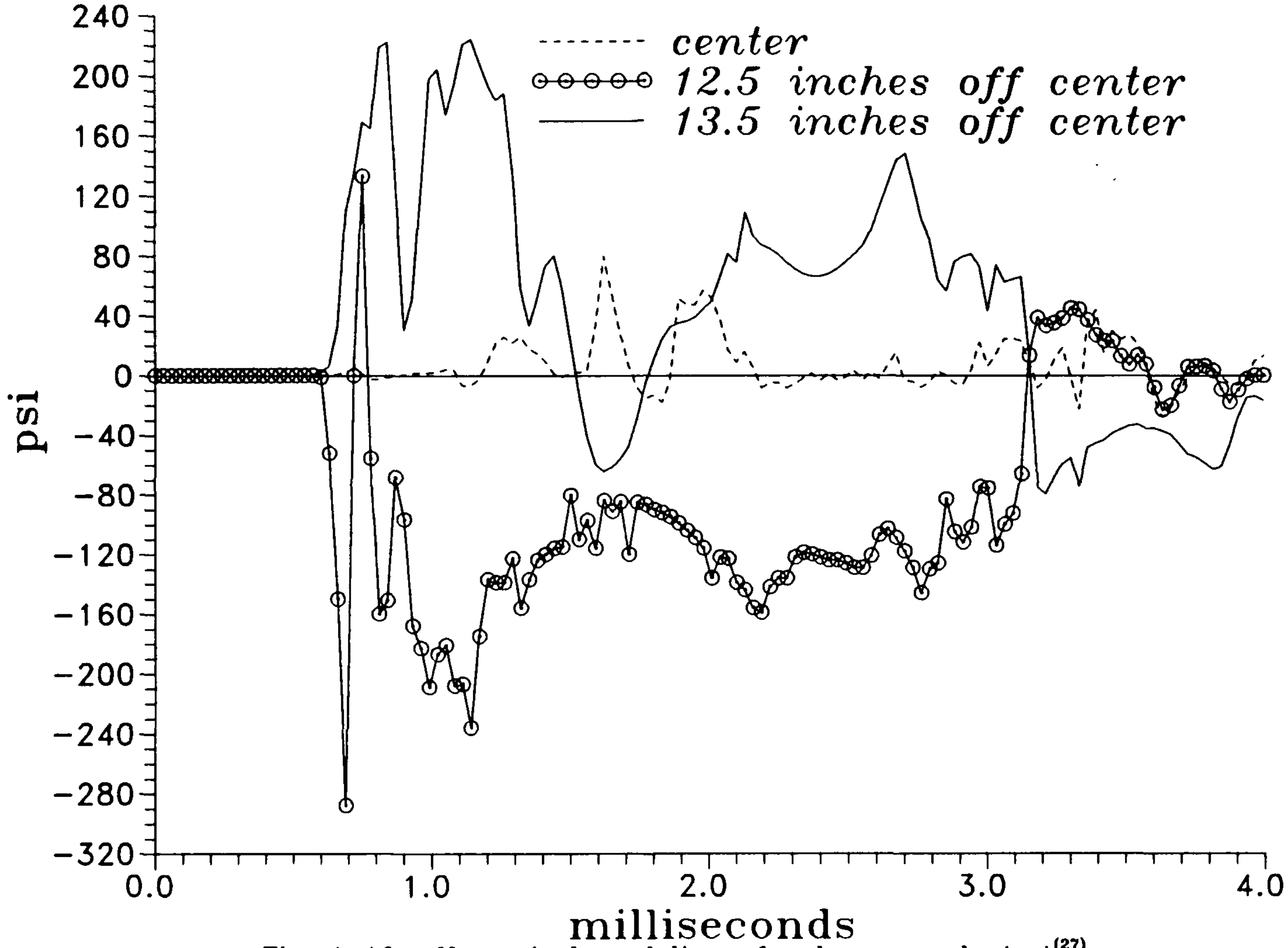

Fig. 4-16: Numerical modeling of a larger scale test[27] – Shear stresses in the soil above the roof.

CHAPTER 5

CONCLUSIONS

5.1 Response of A Soil-Structure System.

The experimental and numerical study of the response of a structure embedded in a shallow depth of burial to an external surface impact was described in previous chapters. From the investigation of the physical mechanisms which influence the behavior of the system, two main phases of the response were observed: an early-time phase and a later-time phase. The early-time response of the system is usually during the first peak of the incident impact, which is first amplified at the initially rigid soil-structure interface, and later attenuated with the arrival of a tension wave reflected from the free bottom surface of the roof. Further decrease of the initial load is due to the interaction between the loading soil and the loaded structure, which is affected first by the velocity of the structure and then by its deflection. The later-time phase of the response involves possible gap between the soil and the center portion of the roof, which releases the load over that region, and rigid body settlement of the structure which tends to decrease the arching action at shallow DOB, increase the load over the roof center, and decrease it over the supports.

According to the peak pressure level and the rise time of the incident impact, whether the structure will sustain the load or fail is determined already during the first early-time phase of the response. The initial performance of the structure depends on its capacity to sustain impact loading and on both the level of the load and on its rise time and duration. Therefore, for very short rise times (about 1/4 to 1/2 of the natural period) the total impulse might need to be considered as a loading criterion for failure (rather than just the peak pressure).

The propagation speed of transient elastic waves in the concrete roof is relatively high, because of the large stiffness of concrete. Since the thickness of the roof is, usually, relatively small, the reflection of a tension wave from the bottom free surface of the roof occurs soon after it is hit by the pressure wave (order of magnitude of 0.010 msec). When it reaches the upper surface of the roof the amplified incident pressure is released approximately to the level of the free field pressure. The tension in the lower surface of the roof might also cause spalling of concrete, which should be considered during the design phase.

The subsequent interaction mechanisms are important in decreasing the load and thereby limiting the impulse acting on the structure. The general trend of this portion of the response is to release the load from the centrally loaded zone of the structure, and to lower the pressure over it relative to the free field pressure. The drop of the pressure, which is faster than the free field drop, is initiated by the downward movement of the structure and corresponds to its velocity. Further drop of loading over the central zone of the deflecting roof is caused by arching, which develops in non-cohesive soils over the relatively flexible displacing structure. The release of the pressure over the center of the roof due to arching is typically accompanied by a corresponding increase of the load over its stiffer supports. In the absence of these mechanisms the structure would have been loaded over a longer time, and probably experienced further damage.

It was also observed that the soil-structure interface friction influences the response. More interface friction enhances the arching mechanism and causes further decrease of the load (after the first peak) over the center region of the roof. However, interface friction increases the shear loading at the structure upper surface, which should also be considered.

The boundary conditions of the roof may contribute to its capacity in sustaining the initial portion of the loading. They are less important in the later-time response, especially when multiple hits are considered. In the case of a repeated loading, plastic hinges at the clamping supports produce a response which is similar to the response of a non-clamping support, as the deflection shape of both become similar.

Finally, the rigid body settlement motion of the whole structure needs consideration, as it has a similar effect on the later-time velocity-load, and arching mechanisms. Although the motion develops later than that of the roof, it can further contribute to the process of load release over the supports.

5.2 Application of the Small Scale System Observations and of the Computer Code.

This work employed an experimental portion which was performed in the laboratory with a small scale model system. The associated dimensional analysis shows the ratios for an extrapolation of the small scale results into a larger scale system. It was shown that if the gravitational portion of the involved mechanisms is not dominant, the distortion in such an extrapolation is limited to the order of magnitude of the experimental error.

The axisymmetric system which was used did not model a specific larger scale prototype. However, when compared with another larger scale system of the same nature, similar mechanisms were observed. The extrapolation ratios together with the expression for the amount of distortion (due to gravitational effects) propose a useful way of using the results of a small scale model system for a larger, geometrically similar system.

One of the aspects of the small scale modeling was the use of micro-concrete reinforced with steel wires to model reinforced concrete. The employment of micro-concrete in this work was based on previous comprehensive research which investigated the optimal way to model reinforced concrete in small scale systems. It was further based on static tests with micro-concrete slabs (which were performed during this research). The micro-concrete showed general mechanical behavior which is typical of concrete. It should be noted that there were indications that the elastic modulus of the micro-concrete was lower than that of concrete. Therefore, it is recommended to examine and verify adequately the initial elastic modulus of the modeling material together with the testing of its compressive strength.

The "SAMSON2" computer code which was developed in the Air-Force, offers flexible features for geometrical and material modeling. The main features which correspond to modeling of soil-structure systems, are the material models and the sliding interfaces. However, these features are not developed yet to their full potential. The sliding interfaces, which are important in the modeling of the contact surface between two different materials, should be developed further and improved to enable better definition and determination of the "capture distance" parameter, to limit its influence on the results.

APPENDIX A

MEASUREMENTS OF LOADS

Two commercially available load transducers were considered for the measurements of the pressure induced by the sand on the roof of the structure:

1. "Kulite" pressure transducer, was successfully used in the Foam HEST experiments[18,19,25], and was designed to measure pressure at the soil-structure interface. The major drawback of this transducer with regard to the current experimental setup is its 1 inch diameter size and that it must also be mounted within the roof of the structure so that its face is leveled with the roof upper surface. For these reasons it was used only as a reference transducer for another, smaller, load cell which was modified adequately to match the manufacturer's instructions.

2. "Entran" ELF-500-100 load cell, was successfully used by Chen[8] to measure the load over the center of the roof in a former stage of this experimental program. This load cell is only 0.5 inch in diameter and 0.11 inch in thickness, has low mass and it is capable of measuring dynamic load signals in excess of 20 KHz. According to the manufacturer's instructions[17], for use over parts of the roof which are off center, all nonuniform and horizontal components of the pressure must be isolated to insure that the load cell is only loaded by a uniform

normal pressure over its load button.

In a series of tests several techniques were examined in order to obtain a reliable pressure signal. The criterion for the quality of the load cell output was a reference signal from a "Kulite" pressure gauge (Figure A-1), which was acquired by using a small "thumb tack" type of steel support glued to the loading button of the load cell. By mounting the load cell on a relatively rigid pin pointed support, with the back of the load cell facing the loading medium (i.e. the sand), the load which was transferred to the loading button of the load cell was distributed uniformly and directed normal to the loading face of the transducer, as required.

The output records of the two load cells, when using this technique, is described in figure A-2. As it can be seen the output records of the two load cells were very similar and was adopted as the method with which pressure was recorded over the roof. The total load indicated by the load cell was divided by its area (0.1963 in^2) to obtain the average pressure. Additional verification for the pressure measurements is discussed in Chapter 2, section 2.2.1.1.

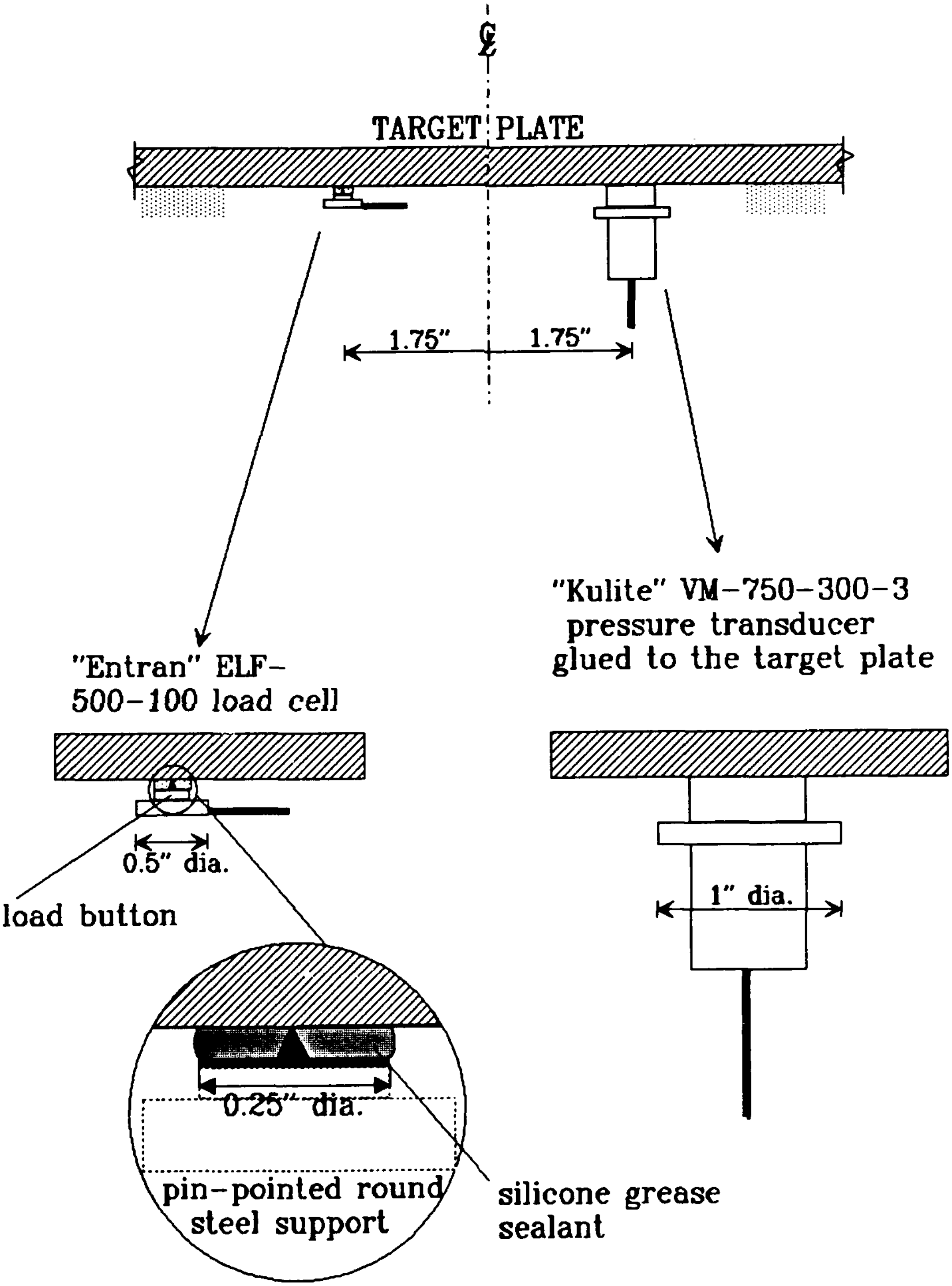
℄
TARGET PLATE
1.75"
1.75"
"Kulite" VM-750-300-3 pressure transducer glued to the target plate
"Entran" ELF-500-100 load cell
0.5" dia.
load button
1" dia.
0.25" dia.
pin-pointed round steel support
silicone grease sealant

Fig. A-1: Load cells measurements configuration.

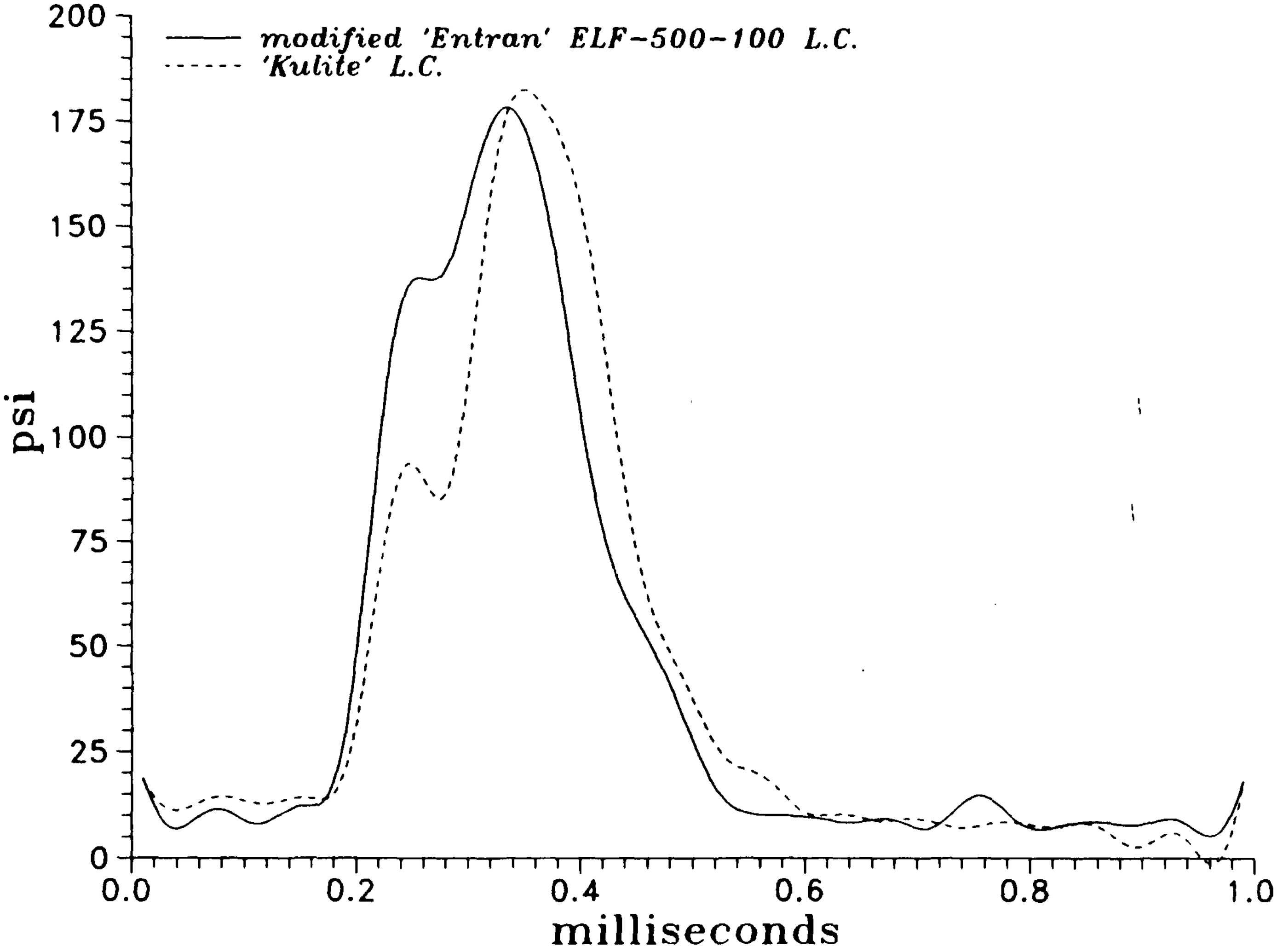

Fig. A-2: Output of the load cells, located under the target plate as described in Fig. A-1.

APPENDIX B

MEASUREMENTS OF DYNAMIC DISPLACEMENTS

Two alternative methods to measure a dynamic displacement (or its time derivatives) were examined. One was the use of an accelerometer to obtain a time record of the acceleration, which can then be integrated to give the velocity and the displacement. An alternative way was the use of an LVDT (Linear Variable Displacement Transformer) which gives a direct record of the displacement. Time derivatives of that record gives the velocity and acceleration record.

In order to examine the two methods, the following "calibration test" was performed: At the free end of an aluminum cantilever beam a Type 4374 Brüel & Kjaer accelerometer, and an LVDT were mounted. The signals of the transducers were recorded by a 4094 Nicolet digital oscilloscope. In some of the tests the signal of the accelerometer was recorded directly, and in others through a charge amplifier (Kistler S/N 216 model 504). The LVDT's signal was recorded using a Chaevitz amplifier with excitation frequency of 20 kHz to provide accurate measurements of the dynamic signal. The other end of the beam was clamped between two aluminum blocks (Figure B-1). The cross section of the beam was 2 in by 0.25 in, and the span , l, was variable.

Neglecting damping, the equation of motion of the beam is:

$$\frac{\partial^4 y}{\partial x^4} = -\frac{1}{b^2}\frac{\partial^2 y}{\partial t^2} \qquad \text{(B-1)}$$

where: $b^2 = \frac{EI}{\rho A}$

E - Young's modulus (11×10^6 for aluminum).

I - moment of inertia of the cross section.

A - area of the cross section.

ρ - mass density ($0.093/386.4=2.407\times10^{-4}$ lb-sec^2/in^4 for aluminum).

The free end was deflected by a string until w=0.05 in was read at that point in a dial gage attached to the beam. The dial gage was then removed and the string cut, thus providing the following initial conditions :

$$\begin{aligned} y(x=l,t=0) &= w(t=0) = 0.05 \text{ in} \\ \dot{y}(x=l,t=0) &= \dot{w}(t=0) = 0 \quad \text{in/sec} \end{aligned} \qquad \text{(B-2)}$$

The general solution for equation B-1 is:

$$y(x,t) = X(x)\,(A\cos(\omega t) + B\sin(\omega t)) \qquad \text{(B-3)}$$

for which X(x) must satisfy:

$$\frac{\partial^4 X}{\partial x^4} - k^4 X = 0 \qquad \text{(B-4)}$$

where: $k^4 = \dfrac{\omega^2}{b^2}$

A convenient form for the solution of equation B-4 is:

$$\begin{aligned} X(x) = \quad & C_1(\cos(kx) + \cosh(kx)) + C_2(\cos(kx) - \cosh(kx)) + \\ & C_3(\sin(kx) + \sinh(kx)) + C_4(\sin(kx) - \sinh(kx)) \qquad \text{(B-5)} \end{aligned}$$

The constant k is obtained from the boundary conditions. For a fully clamped cantilever the boundary conditions are :

$$X(0) = 0 \quad ; \quad \frac{\partial X}{\partial x}(0) = 0$$

$$V(l,t) = 0 \quad or \quad \frac{\partial^3 X}{\partial x^3}(l) = 0 \quad ; \quad M(l,t) = 0 \quad or \quad \frac{\partial^2 X}{\partial x^2}(l) = 0$$

From these boundary conditions we get :

$$\cos(kl)\cdot\cosh(kl) = -1 \tag{B-6}$$

The natural frequencies for the vibration modes of the beam are $\omega_i = bk_i^2$ (b is defined in the equation of motion, B-1). The first five eigenvalues for kl are listed in Table B-1:

Table B-1

First Five Eigenvalues of kl for a Cantilever Beam

k_1l	k_2l	k_3l	k_4l	k_5l
1.875	4.694	7.855	10.996	14.137

It should be noted, however, that a fully fixed end is very hard to obtain, and even a slight slope at the "fixed" support alters the boundary condition and actually gives a moment of finite magnitude, K (Figure B-1(b)). In that case the boundary conditions at the support (x=0) become:

$$X(0) = 0$$
$$M(0,t) = K\frac{\partial X}{\partial x}(0) = EI\frac{\partial^2 X}{\partial x^2}(0)$$

While the conditions at the free end remain unchanged.

From these boundary conditions we get the following equation:

$$
\begin{aligned}
&(\cos kl+\cosh kl)\left(\cos kl+\cosh kl+\frac{EIk}{K}(-\sin kl+\sinh kl)\right)+ \\
&(\sin kl+\sinh kl)\left(\sin kl-\sinh kl+\frac{EIk}{K}(\cos kl-\cosh kl)\right) = 0
\end{aligned}
\tag{B-7}
$$

The moment stiffness of the support, K, can be either estimated or found in a semi-empirical way by measuring the frequency, ω, from which the value of k can be derived and substituted into equation B-7. Then, repeating the test with a different span, l, the same K is used to calculate the new k, which corresponds to the new frequency, ω for that span.

Once ω is obtained, the solution for the motion of the free end (w and its derivatives) is:

$$
\begin{aligned}
w(t) &= w_0\cos(\omega t) \\
\dot{w}(t) &= -\omega w_0\sin(\omega t) \\
\ddot{w}(t) &= -\omega^2 w_0\cos(\omega t)
\end{aligned}
\tag{B-8}
$$

where w_0 is the initial displacement of the free end of the cantilever (0.05 inch in this case).

The experiments were performed with three spans (l): 6.625 in, 8.0 in, and 9.4375 in. From the output of the LVDT in the test performed with a span $l=6.625$ in (Fig. B-2) the measured period of the first mode was $T=10$ msec. The lowest frequency was then, $\omega=2\pi/T=628.32$ rad/sec, which gives $kl=1.337$. Substituting kl into equation B-7, $K=6162.8$ lb-in. It can be shown that this value of K allows, for an initial deflection of 0.05 in, a maximum slope at the support of 0.8 degrees. Such a small slope is indeed undetectable by the naked eye, but causes a difference when the frequency response of the beam is considered. A fully clamped beam of the same span would have a period twice as long, i.e. $T_{clamped}=5$ msec (see Table B-1).

Using this value of K, the following predictions can be made for the other spans:

For l = 6.625 inch (compare Fig. B-2)

$V_{max} = 0.05\omega = 31.4$ in/sec

$a_{max} = 0.05\omega^2 = 51$ g

For l = 8.0 inch (compare Fig. B-3)

$k = 0.1729$

$\omega = 461.45$ rad/sec, $T = 13.62$ msec.

$V_{max} = 0.05\omega = 23.1$ in/sec

$a_{max} = 0.05\omega^2 = 27.55$ g

For $l = 9.4375$ inch (compare Fig. B-4)

$k = 0.1508$

$\omega = 351$ rad/sec, $T = 17.9$ msec.

$V_{max} = 0.05\omega = 17.55$ in/sec

$a_{max} = 0.05\omega^2 = 15.95$ g

Figures B-2, B-3, and B-4 show the experimental results. From these figures the following conclusions can be drawn:

1. The output of the LVDT is accurate and stable, and measures well the amplitude of the motion as well as its frequency and can also be used to obtain the velocity record by taking the first time derivative.

2. The output of the accelerometer, when amplified, measures well the frequency of the motion signal but seems to "drift" giving an unstable integrated record for the velocity and the displacement, after about half a period of the motion.

3. When not amplified, the raw signal coming out of the accelerometer might be too weak (compared to the noise recorded with it), thus yielding erroneous output of both the amplitude and the frequency (compare figures B-2, B-3, with figure B-4).

4. A close observation of the two records shows that the accelerometer responds faster than the LVDT to the exciting motion by 50-100 μsec. In some types of experiments (such as the soil-structure system considered in this work) the relationship between the motion of the structure and the load acting on it is sought, and this response time might be important. Therefore, the accelerometer should be used together with the LVDT to detect the actual starting time of the motion, so that the signal of the LVDT could be shifted accordingly.

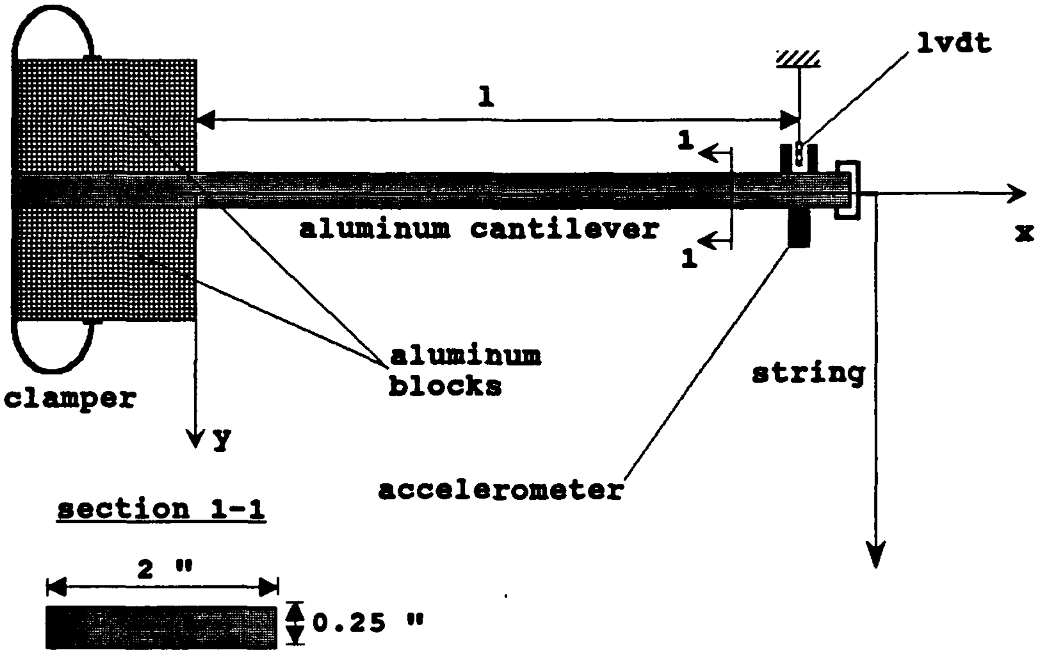
lvdt
l
1
1
aluminum cantilever
x
aluminum blocks
clamper
string
y
accelerometer
section 1-1
2 "
0.25 "

possible boundary conditions at the support

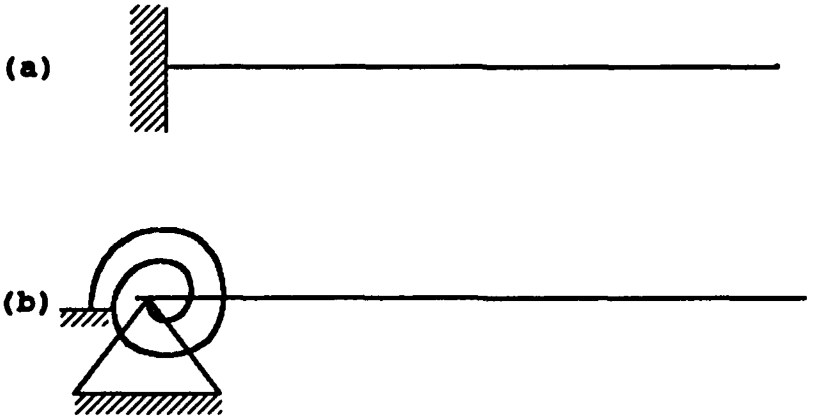

Fig. B-1 : Setup for the dynamic calibration test.

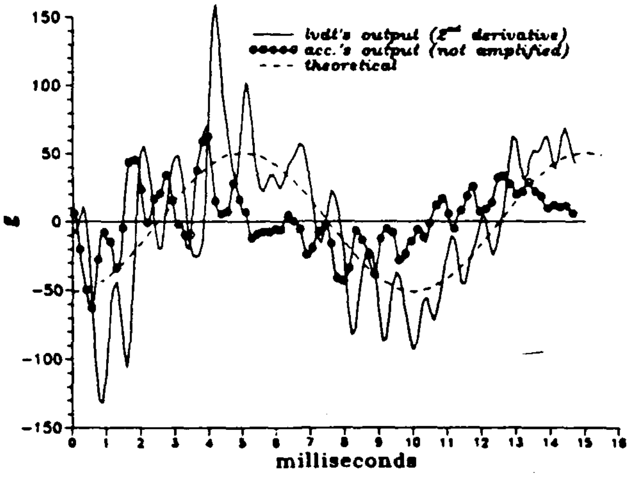

Fig. B-2(c): Acceleration of a cantilever end at L = 6 5/8 in.

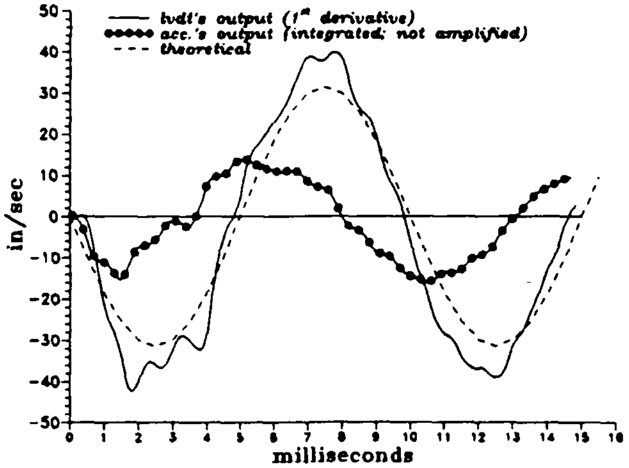

Fig. B-2(b): Velocity of a cantilever end at L = 6 5/8 in.

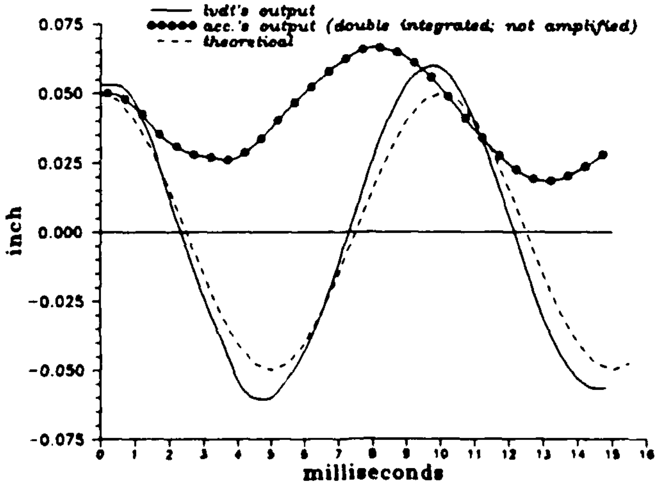

Fig. B-2(a): Displacement of a cantilever end at L = 6 5/8 in.

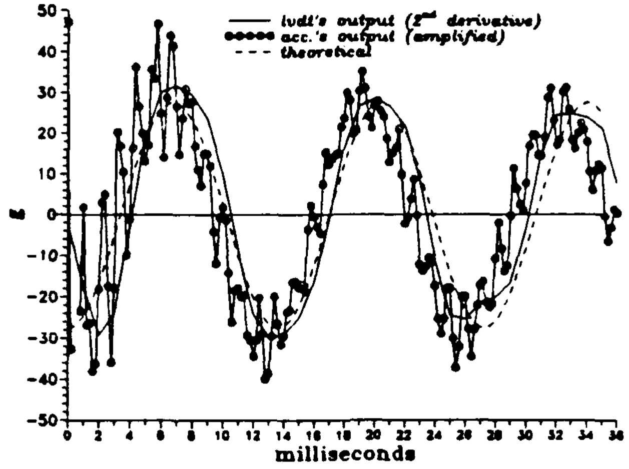

Fig. B-3(c): Acceleration of a cantilever end at L = 8 in.

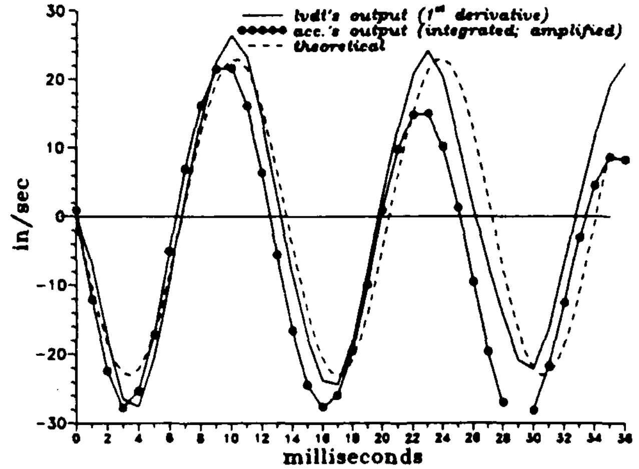

Fig. B-3(b): Velocity of a cantilever end at L = 8 in.

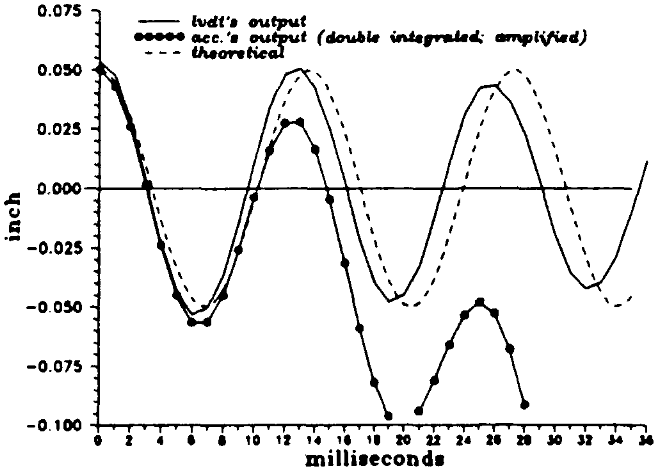

Fig. B-3(a): Displacement of a cantilever end at L = 8 in.

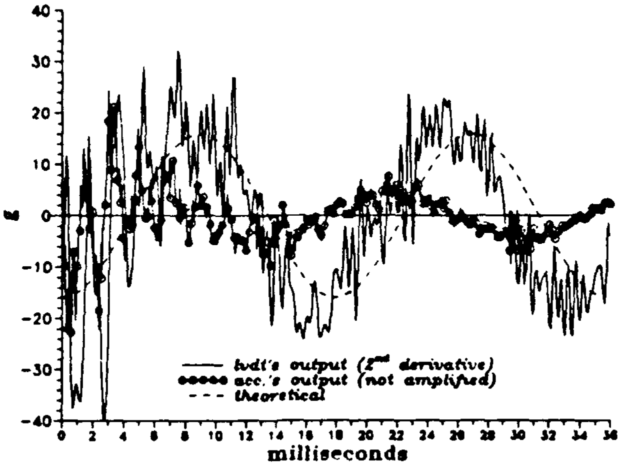

Fig. B-4(c): Acceleration of a cantilever end at L = 9 7/16 in.

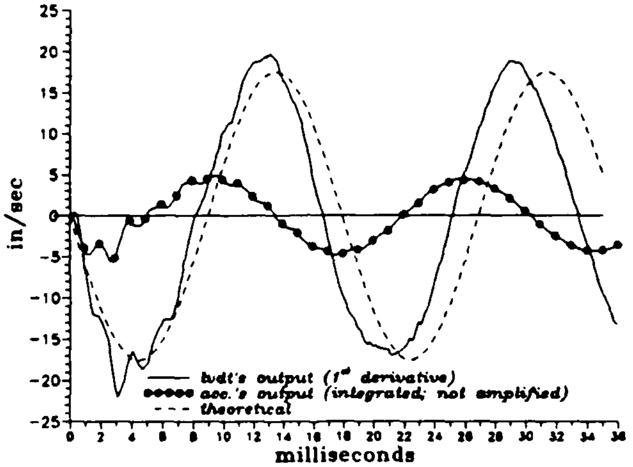

Fig. B-4(b): Velocity of a cantilever end at L = 9 7/16 in

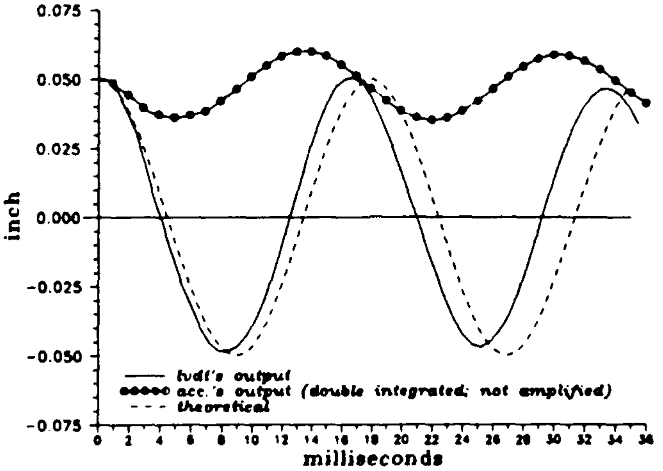

Fig. B-4(a): Displacement of a cantilever end at L = 9 7/16 in.

APPENDIX C

DIMENSIONAL ANALYSIS OF A SMALL SCALE SOIL-STRUCTURE SYSTEM.

Figure C-1 describes the system and some of the parameters which are scaled and analyzed. Notations of the dimensions are as follows:

[mass] $= M$

[length] $= L$

[time] $= T$

[force] $= F = M\,L / T^2$

The variables (and their dimensions) are:

Variables with length dimension, L:

DOB, h, l, D, r- see Fig. C-1

u - average grain size of the soil

w - mid roof's deflection

Variables with area dimension, L^2:

A_r - reinforcement's area

Variables with pressure dimension, $F/L^2 = M/\,L\,T^2$:

σ_s - stress in the soil

σ_r - reinforcement (of structure's roof) stress

σ_c - concrete (of structure's roof) stress

f'_c - compressive strength of concrete

f_y - yield stress of reinforcement

q_0 - peak external pressure (see Fig. C-1)

σ - stress acting on the roof

E_c - concrete Young's modulus (initial)

E_r - steel Young's modulus

K_l - soil's bulk modulus for loading

K_{ul} - soil's bulk modulus for unloading

Variables with mass density dimension, M/L^3:

ρ_s - soil's density

ρ_c - roof's (concrete) density

Variables with velocity dimension, L/T:

v - mid roof's velocity ($= \dot{w}$)

Variables with acceleration dimension, L/T^2:

g - gravitational acceleration

a - mid roof's acceleration

Variables with time dimension, T:

t - time

t_0 - typical time of external loading (see Fig. C-1)

Nondimensional variables:

ϵ_c - concrete strain

ϵ_r - steel strain

ϵ_s - soil strain

ν_c - concrete Poisson ratio

ν_r - steel Poisson ratio

ν_s - soil Poisson ratio

$f(r)$ - distribution of external pressure (see Fig. C-1)

Assumptions:

1. All variables of length dimension are scaled identically:

$$\frac{r_p}{r_m} = \frac{DOB_p}{DOB_m} = \dots \frac{w_p}{w_m} = n \tag{C-1}$$

where the subscript "p" denotes prototype, the subscript "m" denotes model, and n is the scale factor for the length. Hence, only one typical length variable, λ, may be considered for the dimensional analysis.

2. Materials of the prototype and of the model systems have the same properties, hence:

   a. The stress-strain relations of the prototype soil is identical to that of the model, yielding:

      $(\epsilon_c)_p = (\epsilon_c)_m, \quad (\epsilon_r)_p = (\epsilon_r)_m, \quad (\epsilon_s)_p = (\epsilon_s)_m$

      Note: This was verified for the micro-concrete and for the micro-reinforcement in Reference 12.

   b. The mass density of the soil, concrete, and reinforcement is the same for the model and for the prototype:

      $(\rho_c)_p = (\rho_c)_m, \quad (\rho_r)_p = (\rho_r)_m, \quad (\rho_s)_p = (\rho_s)_m$

Following the "formal procedure" of a dimensional analysis, the behavior of the system is according to the general equation C-2, in which C is a nondimensional constant:

$$d^{\alpha 1}\, q_0^{\alpha 2}\, \sigma_c^{\alpha 3}\, \sigma_s^{\alpha 4}\, \sigma_r^{\alpha 5}\, \sigma^{\alpha 6}\, f_c^{\alpha 7}\, f_y^{\alpha 8} K_l^{\alpha 9} K_{ul}^{\alpha 10}\, E_c^{\alpha 11}\, E_r^{\alpha 12}\, \rho_s^{\alpha 13}\, \rho_c^{\alpha 14}$$

$$v^{\alpha 15}\, a^{\alpha 16}\, g^{\alpha 17}\, t^{\alpha 18}\, t_0^{\alpha 19} A_r^{\alpha 20} = C \qquad \text{(C-2)}$$

Note that formally, the nondimensional variables may also be part of equation C-2, but since they can not contribute to the **dimensional analysis** they are assumed to be included in the constant C.

To keep equation C-2 dimensionally consistent the sum of the powers of each of the three basic dimensions, L, M, and T, must be equal to zero. Substituting the dimensions of the variables into equation C-2 and collecting the powers of each dimension, the three following equations are obtained:

$$\text{for L:} \quad \alpha_1-\alpha_2-\alpha_3-\alpha_4-\alpha_5-\alpha_6-\alpha_7-\alpha_8-\alpha_9-\alpha_{10}-\alpha_{11}-\alpha_{12}-3\alpha_{13}-3\alpha_{14}+\alpha_{15}+\alpha_{16}+\alpha_{17}+ \\ 2\alpha_{20} = 0 \qquad \text{(C-3)}$$

$$\text{for M:} \quad \alpha_2+\alpha_3+\alpha_4+\alpha_5+\alpha_6+\alpha_7+\alpha_8+\alpha_9+\alpha_{10}+\alpha_{11}+\alpha_{12}+\alpha_{13}+\alpha_{14} = 0 \qquad \text{(C-4)}$$

$$\text{for T:} \quad -2\alpha_2-2\alpha_3-2\alpha_4-2\alpha_5-2\alpha_6-2\alpha_7-2\alpha_8-2\alpha_9-2\alpha_{10}-2\alpha_{11}-2\alpha_{12}-\alpha_{15}-2\alpha_{16}-2\alpha_{17}+ \\ \alpha_{18}+\alpha_{19} = 0 \qquad \text{(C-5)}$$

Any (and only) three of the power α's may therefore be determined. Writing the algebraic relations as functions of α_1,α_{14}, and α_{18} we get, from equations C-3, C-4, and C-5:

$$\alpha_1 = \quad -2\alpha_2-2\alpha_3-2\alpha_4-2\alpha_5-2\alpha_6-2\alpha_7-2\alpha_8-2\alpha_9-2\alpha_{10}-2\alpha_{11}-2\alpha_{12}-\alpha_{15}-\alpha_{16}-\alpha_{17}- \\ 2\alpha_{20} \qquad \text{(C-6)}$$

$$\alpha_{14} = -\alpha_2-\alpha_3-\alpha_4-\alpha_5-\alpha_6-\alpha_7-\alpha_8-\alpha_9-\alpha_{10}-\alpha_{11}-\alpha_{12}-\alpha_{13} \qquad \text{(C-7)}$$

$$\alpha_{18} = 2\alpha_2+2\alpha_3+2\alpha_4+2\alpha_5+2\alpha_6+2\alpha_7+2\alpha_8+2\alpha_9+2\alpha_{10}+2\alpha_{11}+2\alpha_{12}+\alpha_{15}+2\alpha_{16}+ 2\alpha_{17}-\alpha_{19} \qquad \text{(C-8)}$$

Take log of equation C-2 and substitute α_1, α_{14}, and α_{18}, to get:

$$\sum_{\substack{i=2 \\ i\neq 14,18}}^{20} \alpha_i \log\pi_i = \log C \qquad \text{(C-9)}$$

The π numbers are nondimensional, and provide the scaling ratios (for a true, undistorted model) for each variable, by requiring:

$$\pi_p = \pi_m \qquad \text{(C-10)}$$

The π numbers are:

$$\pi_2 = \frac{q_0 t^2}{\lambda^2 \rho_c} \qquad \pi_3 = \frac{\sigma_c t^2}{\lambda^2 \rho_c} \qquad \pi_4 = \frac{\sigma_s t^2}{\lambda^2 \rho_c}$$

$$\pi_5 = \frac{\sigma_r t^2}{\lambda^2 \rho_c} \qquad \pi_6 = \frac{\sigma t^2}{\lambda^2 \rho_c} \qquad \pi_7 = \frac{f'_c t^2}{\lambda^2 \rho_c}$$

$$\pi_8 = \frac{f_y t^2}{\lambda^2 \rho_c} \qquad \pi_9 = \frac{K_l t^2}{\lambda^2 \rho_c} \qquad \pi_{10} = \frac{K_{ul} t^2}{\lambda^2 \rho_c}$$

$$\pi_{11} = \frac{E_c t^2}{\lambda^2 \rho_c} \qquad \pi_{12} = \frac{E_r t^2}{\lambda^2 \rho_c} \qquad \pi_{13} = \frac{\rho_s}{\rho_c}$$

$$\pi_{15} = \frac{vt}{\lambda} \qquad \pi_{16} = \frac{at^2}{\lambda} \qquad \pi_{17} = \frac{gt^2}{\lambda}$$

$$\pi_{19} = \frac{t_0}{t} \qquad \pi_{20} = \frac{A_r}{\lambda^2}$$

When variables with the same dimension are scaled in the same way, the number of scaled variables is eight and the number of the non-dimensional π numbers can be reduced to five:

$$\pi_1 = \frac{at^2}{\lambda}, \quad \pi_2 = \frac{vt}{\lambda}, \quad \pi_3 = \frac{M}{\lambda \sigma t^2}, \quad \pi_4 = \frac{F}{\lambda^2 \sigma}, \quad \pi_5 = \frac{\rho \lambda^2}{\sigma t^2}$$

Table C-1 summarizes three possible prototype - model ratios: Each column represents a different set of possible scaling ratios for an undistorted system. Note that for each column only three basic ratios can be determined independently (bold letters in Table C-1). The ratios listed in the remaining rows are determined according to the three basic independent ratios and the above π numbers. According to the assumptions listed above, the geometrical scaling ratio is set to **n**, and the stresses in the model and prototype systems are the same. The third independent ratio might be, for example, an acceleration ratio of one, indicating identical accelerations for the model and the prototype (second column in Table C-1). Thus proper modelling of the gravitational acceleration for systems that do not involve the means to change it, such as a centrifuge, is ensured. Note that in this case the mass densities of the model materials should be increased by a factor of n in order to keep the scaled model undistorted. If the mass densities are kept identical (as shown in the third column of Table C-1) then any acceleration of the model system should be decreased by a factor of n when extrapolated to a prototype system. Similarly, the prototype time is larger than the model time by a factor of n, the prototype velocities are equal to the model velocities, and any prototype force should be extrapolated from the corresponding model value by increasing it by a factor of n^2.

Since the gravitational acceleration in the current system is $g=386.4$ in/sec^2, and at the same time the mass densities of the soil and of the micro-concrete are similar to the prototype materials of a similar larger scale system, an extrapolation of the experimental results to a larger scale system involves some distortion. However, the dynamic nature of this system makes the effect of gravitational acceleration relatively negligible, and reduces the distortion in the range of other experimental errors. Evaluation of the distortion can be demonstrated through the following examples:

Example 1: Effect of the gravitational acceleration on small scale model predictions in a single degree of freedom system.

Consider a single degree of freedom mass-spring system. Under the above assumptions and if modelling a larger scale similar system, the prototype-model ratios are $\lambda_p = n\lambda_m$, and $g_p = g_m = g$. The equation of motion is:

$$Ma + Kx = Mg \tag{C-11}$$

where "a" is the acceleration of the mass, "x" is the displacement, "M" is the lumped mass, and "K" is the spring constant. The spring constant has a dimension of Force/Length. The displacement of the mass, "x", can be written as a summation of two components: a time dependant component, x_{dy}, and a static component, x_{st}, which depends on K, M, and g:

$$x = x_{dy} + x_{st}; \qquad \text{where: } x_{dy} = x_{dy}(t), \; x_{st} = x_{st}(K,M;g) \tag{C-12}$$

Substituting from equation C-11, yields:

$$Ma_{dy} + Kx_{dy} + Kx_{st} = Mg; \qquad x_{st} = Mg/K \tag{C-13}$$

where $x_{dy} = f(\omega, t, \text{initial conditions}$, and $\omega^2 = K/M$.

It is assumed that the similitude requirements following the dimensional analysis for the soil-structure system also hold for this simple system. Hence, for a true, undistorted model the mass densities ratio should be $\rho_p = \rho_m/n$, which follows $M_p = n^2M_m$ and is a consequence of the first column in Table C-1 that can be checked as follows: Certifying that the spring constant is modelled properly ($K = F/x$, therefore $K_p = n^2F_m/(nx_m) = nK_m$), the prototype displacement, x_p, can be written in the model terms as follows:

$$x_p = \quad x_{pdy} + x_{pst} = nx_{mdy} + M_pg/K_p = nx_{mdy} + n^2M_mg/(nK_m) = n(x_{mdy} + x_{mst}) = nx_m \tag{C-14}$$

The distortion is caused if $\rho_p = \rho_m$ (or $M_p = n^3M_m$), $a_p = a_m/n$ but "g" remains unscaled. From x_m measured in the experiment it follows:

$$x_p = nx_m \tag{C-15}$$

True scaling, however, yields:

$$x_p = \quad nx_{mdy} + x_{pst} = nx_{mdy} + M_pg/K_p = nx_{mdy} + n^3M_mg/(nK_m) = nx_{mdy} + n_2x_{mst} = nx_m + \underline{n(n-1)x}_{mst} \tag{C-16}$$

where the underlined term is the distortion, which results from the model to prototype extrapolation under the conditions listed above. The percentage of the distortion can be defined as follows:

$$\%\,Distortion = \frac{x_p^{true} - x_p}{x_p^{true}} \cdot 100 = \frac{n(n-1)x_{mst}}{nx_m + n(n-1)x_{mst}} \cdot 100 = \frac{100}{1 + \frac{1}{(n-1)} \cdot \frac{x_m}{x_{mst}}} \qquad \text{(C-17)}$$

From equation C-17, it can be seen that if the static portion of the total displacement in the model is less than 1/200, and the geometrical scaling factor is less than 50, the distortion in the displacement is less than 20%.

Example 2: **Effect of the gravitational acceleration on small scale model predictions of the displacement of the roof center in the current system.**

The distortion in the model to prototype prediction of the roof center displacement can be evaluated by assuming a dominant first mode motion of the roof slab. In this case equation C-17 can be applied. Consider a micro-concrete circular roof slab embedded in the sand at a depth, d_m, with a thickness h_m, modulus of elasticity E_m, and a Poisson's ratio ν_m. Typical values of these properties are listed below, and yield a slab stiffness, D_m:

$$\left.\begin{array}{l} h_m = 0.38'' \\ E_m = 2\cdot 10^6 \text{ psi} \\ \nu_m = 0.2 \end{array}\right\} \rightarrow D_m = Eh^3/12(1\text{-}\nu^2) = 9830 \text{ lb-in} \qquad \text{(C-18)}$$

The clear span of the slab is 5 inches. Assuming a uniformly distributed static pressure within the slab elastic range, the static deflection at the center of the slab is:

$$x_{mst} = \frac{p_{mst}R_m^{\ 4}}{64D_m} \cdot \begin{cases} \dfrac{(5+\nu)}{(1+\nu)} & \text{; simply supported} \\ 1 & \text{; clamped} \end{cases} \qquad \text{(C-19)}$$

The maximum experimentally measured displacements for that slab were:

$$x_m^{\ total} = \begin{cases} 0.04 \text{ inch} & \text{; simply supported} \\ 0.01 \text{ inch} & \text{; clamped} \end{cases} \qquad \text{(C-20)}$$

The maximum static uniform pressure (ignoring static arching) which is loading the roof, p_{mst} in equation C-19, is equal to:

$$p_{mst} = \gamma_{mc}h_m + \gamma_{ms}d_m = (150/12^3)0.38 + (104/12^3)d_m \qquad \text{(C-21)}$$

where γ_{mc} and γ_{ms} are the weight densities of the micro-concrete and of the soil, respectively.

Substituting p_{mst} into equation C-19, and x_{mst} from equation C-19 and x_m^{total} from equation C-20, into equation C-17, yields the distortion for the above conditions and material properties as a function of the depth d_m and the geometric scaling factor, n, as a parameter and is shown in figure C-2 and C-3 for a clamped and simply supported slab, respectively. As can be seen in these figures, the distortion in the prediction of the roof center displacement does not exceed 10%.

Example 3: **Effect of the gravitational acceleration on small scale model predictions of the vertical pressure over the embedded roof in the current system.**

When extrapolating a small scale model stress, p_m, to a prototype stress p_p, true modelling requires (Table C-1):

$$p_p = p_m \tag{C-22}$$

However, when writing the pressure as a summation of dynamic and static portions, true extrapolation yields:

$$\begin{aligned} p_p^{true} &= p_{pdy} + p_{pst} = p_{mdy} + \gamma_{ms}(nd_m) = p_{mdy} + np_{mst} = \\ &\quad p_{mdy} + p_{mst} + (n-1)p_{mst} = p_m + (n-1)p_{mst} \end{aligned} \tag{C-23}$$

Applying the previous definition for the percentage of distortion, an expression for the pressure distortion is obtained, similar to the displacement distortion (equation

C-17):

$$\%\,Distortion = \frac{p_p^{true} - p_p}{p_p^{true}} \cdot 100 = \frac{(n-1)p_{mst}}{p_m + (n-1)p_{mst}} \cdot 100 = \frac{100}{1 + \frac{1}{(n-1)} \cdot \frac{p_m}{p_{mst}}} \qquad \text{(C-24)}$$

Figures C-4 and C-5 describe the pressure distortion percentage for a total peak experimental pressure of 100 psi and 25 psi, respectively. These represent some actual peak pressure values that were measured in the tests. The static portion of the pressure, p_{mst} was expressed as a function of the depth of burial, d_m, according to equation C-21. It can be seen in these figures that in the range of depth of burial which was used in this research (2.5 to 3 inches) the distortion in the peak pressure predictions is less than 30%, for a geometrical scaling factor as high as 60, and less than 20% for depth of burial of 2.5 inches and a scaling factor of 40.

Using a similar procedure, it can be shown that in general, the model to prototype prediction of any variable in the system, "VAR", is distorted due to lack of gravitational acceleration scaling in the model system, according to the static portion of that variable and to the geometrical scaling factor, n:

$$\%\,Distortion = \frac{VAR_p^{true} - VAR_p}{VAR_p^{true}} \cdot 100 = \frac{100}{1 + \frac{1}{(n-1)} \cdot \frac{VAR_m}{VAR_{mst}}} \tag{C-25}$$

Figures C-6 (a and b) illustrate how the distortion changes with the geometrical scaling factor, n, and with the static portion of the variable VAR^{total}/VAR^{static}. Figure C-6(a) describes the full range of this ratio, and figure C-6(b) the typical range in the current research. It can be seen that the distortion due to gravitation decreases as the dynamic nature of the phenomenon increases, and as the geometrical scaling factor decreases. It can also be seen, that the distortion in the current experimental system falls well within other experimental errors, and therefore is, indeed, insignificant.

Table C-1

Three Possible Prototype/Model Ratios

$\frac{\lambda_p}{\lambda_m}$	n	n	n
$\frac{\sigma_p}{\sigma_m}$	1	1	1
$\frac{\rho_p}{\rho_m}$	n^{-1}	n^{-3}	1
$\frac{M_p}{M_m}$	n^2	1	n^3
$\frac{a_p}{a_m}$	1	n^2	n^{-1}
$\frac{t_p}{t_m}$	$n^{1/2}$	$n^{-1/2}$	n
$\frac{v_p}{v_m}$	$n^{1/2}$	$n^{3/2}$	1
$\frac{F_p}{F_m}$	n^2	n^2	n^2

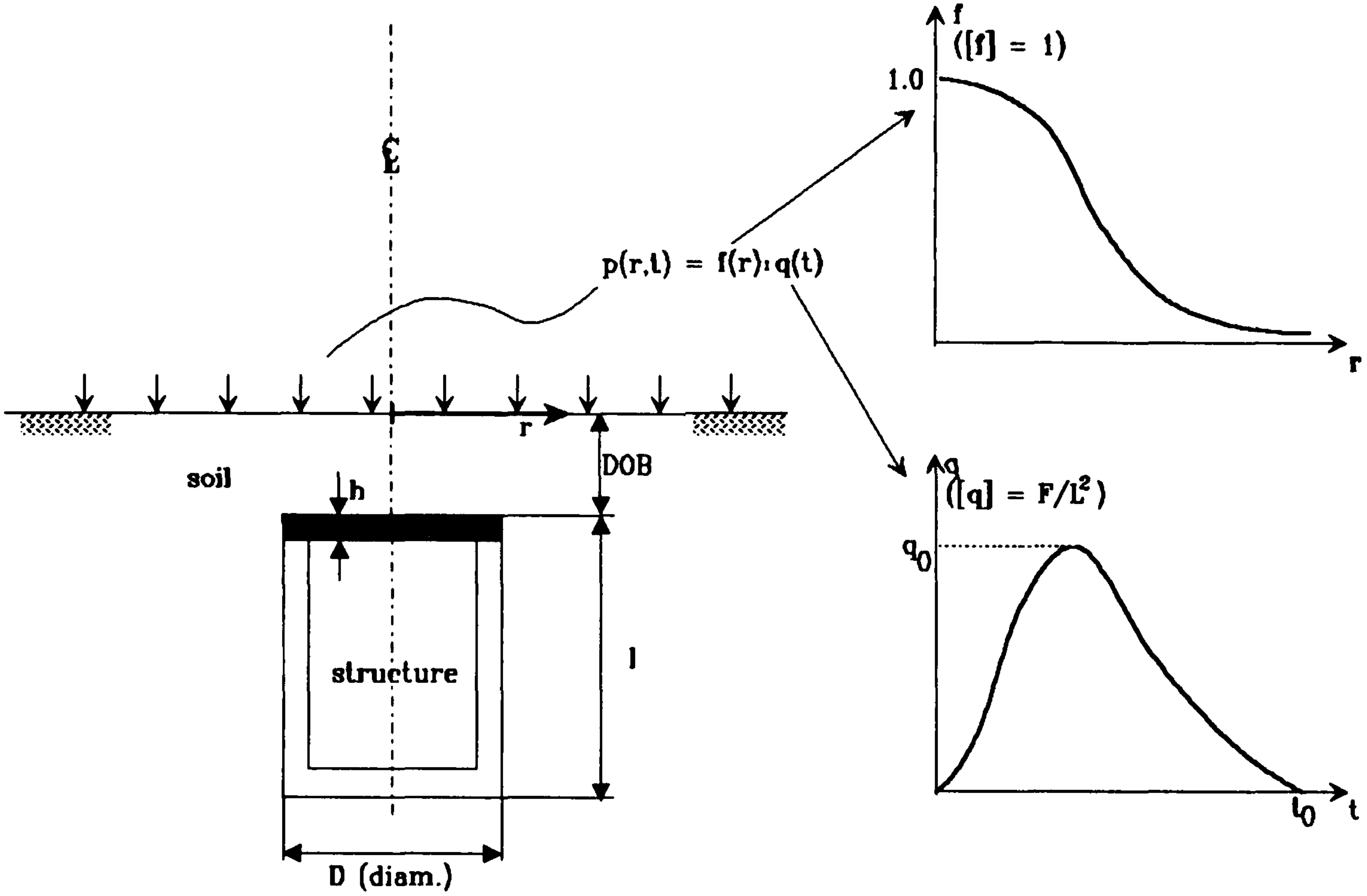
℄
p(r,t) = f(r)·q(t)
soil
h
DOB
structure
l
D (diam.)
r
f
([f] = 1)
1.0
r
q
([q] = F/L²)
q0
t0
t

Fig. C-1: Soil-structure system for dimensional analysis.

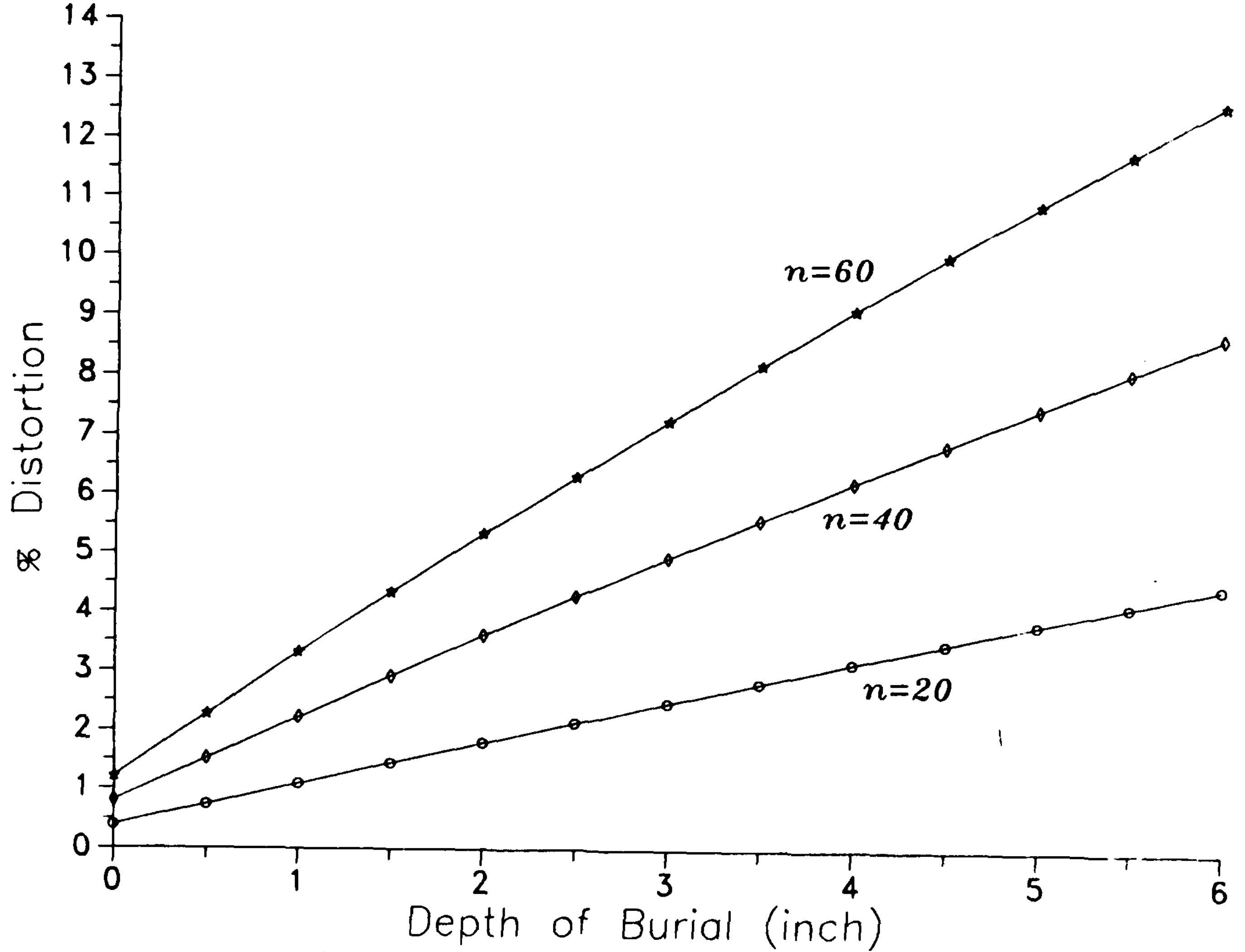

Fig. C-2: Distortion in displacement modeling h=0.38 inch, x_m(total)=0.01 inch (clamped slab).

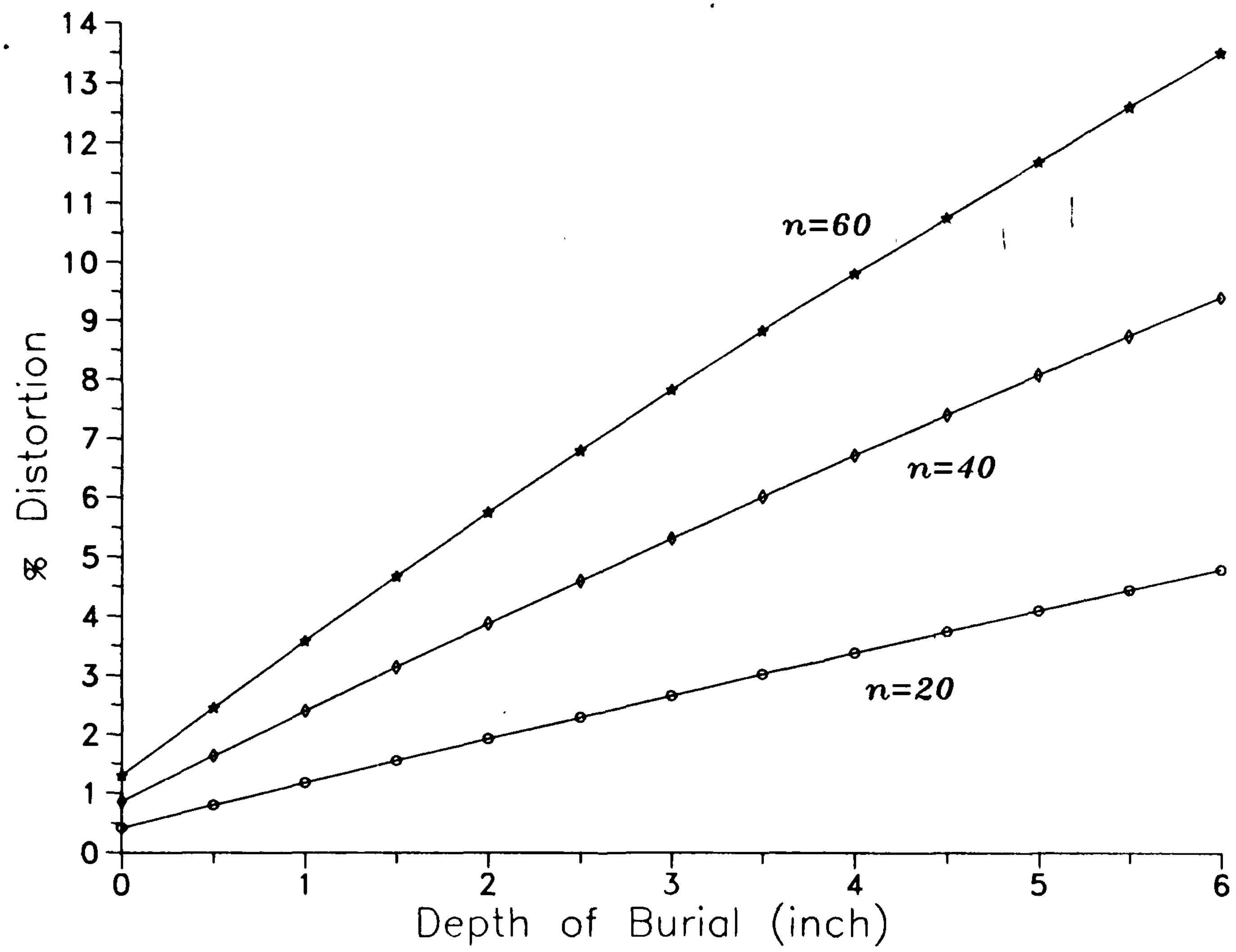

Fig. C-3: Distortion in displacement modeling
$h=0.38$ inch, x_m(total)$=0.04$ inch (simply supported slab).

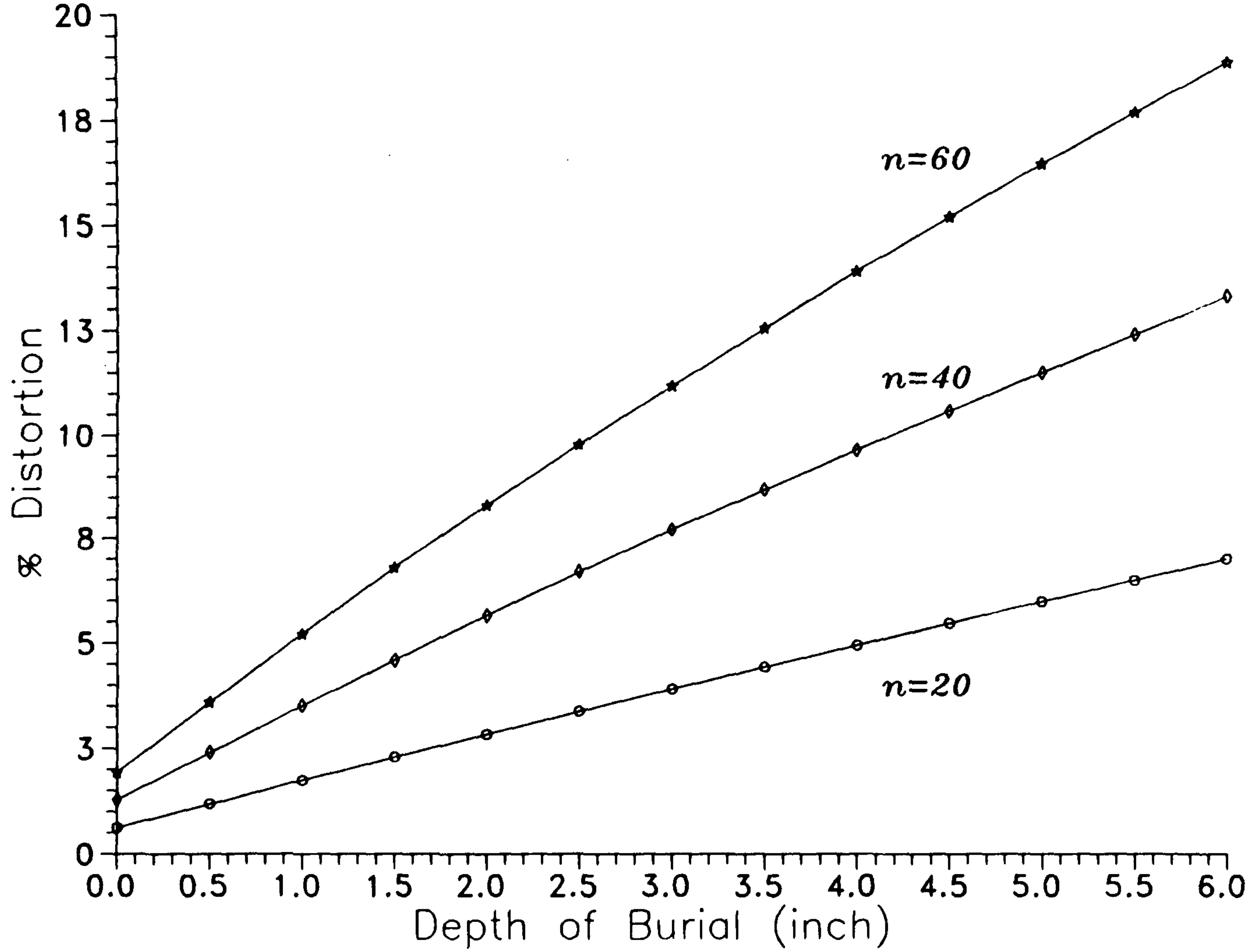

Fig. C-4: **Distortion in stress modeling**
h=0.5 inch, σ_m(total)=100 psi.

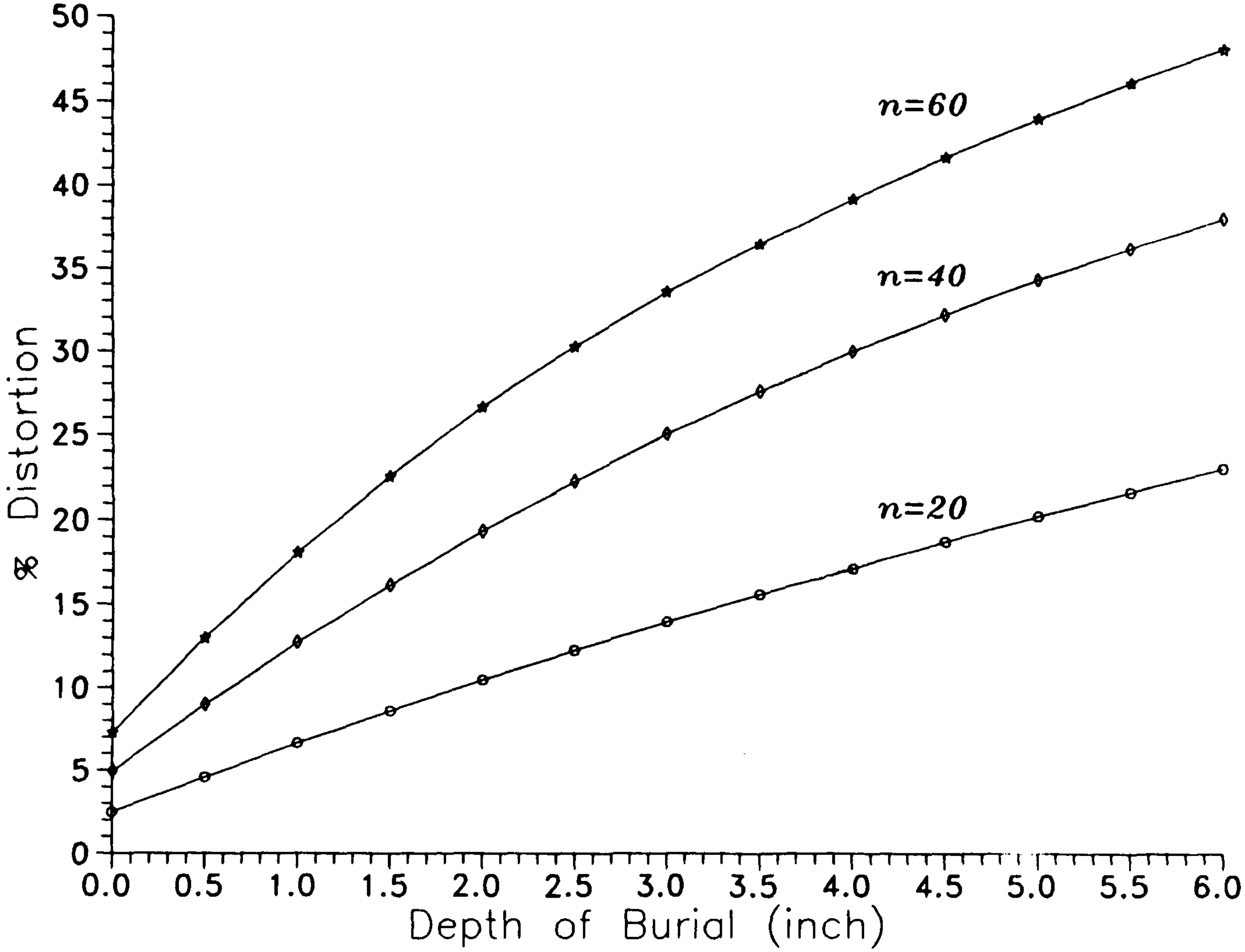

Fig. C-5: Distortion in stress modeling
h=0.5 inch, σ_m(total)= 25 psi.

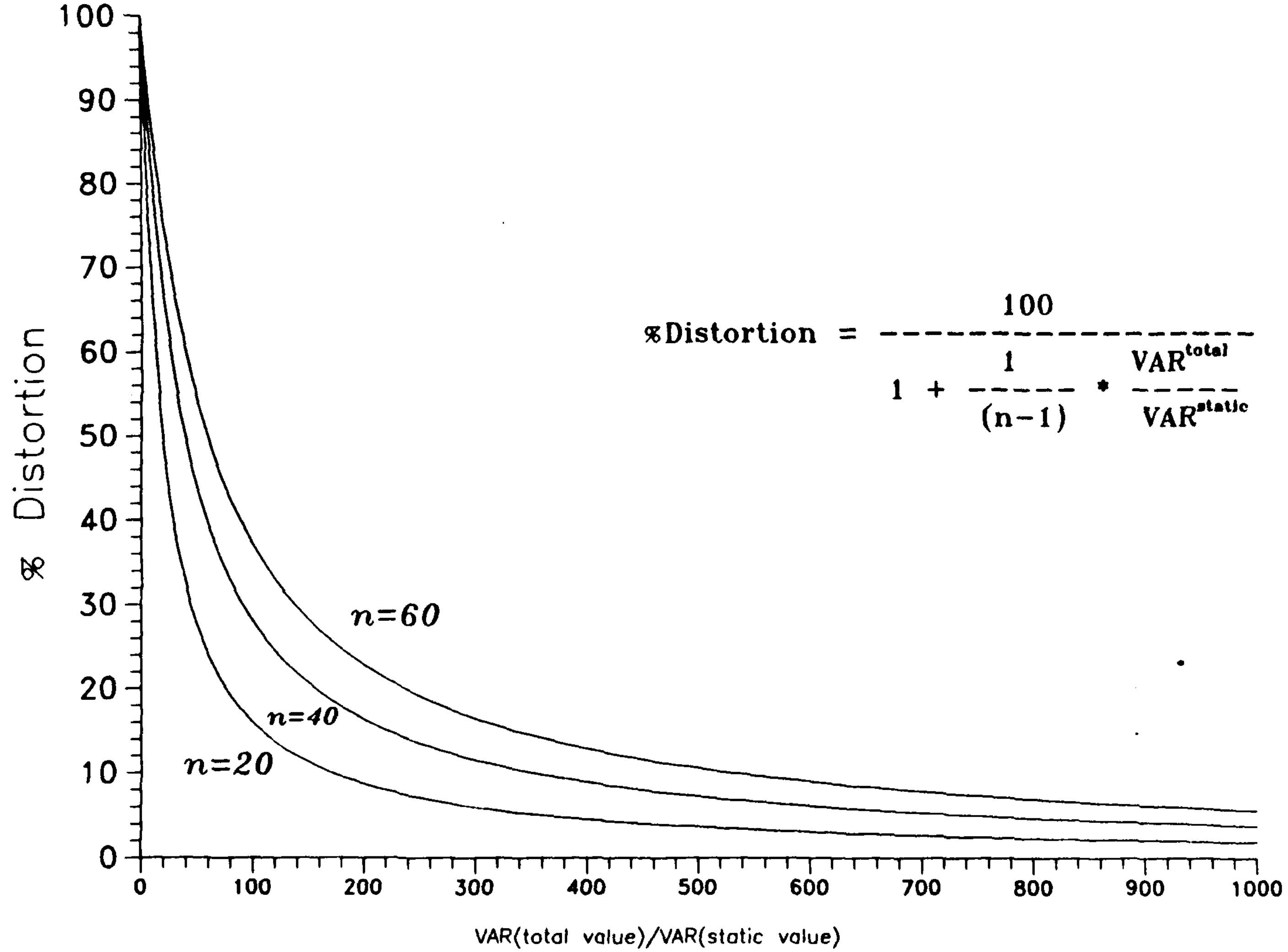

Fig. C-6(a): Distortion in modeling of time dependent variables.

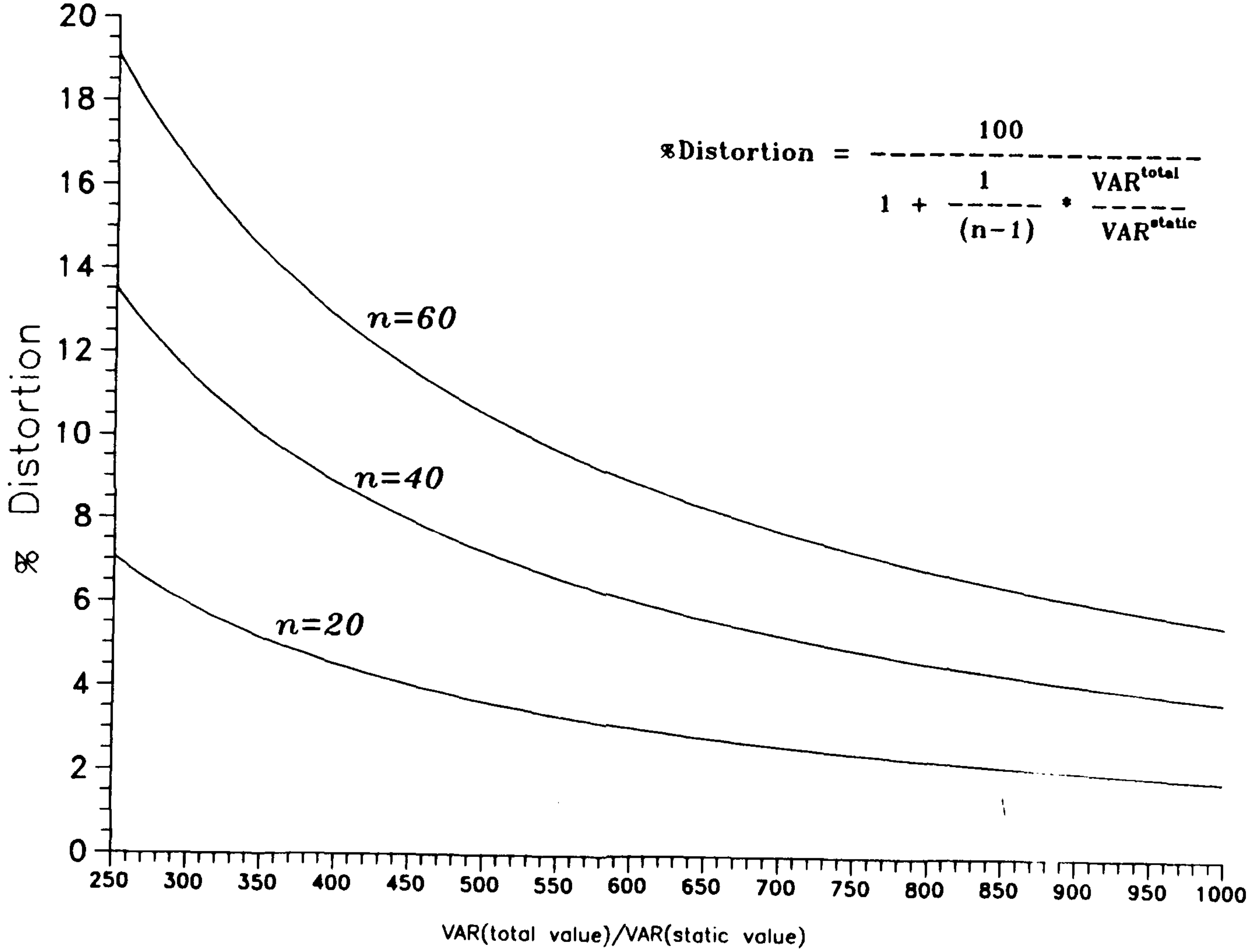

Fig. C-6(b): Distortion in modeling of time dependent variables.

APPENDIX D

EXPERIMENTAL RESULTS

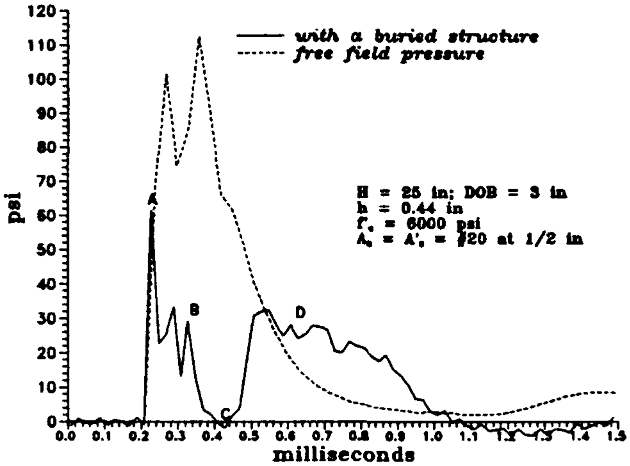

AT THE CENTER

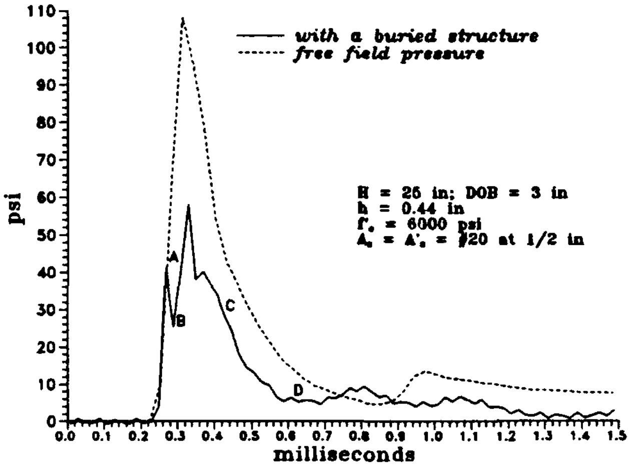

2 in FROM CENTER

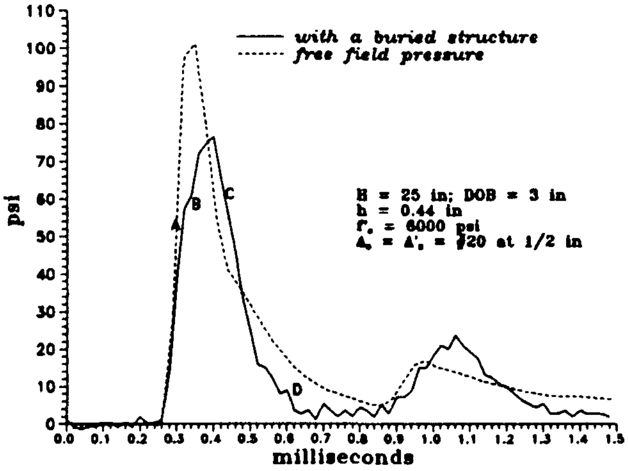

2.5 in FROM CENTER

Fig. D-1: Pressure records over a simply supported roof in test 2 v.s. free field (4th hit).

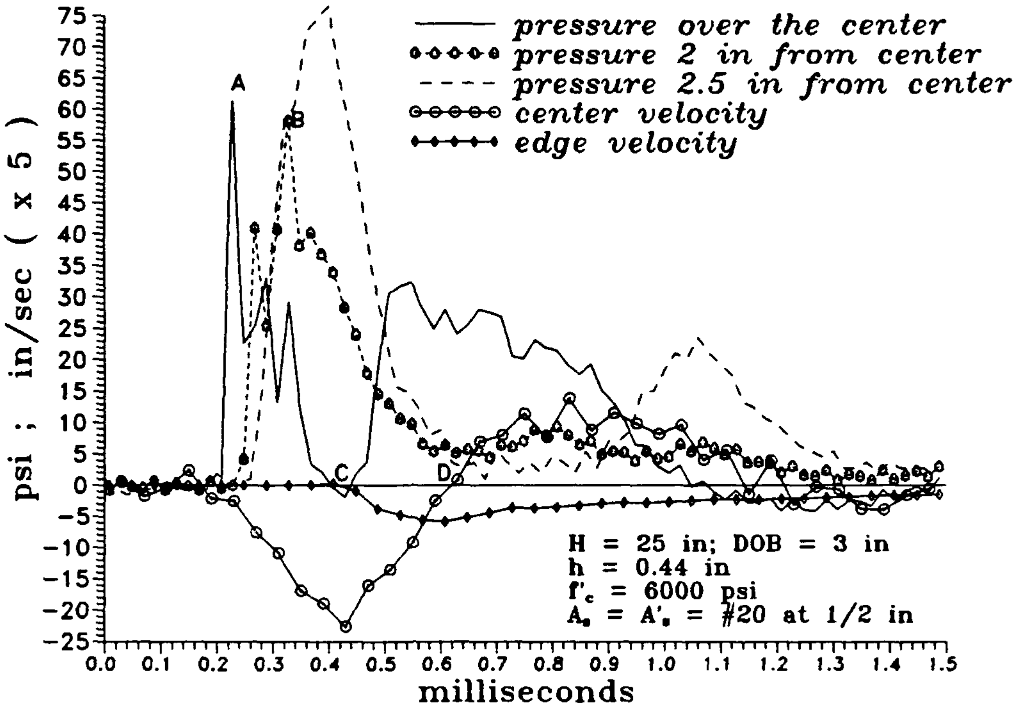

PRESSURE and VELOCITY

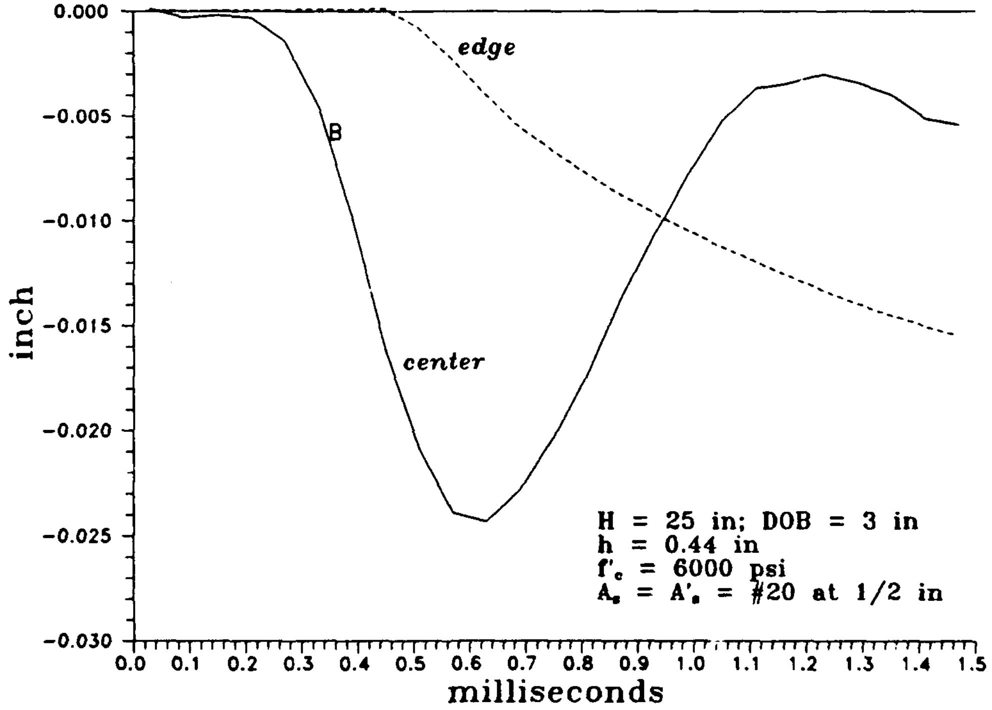

DISPLACEMENTS

Fig. D-2: Response of the simply supported roof in test 2.

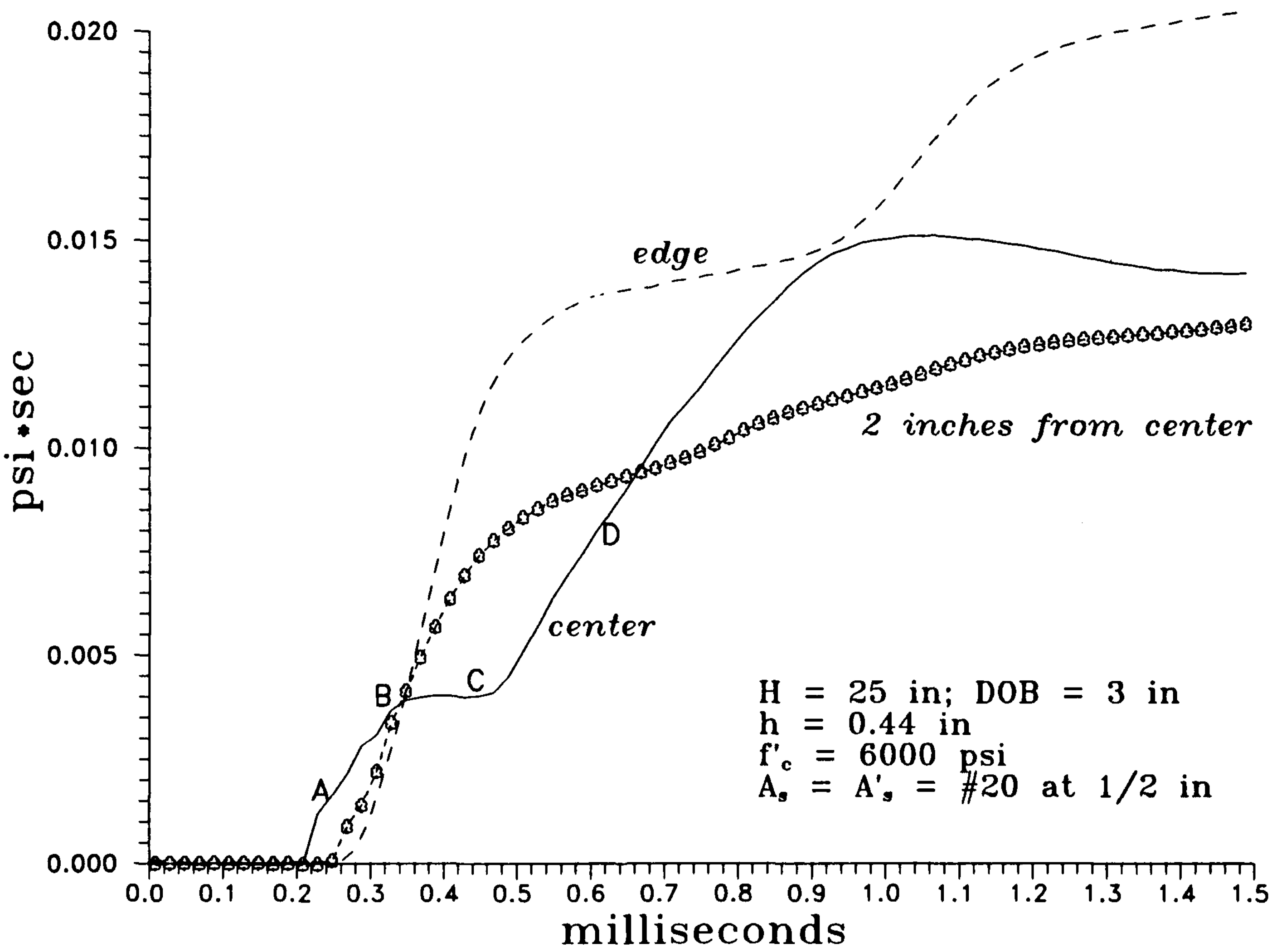

Fig. D-3: Impulse records over a SIMPLY SUPPORTED roof in test 2 (4th hit).

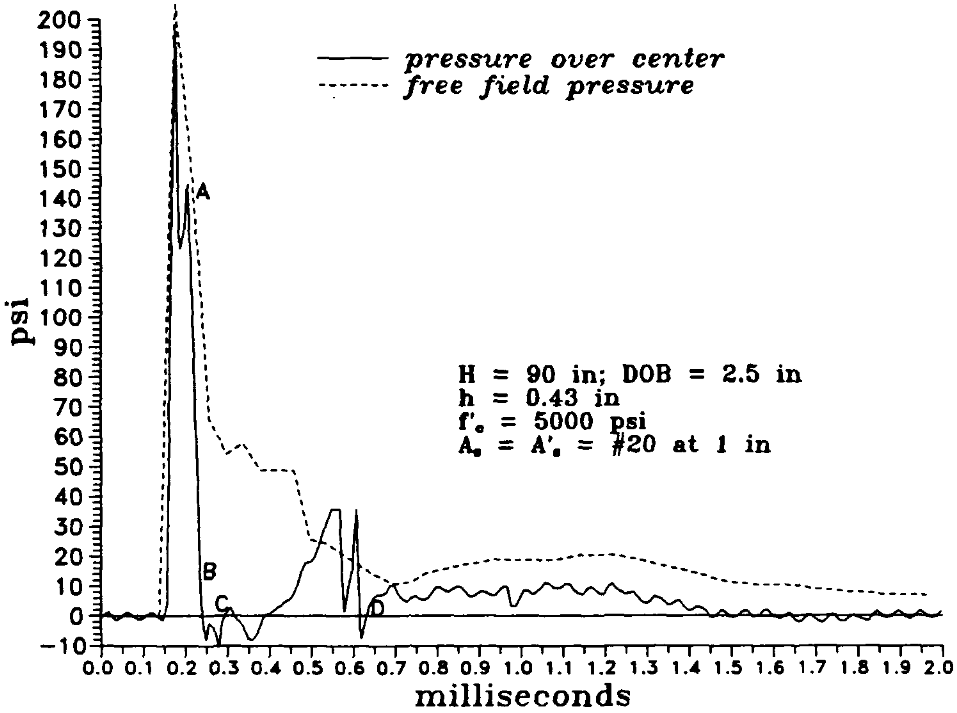

AT THE CENTER

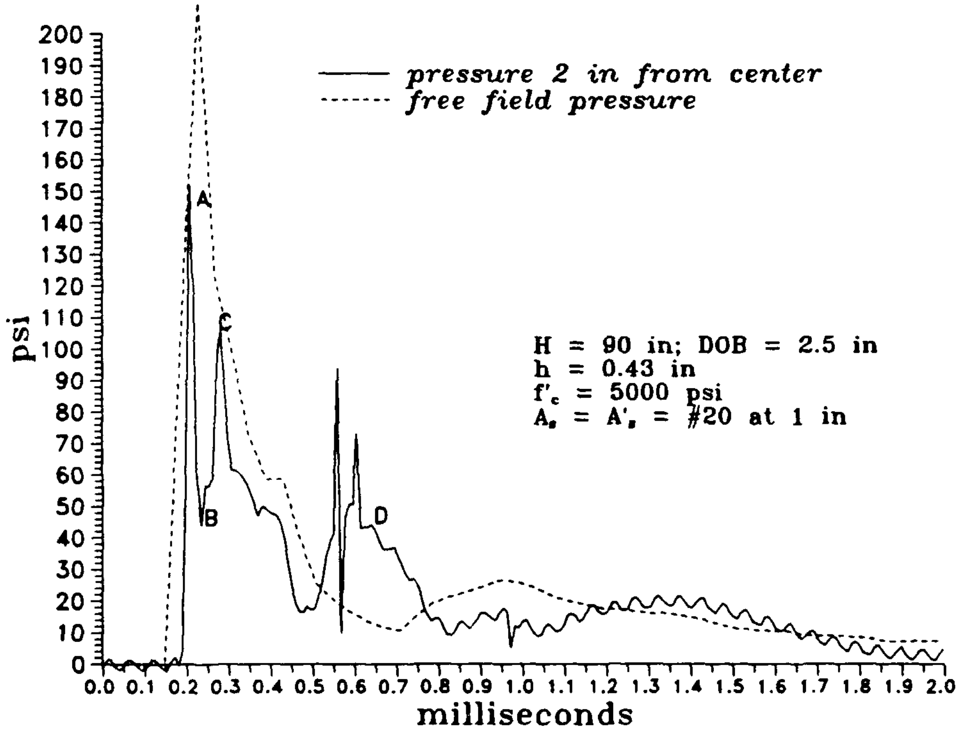

OVER THE EDGE

Fig. D-4: Pressure over the simply supported roof in test 6 (4th hit) v.s. free field.

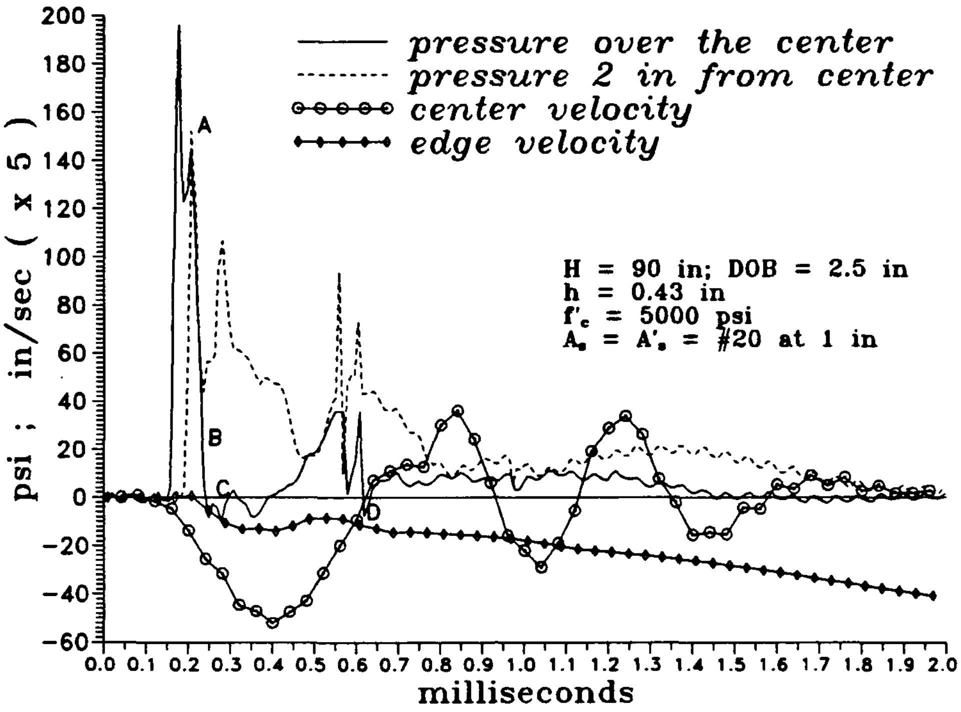

PRESSURE AND VELOCITY

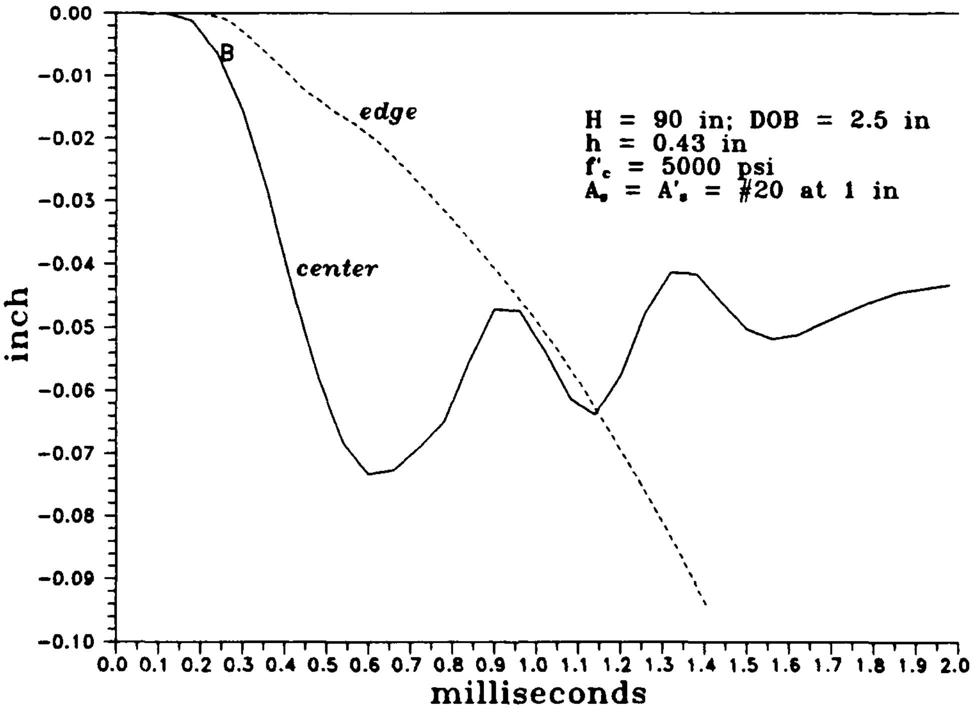

DISPLACEMENTS

Fig. D-5: Response a simply supported roof in test 6 (4th hit).

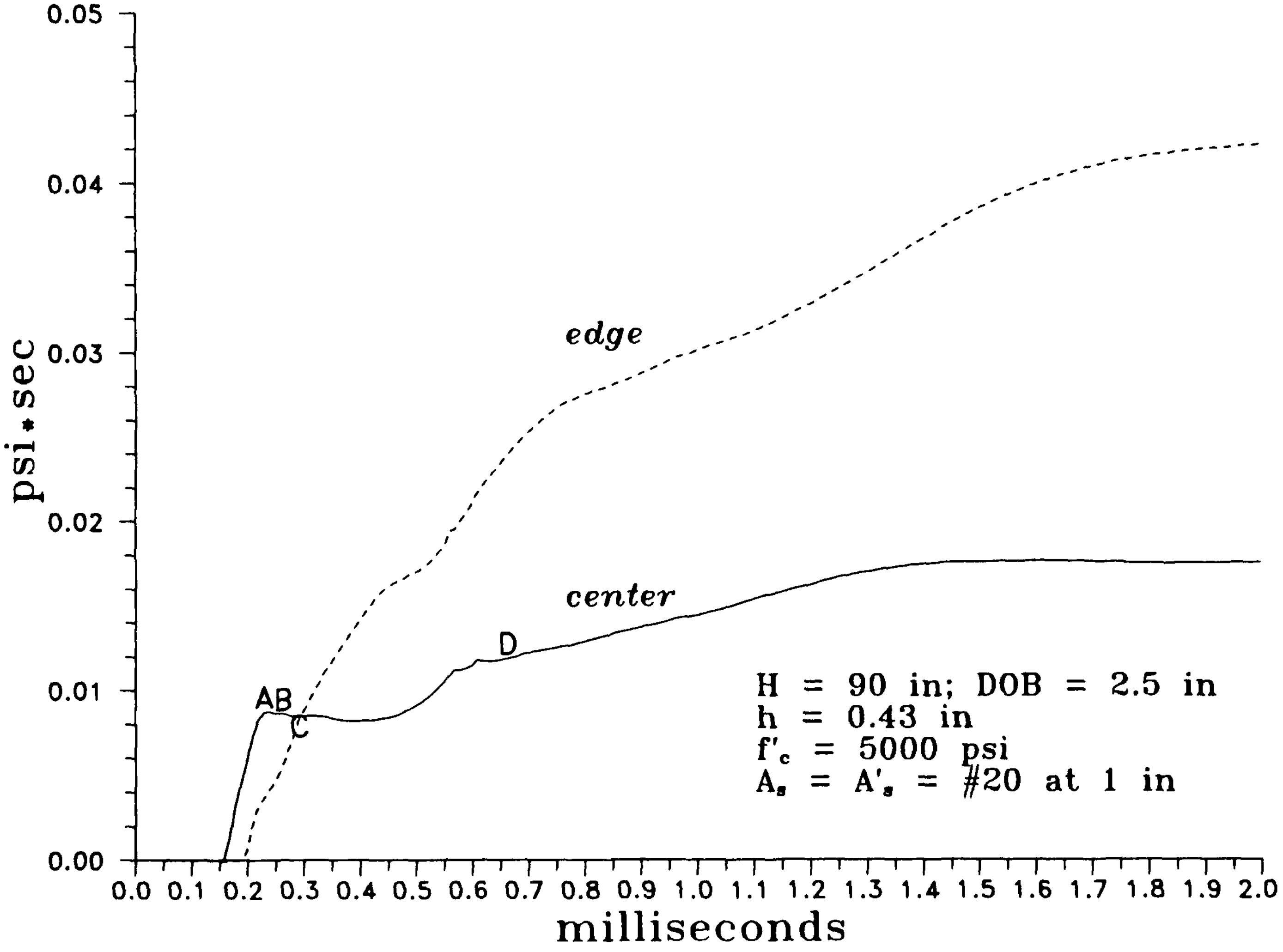

Fig. D-6: Impulse records over the simply supported roof in test 6 (4th hit).

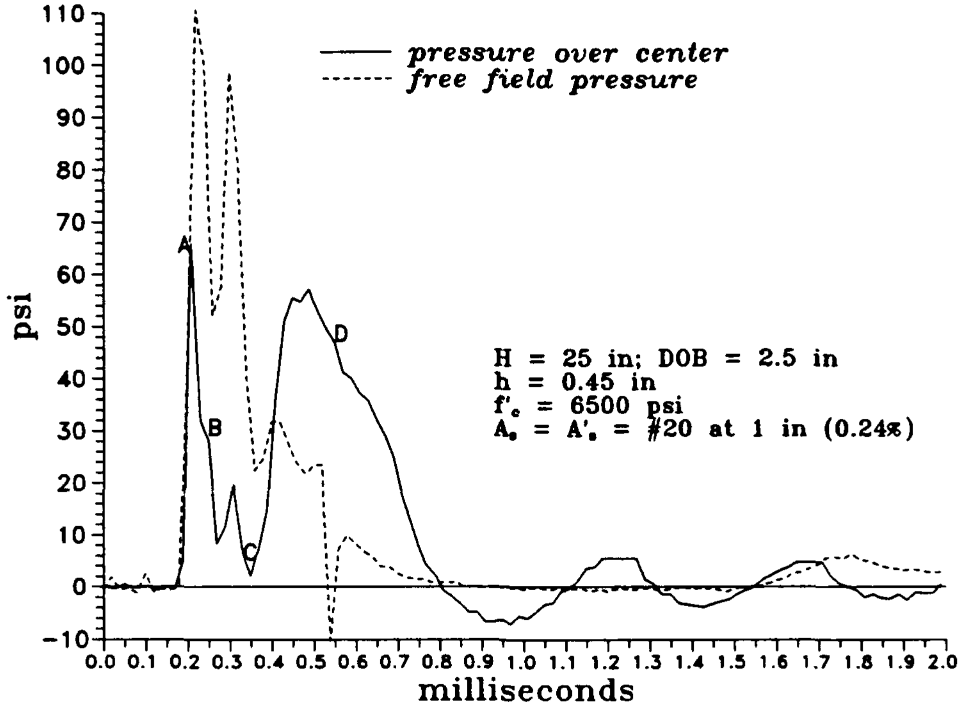

At THE CENTER

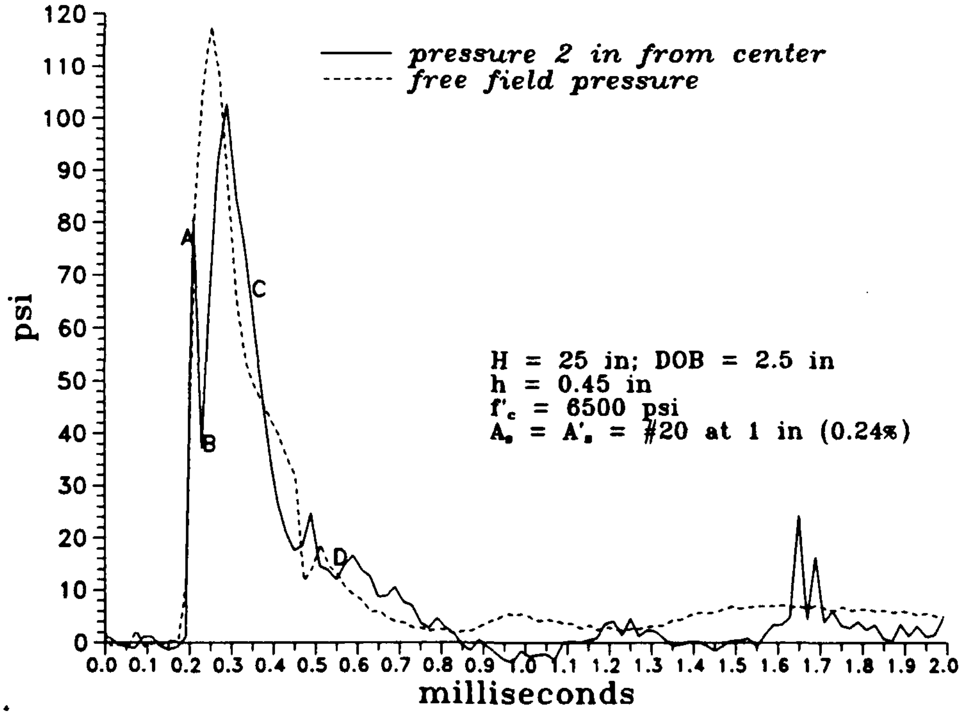

OVER THE EDGE

Fig. D-7: Pressure over the clamped roof in test 8 v.s. free field (3rdhit).

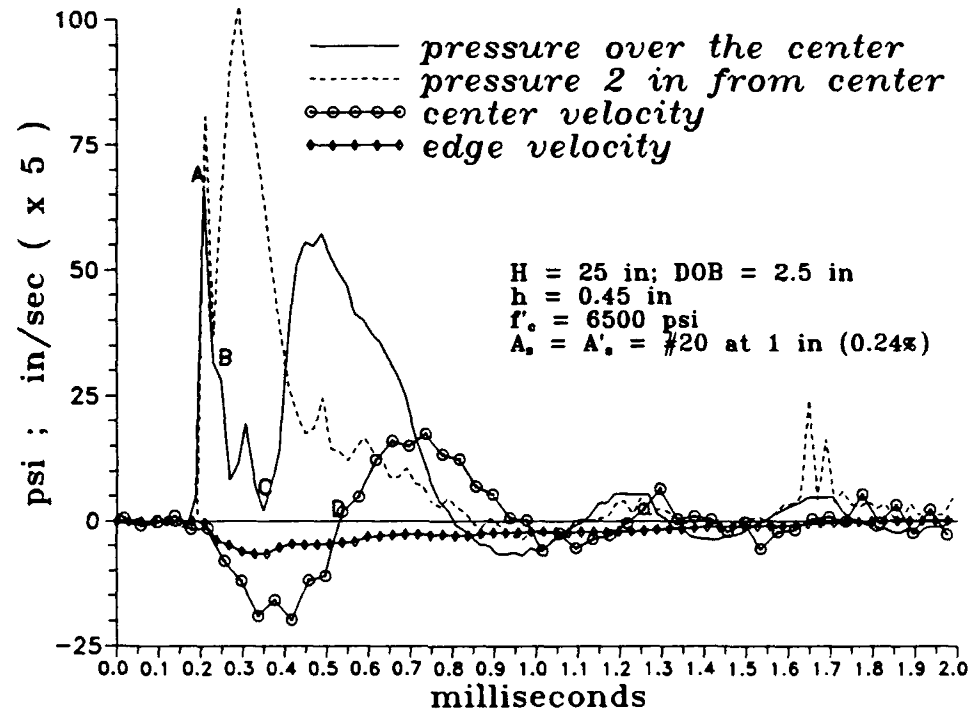

PRESSURE and VELOCITY

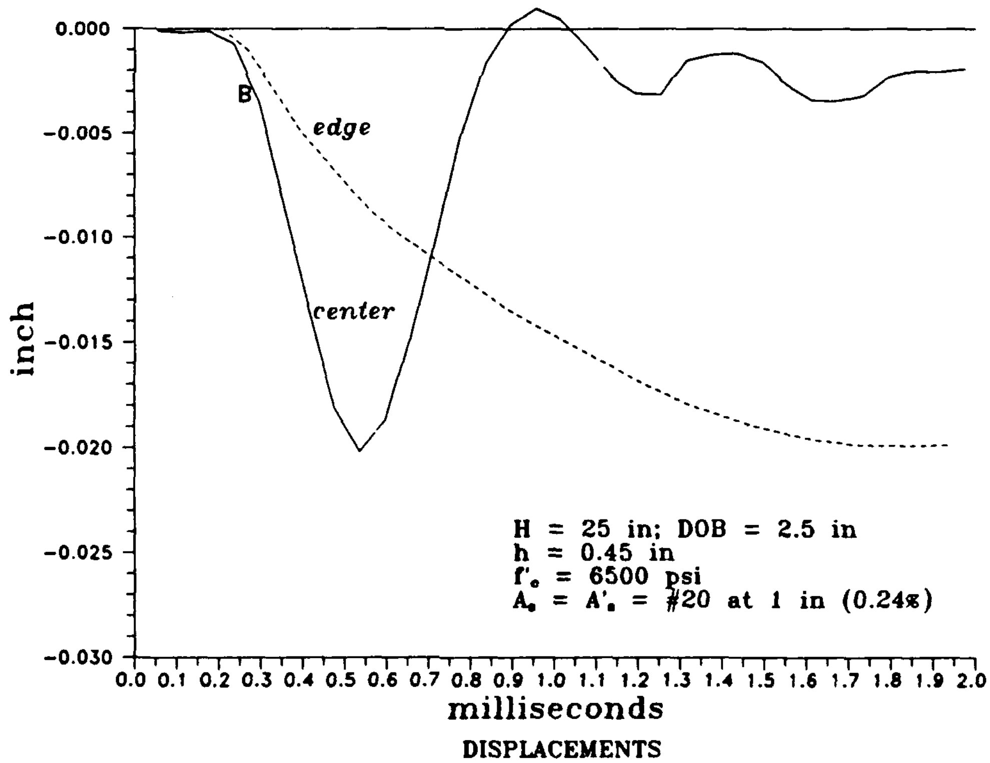

DISPLACEMENTS

Fig. D-8: Response of a clamped roof in test 8 (3^{rd} hit).

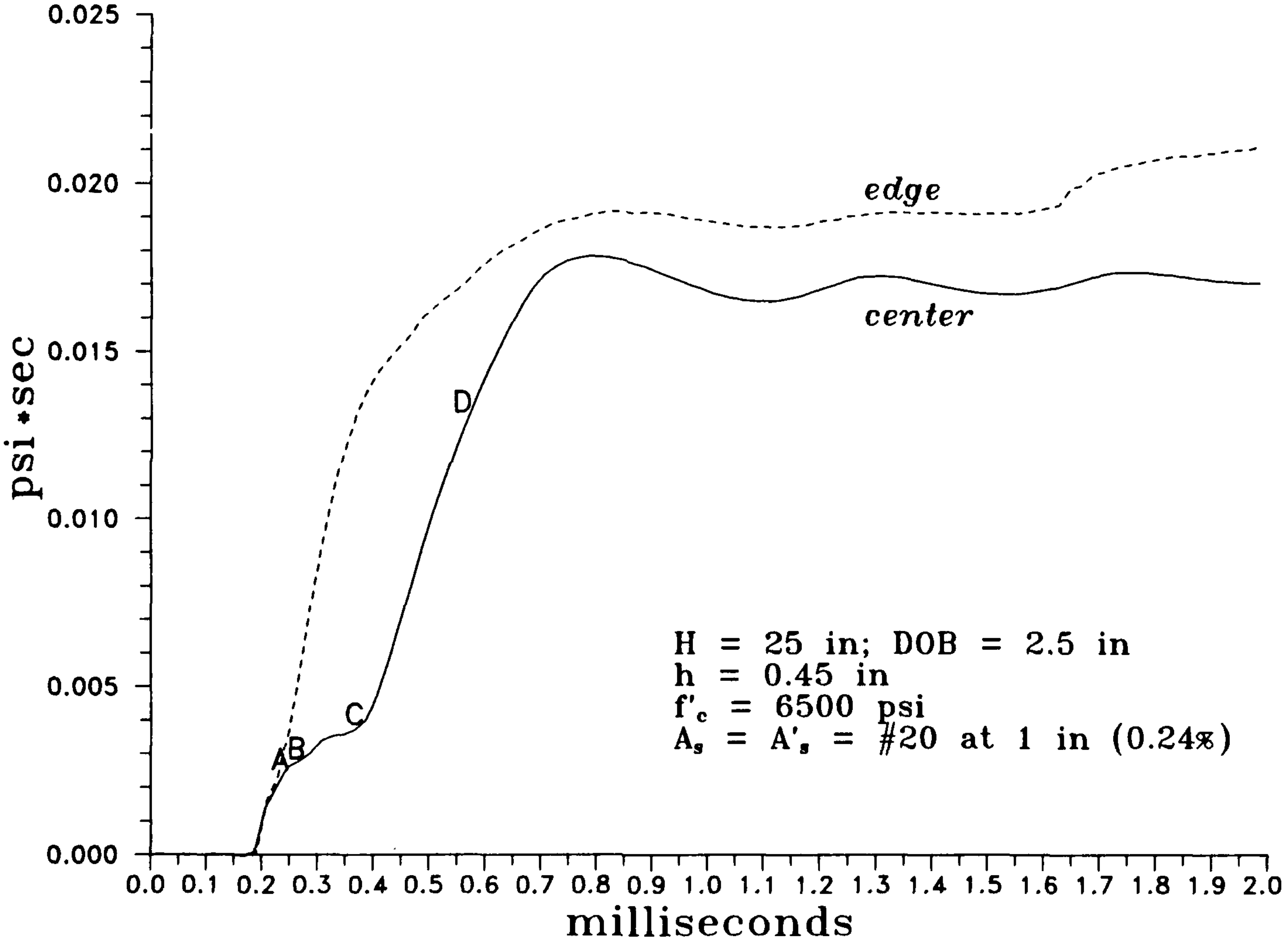

Fig. D-9: Impulse records over a clamped roof in test 8 (3^{rd} hit).

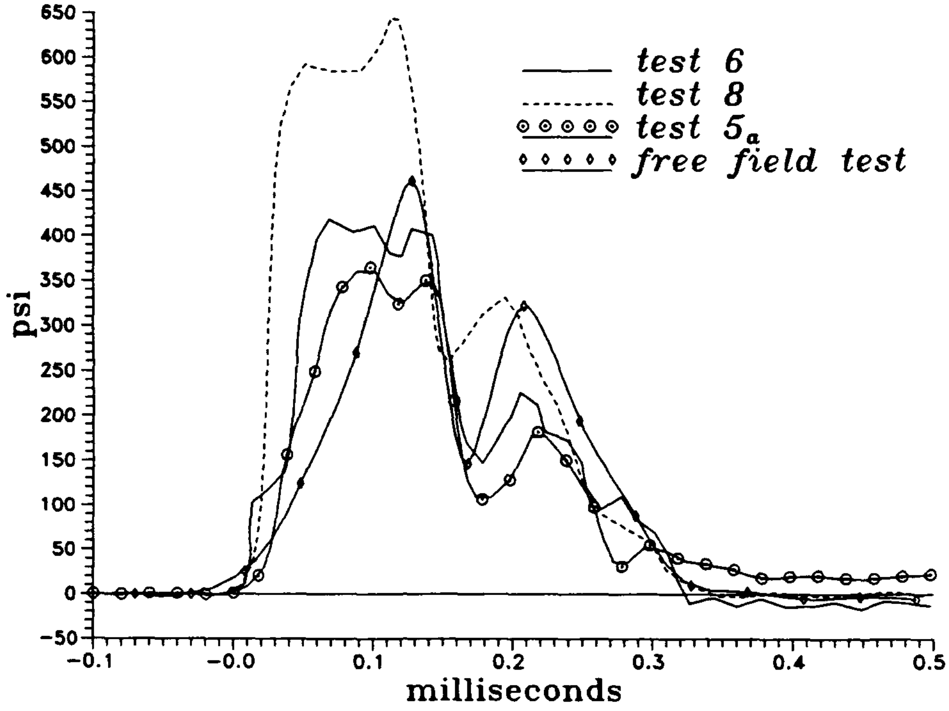

H = 90 inches

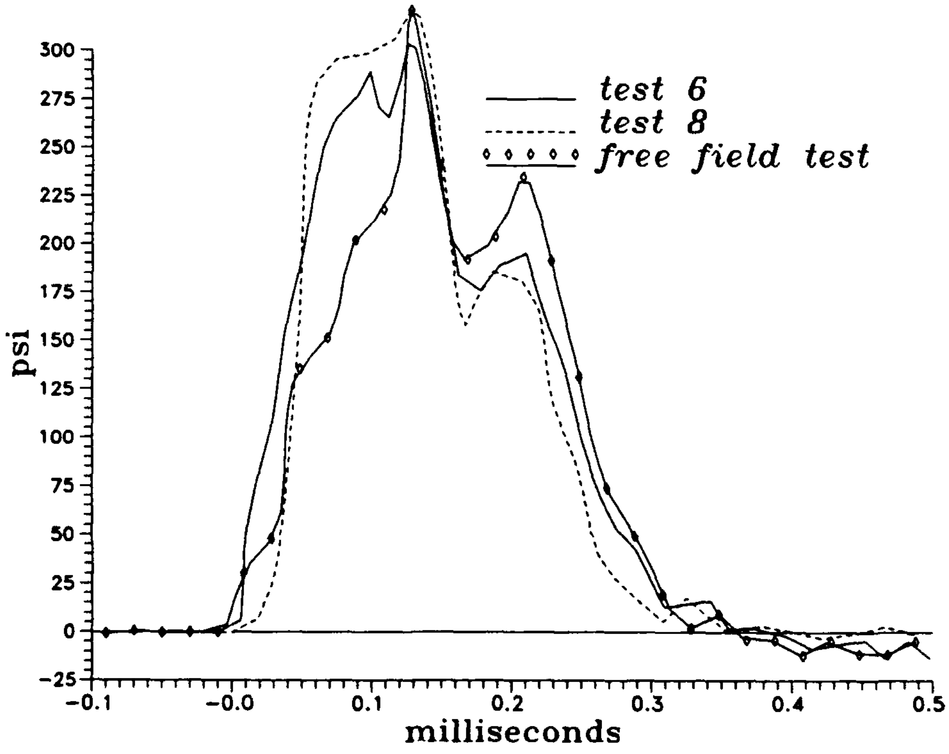

H = 25 inches

Fig. D-10: Pressure induced under the target plate center in the tests with DOB = 2.5 inches.

REFERENCES

1. Abbott P. A., "Non-Linear Static Arching for Vertically Buried Prismatic Structures", AFWL-TR 65-160, AD-801487, Kirtland, New Mexico, August, 1966.

2. Allgood J. R., "Summary of Soil-Structure Interaction", Technical Report R-771, AD-748581, NCEL, Port Hueneme, California, July, 1972.

3. American Concrete Institute, "Building Code Requirements for Reinforced Concrete (ACI 318-83)", Detroit, 1986.

4. Baker W. E., Westine P. S., Dodge F. T., "Similarity Methods in Engineering Dynamics", Hayden Book Company, Inc., New Jerset, 1978.

5. Bazant, Z. P., "Size Effect in Blunt Fracture: Concrete, Rock, Metal", ASCE, Journal of Engineering Mechanics, Vol. 110, No. 4, April 1984.

6. Bazant, Z. P., Kazemi M. T., "Determination of fracture energy, process zone length and brittleness number from size effect, with application to rock and concrete", International Journal of Fracture, Vol. 44, pp. 111-131, 1990.

7. Braja, M. D., "Principles of Geotechnical Engineering", PWS Publishers, Boston,

1985.

8. Chen H. L., "Dynamic Response of Embedded Structures", Ph.D. thesis, Department of Civil Engineering, Northwestern University, Evanston, IL., 1988.

9. Chen W. F., "Plasticity in Reinforced Concrete", McGraw-Hill, 1982.

10. Chen Y. J., Chen H. L., Dancygier A. N., Shah S. P., Keer L. M., "Tests of Model Reinforced Concrete Circular Slabs", ACI Structural Journal, V. 87, No. 6, November-December 1990.

11. Chung, L., Shah, S. P., "Effect of Loading Rate on Anchorage Bond and Beam-Column Joints", ACI Structural Journal, Vol. 86, No. 2, March-April, 1989.

12. Cunningham C. H., Townsend F. C., Fagundo F. E., "Development of Micro-concrete for Scale Model Testing of Buried Structures", Technical Report ESL-TR-85-49, Department of Civil Engineering, University of Florida, Gainesville, Florida, 1986.

13. Dallriva F. D., Kiger S. A., "Vibration Characteristics of a Large-Scale Buried Structure", The Shock and Vibration Bulletin, No. 56, August 1986.

14. Dancygier, A. N., "Analysis of Arching in NonHomogeneous Medium over a Buried Structure", M. Sc. thesis, Technion - Israel Institute of Technology, Haifa, 1985.

15. Denton, D. R., Flathau W. J., "Model Study of Dynamically Loaded Arch Structures", ASCE, Journal of the Engineering Mechanics Division, Vol. 92, EM3, June 1966, pp. 17-32.

16. Drake J. L., Walker R. E., Slawson T., "Backfill Effect on Buried Structure Response", Proc. of the Fourth International Symposium on the Interaction of Non-Nuclear Munitions with Structures, Vol. 2, Panama City Beach, Florida, April, 1989.

17. Entran Devices, Inc., "Load Cell Instruction and Selection Manual", February, 1985.

18. Getchell J. V., Kiger S. A., "Vulnerability of Shallow-Buried Flat-Roof Structures; Report 4, Foam HEST 3 and 6", Technical Report SL-80-7, Waterways Experiment Station, Structures Laboratory, Vicksburg, Miss., December 1981.

19. Getchell J. V., Kiger S. A., "Vulnerability of Shallow-Buried Flat-Roof Structures; Report 2, Foam HEST 4", Technical Report SL-80-7, Waterways Experiment

Station, Structures Laboratory, Vicksburg, Miss., October, 1980.

20. Getzler Z., Gellert M., Eitan R., "Analysis of Arching Pressures in Ideal Elastic Soil", ASCE, Journal of the Soil Mechanics and Foundations, Vol. 96, No. SM4, July, 1970.

21. Gill H. L., True D. G. ,"Active Arching of Sand During Static Loading", Technical Note N-759, AD-684455, NCEL, Port Hueneme, California, November, 1966.

22. He Y. A., "Soil-Structure Interaction Under Blast Loading", Proc. of the Second Symposium on The Interaction of Non-Nuclear Munitions with Structures, Panama City Beach, Florida, April, 1985.

23. Jester G. E., "An Experimental Investigation of Soil-Structure Interaction in a Cohesive Soil", Technical Report N-70-7, AD-706210, Waterways Experiment Station, Structures Laboratory, Vicksburg, Miss., March, 1970.

24. John, R., Shah S. P., "Constitutive Modelling of Concrete under Impact Loading", Proceedings of the First International Conference on Effects of Fast Transient Loading, Lausanne, August 1987, pp. 37-65.

25. Kiger S. A., Getchell J. V., "Vulnerability of Shallow-Buried Flat-Roof Structures; Report 1, Foam HEST 1 and 2", Technical Report SL-80-7, Waterways Experiment Station, Structures Laboratory, Vicksburg, Miss., September 1980.

26. Kiger S. A., Balsara J. P., "Response of Shallow Buried Structures to Blast Loads", AD-A056455, Waterways Experiment Station, Structures Laboratory, Vicksburg, Miss., June, 1978.

27. Kiger S. A., Eagles P. S., Baylot J. T., "Response of Earth-Covered Slabs in Clay and Sand Backfills", Technical Report SL-84-18, AD-A149296, Waterways Experiment Station, Structures Laboratory, Vicksburg, Miss., October 1984.

28. Ko H. Y., Scott R. F., "Deformation of Sand at Failure", ASCE, Journal of the Soil Mechanics and Foundations Division, Vol. 94, No. SM4, Sept. 1967, pp. 883-898.

29. Ko H. Y., Scott R. F., "Deformation of Sand in Hydrostatic Compression", ASCE, Journal of the Soil Mechanics and Foundations Division, Vol. 93, No. SM3, May 1967, pp. 137-156.

30. Krauthammer T., Flathau W. J., Smith J. L., Betz J. F., "Lessons from Explosive Tests on RC Buried Arches", ASCE, Journal of Structural Engineering, Vol. 115,

No. 4, April, 1989.

31. Lambe T. W., Whitman R. V., "Soil Mechanics", John Wiley & Sons, Inc., New York, 1969.

32. Leissa A. W., "Vibration of Plates", NASA SP-160, 1969.

33. Murtha R. N., "Arching in Soils with Cohesion and Intergranular Friction", Technical Report R-793, AD-766100, NCEL, Port Hueneme, California, July, 1973.

34. Newmark, N. M., "The Basis of Current Criteria for the Design of Underground Protective Construction", Proc. of the Symposium on Soil-Structure Interaction, Tucson, Arizona, September, 1964.

35. Ottosen, N. S., "A Failure Criterion for Concrete", ASCE, Journal of the Engineering Mechanics Division, Vol. 103, EM4, 1977, p. 527.

36. Rudeen D. K., Rath J. S., "SAMSON2, A Nonlinear Two-Dimensional Structure-Media Interaction Computer Code: User's Manual (Revised)", New Mexico Engineering Research Institute, University of New Mexico, Albuquerque, New Mexico, September 1986.

37. Sabnis G. M., Harris H. G., White R. N., Mirza M. S., "Structural Modeling and Experimental Techniques", Prentice-Hall, Engelwood Cliffs, 1983.

38. Schmertmann J. H., "Comparison of One and Two Specimen CFS Tests", ASCE, Journal of the Soil Mechanics and Foundations Division, Vol. 88, No. SM6, December 1962, p. 169.

39. Selig E. T., Vey E. E., "Shock induced Stress Wave Propagation in Sand", ASCE, Journal of the Soil Mechanics and Foundations, Vol. 91, SM3, May 1965, pp. 19-49.

40. Shin C. J., "Dynamic Soil-Structures Interaction", Doctoral thesis, Department of Civil Environmental and Architectural Engineering, University of Colorado, Boulder, CO., 1987.

41. Spangler M. G., "Protection of Underground Structures by Arch Action Associated with the Imperfect Ditch Method of Construction", Proc. of the Symposium on Soil-Structure Interaction, Tucson, Arizona, September, 1964.

42. Suaris W., Shah S. P., "Properties of Concrete Subjected to Impact", ASCE, Journal of Structural Engineering, Vol. 109, No. 7, July, 1983.

43. Szilard R., "Theory and Analysis of Plates - Classical and Numerical Methods", Prentice-Hall, 1974.

44. Takahashi S. K., "Effect of Backpacking and Internal Pressurization on Stresses Transmitted to Buried Cylinders", Technical Report R-789, AD-764058, NCEL, Port Hueneme, California, May, 1973.

45. Talda P. M., Mosborg R. J., "An Experimental Investigation of the Arching Phenomenon Occurring over a Buried Rectangular Plate", AFWL-TR 65-78, AD-484717, Kirtland, New Mexico, June, 1966.

46. Taylor E. S., "Dimensional Analysis for Engineers", Clarendon Press, Oxford, 1974.

47. Terzaghi K., "Theoretical Soil Mechanics", John Wiley & Sons, Inc., New York, 1943.

48. Timoshenko, S., "Strength of Materials", Van-Nostrand, Part II, 1970, p. 99.

49. Timoshenko S., "Vibration Problems in Engineering", Van-Nostrand, 1941.

50. Ueng T. S., Tzou Y. M., Lee C. J., "The Effect of End Restraint on Volume

Change and Particle Breakage of Sands in Triaxial Tests", ASTM, STP 977, Advanced Triaxial Testing of Soil and Rock, Philadelphia, 1988, pp. 679-691.

51. Weidlinger P., Hinman E., "Analysis of Underground Protective Structures", ASCE, Journal of Structural Engineering, Vol. 114, No. 7, July, 1988.

52. Westine, P. S., "Replica Modeling in Soil Dynamics", ASCE, Journal of the Soil Mechanics and Foundations, Vol. 92, SM6, Nov. 1966, pp. 169-187.

53. Whitman R. V., Healy K. A., "Shear Strength of Sands During Rapid Loadings", ASCE, Journal of the Soil Mechanics and Foundations, Vol. 88, SM2, April 1962, pp. 99-132.

54. Windham J. E., "Effect of Backfill Compaction on Design Criteria for Hardened Facilities: Result of Soil-Structure Interaction Calculations for Dry Types I and II Backfill Materials", Technical Report S-76-4, AD-A026936, Waterways Experiment Station, Vicksburg, Miss., June 1976.

55. Yankelevsky D., "Analysis of Arching in Granular Medium over Buried Structure", Research Thesis, Submitted in partial fulfillment of the requirements for the degree of Master of Science in Civil Engineering, Technion - Israel Institute of Technology, May 1972.

PUBLICATIONS

Chen, Y.J., Chen, H.L., Dancygier, A.N., Shah, S.P., Keer, L.M., "Tests of small scale reinforced concrete circular slabs", ACI Structural Journal, V. 87, No. 6, November-December 1990.

Dancygier, A.N., Shah, S.P., Keer, L.M., "Dynamic response of embedded circular reinforced micro-concrete slabs - an experimental study", Proceedings of the Fifth International Symposium on Interaction of Conventional Munitions with Protective Structures, Mannheim, Germany.